

**FTIR-Spectroscopic Measurement of
Directional Spectral Emissivities
of Microstructured Surfaces**

Lila Raj Koirala

FTIR-Spectroscopic Measurement of Directional Spectral Emissivities of Microstructured Surfaces

DISSERTATION

A Thesis Accepted
by the Department of Mechanical Engineering
of the Helmut - Schmidt University,
University of the Federal Armed Forces Hamburg, Germany
in Partial Fulfilment of the Requirements
for the Academic Degree of Doktor-Ingenieur

by

Dipl.-Ing. Lila Raj Koirala

from Pokhara, Nepal

Hamburg, October 2004

Acknowledgement

This research has been carried out during my stay as research assistant at the institute of Thermodynamics of the Helmut-Schmidt University/ University of the Federal Armed Forces Hamburg, Germany, under supervision of Professor Dr.-Ing. S. Kabelac. I am very much grateful to him for his guidance, constructive criticism, help in steering my way on the correct scientific path and for providing most congenial working conditions. I am also thankful to Professor Dr.-Ing. J. Ahrendts for accepting to be the second examiner and giving an intellectual support.

The cooperation by Professor Dr.-Ing. W. Roetzel and guest Professor Dr.-Ing. T. Bes from Poland made me possible to be in contact with Professor Kabelac. Without their support my research stay at this University could not have been realized. I thank them all collectively.

The professional advice provided by Dr.-Ing. D. Labuhn and the support by Dipl.-Ing. M. Meschkat in experimental works are invaluable for which I am thankful. I am also grateful to Mr. B. Flashaar, Mr. M. Schütt and all other staff members of our institute for their support in several aspects of this work.

I would like to express my deepest thanks to Brigadier General Amrit Lal Shrestha and Brigadier General Shambhu Dhoj Shah who effectively made it possible that I could take up this research work.

I would also like to thank my parent as well as parents-in-law for the motivation and encouragement given to me to do this research.

Last but not least, I thank my wife Sheela and our children Arya and Shreya for providing the supportive and harmonious conditions during this work which are the basic gradients for its success.

Contents

Nomenclature	IV
1 Introduction	1
1.1 General Overview.....	1
1.2 Aims of Investigation.....	4
2 Theoretical Background	5
2.1 Radiative Properties of Materials and Governing Laws of Radiation.....	5
2.1.1 Planck's Radiation Law.....	6
2.1.2 Emissivity.....	7
2.1.3 Absorptivity.....	11
2.1.4 Reflectivity.....	12
2.1.5 Transmissivity.....	15
2.1.6 Kirchhoff's Law of Radiation.....	16
2.1.7 Relationships between Radiative Properties of Materials.....	17
2.2 Radiative Heat Exchange and View Factor.....	19
2.3 Optical Constants.....	21
2.4 Fresnel's Equations.....	24
3 Literature Survey	29
3.1 Calorimetric Methods.....	29
3.2 Radiometric Methods.....	32
3.2.1 FTIR-Emission Spectroscopy.....	39
3.2.2 Regular Surface Macrostructures.....	43
3.2.3 Periodic Microstructured Surfaces.....	47
4 Modeling of Emission from Periodic Surface Structures	54
4.1 Geometric Optic Model.....	54
4.2 Electromagnetic Theory.....	60
4.3 Classical Optical Grating Theory.....	65

5 Principle and Methods of Measurement of Emissivity	76
5.1 Calorimetric Measurement Technique.....	76
5.2 Radiometric Measurement Technique.....	78
5.2.1 Indirect Determination of Emissivity.....	78
5.2.2 Direct Determination of Emissivity.....	80
6 Numerical Simulation and calculation of Sample Surface Temperature	84
6.1 Theoretical Estimation of Temperature of Sample Surface.....	85
6.2 Heat Transfer in Vacuum.....	91
6.3 Simulation of Temperature Distribution on Sample Surface by Finite Element Method (FEM).....	95
6.4 Surface Temperature Measurement with an Infrared Thermo-camera.....	102
6.5 Effect of Temperature Measurement Errors on Emissivity.....	109
7 Understanding of FTIR-Spectroscopy	111
7.1 The FTIR-Spectrometer.....	111
7.1.1 Advantages and Disadvantages of FTIR-Spectrometer.....	115
7.1.2 Calibration Formula for FTIR-Spectrometer.....	117
7.2 Method of Conversion of Interferogram to Spectrum.....	121
7.3 Correction of Reflection of Radiation from Surroundings.....	124
8 Measurement of Directional Spectral Emissivity	128
8.1 Experimental Set up.....	128
8.1.1 Sample Chamber in connection with FTIR-Spectrometer.....	130
8.1.2 Sample Heating System.....	133
8.1.3 Technical Realization of Blackbody Radiator.....	134
8.2 Fabrication of Microstructured Silicon Surfaces.....	136
9 Results and Discussion	139
9.1 Calibration Parameters.....	139
9.2 Spectral Emissivity of Blackbody Cavity.....	141
9.3 Validation of Results of Emissivity Measurements.....	143
9.3.1 Nextel-Velvet-Coating 811-21.....	144
9.3.2 Borosilicate Glass B 270.....	147

9.3.3 Sand Blasted Aluminium.....	152
9.3.4 Undoped Silicon.....	154
9.4 Periodic Microstructured Silicon Surface.....	158
9.4.1 Normal Spectral Emissivity.....	159
9.4.2 Directional Spectral Emissivity at Azimuthal Angle, $\varphi = 0^\circ$	163
9.4.3 Directional Spectral Emissivity at Azimuthal Angle, $\varphi = 90^\circ$	169
9.4.4 Azimuthal Angle Dependence of Directional Spectral Emissivity.....	174
10 Conclusions and Suggestions for Further Works.....	180
10.1 Conclusions.....	180
10.2 Further Works.....	182
10.3 Applications.....	183
Appendix.....	184
A Measurement Data.....	184
B Measurement Diagrams.....	202
C References.....	219

Nomenclature

Latin Letters

Symbol	Unit	Quantity
A	m ²	surface area
A	-	auxiliary coefficient, equation (6.15)
<i>a</i>	-	auxiliary parameter, equation (2.48)
<i>a</i>	m ² s ⁻¹	thermal diffusivity
<i>a_E</i>	-	accommodation coefficient
B	-	auxiliary coefficient, equation (6.16)
B	Wm ⁻²	background radiation
b	-	auxiliary parameter, equation (2.49)
c	ms ⁻¹	velocity of light
\bar{c}	ms ⁻¹	mean velocity of molecules
C _{m,v}	Jmol ⁻¹ K ⁻¹	molar isochoric heat capacity
C ₁	Wm ²	first constant of radiation
C ₂	mK	second constant of radiation
D	m	diameter
d	m	diameter
d	m	characteristic dimension (distance)
E	Vm ⁻¹	electric field strength
e	C	electron charge
F	-	correction factor, equation (7.3)
F	-	view factor, equation (2.29)
g	ms ⁻²	acceleration due to gravity
G	Wm ⁻² sr ⁻¹	instrument radiance
Gr	-	Grashof number
H	Am ⁻¹	magnetic field strength
H	m	depth or height
H	Wm ⁻²	Planck function
h	Js	Planck's constant

h	m	thickness
I	Wm^{-2}	reflected background radiation
I	-	interferogram
i	-	integer
K_n	-	Knudsen's number
\mathbf{K}	-	wave vector
k	JK^{-1}	Boltzmann constant
k	-	extinction coefficient
l	m	length
\bar{l}	m	mean free path of molecules
L	$\text{Wm}^{-2}\text{sr}^{-1}$	total intensity or radiance
L	m	characteristic length
M	Wm^{-2}	emissive power
m	kg	mass
m	-	diffraction order
\dot{m}	kgs^{-1}	mass flow
N	-	number of discrete points
N	m^{-3}	number density of free carriers
N_A	mol^{-1}	Avogadro constant
Nu	-	Nusselt number
n_m	m^{-3}	number density of molecules
n	-	index of refraction
n	-	number of surface contacts
\mathbf{n}	-	unit normal vector
P	W	power
Pr	-	Prandtl number
p	Nm^{-2}	pressure
\dot{Q}	W	heat flow
\dot{q}	Wm^{-2}	heat flux
r	m	radius or distance
r	-	scattering or reflection function
R	$\text{Jmol}^{-1}\text{K}^{-1}$	universal gas constant
R	Instr. unit/ $\text{Wm}^{-2}\text{sr}^{-1}$	spectral response
R	degree	resolution of transducer, equation (8.1)

Ra	-	Rayleigh number
S	-	spectrum
s	m	penetrating length
t	s	time
T	K	thermodynamic temperature
U	-	auxiliary parameter, equation (6.18)
W	m	width
x	m	cartesian coordinate
y	m	cartesian coordinate
z	m	cartesian coordinate

Greek Letters

Symbol	Unit	Quantity
α	-	absorptivity
α	$\text{Wm}^{-2}\text{K}^{-1}$	heat transfer coefficient
β	K^{-1}	thermal expansion coefficient
δ	m	thickness
ϵ	-	relative electrical permittivity or relative dielectric constant
ϵ	-	emissivity
$\epsilon_{1,2}$	-	radiative exchange factor
μ	-	relative magnetic permeability
ϑ	degree	polar or zenith angle
Θ	degree	profile angle
Φ	W	radiant power or radiation flow
κ	m^{-1}	absorption coefficient
Λ	m	repeat distance or period
φ	degree	azimuthal angle
λ	m	wavelength
λ	$\text{Wm}^{-1}\text{K}^{-1}$	thermal conductivity
ν	m^{-1}	wavenumber
ν	m^2s^{-1}	kinematic viscosity

ρ	-	reflectivity
σ	$\text{Wm}^{-2}\text{K}^{-4}$	Stefan-Boltzmann constant
σ	$\Omega^{-1}\text{m}^{-1}$	electrical conductivity
ζ	-	surface interface function
τ	-	transmissivity
τ	s	relaxation time
ω	s^{-1}	angular frequency
Ω	sr	solid angle
Δ	-	difference

Indices and Abbreviations

Symbol	Quantity
<i>a</i>	output
<i>a</i>	air
A	amplifier
abs	absorbed
bc	blackbody cavity
b	blackbody, equation (2.1)
BS	beam splitter
c	convective
c	chamber
cal	calculated
cav	cavity
Cu	copper
Cr	chromium
d	diffuse
D	detector
DC	direct current
DFT	discrete Fourier transformation
DTGS	deuterated triglycine sulphate
<i>e</i>	input

eff	effective
f	flat
FCA	free carrier absorption theory
FEM	finite element method
FT	Fourier transformation
FFT	fast Fourier transformation
FTIR	Fourier transform infrared
g	grease
g	grating
im	imaginary part
in	incident
i	illuminated
i	internal
ILS	instrumental line shape
ISIT	Fraunhofer Institut Siliziumtechnologie
meas	measured
m	mean
m	molar
M	mirror
MCT	mercury cadmium telluride
n	normal
o	surface
0	vacuum
p	sample (probe)
p	plasma
p	parallel to incident plane polarized
Pt	platinum
PTB	Physikalisch-Technische Bundesanstalt
r	radiant
ref	reflected
re	real part
REM	Rasterelektronenmikroskop
rms	root mean square
s	perpendicular to incident plane polarized

s	specular
S	source
sp	surface plasmon
ss	stainless steel
tra	transmitted
t	total
u	surrounding
v	volume
WHH	width at half height
x	path difference
x	x-axis component
y	y-axis component
z	z-axis component
ZFF	zero filling factor
λ	spectral
1	body 1
2	body 2
	parallel
\perp	perpendicular
,	directional
''	bi-directional
<	below the surface
>	above the surface
*	effective
-	complex quantity

1 Introduction

1.1 General Overview

Energy transfer through radiation is one of the most fundamental and pervasive processes in the universe. It plays an important role in the operation of many natural and man-made systems on our earth. Radiative heat transfer in the earth's atmosphere determines the temperature on the surface of our planet and ensures the possibility of life here. In this scientific age, the knowledge of the thermal radiation is also very essential in satellite and other space systems because of the absence of convective heat transfer due to the vacuum in space. Space systems are exposed to both solar radiation and near-zero Kelvin blackbody radiation of deep space so that they must face severe radiant heating and cooling conditions. Radiative thermal energy transfer is also of great importance in terrestrial energy systems such as fossil-fuel-fired utility boilers and thermal- as well as solar photovoltaic energy systems [42, 80].

Thermodynamic evaluation of energy conversion processes with the help of the energy balance equations needs all energy and entropy fluxes involved in the system to be known. The incoming radiation fluxes can be calculated from models of the atmosphere, whereas the outgoing radiation fluxes strongly depend on the radiative properties of the surface. The radiative properties of the surface can be obtained from models such as the Fresnel's equations or from the experimental measurements. For the sake of the simplicity, the radiative energy transfer in engineering science is often described with the help of hemispherical and over total range of wavelength integrated quantities of radiative properties of the surface. But for the detailed description of radiative energy transfer spectral and directional quantities of radiative surface properties are required. For example, the entropy content of a radiation energy flux depends on its spectral and directional distribution [73]. Therefore, one of the aims of this thesis is to present an apparatus which is capable of measuring the directional spectral quantities of surface properties such as emissivity of technical solid surfaces.

For optical temperature measurements done by radiation thermometers and for modelling of the radiative heat transfer between objects, the precise knowledge of the emissivity is of great importance. The emissivity describes the thermal radiative property of the surface. It has therefore been the subject of extensive experimental and theoretical research [32, 36, 151]. Due to the expansion of the field of application of infrared radiation

thermometry near ambient temperatures, more efforts are being made to improve the accuracy of the spectral emissivity data in the thermal infrared wavelength region.

Emissivity is simply defined as the ratio of the radiation emitted by the investigated surface to the radiation emitted by a blackbody at the same temperature. As emissivity values can change significantly with surface conditions of materials, for example surface roughness and surface oxidized film, the values of emissivity given in various literatures sometimes differ significantly from each other [151]. On the other hand, accurate measurement of temperature of the investigated surface is also a great challenge. The reason for this is not as much that the emissivity is very sensitive to temperature, but that most measurements are intensity based, since the measurement signal is proportional to the fourth power of the surface temperature. The use of temperature measuring contact sensor directly on the sample surface may introduce errors in the emissivity measurement. Therefore, the surface temperature has to be estimated theoretically. Much effort should be put into the estimation of the temperature of the sample surface and into the measurement of its emissivity as accurately as possible, which is one of the goals of this work.

Directional and spectral control of thermal radiation has been one of the most important issues in improving efficiency or saving energy consumption in various thermal systems. Nowadays, new concepts of periodic surface microstructures are becoming one of the attractive options for controlling spectral radiative properties of a surface such as emissivity and reflectivity. It has also many advantages, such as adjustability of the period, freedom of material choice, etc. Recent developments in the field of micromachining have made it possible to manufacture periodic microstructures with the size of light wavelengths (micrometer). As a result, the resonance effect between the electromagnetic field and periodic microstructures has become one of the most promising ways to vary optical properties artificially. When regular structures on the sample surface have dimensions in micrometer range like wavelength of radiation, interference effects are expected to arise due to electromagnetic radiant interactions. To the best of our knowledge, there has not been much extensive experimental and theoretical research conducted on thermal emission from regular microstructures except few works reported in section 3.2.3.

The main goal of this thesis is the study of thermal radiant emission from such microstructures whose dimensions are in the order of the wavelength of radiation. The radiant emission from microstructured, undoped, pure silicon surfaces is investigated to examine such interference effects mentioned earlier. These surfaces are micromachined using an existing dry etching method to form regular periodic structures. Two different classes of surface

structures are studied, shallow gratings (depths up to 4 μm) and deep gratings (depths above 4 μm) with a period of 10 μm and a groove width of 6.5 μm . The systematic measurements obtained provide information on the influence of the surface geometry on the characteristics of the electromagnetic energy emitted from a heated pure silicon surface. The information about interference emission gained here may also be applied to the absorption of electromagnetic energy at microstructured surfaces, because from Kirchhoff's law, absorption at one wavelength equals emission [137]. Scattering and absorption of electromagnetic energy from rough surfaces and particles, when their dimensions are in the order of the wavelength of the radiation, is an important area of current research. Such surfaces are also in use in enhanced Raman spectroscopy [23] and resonant growth of metal gratings [25].

The previous work on the emittance properties of roughened or geometrically modified surfaces can be categorized into two branches. One branch is the measurement of the influence of largely random surface roughness on emission and of irregular asperities on absorption. The other is the calculation and measurement of the effect of regular surface structures on radiant emission and absorption. This will be explained in detail in the literature survey (chapter three).

In this work, the thermal radiant emission from the undoped pure silicon surfaces with microstructured rectangular cavities is studied. For this achievement the work is prepared as follows: The second chapter gives an overview of the radiative properties that are useful to perform the radiative heat transfer calculations. In chapters three and four, a broad review of the literature survey about the theoretical and experimental researches on thermal radiative properties of materials and a theoretical approach for the modelling of emission from regular surface macro- und microstructures are reported. Chapters five, six and seven describe the methods of measurement of the radiative properties, determination of the sample surface temperature and understanding of Fourier transform infrared (FTIR)-spectroscopy, respectively. In chapter eight the experimental facilities and microstructured surface fabrication are discussed. The results of the measurements of the directional spectral emissivity of some clean smooth surfaces and regular microstructured pure undoped silicon surfaces are presented and discussed in chapter nine. Because of applications in spectroscopic instruments, research and development have been focused on one-dimensional gratings, which consist of infinitely long grooves and where surface height varies in one direction and remains constant in the other direction. Although electromagnetic theory for one-dimensional gratings is described in section 4.2, the complex numerical calculations of the electromagnetic theory are not incorporated within the framework of this dissertation. This is why

experimental results obtained in this work are compared with the existing classical theories (e.g. the specular geometric optic model and the grating theory) quantitatively. The work concludes with the suggestions for further works and some applications of present investigation given in chapter ten.

1.2 Aims of Investigation

As mentioned earlier, the major aim of the present investigation is to study the thermal radiant emission from two types of solid surfaces such as clean smooth surfaces and periodic microstructured surfaces whose dimensions are in the order of the wavelength of radiation. In order to achieve this, the following objectives are formulated:

1. To present an apparatus which enables the measurement of the directional spectral emissivity of the solid surfaces for different polar and azimuthal angles.
2. To develop a method of determination of the exact temperature of the surface to be investigated theoretically.
3. To simulate the temperature distribution of the surface to be investigated by using the Finite Element Method (FEM).
4. To modify and calibrate the Fourier transform infrared (FTIR)-spectrometer for the use of directional spectral emissivity measurement of an external radiation source (radiation from a sample that lies outside the spectrometer).
5. To measure the hemispherical total emissivity of the investigated surface by the use of two different methods simultaneously, namely the calorimetric- and radiometric method.

2 Theoretical Background

This chapter describes fundamentals of radiation from a black body and from real surfaces and provides the relations that are required to perform the radiation heat transfer calculations for particular surfaces of interest.

2.1 Radiative Properties of Materials and Governing Laws of Radiation

A blackbody is a theoretical object that absorbs all the electromagnetic radiation falling on its surface. Therefore, it reflects no radiation and appears perfectly black. In other words, a blackbody is defined as an ideal body that allows all the incident radiation to pass into it and absorbs internally all the incident radiation without reflecting and transmitting it. This behaviour of blackbody radiation is true for all wavelengths and for all angles of incidence. A blackbody is therefore a perfect absorber and as a consequence a perfect emitter of radiation. The radiation emitted by a blackbody is a function of surface temperature only. This ideal behaviour of the blackbody can be used as a standard for comparison with the radiation properties of real bodies.

With respect to the directional dependence and the spectral distribution of the radiated energy, the radiation properties of real bodies are entirely different from the properties of a blackbody. The radiative behaviour of a real body (i.e., wavelength and angle at which radiation is being emitted by the surface) depends on many factors such as composition, surface finish, temperature and the spectral distribution of the radiation incident on the surface. Thus, various dimensionless quantities such as emissivity, absorptivity, reflectivity and transmissivity are required to explain the radiative properties of real bodies relative to that of a black body. These are described in the coming section.

The magnitude, the angular distribution, and the wavelength dependence of the radiation properties are all very sensitive to the condition of the surface. The surface condition includes factors such as random surface roughness, periodic surface macro- and microstructures, oxide layers and physical and chemical contamination. In the case of dielectric materials, the grain structure of the material may also affect the radiation properties. The qualitative description of a surface by terms such as smooth, polished, rough and oxidized is generally insufficient to permit an accurate specification of the radiation properties.

2.1.1 Planck's Radiation Law

The primary law governing the blackbody radiation is Planck's radiation law, which determines the intensity of radiation emitted by unit surface area into a fixed direction (solid angle) from the blackbody as a function of the wavelength for a fixed temperature. Planck's law gives the spectral emissive power of the blackbody radiation and can be expressed by the following equation [121]

$$M_{\lambda,b}(\lambda, T) = \pi L_{\lambda,b} = \frac{2\pi hc_0^2}{n^2 \lambda^5 \left(e^{hc_0/n\lambda kT} - 1 \right)} \quad (2.1)$$

where $h = 6.6260755 \times 10^{-34}$ Js and $k = 1.380658 \times 10^{-23}$ J/K are the Planck and the Boltzmann constant, respectively. $L_{\lambda,b}$ is the spectral intensity or radiance and λ is the wavelength of the blackbody radiation, T is the thermodynamic temperature and c_0 is the velocity of light in a vacuum. The index of refraction n refers to the medium bounding the blackbody and is equal to unity for a vacuum. A derivation of equation (2.1) is to be found in the reference [121].

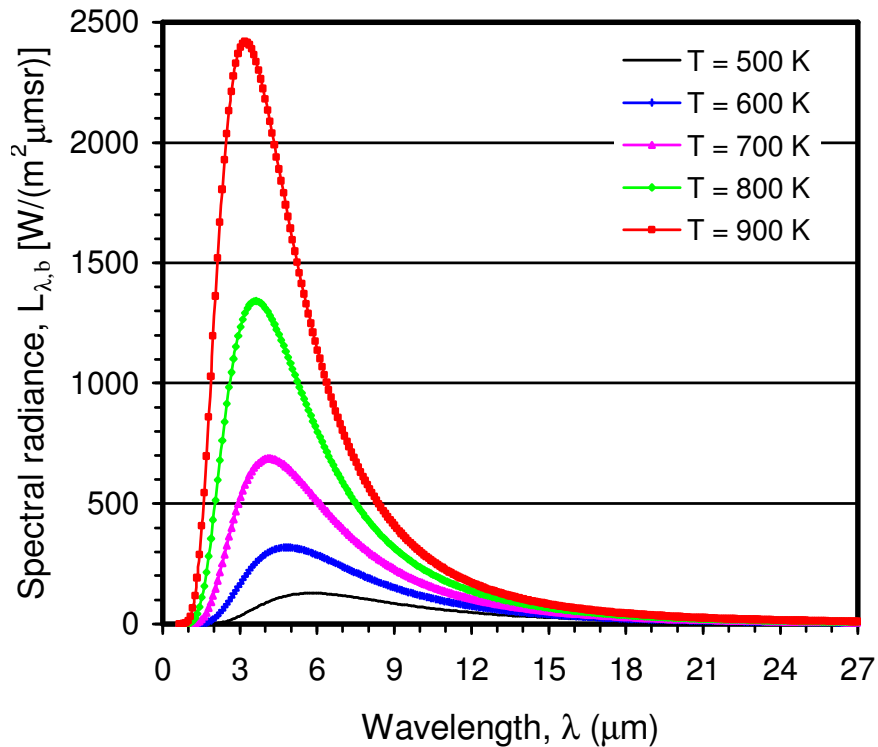


Fig. 2.1. Spectral distribution of blackbody intensity for several different temperatures.

Blackbody radiation is isotropic, i.e., its intensity does not depend on direction. The behaviour of the blackbody radiation is illustrated in figure 2.1 for several isotherms. Planck's law gives a distribution that peaks at a certain wavelength, the peak shifts to shorter wavelengths for higher temperatures, and the area under the curve grows rapidly with increasing temperature. The area under the curve is proportional to the total energy being emitted at all wavelengths by the blackbody. Mathematically, this quantity can be calculated by integrating the spectral emissive power of the blackbody from the Planck's law, equation (2.1) over all wavelengths from zero to infinity, i.e. the total emissive power of the blackbody can be expressed as:

$$M_b(T) = \int_0^{\infty} M_{\lambda b}(\lambda, T) d\lambda = \int_0^{\infty} \frac{2\pi h c_0^2}{n^2 \lambda^5 \left(e^{hc_0/n\lambda kT} - 1 \right)} d\lambda \quad (2.2)$$

Integrating equation (2.2) and assuming that the index of refraction n of the bounding medium is independent of wavelength, we get

$$M_b(T) = n^2 \sigma T^4 \quad (2.3)$$

where σ is known as the Stefan-Boltzmann constant and it is defined by

$$\sigma = \frac{2\pi^5 k^4}{15c_0^2 h^3} = 5.67051 \cdot 10^{-8} \text{ W/m}^2 \text{ K}^4 .$$

Equation (2.3) is the well-known Stefan-Boltzmann law for blackbody radiation, which explains the growth in the height of the curve (i.e., in the spectral radiance) as the temperature enters with the fourth power and is conventionally expressed with $n = 1$ for a vacuum.

2.1.2 Emissivity

Emissivity is a measure of the thermal emission capability of a surface. It is defined as the fraction of energy being emitted from a real surface relative to that emitted by a blackbody surface at the exact same temperature. A blackbody is a material which is a perfect emitter of radiative heat energy. Since maximum absorption implies maximum emission, it emits all energy that it absorbs. Therefore its emissivity is taken as unity. In the real world, there are no perfect blackbodies, so almost objects have an emissivity between 0 and 1.

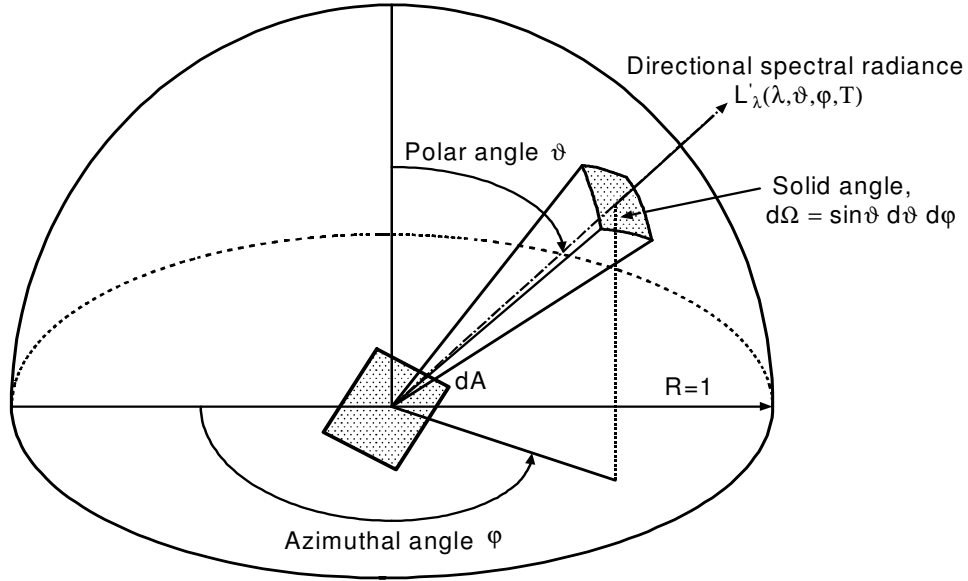


Fig. 2.2. Definition of angles concerning a radiating surface.

The emissivity can depend on factors such as the body temperature, the particular wavelength being considered for the emitted energy, and the angle at which the energy is being emitted. When calculating the energy loss of a body, the emission in all directions has to be considered. For such a calculation the emissivity is averaged over all wavelengths and solid angles of a hemispherical envelope placed over the body. By definition a solid angle anywhere above the elemental area dA is equal to the intercepted area on the unit hemisphere as shown in figure 2.2. An element of this hemispherical area is given by $d\Omega = \sin \vartheta d\vartheta d\varphi$.

The consideration of the emission from a surface into all solid angles and wavelengths leads to the definition of four dimensionless quantities: spectral directional emissivity, hemispherical spectral emissivity, directional total emissivity and hemispherical total emissivity. Among them the basic quantity is the directional spectral emissivity which can be determined experimentally. The other three quantities can be derived from it as explained below.

I. Directional Spectral Emissivity

The directional spectral emissivity is defined as the ratio of the emissive ability of the real surface in terms of the directional and the wavelength distribution to that of a black body at the same temperature:

$$\varepsilon_{\lambda}'(\lambda, \vartheta, \varphi, T) = \frac{L_{\lambda}(\lambda, \vartheta, \varphi, T)}{L_{\lambda,b}(\lambda, T)} \quad (2.4)$$

Here $L_\lambda(\lambda, \vartheta, \varphi, T)$ is the directional spectral intensity of radiation from the real material at the surface temperature T for the wavelength interval $\lambda, (\lambda + d\lambda)$ in the direction (ϑ, φ) and $L_{\lambda,b}(\lambda, T)$ is the directional spectral intensity of the blackbody radiation given by equation (2.1) at the same surface temperature T for the wavelength λ .

Because of the dependence on wavelength, direction and surface temperature, directional spectral emissivity is the most fundamental quantity in the thermal radiation. The value of the spectral emissivity in the direction normal to the radiating surface is known as normal spectral emissivity.

II. Hemispherical Spectral Emissivity

The hemispherical spectral emissivity is defined as the ratio of the hemispherical spectral emissive power of a real body to the hemispherical spectral emissive power of a black body at the same temperature:

$$\varepsilon_\lambda(\lambda, T) = \frac{M_\lambda(\lambda, T)}{M_{\lambda,b}(\lambda, T)} \quad (2.5)$$

This quantity can be also calculated by integrating the directional spectral emissivity over all directions of a hemispherical envelope covering the surface. Then we obtain the following equation,

$$\varepsilon_\lambda(\lambda, T) = \frac{1}{\pi} \int_{\vartheta=0}^{2\pi} \int_{\varphi=0}^{\pi/2} \varepsilon'_\lambda(\lambda, \vartheta, \varphi, T) \cos \vartheta \sin \vartheta \, d\vartheta \, d\varphi \quad (2.6)$$

Equation (2.6) gives the relationship between hemispherical spectral emissivity and directional spectral emissivity of a real body.

III. Directional Total Emissivity

The directional total emissivity can be defined as the ratio of the directional total intensity of a real body to the total intensity of a black body at the same temperature,

$$\varepsilon'(\vartheta, \varphi, T) = \frac{L(\vartheta, \varphi, T)}{L_b(T)} \quad (2.7)$$

where the total intensity of the black body can be replaced by

$$L_b(T) = \frac{\sigma T^4}{\pi}. \quad (2.8)$$

To express the directional total emissivity in terms of directional spectral emissivity, one has to integrate the directional spectral emissivity of the material over all wavelengths, which leads to the following relation:

$$\varepsilon'(\vartheta, \varphi, T) = \frac{\pi}{\sigma T^4} \int_{\lambda=0}^{\infty} \varepsilon'_\lambda(\lambda, \vartheta, \varphi, T) L_{\lambda,b}(\lambda, T) d\lambda \quad (2.9)$$

The directional total emissivity in the normal direction (i.e. $\vartheta = 0$) is a particularly privileged kind of the directional total emissivity.

IV. Hemispherical Total Emissivity

The hemispherical total emissivity is defined as the ratio of the hemispherical total emissive power of a real material to the hemispherical total emissive power of a black body at the same temperature:

$$\varepsilon(T) = \frac{M(T)}{M_b(T)}. \quad (2.10)$$

With the help of the known value of the directional spectral emissivity it is possible to calculate the hemispherical total emissivity by integrating directional spectral emissivity of the material over all wavelengths and all directions which gives a relation between them as:

$$\varepsilon(T) = \frac{1}{\sigma T^4} \int_{\varphi=0}^{2\pi} \int_{\vartheta=0}^{\pi/2} \left[\int_{\lambda=0}^{\infty} \varepsilon'_\lambda(\lambda, \vartheta, \varphi, T) L_{\lambda,b}(\lambda, T) d\lambda \right] \cos \vartheta \sin \vartheta d\vartheta d\varphi \quad (2.11)$$

By using the definition of the directional total emissivity given in equation (2.9) the hemispherical total emissivity can be expressed as

$$\varepsilon(T) = \frac{1}{\pi} \int_{\varphi=0}^{2\pi} \int_{\vartheta=0}^{\pi/2} \varepsilon'(\vartheta, \varphi, T) \cos \vartheta \sin \vartheta d\vartheta d\varphi. \quad (2.12)$$

If the radiative properties of the investigating surface do not depend on the azimuthal angle φ , then the relation for the hemispherical total emissivity given in equation (2.12) can be simplified to

$$\varepsilon(T) = \int_{\vartheta=0}^{\vartheta=\pi/2} \varepsilon'(\vartheta, T) \sin 2\vartheta \, d\vartheta. \quad (2.13)$$

Thus, the hemispherical total emissivity presents information about the emission of a surface into the whole hemisphere and at the entire spectral range. Its value lies between 0 and 1 ($0 \leq \varepsilon \leq 1$).

2.1.3 Absorptivity

Absorptivity is a material property of the body surface and the radiation striking it. It is dependent on the temperature of the body, the wavelength and direction of the incident radiation. It is defined as the fraction of the incident radiation that is absorbed by the body. The incident radiation is the result of the radiative conditions at an external source and does not depend on the temperature or physical nature of the absorbing surface. Compared to the emissivity, the absorptivity introduces additional difficulties, because not only the surface properties of the absorbing surface, but also the directional and spectral characteristics of the incident radiation must be taken into account.

The radiative energy falling on a body can be partially reflected at its surface, while the rest of the portion penetrates the body. The penetrated radiative energy is absorbed by the body and thereby converted into internal energy. Sometimes it may happen that part of it is allowed to pass through the body. The absorbed energy portion is very important in terms of heat transfer. This is described by four absorptivity quantities namely directional spectral absorptivity, hemispherical spectral absorptivity, directional total absorptivity and hemispherical total absorptivity. Most important among these quantities is the directional spectral absorptivity, because it is possible to derive the relations for the other three absorptivity quantities from it as in analogous way to the emissivities as discussed in section 2.1.2.

The directional spectral absorptivity gives for every wavelength λ and for each direction (ϑ, φ) an absorbed part $d^3\Phi^{abs}(\lambda, \vartheta, \varphi, T)$ of the incident radiant power $d^3\Phi^{in}(\lambda, \vartheta, \varphi)$

in a wavelength interval $d\lambda$, which comes from a solid angle element ($d\Omega = \sin \vartheta d\vartheta d\varphi$) to a surface element dA , i.e.

$$\alpha'_\lambda(\lambda, \vartheta, \varphi, T) = \frac{d^3\Phi^{abs}(\lambda, \vartheta, \varphi, T)}{d^3\Phi^{in}(\lambda, \vartheta, \varphi)} = \frac{d^3\Phi^{abs}(\lambda, \vartheta, \varphi, T)}{L_\lambda^{in}(\lambda, \vartheta, \varphi)dA \cos \vartheta d\Omega d\lambda} \quad (2.14)$$

where $L_\lambda^{in}(\lambda, \vartheta, \varphi)$ is the spectral intensity of the incident radiation.

The directional spectral absorptivity can be expressed in terms of spectral absorption coefficient of the absorbing surface as defined by Born and Wolf [15]:

$$\alpha'_\lambda(\lambda, s) = 1 - \exp[-\kappa(\lambda)s] \quad (2.15)$$

Here s is the penetrating length of the incident radiation in the absorbing medium and $\kappa(\lambda)$ is the spectral absorption coefficient which is one of the material properties dependent on the wavelength of radiation λ through the following relation:

$$\kappa(\lambda) = \frac{4\pi k}{\lambda} \quad (2.16)$$

In this equation, k is the extinction coefficient of the absorbing surface.

2.1.4 Reflectivity

The reflectivity is defined as the fraction of the incident radiation that is reflected from the body. It is a material property of the reflecting body surface and the incoming radiation. It is dependent on the temperature of the body, the wavelength and direction of the incident radiation. The reflective properties of a surface are more complicated than the emissive and absorptive properties. This is because the reflected energy depends not only on the angle at which the incident radiation hits on the surface, but also exhibits a possibly intricate directional distribution.

If the reflectivities are considered which only provide the overall incident radiation that is reflected, without specifying what proportion of the reflected energy is sent back in which direction, then they can be defined in a simple way by using polar angle, ϑ and azimuthal angle, φ of the incident radiation. These quantities are directional hemispherical

spectral reflectivity, (bi)-hemispherical spectral reflectivity, directional hemispherical total reflectivity and (bi)-hemispherical total reflectivity. Among these four quantities the directional hemispherical spectral reflectivity is a basic quantity, because the other three reflectivities can be defined with the help of this quantity [6].

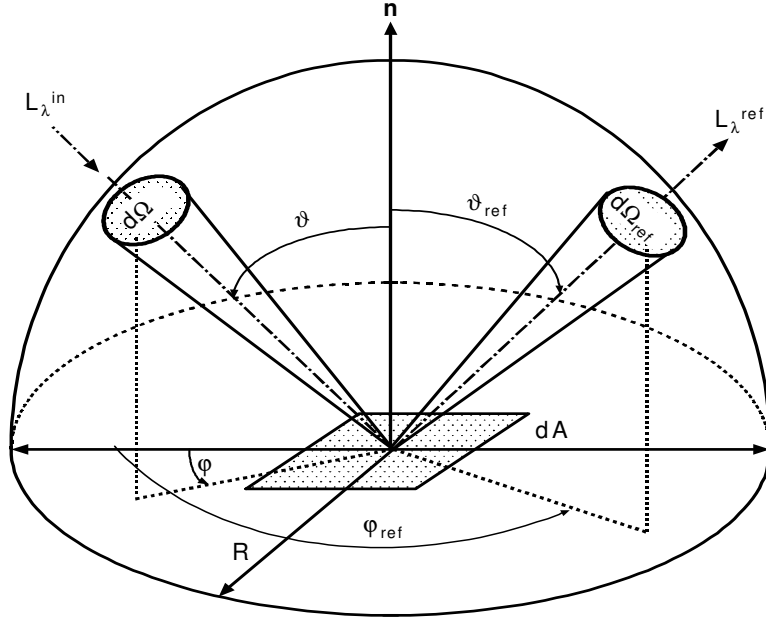


Fig. 2.3. Bi-directional reflectivity geometry.

The complex relationships for the consideration of the directional distribution of the reflected radiation have to be described by bi-directional reflectivities, which are dependent on two pairs of polar and azimuthal angles (ϑ, φ) and $(\vartheta_{ref}, \varphi_{ref})$ for the incident and reflected radiation respectively (see figure 2.3). The bi-directional spectral reflectivity is defined as the ratio of the spectral intensity of the radiation reflected from area element dA in direction $(\vartheta_{ref}, \varphi_{ref})$ to the flux (power per unit surface area) of the radiation incident to dA from direction (ϑ, φ) [138], i.e.

$$\rho_{\lambda}''(\lambda, T, \vartheta, \varphi, \vartheta_{ref}, \varphi_{ref}) = \frac{L_{\lambda}^{ref}(\lambda, T, \vartheta, \varphi, \vartheta_{ref}, \varphi_{ref})}{L_{\lambda}^{in}(\lambda, \vartheta, \varphi) \cos \vartheta d\Omega}. \quad (2.17)$$

In this equation L_{λ} is the spectral intensity and Ω is the solid angle. The subscripts *in* and *ref* denote the incident and reflected quantities, respectively. The bi-directional spectral reflectivity is the most fundamental physical property in radiation scattering from interfaces

and is used to evaluate other properties. For example, integrating the bi-directional spectral reflectivity over all the reflection angles (hemisphere) for a given incidence angle yields the directional hemispherical spectral reflectivity as given by [138]

$$\rho'_\lambda(\lambda, T, \vartheta, \varphi) = \frac{d^3\Phi^{ref}(\lambda, T, \vartheta, \varphi)}{d^3\Phi^{in}(\lambda, \vartheta, \varphi)} = \int_{\Omega_{ref}} \rho''_\lambda(\lambda, T, \vartheta, \varphi, \vartheta_{ref}, \varphi_{ref}) \cos \vartheta_{ref} d\Omega_{ref}. \quad (2.18a)$$

The directional spectral emissivity for a perfectly opaque surface is found by subtracting the directional hemispherical spectral reflectivity from unity, see equation (2.28).

The directional hemispherical spectral reflectivity is the radiation flow reflected into all directions divided by the incident radiation flow from one direction. Another directional reflectivity is useful when one is concerned with the reflected intensity into one direction resulting from incident radiation flow from all directions. It is known as the hemispherical directional spectral reflectivity and defined as the reflected intensity in the $(\vartheta_{ref}, \varphi_{ref})$ direction divided by the integrated average incident intensity:

$$\rho'_\lambda(\lambda, T, \vartheta_{ref}, \varphi_{ref}) = \frac{\int \rho''_\lambda(\lambda, T, \vartheta, \varphi, \vartheta_{ref}, \varphi_{ref}) L_\lambda^{in}(\lambda, \vartheta, \varphi) \cos \vartheta d\Omega}{(1/\pi) \int_{\Omega} L_\lambda^{in}(\lambda, \vartheta, \varphi) \cos \vartheta d\Omega} \quad (2.18b)$$

If the incident intensity is uniform over all incident directions, a reciprocity relation can also be found which states that the hemispherical directional spectral reflectivity of a sample is equal to the directional hemispherical spectral reflectivity for the same angles (ϑ, φ) and $(\vartheta_{ref}, \varphi_{ref})$ of the incident and reflected radiation, i.e., $\rho'_\lambda(\lambda, T, \vartheta, \varphi) = \rho'_\lambda(\lambda, T, \vartheta_{ref}, \varphi_{ref})$ [138].

Finally, two idealized limiting types of reflections should be distinguished. A reflection is known as specular if the incident and the reflected rays lie symmetrically with respect to the normal at the point of incidence, and the solid angle of reflection is equal to the solid angle of incidence (i.e., $d\Omega = d\Omega_{ref}$). A reflection is known as diffuse if the intensity or radiance of the reflected radiation is constant for all angles of reflection and is independent of the angle of incident radiation. Because a real surface encountered in engineering applications is neither a perfectly specular nor a perfectly diffuse reflector, the assumption of the specular

and diffuse reflections has been frequently used in the analysis of radiative heat transfer problems for simplification.

2.1.5 Transmissivity

The transmissivity is defined as the fraction of incident radiation that is transmitted through the body. Opaque bodies like metals and most electrical insulators completely absorb the non-reflected part of the incident radiation in a layer of only a few micrometers thickness close to the surface. But when radiation is incident on a semitransparent body of finite thickness like glass, only a part of the non-reflected radiation is absorbed while the remainder is transmitted through the body as shown in Figure 2.4.

In order to describe the radiation transmitted through a body, the directional spectral transmissivity is defined as the ratio of the radiant power transmitted through the body to the radiant power in the wavelength interval $d\lambda$ incident on an element dA of the surface of the body, i.e.

$$\tau'_\lambda(\lambda, \vartheta, \varphi, T) = \frac{d^3\Phi^{tra}}{d^3\Phi^{in}} \quad (2.19)$$

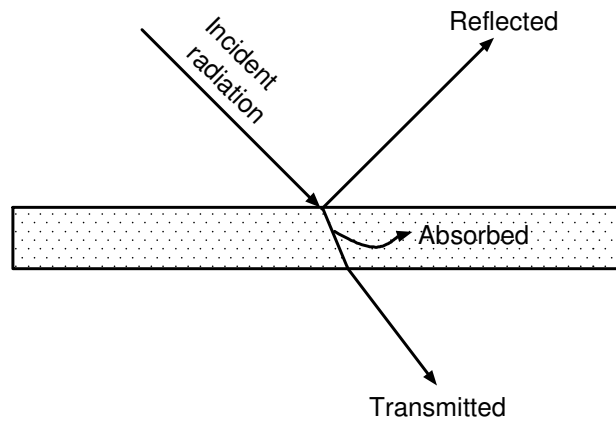


Fig 2.4. Reflection, absorption and transmission of incident radiation by a semitransparent material.

The reflectivity, absorptivity and transmissivity of a semitransparent material depend not only on the surface conditions and the wavelength of the radiation but also on the composition of the material, the thickness of the body and the angle of the incident of radiation on the body, since the radiation incident on the surface penetrates into the depths of the material. The determination of the reflectivity and the transmissivity of a semitransparent

material is more complicated because the attenuation of radiation within the body should be treated as a bulk process where multiple reflection takes place. After considering this multiple reflection phenomena within the semitransparent material Sato [134] has derived an expression for the transmissivity as a function of the reflectivity and the penetrating length of the radiation within the body:

$$\tau(\rho, s) = \exp(-\kappa s) \frac{(1-\rho)^2}{1-\rho^2 \exp(-2\kappa s)} \quad (2.20)$$

Here ρ is the directional spectral reflectivity of the body assuming that the reflection is completely specular (according to Fresnel) and s is the penetrating length of the radiation within the material. κ is the absorption coefficient of the material as defined in equation (2.16). As the directional spectral reflectivity is a function of the incident angles and the wavelength of radiation, the transmissivity given in equation (2.20) is also, of course, a function of the incident angles and the wavelength of radiation.

2.1.6 Kirchhoff's Law of Radiation

The Kirchhoff's law provides the relation between the emitting and absorbing abilities of a body. This law can have various forms depending on whether spectral, total, directional or hemispherical quantities are being considered. The most general form of Kirchhoff's law states that at local thermodynamic equilibrium of an element of material surface, the directional spectral emissivity is equal to the directional spectral absorptivity:

$$\varepsilon'_\lambda(\lambda, \vartheta, \varphi, T) = \alpha'_\lambda(\lambda, \vartheta, \varphi, T). \quad (2.21)$$

Equation (2.21) gives a fixed relation between the properties of the material. This equation also means that the material's ability to emit radiation into the direction (ϑ, φ) is directly connected to its ability to absorb radiation from the same direction.

The Kirchhoff's law for other radiative quantities can be written in a similar manner to the directional spectral quantities given in equation (2.21), but the following restrictions should be taken into account.

I. Directional total quantities:

$$\varepsilon'(\vartheta, \varphi, T) = \alpha'(\vartheta, \varphi, T) \quad (2.22)$$

Restriction: The directional spectral emissivity should be independent of the wavelength (directional-grey surface) or the spectral distribution of the incident radiation must be proportional to that of a blackbody.

II. Hemispherical spectral quantities:

$$\varepsilon_\lambda(\lambda, T) = \alpha_\lambda(\lambda, T) \quad (2.23)$$

Restriction: The spatial distribution of the incident or emitted radiation should be homogeneous, i.e. the radiation must be independent of the polar and azimuthal angles (diffuse-spectral surface). In other words, the body has a diffuse radiating surface (Lambert radiator).

III. Hemispherical total quantities:

$$\varepsilon(T) = \alpha(T) \quad (2.24)$$

Restriction: This equation is valid in following four cases: (a) The body is both a diffuse and grey radiator (diffuse-grey surface). (b) The body is a diffuse radiator and the incident radiation from each direction has spectral distribution proportional to that of a blackbody at the temperature of the absorbing body (diffuse-spectral surface). (c) The body is a grey radiator and incident radiation is independent of the direction. (d) The incident radiation is independent of direction and has a spectral distribution proportional to that of a blackbody at the temperature of the absorbing surface (directional-grey surface).

2.1.7 Relationships between Radiative Properties of Materials

There are two most important relationships between radiative properties of materials. The first is the radiative energy balance that connects absorptivity, reflectivity and transmissivity. The second is Kirchhoff's law that relates absorptivity and emissivity.

Applying the energy balance on the surface element represented in the above figure 2.4, the incident radiative energy flux must be equal to the sum of the reflected, absorbed and transmitted portion of the radiative energy flux, i.e.

$$d^3\Phi^{in} = d^3\Phi^{abs} + d^3\Phi^{ref} + d^3\Phi^{tra} \quad (2.25)$$

Dividing both sides of the equation (2.25) by $d^3\Phi^{in}$ and using the equations (2.14), (2.18) and (2.19) for the definitions of the absorptivity, reflectivity, and transmissivity, the following relation among radiative properties can be derived:

$$\alpha'_\lambda(\lambda, \vartheta, \varphi, T) + \rho'_\lambda(\lambda, \vartheta, \varphi, T) + \tau'_\lambda(\lambda, \vartheta, \varphi, T) = 1 \quad (2.26)$$

Here $\alpha'_\lambda(\lambda, \vartheta, \varphi, T)$ is the directional spectral absorptivity of radiation from the direction (ϑ, φ) , $\rho'_\lambda(\lambda, \vartheta, \varphi, T)$ is the directional-hemispherical spectral reflectivity of radiation from the direction (ϑ, φ) into hemisphere and $\tau'_\lambda(\lambda, \vartheta, \varphi, T)$ is the directional spectral transmissivity. Equation (2.26) can have various forms depending on whether spectral, total, directional or hemispherical quantities are being considered.

Equation (2.21) from Kirchoff's law of radiation and equation (2.25) from the radiative energy balance enable indirect determination of the directional spectral emissivity $\varepsilon'_\lambda(\lambda, \vartheta, \varphi, T)$ when the directional-hemispherical spectral reflectivity and the directional spectral transmissivity are known:

$$\varepsilon'_\lambda(\lambda, \vartheta, \varphi, T) = 1 - \rho'_\lambda(\lambda, \vartheta, \varphi, T) - \tau'_\lambda(\lambda, \vartheta, \varphi, T). \quad (2.27)$$

For opaque materials [i.e., $\tau'_\lambda(\lambda, \vartheta, \varphi, T) = 0$] equation (2.27) can be transformed to a new form

$$\varepsilon'_\lambda(\lambda, \vartheta, \varphi, T) = 1 - \rho'_\lambda(\lambda, \vartheta, \varphi, T). \quad (2.28)$$

The principle of temperature measurements with radiating systems is based on equations (2.27), (2.28) as they enable an indirect way of emissivity determination by measuring the reflectivity and transmissivity.

2.2 Radiative Heat Exchange and View Factor

The radiative heat exchange among the surfaces separated by a non-participating medium depends not only on the hemispherical total emissivities and the temperatures of each surface, but also on the geometric orientation of the surfaces with respect to each other. The effects of the position and the orientation of surfaces on the radiative heat exchange between them are characterized with the help of a so-called view factor. The terms shape factor, configuration factor, and angle factor have also been used in the literature synonymously. The view factor is physically defined as the fraction of the radiative energy leaving one surface element that strikes the other surface directly. As per this definition, the view factor is a function of the size, geometry, relative position, and orientation of the two surfaces. In the following, an expression is presented for the calculation of the view factor between two elementary surfaces.

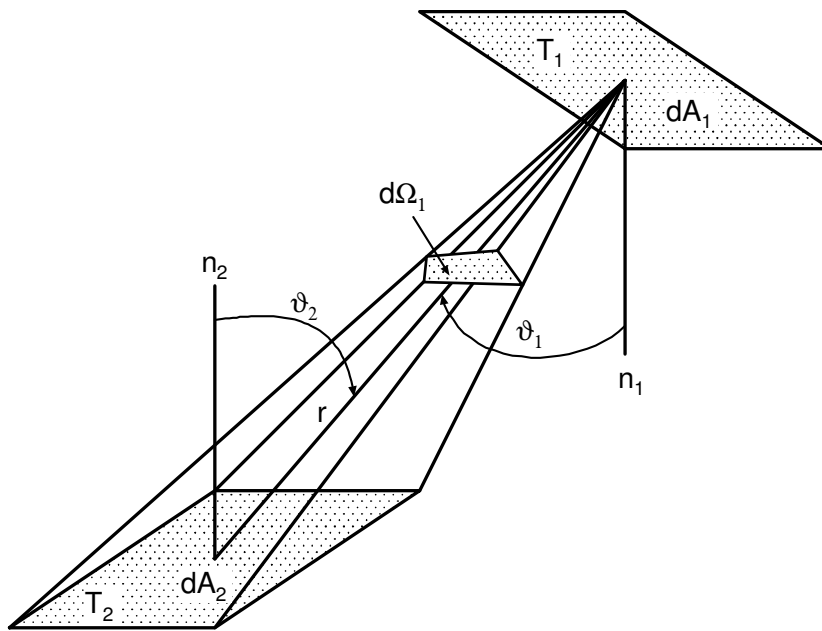


Fig. 2.5. Radiative heat exchange between two elemental surfaces.

As illustrated in figure 2.5, two elementary surfaces dA_1 and dA_2 separated by a distance r with the corresponding temperatures T_1 and T_2 . Let ϑ_1 and ϑ_2 be the polar angles between the corresponding normals to the surfaces and middle line r joining the elemental surfaces dA_1 and dA_2 , respectively. It is supposed that homogeneous radiation flow is taking place from surface element dA_1 to the surface element dA_2 with a solid angle $d\Omega_1$. After calculating the total radiation flow emitted by the finite surface 1 into the hemisphere and the

radiation flow emitted from the finite surface 1 that falls on the finite surface 2, Özisik [114, 115] and Siegel [139] have derived a general expression for the view factor F_{1-2} from the surface 1 to the surface 2:

$$F_{1-2} = \frac{1}{A_1} \int_{A_1} \int_{A_2} \frac{\cos \vartheta_1 \cos \vartheta_2 dA_1 dA_2}{\pi r^2} \quad (2.29a)$$

This equation is only valid if surface 1 radiates diffusely obeying the Lambert's cosine law (i.e., $M'_{\lambda,b}(\lambda, \vartheta, \varphi) = L'_{\lambda,b}(\lambda) \cos \vartheta$), and it has a constant temperature and the same radiation properties over the entire area. The view factor F_{2-1} from surface 2 to surface 1 can be easily obtained from equation (2.29a) by just interchanging the subscripts 1 and 2

$$F_{2-1} = \frac{1}{A_2} \int_{A_2} \int_{A_1} \frac{\cos \vartheta_1 \cos \vartheta_2 dA_1 dA_2}{\pi r^2} \quad (2.29b)$$

which gives the proportion of the radiation flow emitted by surface 2 that strikes surface 1.

The equations (2.29a) and (2.29b) provide the important reciprocity relation for the view factors between the two surfaces A_i and A_j :

$$A_i F_{i-j} = A_j F_{j-i}, \quad \text{for } i = 1, 2, \dots, n. \quad (2.30)$$

The sum of the view factors from a surface to all surfaces of an enclosure, including the surface itself, should be equal to unity. This is known as the summation relation among the view factors for an enclosure, and it can be written for n surfaces in the enclosure as

$$\sum_{k=1}^n F_{i-k} = 1, \quad \text{for } i = 1, 2, \dots, n. \quad (2.31)$$

The radiative heat exchange and the view factors for various selected geometrical arrangements are to be found in literature [114, 115, 139].

2.3 Optical Constants

The polarization and all other radiative properties of a material are determined by two or more phenomenological parameters called optical constants. The optical constants are a function not only of the atomic nature and the temperature of the material, but also the wavelength of the incident radiation. The concept of optical constants is extremely useful and facilitates the quantitative prediction of the radiative behavior of a material.

Born and Wolf [15] have shown that optically absorbing materials, namely metals and dielectrics can be characterized by two optical constants which are known as the refractive index n and the extinction coefficient k . Because these constants describe the behavior and performance of conducting materials, it is very important to know these constants over the entire optical spectrum. The phenomenon of electrical conductivity of a conductor is associated with the appearance of heat. This is a thermodynamically irreversible process in which electromagnetic energy is transformed to heat. As a result, the optical field within a conductor is attenuated. The extinction coefficient k for the medium indicates the absorption of the energy of the electromagnetic wave travelling through the medium.

The thermal radiation from a surface can be treated as an electromagnetic wave. The relations between the radiative properties of a material and its optical and electrical parameters are found by considering the interaction that occurs when an electromagnetic wave travelling through one medium is incident on the surface of another medium. The wave propagation and the surface interaction have been investigated by Born and Wolf [15] using Maxwell's fundamental equations relating electric and magnetic fields. Expressing the solution of the Maxwell's wave equation as a function of optical constants, the following relations have been derived between the optical constants and the electrical properties of a material:

$$n = c_0 \sqrt{\frac{\mu\mu_0\epsilon\epsilon_0}{2} \left[1 + \sqrt{1 + \left(\frac{\sigma}{\omega\epsilon\epsilon_0} \right)^2} \right]} \quad (2.32)$$

$$k = c_0 \sqrt{\frac{\mu\mu_0\epsilon\epsilon_0}{2} \left[-1 + \sqrt{1 + \left(\frac{\sigma}{\omega\epsilon\epsilon_0} \right)^2} \right]} \quad (2.33)$$

where c_0 , μ_0 and ϵ_0 are the velocity of light, magnetic permeability and dielectric constant or electrical permittivity in vacuum, respectively. Further, μ , ϵ , σ , and ω are relative magnetic permeability, relative dielectric constant, electrical conductivity of the material, and angular frequency ($\omega = 2\pi c_0/\lambda_0$) of the electromagnetic wave, respectively. These quantities are dependent of the wavelength of the incident radiation and the temperature of the material so that the optical constants n and k depend also on both wavelength and temperature. For good conductors, the electrical conductivity σ is generally very large; hence $\sigma/(\omega\epsilon\epsilon_0) \gg 1$ if ω is not very large. Then equations (2.32) and (2.33) simplify to

$$n \cong k \cong c_0 \sqrt{\frac{\mu\mu_0\sigma}{2\omega}} \quad \text{for} \quad \frac{\sigma}{\omega\epsilon\epsilon_0} \gg 1. \quad (2.34)$$

For nonconductors (perfect dielectric medium) or vacuum having negligibly low electrical conductivity (i.e., $\sigma = 0$), equations (2.32) and (2.33) transform into

$$n = c_0 \sqrt{\mu\mu_0\epsilon\epsilon_0} = \frac{c_0}{c}, \quad \text{and} \quad k = 0. \quad (2.35)$$

From equation (2.35) it is clear that the simple refractive index n is the ratio of the velocity of the wave in vacuum c_0 to the velocity in the medium $c = 1/\sqrt{\mu\mu_0\epsilon\epsilon_0}$.

The optical constants n and k can also be expressed in terms of the angle of incidence ϑ_1 and the angle of refraction ϑ_2 when an electromagnetic wave is incident from one conducting medium 1 to another conducting medium 2. When the two media are electric conductors having complex refractive indices \bar{n}_1 and \bar{n}_2 defined as $\bar{n} = n - ik$, the required expression takes the form [137]:

$$\frac{\sin \vartheta_2}{\sin \vartheta_1} = \frac{\bar{n}_1}{\bar{n}_2}. \quad (2.36)$$

Equation (2.36) is known as Snell's law of refraction.

According to the Drude free-electron theory for electrical conductors (metals) a spherical cloud of electrons that surrounds each atom can be divided into two regions, with

the electrons in the inner region tightly bound to the nucleus while those in the outer region remain free to move from atom to atom under the influence of an applied electric field. Consistent with this theory which relates the harmonic motion of the free electrons to the periodic electric field in the metal, the complex refractive index ($\bar{n} = n + ik$) can be expressed as a function of complex relative dielectric constant ($\bar{\epsilon} = \epsilon_{re} + i\epsilon_{im}$) of a conducting medium [59]:

$$n + ik = \sqrt{\epsilon_{re} + i\epsilon_{im}} = \sqrt{1 - \frac{\omega_p^2}{\omega^2 + i\omega/\tau}} \quad (2.37)$$

Here ϵ_{re} and ϵ_{im} are the real and imaginary parts of the complex relative dielectric constant of a conducting medium, respectively. These quantities can be determined by equating the real and imaginary parts of equation (2.37) as:

$$\epsilon_{re} = n^2 - k^2 = \left[1 - \frac{\omega_p^2}{(\omega^2 + 1/\tau^2)} \right] \quad (2.38)$$

$$\epsilon_{im} = 2nk = \frac{\omega_p^2}{\omega\tau(\omega^2 + 1/\tau^2)} \quad (2.39)$$

Here ω ($=2\pi c/\lambda$) is the angular frequency of the incident radiation, and τ is the relaxation time required for a transient electric current to decay to 1/e of its initial value after the electric field is removed. ω_p is the so called plasma frequency for the metal given by the relation

$$\omega_p^2 = \frac{Ne^2}{m^* \epsilon_0} \quad (2.40)$$

with the number density of free carriers N , their optical effective mass m^* , charge e , and the electrical permittivity or dielectric constant of vacuum ϵ_0 . The relaxation time is given by

$$\tau = \frac{m^* \sigma}{Ne^2} \quad (2.41)$$

where σ is the electrical conductivity of the metal.

By the use of equations (2.40) and (2.41) in equations (2.38) and (2.39), the optical constants can be expressed in terms of the number density of free carriers, their optical effective mass and relaxation time. This is also known as the free carrier absorption theory (FCA).

2.4 Fresnel's Equations

The behavior of the interaction of an electromagnetic wave with dielectric as well as conducting surfaces and its subsequent reflection and transmission is expressed mathematically by a set of equations known as Fresnel's equations for reflection and transmission. Fresnel's equations can be derived from Maxwell's equations, and excellent treatments are presented by Born and Wolf [15], Siegel et al. [138] and Kabelac [73]. Because in this work only the emission properties of opaque materials (i. e. no transmission) are investigated, more emphasis will be given here for Fresnel's equations for reflection.

Let us consider that a beam of an electromagnetic plane wave propagating in medium 1 is incident upon the interface between the ideal dielectric media 1 and 2 at an angle of incidence ϑ_1 (i.e., angle between the direction of propagation and the normal \mathbf{n} to the interface) as illustrated in figure 2.6. Part of this radiation will be reflected, and the rest will propagate in medium 2 at an angle of refraction ϑ_2 . The incident and the reflected electric field vectors can be resolved into two components of polarization. One of these components is polarized parallel to the plane of incidence (i.e., the plane that includes the direction of incidence and the normal to the interface at the point of incidence) and the other is polarized perpendicular to the plane of incidence. The parallel and the perpendicular components of the incident beam will be denoted by $E_{in,p}$ and $E_{in,s}$, and those of the reflected beam by $E_{re,p}$ and $E_{re,s}$, respectively. Then the components of the reflected beam are related to the components of the incident beam by the following two equations as given in [138],

$$\frac{E_{re,s}}{E_{in,s}} = -\frac{\sin(\vartheta_1 - \vartheta_2)}{\sin(\vartheta_1 + \vartheta_2)} \quad (2.42)$$

and

$$\frac{E_{re,p}}{E_{in,p}} = \frac{\tan(\vartheta_1 - \vartheta_2)}{\tan(\vartheta_1 + \vartheta_2)}. \quad (2.43)$$

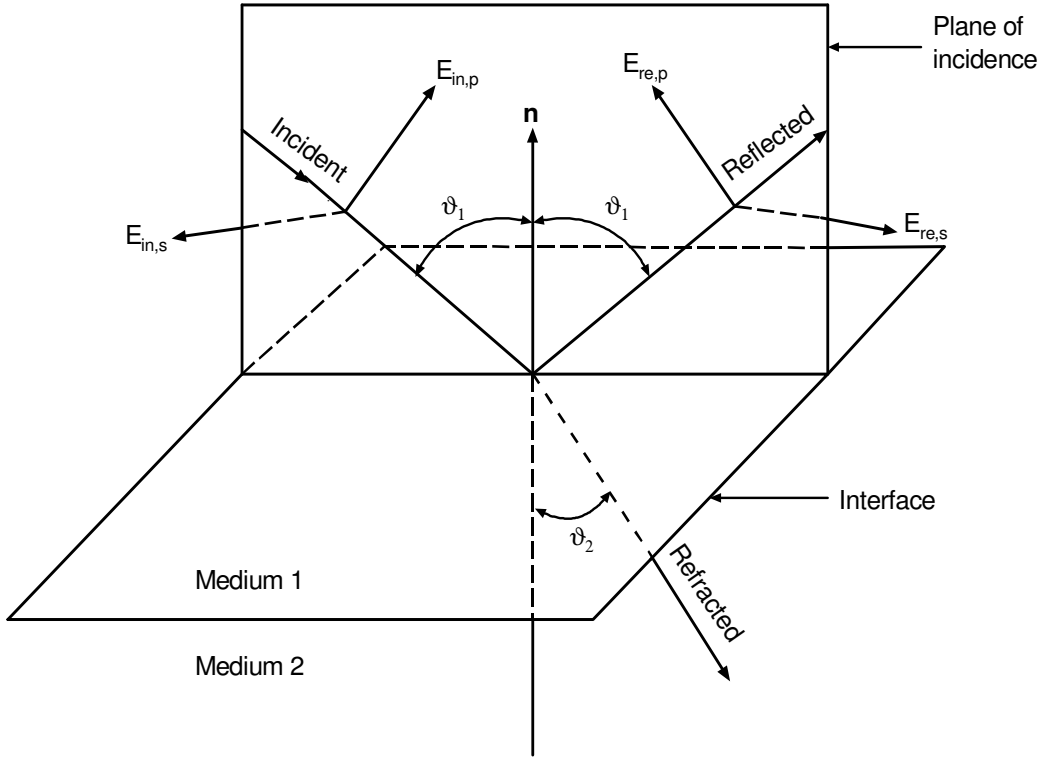


Fig. 2.6. Two components of polarization of the incident and reflected rays.

By using Snell's law of refraction, equation (2.36), to eliminate the angle of refraction ϑ_2 , equations (2.42) and (2.43) can be written in alternative forms as functions of optical constants of both media. However, in this work the radiative properties of an opaque material in air or vacuum is of interest, so that air or vacuum is considered as medium 1 (i.e., refractive index, $n_1 = 1$, $k_1 = 0$). This consideration will simplify the further mathematical manipulations.

As the energy transported by the electromagnetic plane wave which is proportional to the square of the components of the electric field vector, the directional hemispherical spectral reflectivities for the perpendicular and parallel components of the radiation incident on a perfect dielectric medium (i.e., $k = 0$) can be determined by using equations (2.36), (2.42) and (2.43) as

$$\rho'_{\lambda,s}(\lambda, \vartheta_1) = \left[\frac{\sqrt{n^2 - \sin^2 \vartheta_1} - \cos \vartheta_1}{\sqrt{n^2 - \sin^2 \vartheta_1} + \cos \vartheta_1} \right]^2 \quad (2.44)$$

and

$$\rho'_{\lambda,p}(\lambda, \vartheta_1) = \left[\frac{n^2 \cos \vartheta_1 - \sqrt{n^2 - \sin^2 \vartheta_1}}{n^2 \cos \vartheta_1 + \sqrt{n^2 - \sin^2 \vartheta_1}} \right]^2 \quad (2.45)$$

where n is the refractive index of the dielectric medium lying in air or vacuum. Equations (2.44) and (2.45) are known as Fresnel's equations of reflection for an ideal dielectric medium.

The equations (2.42) and (2.43) can be generalized for the more complicated case of conducting media where complex refractive index has to be considered. Moreover, as the refractive index of the medium 2 is complex, from equation (2.36) $\sin \vartheta_2$ is also a complex quantity and the angle ϑ_2 can no more be interpreted physically as the angle of refraction while propagating within the conducting material. This fact brings no complication in its use, since the angle of refraction can be expressed in terms of the angle of incidence and the optical constants of the conducting medium (see equation 2.36). Siegel et al. [138] and Kabelac [73] have derived the following two relations for the determination of the directional hemispherical spectral reflectivities for the perpendicular and parallel polarizations for the conducting medium:

$$\rho'_{\lambda,s}(\lambda, \vartheta_1) = \frac{(a - \cos \vartheta_1)^2 + b^2}{(a + \cos \vartheta_1)^2 + b^2} \quad (2.46)$$

$$\rho'_{\lambda,p}(\lambda, \vartheta_1) = \frac{(a - \cos \vartheta_1)^2 + b^2}{(a + \cos \vartheta_1)^2 + b^2} \cdot \frac{(a - \sin \vartheta_1 \tan \vartheta_1)^2 + b^2}{(a + \sin \vartheta_1 \tan \vartheta_1)^2 + b^2} \quad (2.47)$$

respectively. Here a and b are auxiliary parameters given by the equations

$$a = \left\{ \frac{1}{2} \left[\sqrt{(n^2 - k^2 - \sin^2 \vartheta_1)^2 + 4n^2 k^2} + (n^2 - k^2 - \sin^2 \vartheta_1) \right] \right\}^{1/2} \quad (2.48)$$

$$b = \left\{ \frac{1}{2} \left[\sqrt{(n^2 - k^2 - \sin^2 \vartheta_1)^2 + 4n^2 k^2} - (n^2 - k^2 - \sin^2 \vartheta_1) \right] \right\}^{1/2}. \quad (2.49)$$

In equations (2.48) and (2.49) n and k are the index of refraction and extinction coefficient of the investigating material lying in air or vacuum (i.e., here medium 2). Equations (2.46) and (2.47) are known as Fresnel's equations of reflection for a conducting medium. For unpolarized radiation the parallel and perpendicular components of the incident radiation are of equal intensity. Then the directional hemispherical spectral reflectivity of unpolarized radiation is determined as the average of the directional hemispherical spectral reflectivities for the perpendicular and parallel polarizations given by the equations (2.46) and (2.47).

Taking the arithmetical average of the two components of polarizations, the directional spectral emissivity of the opaque material can be easily calculated by using equation (2.28)

$$\varepsilon'_\lambda(\lambda, \vartheta_1) = \frac{\varepsilon'_{\lambda,s} + \varepsilon'_{\lambda,p}}{2} = \frac{(1 - \rho'_{\lambda,s}) + (1 - \rho'_{\lambda,p})}{2} \quad (2.50)$$

if the spectral values of the optical constants n and k , and the angle of incidence ϑ_1 of the radiation are known. The values of the optical constants of different materials as the function of the wavelength of radiation are to be found in Touloukian [151], Gray [51], and Palik [116]. An alternative way of finding the values of the optical constants is to use the equations (2.32) and (2.33), provided that the electric and magnetic properties of the material for the different wavelengths of the radiation are known.

A very simple relation of the normal spectral emissivity for an opaque metal surface can be obtained from equation (2.50) by putting the angle of incidence of the radiation equal to zero, i.e. $\vartheta_1=0$, in equations (2.46)-(2.49) as

$$\varepsilon'_{\lambda,n}(\lambda) = \varepsilon'_{\lambda,n,s} = \varepsilon'_{\lambda,n,p} = \frac{4n}{(n+1)^2 + k^2}. \quad (2.51)$$

Similarly, the normal spectral emissivity for a dielectric surface can be derived from equation (2.50) with the help of the equations (2.44) and (2.45) as

$$\varepsilon'_{\lambda,n}(\lambda) = \varepsilon'_{\lambda,n,s} = \varepsilon'_{\lambda,n,p} = \frac{4n}{(n+1)^2}. \quad (2.52)$$

It is clear from equation (2.51) that the normal spectral emissivity of a metal surface is equal for both, the s- and p-polarized electric field (see figure 2.6). It depends on the number

density of free carriers N through the imaginary part ε_{im} of the relative dielectric constant which is proportional to N , equation (2.39) with equation (2.40). It has to be noted that the extinction coefficient k is proportional to the imaginary part ε_{im} of the relative dielectric constant, see equation (2.39) and hence as the number density of free carriers N increases, the normal spectral emissivity $\varepsilon'_{\lambda,n}$ decreases, see equation (2.51). This explains why the emissivity of a metal surface is less than the emissivity of a dielectric surface, for which k is negligible compared to the refractive index n .

The foregoing Fresnel's equations for directional spectral reflectivity and emissivity are applicable only to ideal surfaces, i.e. surfaces that are optically smooth, free of roughness, oxidation, and contamination. A surface is said to be optically smooth if the surface imperfections are much smaller than the wavelength of the radiation being considered. A surface that is optically smooth for long wavelengths may be comparatively quite rough for short wavelengths. An important parameter in characterizing roughness effects is the optical roughness which is defined as the ratio of a characteristic roughness height (i.e. root mean square roughness) to the wavelength of the radiation. According to Siegel et al. [138], a surface is optically smooth when this ratio (the optical roughness) is smaller than unity.

3 Literature Survey

This chapter contains a literature review on the research of optical properties such as emissivity and reflectivity of electrical good conductors, semiconductors, insulators and coatings. The review covers two aspects: methods for measurements of the optical properties of surfaces and geometrical conditions of the investigated surfaces. The methods for measurements of the optical properties can mainly be divided into two groups: calorimetric techniques and radiometric techniques of measurement, which will be described in chapter five. The geometrical conditions of the investigated surfaces include smooth clean surfaces, random surface roughness, irregular impurities on the surface (e.g. oxide films, surface coatings), regular surface macrostructures, whose dimensions are much larger than the wavelength of radiation, and regular surface microstructures with dimensions in the order of the wavelength of radiation.

3.1 Calorimetric Method

Calorimetric methods for the measurement of the total emissivity of surfaces being investigated are mainly transient methods based on the evaluation of the temperature-time behavior of the sample, which is in radiation exchange with its environment. Measurements can be carried out in a vacuum or at atmospheric conditions. The specific heat capacity of the sample should be known or measured independently. Heat flow from the sample due to free convection should also be known if the measurement is carried out at atmospheric conditions. The disadvantage of this method is that one can only measure the hemispherical total emissivity of the sample, which does not provide information about the directional and spectral behavior of the radiation emitted by the sample.

Calorimetric measurements on good conductors such as metals were performed by Kola et al. [77]. They calculated hemispherical total emissivity values from experimental heating and cooling curves. Measurements of the specific heat capacity and hemispherical total emissivity were performed by Matsumoto and Ono [101, 104, 105] by solving the time-dependent differential equations for the temperature of an electrically conducting sample, which was heated by using a feedback-controlled pulse current. The schematic of their experimental set up is represented in figure 3.1. The hemispherical total emissivities of tantalum and molybdenum measured by them are shown in figure 3.2. Smetana and Reicher [140] determined spectral emissivity indirectly with the help of Kirchhoff's law where the time of heating of a thin sample due to absorption of laser radiation falling on its surface was

evaluated. Zhang et al. [164] measured the heat flux and calculated the hemispherical total emissivity of glass coatings by balancing the heat flux radiated from the sample surface with the electrical power supplied to the sample.

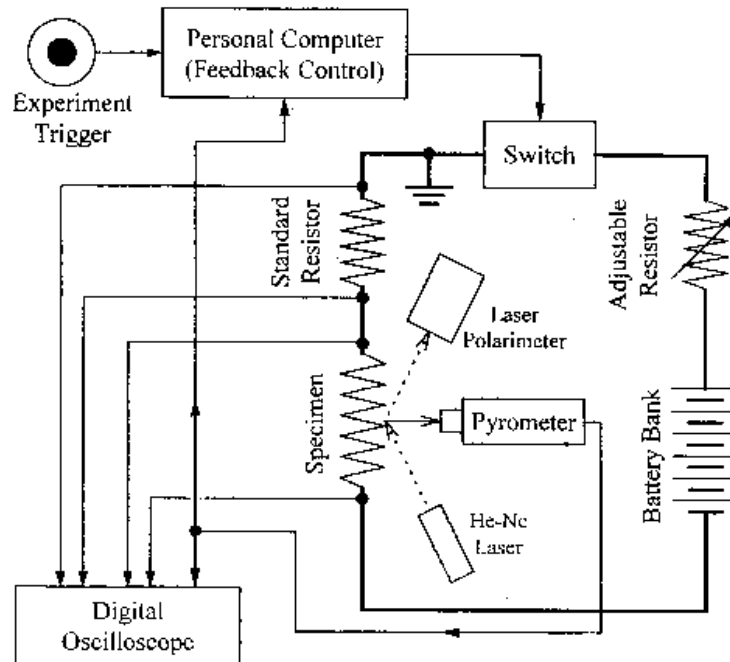


Fig. 3.1. Schematic diagram of the calorimetric measurement system that uses the feedback control technique as developed by Matsumoto et al. [101,102, 103,104,105].

Masuda and Higano [99] presented a transient calorimetric technique for measuring the hemispherical total emissivity of metal wires with high accuracy. In this method, the heat loss through the temperature sensor leads could be reduced by using guard wires. Since the cooling rates for wire specimens are relatively high in comparison with those for block-shaped specimens, this technique is more useful in a low temperature range below room temperature. Ramanathan et al. [125] studied the temperature variation of the hemispherical total emissivity of very good conductors like silver, copper and aluminium with the help of a temperature decay method (transient) in the 150-1000 K range. Roger et al. [127] determined experimentally for the first time hemispherical total emissivity values of a mechanically polished surface and an electropolished surface of stainless steel (type AISI 304). An absolute method incorporating the transient calorimetric technique was used in these measurements.

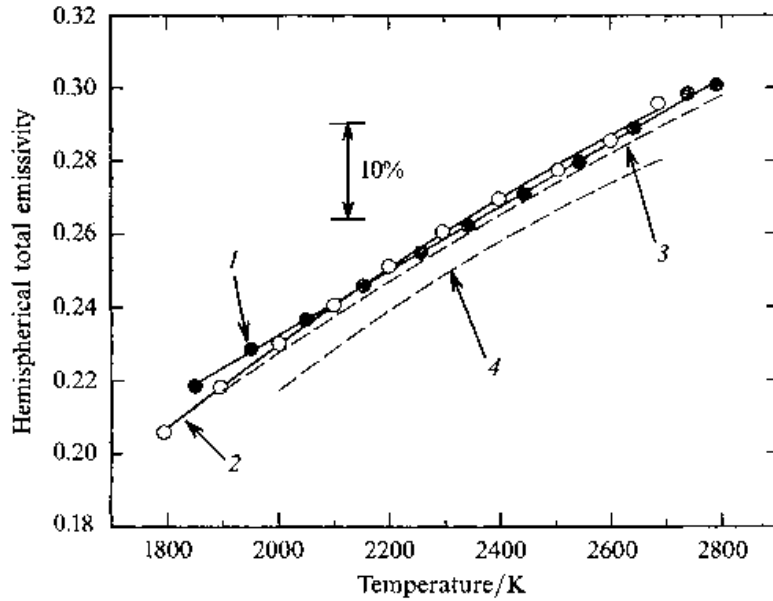


Fig. 3.2. Hemispherical total emissivities of tantalum (solid curve 1) and molybdenum (solid curve 2) measured using calorimetric method as given by Matsumoto and Ono [104]. Results obtained in the earlier work on tantalum (broken curve 3) by Matsumoto and Cezairliyan [102] and on molybdenum (broken curve 4) by Matsumoto et al. [103] are also shown for the comparison .

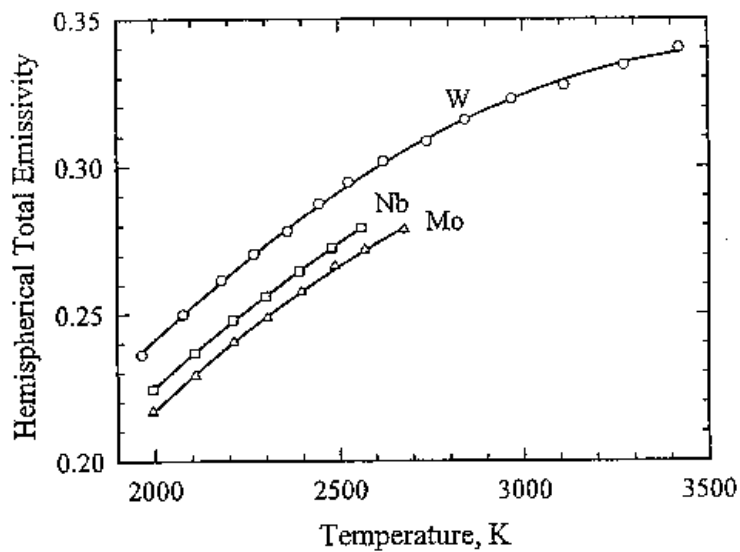


Fig 3.3. Hemispherical total emissivity of niobium (Nb), molybdenum (Mo), and tungsten (W) measured using the feedback control technique as reported by Matsumoto et al. [103].

Masuda et al. [100] proposed an improved transient calorimetric technique for measuring the hemispherical total emissivity of insulating materials like borosilicate glass sheets. The emissivity values of glass sheets with different thicknesses were measured at various temperatures by considering the thermal gradient within the specimens produced in the cooling process. A new combined transient and brief steady state method for measuring

hemispherical total emissivity of electrically conducting materials at high temperatures using a feedback-controlled pulse heating technique (not continuous current supply, see figure 3.1) was developed by Matsumoto et al. [102, 103]. As the measurements were carried out under steady state conditions (state of equilibrium), determination of heating or cooling rates was not required, and random errors were reduced by averaging emissivity over a time period. The measurement results are represented in figure 3.3. Seifter et al. [135] presented an experimental technique for normal spectral emissivity measurement on liquid metals at high temperatures. For the true temperature determination of the sample, the application of simultaneous laser polarimetry and spectral radiometry was demonstrated on liquid niobium.

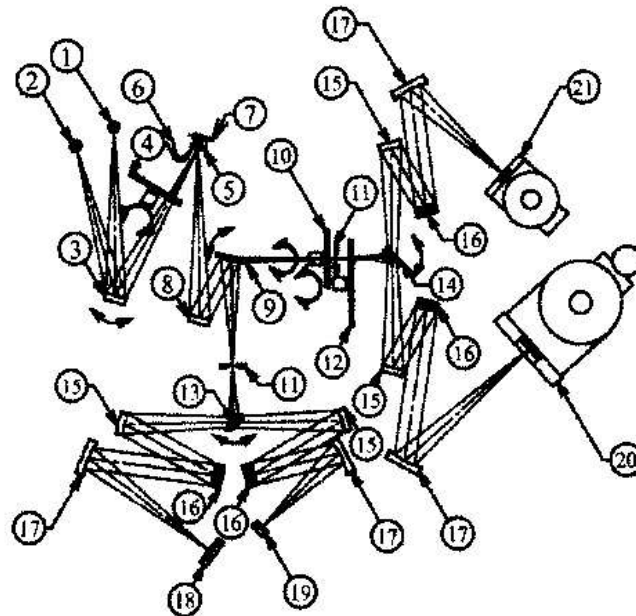
3.2 Radiometric Methods

There are two radiometric methods for the determination of emissivity of an opaque sample surface. One is the indirect method, in which first the reflectivity of the sample surface is measured and then the emissivity of the sample is calculated by using the relation that the sum of the spectral reflectivity and emissivity of the opaque surface is unity [137]. The other is the direct method of measuring emissivity of the sample surface.

The radiometric technique for measuring the reflectivity is based on the comparison of the radiation flux reflected by a sample with the radiation flux reflected by an ideal completely reflecting and perfectly diffusing standard having a known reflectivity value under identical conditions of irradiation. In order to measure the directional reflectivity, a goniometer is used, with the help of which the angle of incidence and angle of reflection of the radiation can be adjusted independently. For measuring hemispherical reflectivity, an integrating-sphere reflectometer is used. The integrating spheres possess diffused reflecting internal walls so that the collection of the radiation flux reflected by the sample over nearly a complete hemisphere is possible. This technique is normally used in visible wavelength range because the spectral intensity of the radiation from a sample is typically low in the visible wavelength range.

Birkebak and Eckert [12] carried out a detailed experimental study to examine the influence of surface roughness conditions on the reflection characteristics of metal surfaces for monochromatic thermal radiation. Agababov [1, 2, 3] proposed some theoretical and experimental methods for the analysis of the effect of the roughness of the surface of a solid body on its radiation properties depending on their form and dimensions. De Silva [34] and Zaworski et al. [163] described an apparatus for measurements of directional reflectivity in detail. The directional reflectivity of several types of common engineering materials was

measured by a goniometer. The hemispherical, spectral emissivities of the walls of a melting furnace were evaluated using an integrating sphere reflectometer by Elich and Wieringa [40]. In the similar manner, Brandenburg [16] measured the directional reflectivity of imperfectly diffused samples as a function of angle of incidence from 15° to 88° over a wide wavelength range. Ford et al. [46] developed a system based on a Fourier transform infrared spectrometer to measure the bi-directional reflectivity of metal surfaces in the infrared wavelength range. Results were presented for rough gold and grooved nickel surfaces considering the variation with incident and reflected angles. Clarke and Larkin [27] designed a diffuse reflectometer to determine a complete set of absolute spectral radiometric quantities (reflectivity, transmittivity, emissivity) for any kind of sample. Measurements were performed over the whole thermal infrared spectrum from $2.5 \mu\text{m}$ to $55 \mu\text{m}$ for a number of black coatings.



- | | |
|---|--|
| 1. tungsten-halogen lamp | 13. rotationary plane mirror 1 |
| 2. Si_3N_4 light source | 14. rotationary plane mirror 2 |
| 3. rotationary concave mirror | 15. collimator |
| 4. shutter disk | 16. diffraction grating |
| 5. specimen | 17. concave mirror |
| 6. K-thermocouple | 18. 35-Si photodiode array |
| 7. heater | 19. 16-Ge photodiode array |
| 8. concave mirror | 20. 32-InSb photovoltaic detector array |
| 9. rotationary plane mirror | 21. 16-HgCdTe photoconductive detector array |
| 10. chopper | |
| 11. entrance slit | |
| 12. filter disk | |

Fig. 3.4. Schematic diagram of spectrophotometer system developed by Wakabayashi and Makino [154].

Recently, some theoretical and experimental work in the field of radiometric quantities determination was done by Makino et al. [92, 93, 94, 95, 96, 154, 155]. A new high-speed spectrophotometer system was developed for the experimental investigation of radiation phenomena of real solid surfaces in actual natural or industrial environments (see figure 3.4). A numerical model of such real surfaces was developed with a description of the reflection characteristics by an electromagnetic wave theory. The hemispherical and bi-directional reflectance measurements were made to investigate the characteristics of each real surface (e.g. rough surface, microsurface). One of the measurement results for nickel surface is represented in figure 3.5.

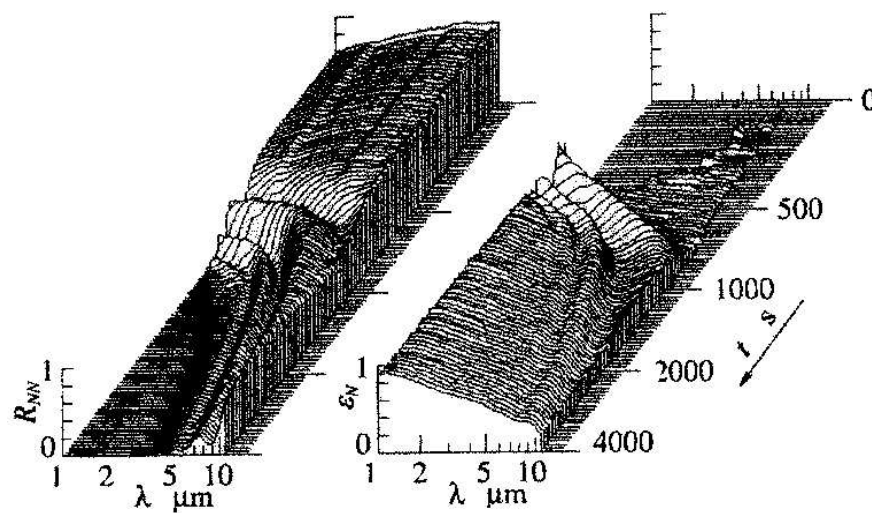


Fig. 3.5. Transition of spectra of reflectivity R_{NN} and emissivity ϵ_N of specular-finished nickel surface in high-temperature air-oxidation process measured by Wakabayashi and Makino [154].

The radiometric technique for the direct evaluation of emissivity is made by comparing (ratioing) the radiances of a heated sample and a black body radiator at the same temperature under the same spectral and geometrical conditions. By using this method both total directional and spectral directional emissivity can be measured. This direct technique for measuring emissivity is more accurate and easier than the indirect one. Therefore, it is preferably applied in the infrared wavelength range, where the spectral intensity of the radiation from a sample is high.

The spectral absorptances of some solids were measured by Stierwalt et al. [144] in the wavelength range from 2 μm to 25 μm at the temperatures between 313 K and 473 K with the help of a spectrophotometer. Sato [134] theoretically and experimentally investigated the emissivities of pure silicon and n-type silicon doped with phosphorus in the spectral range

from 0.4 μm to 15 μm at various temperatures from 340 K to 1070 K by a modified spectrophotometer. The measurement results of normal spectral emissivity are represented in figures 3.6 and 3.7 for pure and doped silicon, respectively. An apparatus was presented by Brandenberg and Clausen [17] for measuring directional spectral emissivity of flat surfaces at angles of emission between 15° and 80° , temperatures between 200°C and 600°C and wavelengths between 1 μm and 25 μm . Lohrengel [86] performed measurements on the bad conductors (e.g. glass, plastic, ceramic, graphite, etc.) to determine the directional total emissivity values in the temperature range from -60°C to 250°C . An experimental method was developed by Janßen [70] for measuring the normal- and hemispherical total emissivities of different kinds of glasses under atmospheric conditions in the temperature range from 50°C to 100°C . Tanaka et al. [146] proposed a method of the derivation of the hemispherical total emissivity from the normal emission spectrum for vycor and fused silica glasses. The normal emission spectrum from a smooth surface has been measured at steady state in the temperature range from 400 K to 750 K by using a Fourier transform infrared spectrometer. The effect of surface roughness on the directional spectral emissivity as well as the directional and hemispherical total emissivities was systematically studied by Sabuga and Todtenhaupt [128] for the precious metals like silver, gold, palladium, platinum, rhodium and iridium in order to avoid or minimize the effect of oxidation and other chemical reactions. The emissivities were measured by a radiometric technique in the wavelength range from 2.5 μm to 51 μm and in the angular range from 0° to 75° at a temperature of 150°C .

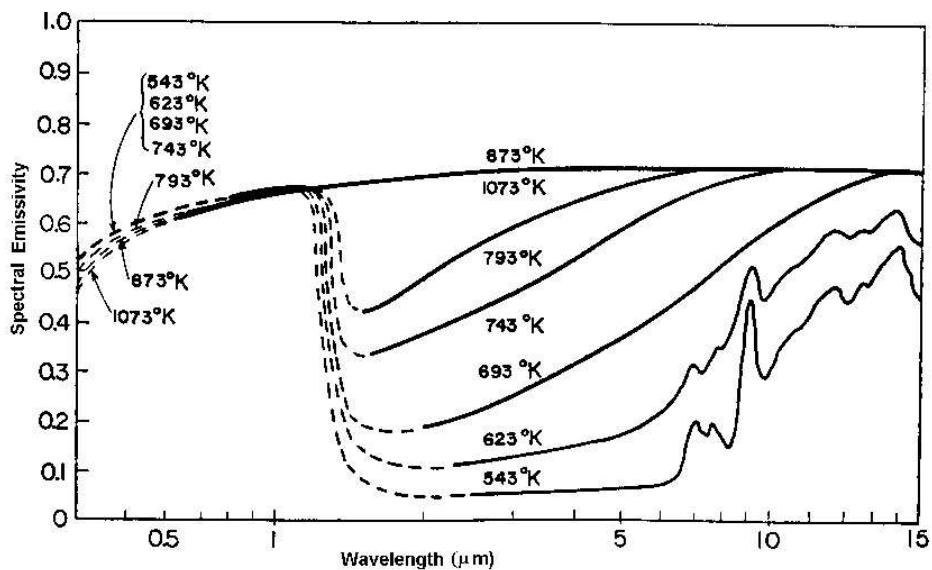


Fig. 3.6. Normal spectral emissivity of pure silicon measured by Sato [134]. Solid curves were obtained from direct method of emissivity measurement and dotted curves were obtained from indirect method of emissivity measurement (i.e., emissivity is calculated from the measured values of reflectivity).

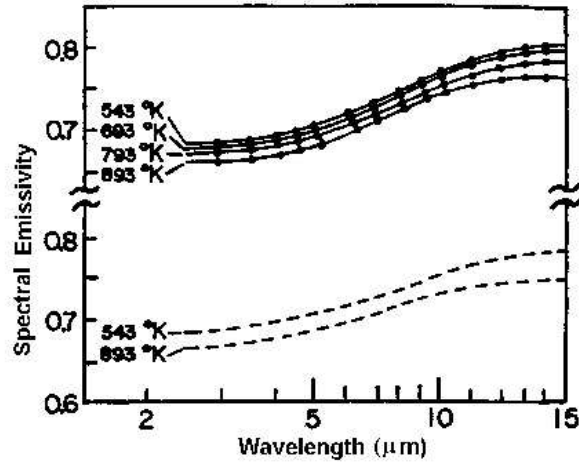


Fig. 3.7. Normal spectral emissivity of n-type silicon doped with phosphorus obtained by Sato [134]. Solid curves are drawn from measured data and dotted curves are drawn from calculated values.

In the high temperature range from 1000 K to 2000 K Neuer et al. [109, 110, 111] measured the spectral and total emissivity of a number of various highly emitting coatings, carbon, carbides and nitrides (highly emitting high-temperature materials). Labuhn and Kabelac [80] developed a novel experimental apparatus for measuring the directional spectral emissivity as well as the degree of polarization of photovoltaic solar cells at angles of emission between 0° and 70° , and wavelengths between $4 \mu\text{m}$ and $20 \mu\text{m}$. The radiation energy and entropy fluxes were calculated by using these optical quantities in order to evaluate the efficiency of a solar energy conversion device. Especel and Mattei [41] carried out simultaneous direct and indirect measurements of the directional total emissivity on samples (e.g. black and aluminium paints) at room temperature. By means of a periodic radiometric method the directional total emissivity measurements were performed without use of an absolute reference at the same temperature of source and sample. A simple high-sensitivity radiometer was designed by Pantinakis and Kortsalioudakis [119] for direct determination of the directional total emissivity of solid surfaces at near ambient temperatures without cooling. Results were obtained for a float glass sample at 50°C over a range of emission polar angles from 10° to 70° by using self-referencing technique, where the sample itself acted as the reference so that no separate reference material was required. Lippig et al. [85] measured the normal spectral emissivity of surfaces at the temperature range from 450°C to 1300°C , which are used in jet engines and space technology. The chance to optimize the spectral emissivity behavior for radiation cooling in space flight vehicles by means of the surface coatings and to evaluate the influence of a hydrocarbon-flame emission spectrum on the walls of the combustion chamber were studied in detail.

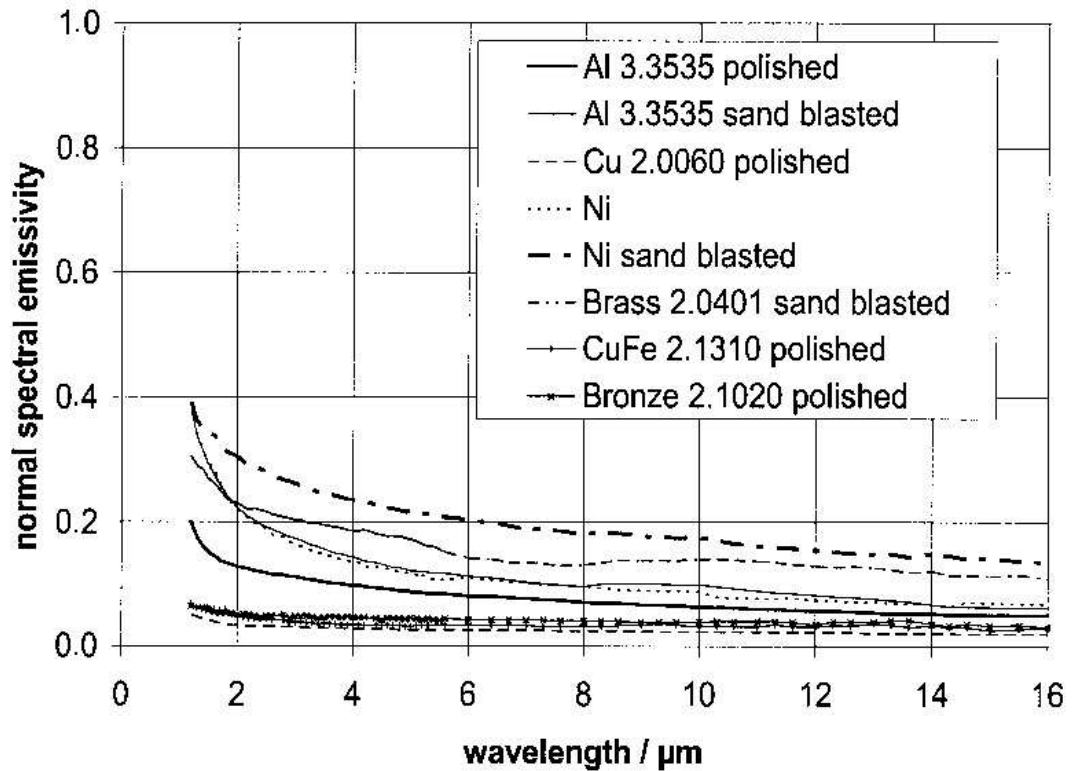


Fig. 3.8. Normal spectral emissivities of selected non-ferrous metals measured by Bauer et al. [9] at 400 °C (material no. according to DIN).

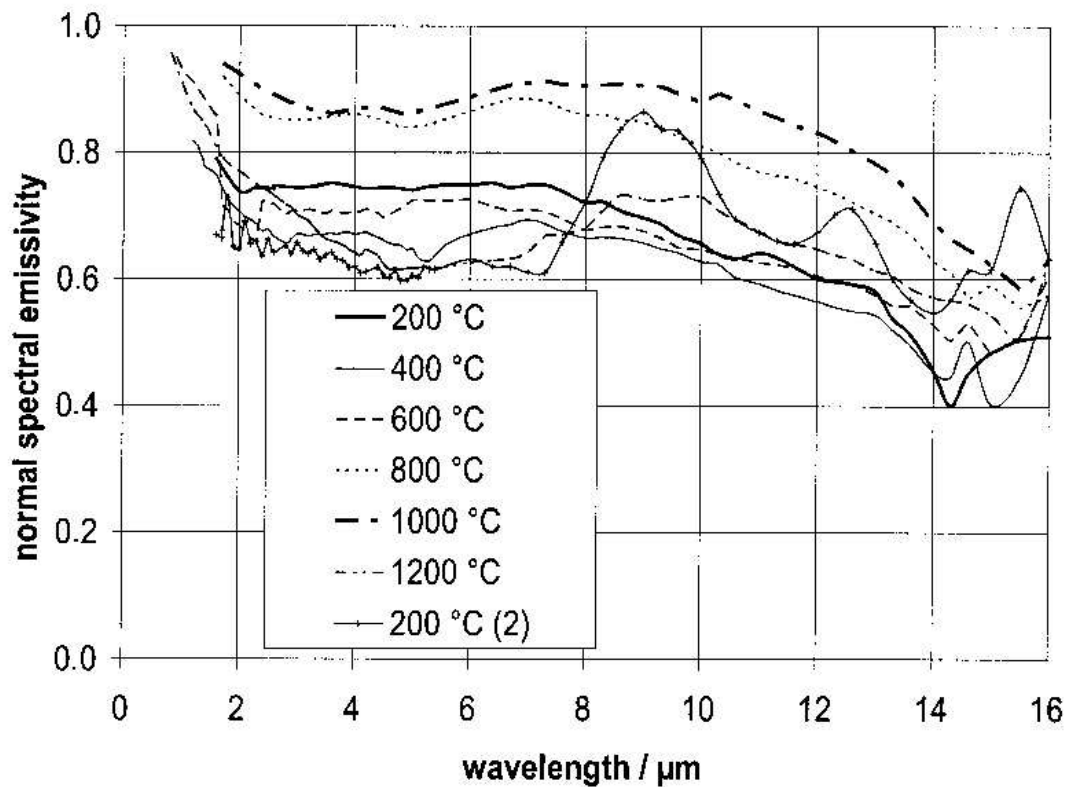


Fig. 3.9. Temperature dependent normal spectral emissivities of pre-oxidized Inconel 600 sample measured by Bauer et al. [9] in nitrogen atmosphere. The emissivity curve denoted by 200 °C (2) is the second measurement at the temperature 200 °C after cooling down from 1200 °C.

Theoretical calculations of the directional spectral reflectivity, absorptivity and transmissivity of glass were performed by Hsieh and Su [66] for the wide range of wavelength between 0.32 μm and 206 μm by using its optical constants (refractive index n , and extinction coefficient k). These radiative properties were also integrated to obtain the directional- and hemispherical total properties. Lohrengel [87] investigated directional total emissivity of different kinds of black coatings with regard to their use as total radiation standard in the temperature range from $-60\text{ }^{\circ}\text{C}$ to $180\text{ }^{\circ}\text{C}$. De Silva and Jones [35] measured the directional total emittance of some metals, solar absorbers and dielectrics at temperature 368 K with a directional total emissometer. A new technique was developed by Yi et al. [162] for the direct measurement of the normal spectral emissivity at several wavelengths in pulse heating conditions. The measurements were performed on niobium over a wide temperature range (300 K-2750 K) with a new pulse heating technique, which is a high speed multi-wavelength reflectometric technique associated with multi-wavelength pyrometry. Jones et al. [72] experimentally determined the directional spectral emissivity of heavily oxidized copper as function of wavelength between 2 μm and 10 μm , of direction from 0° to 84° and of temperature from $400\text{ }^{\circ}\text{C}$ to $700\text{ }^{\circ}\text{C}$. For the determination of the directional spectral emissivity of solids, Lohrengel et al. [89] proposed an experimental set up and measured the directional spectral emissivity in the wide spectral range from 2.5 μm to 45 μm at temperatures between $80\text{ }^{\circ}\text{C}$ and $350\text{ }^{\circ}\text{C}$. An overview of the emissivity measurements and modeling of silicon-related materials were presented by Ravindra et al. [126]. For this purpose, a spectral emissometer was utilized, which is capable of simultaneous measurement of reflectivity, transmissivity, emissivity and temperature in the wavelength range 1 μm to 20 μm . Bauer et al. [9] measured the normal spectral emissivities of bright and oxidized as well as sand blasted metals like steel (inconel 600), nickel, brass, aluminium, copper etc. at high temperatures from $200\text{ }^{\circ}\text{C}$ to $1200\text{ }^{\circ}\text{C}$ in the wavelength range from 0.6 μm to 16 μm as shown in figures 3.8 and 3.9.

A literature review on the radiometric technique for the direct measurement of the emissivity was done above, where almost all authors used different techniques rather than infrared emission spectroscopy technique using Fourier transform infrared (FTIR)-spectrometer. Because of its high spectral resolution and signal to noise ratio as well as high speed of spectrum measurement (see chapter 7), FTIR-spectrometer is becoming a suitable instrument in the field of infrared emission spectroscopy. For the same reason, the FTIR-emission spectroscopy technique is also used in this dissertation. A detailed literature review

of the FTIR-emission spectroscopy with great emphasis will be therefore presented in the following section.

3.2.1 FTIR-Emission Spectroscopy

The measurement of emission and absorption is possible if the sample is not in thermal or radiative equilibrium with the measuring device. A net gain in energy is required for absorption and for emission there must be a net loss of energy from the sample to the detector. The intensity signal of emitted radiation depends on the temperature difference between the sample and the detector ($T_s^4 - T_D^4$) as well as on the amount of material present. For this reason no signal will be recorded for a sample at room temperature if a room temperature detector, such as DTGS (deuterated triglycine sulphate) is used since the sample (source), detector and background are in thermal and radiative equilibrium. Thus, in most cases the sample is heated to moderate temperatures to enforce a thermal or radiative non-equilibrium between the sample and detector.

The detection of weak infrared radiation emitted by a sample is possible with the help of Fourier transform infrared spectrometry because of its high sensitivity. But there is a poor signal to noise ratio due to the large background radiation. This low signal to noise ratio due to background radiation is one reason why the great potential of infrared emission spectroscopy has not yet been fully exploited. Few results have been reported in the literature; however, many of the published papers on emission spectroscopy demonstrate that this sampling technique is a powerful tool for studying emission spectra of technical surfaces. Previous researchers reported emission spectra measurements with FTIR-spectrometer, which are described briefly in the following.

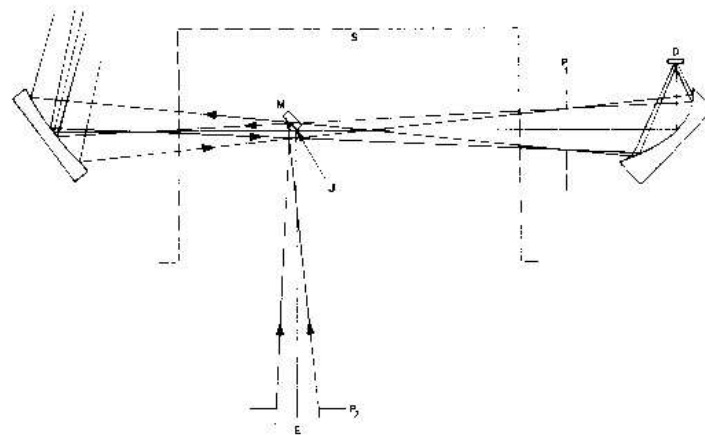
Low [91] applied the Fourier transform infrared (FTIR)-spectrometry to the study of the infrared emission spectra of mineralogical surfaces. Griffiths [52] demonstrated the feasibility of using Fourier transform infrared spectrometry for measurements of emission spectra by his studies of solid samples near ambient temperature. He measured the emission spectra of both thick and thin films of silicone grease on aluminium sheets. A detailed theoretical and experimental review with a history of the infrared emission spectroscopy was presented by Deblase and Compton [32]. From all of the works reported in reference [32] it was clear that the strong background emission was superimposed on a weak emission from the surface. This is the main problem for extending the emission technique to the surface analysis until now. Some authors tried to reduce this background emission by different experimental methods. For example, Durana [39] obtained emission spectra of thin polymer

films with greatly enhanced sensitivity by cooling the spectrometer and sample chamber in liquid nitrogen. This attempt was successful and achieved sensitivities down to fractions of a monolayer of organic adsorbates on metal surfaces. Lauer et al. [81] also tried to remove most of the background emission by a polarisation-modulation method, i.e. the polarisation of the emitted infrared emission of solid samples making use of their orientation. The very small signal intensity is a disadvantage of this technique.

Greenler [49] calculated the angular distribution of the intensity of the emission from molecules adsorbed on metal surfaces. He found that the coherent emission from the oscillator dipole normal to a metal surface has an intensity maximum when the viewing angle is between 70 and 80 degrees from the normal, and it is approximately zero in the direction normal to the surface. According to Greenler, the destructive interference takes place between emitted and reflected light from the interface to the metal surface, and therefore, the intensity minimum results when the dipoles are oriented perpendicular to the surface. This theory was used later by Nagasawa and Ishitani [108]. They measured good quality emission spectra of thin polymer layers on flat aluminium plate using a viewing angle of 70 degrees and reported linear correlations between relative emissivity and coat thickness for thin overlayers on metal substrate, indicating that the detection limit for emission spectroscopy was similar to reflection absorption spectrometry. Wagatsuma et al. [153] combined the large viewing angle with the polarisation-modulation technique for emission spectra measurements of a thin polyvinyl acetate film on a silver mirror and aluminium oxide film on gold. Emission signals could be detected with films as thin as a few nanometers in thickness. Handke and Harrick [54] proposed a new device for infrared emission spectroscopy measurements to increase the emitted signal by collecting it over large solid angles with an ellipsoidal mirror. This device was tested with the use of samples of thin silicate coatings on steel surfaces and hydrated silica gel surfaces. Emission spectra with significantly high signal to noise ratios were achieved.

Ford and Spragg [45] reported a simple method of modifying a Fourier transform infrared spectrometer to measure emission spectra without requiring access to the source. Radiation from the source of emission was directed into the interferometer from the sample chamber as shown in figure 3.10. Good quality emission spectra were obtained by simply placing a plane mirror at 45° into the path of the infrared radiation in the sample chamber. Kember and Sheppard [74] used ratio-recording interferometry for the measurement of infrared emission spectra, where the emission from a given sample is ratioed against that from

a black body emitter at the same temperature. This technique was applied to oxide films on copper surfaces at a temperature of 135 °C.



E = emission source; P₁, P₂ = pupil images; J = Jacquinot stop image ; M = plane mirror ;
S = walls of sample compartment ; and D = detector.

Fig 3.10. Simple optical arrangement for emission measurements developed by Ford and Spragg [45].

Kember et al. [75] developed a procedure for the measurement of weak emission spectra from overlayers on metal surfaces using Fourier transform infrared interferometry. The signal generated by extraneous room temperature radiation such as the beam splitter emission could be eliminated by the subtraction procedure whereby difference spectra were measured from the sample at two different temperatures without any movement of the sample between measurements. Without any explanation it was suggested that subtraction of interferograms as opposed to subtraction of calculated single beam spectra, might be more effective in eliminating the extraneous background emission. It was shown that a mercury cadmium telluride (MCT) photoconductive detector cooled by liquid nitrogen gives a better signal to noise ratio compared with the triglycine sulphate (TGS) room temperature pyroelectric detector.

For the use of cooled detectors, it is necessary to take into account the effects of any ambient background radiation that might reach the detector. This was done by Chase [24] who proposed a standard technique, in which emission spectra of both the sample and a black body reference material were measured at two temperatures, namely at the chosen emission temperature and at room temperature. According to Chase, the measured intensity, $E(\nu, T)$ at a wavenumber ν and temperature T is then given by

$$E(\nu, T) = R(\nu) [\varepsilon(\nu, T) H(\nu, T) + B(\nu) + I(\nu) \rho(\nu)] \quad (3.1)$$

where $R(\nu)$ is the instrument response function, $\varepsilon(\nu, T)$ is the sample emissivity, $H(\nu, T)$ is the Planck function, $B(\nu)$ is the background radiation, and $I(\nu)\rho(\nu)$ is the background radiation reflected from the sample with $\rho(\nu)$ as the reflectivity of the sample. For the blackbody reference material, $\varepsilon(\nu, T) = 1$ and $\rho(\nu) = 0$. This procedure for the calculation of emissivity also eliminates beam splitter emission provided the subtractions are carried out at the interferogram stage rather than spectra so that some phase correction problems can be avoided as explained in reference [75].

Allara et al. [4] showed that the combination of a liquid nitrogen cooled interferometer and a liquid helium cooled photoconductive copper-doped germanium detector permits the measurement of emission spectra of surface species held at ambient temperature. Conroy et al. [30] designed a special emission accessory to be used in connection with a FTIR- spectrometer in order to study the factors which affect the emissivity of low emitting metal surfaces like aluminium from ambient temperature to 450 °C and presented emission spectra as well as emissivity curves of the highly pure aluminium surface. Ballico and Jones [7] demonstrated a useful experimental technique for the measurement of the spectral emissivities in the high temperature range from 500 °C to 1000 °C of samples with poor thermal conductivity and high transparency. Spectral emissivity measurements of Potassium metaborate were made by using an FTIR-spectrometer and these results together with estimates of the sources of uncertainty proved the technique to be practical.

Ishii and Ono [68] described the FTIR-spectrometer system and techniques for measuring the spectral emissivity of opaque solids near room temperatures. The FTIR-spectrometer was calibrated against the two reference blackbodies, a liquid nitrogen cooled blackbody and a variable temperature blackbody, based on the advanced phase correction technique. Size of source effect and the linearity check of the FTIR-spectrometer response was performed and measurement of the normal spectral emissivity of a black paint (Nextel-Velvet-Coating 811-21) was demonstrated with the instrument. A method for the contactless measurement of the spectral emissivity and temperature of a surface with a FTIR-spectrometer was presented by Lindermeir et al. [83]. In order to avoid the need of measuring the blackbodies' surface temperatures a special calibration procedure was described, which used three blackbodies as reference sources. This calibration procedure needs to measure the spectra of three reference blackbodies instead of two, which is a drawback of this method.

Brun et al. [20] introduced a new approach with FTIR-emission spectroscopy to analyze the emissivity spectra of semitransparent materials with high melting temperature, below and above the melting point. The normal spectral emissivities of very pure magnesium oxide (magnesia) and aluminium oxide (alumina) single crystals were measured up to the temperature of 2600 K over the wavelength range from 1.7 μm to 28 μm as shown in figure 3.11.

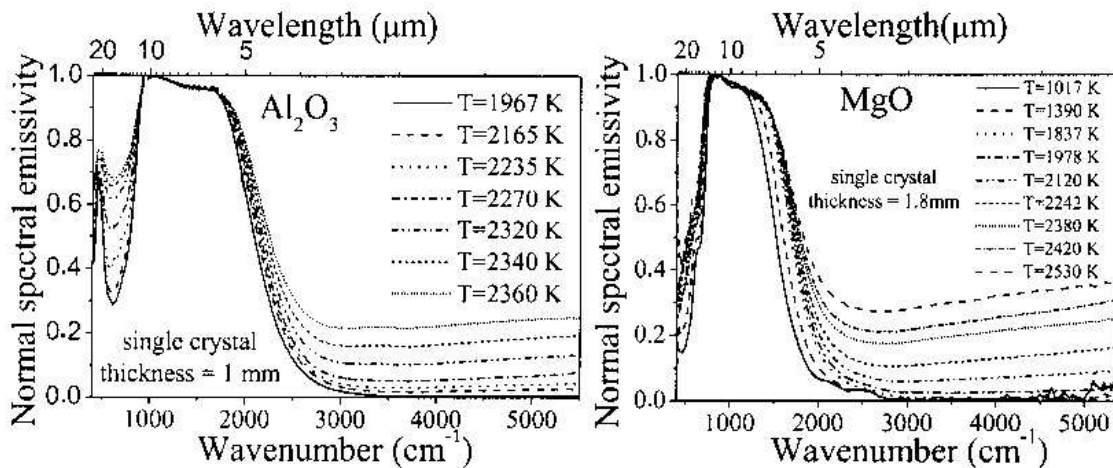


Fig. 3.11. Temperature dependence of the normal spectral emissivity of alumina (Al_2O_3) and magnesia (MgO) obtained by Brun et al. [20].

The effect of geometrical conditions like smoothness, irregular surface roughness, surface impurities, such as oxide films and coatings on the radiative properties of the surface were studied by many researchers using FTIR-spectroscopy as explained above. In the following chapters regular surface macrostructures, in which the dimensions of the structure is much larger than the wavelength of the radiation and the periodic surface microstructures with the dimensions of the order of the wavelength of the radiation will be discussed in detail.

3.2.2 Regular Surface Macrostructure

In order to achieve good performance from any radiant heat transfer device except for insulation duties, its surface should have the emissivity as close to unity as possible. One way for the emissivity enhancement of a surface is to use grooved surfaces. Rectangular, triangular and other forms of the groove cavities with the dimension much greater than the wavelength of the radiation are called regular surface macrostructures.

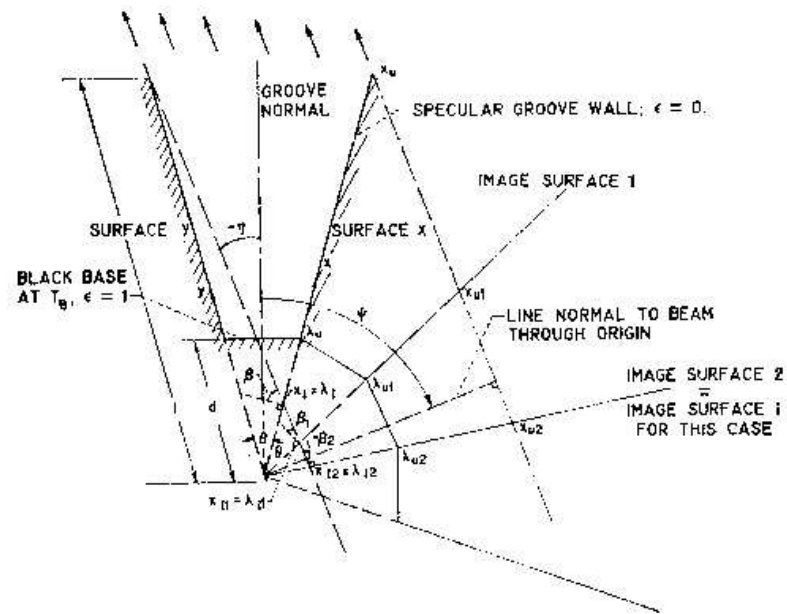


Fig. 3.12. Geometrical relation with images of surfaces for a groove having specular walls with a reflectivity of one and a black base used as a strongly directional emitting and absorbing surface by Perlmutter and Howell [120].

The variation of the effective emissivity of a v-shaped groove with the angle of observation was calculated by Daws [31] for a graphite surface. Psarouthakis [123] experimentally studied the radiant interchange within an infinitely long v-shaped groove on a molybdenum sample and its apparent thermal emissivity was found to be a function of the included angle of the groove assuming the bounding surfaces of the groove are isothermal and gray diffuse. When radiation from an external source arrives at the rectangular- and v-groove cavities in a bundle of parallel rays or in a diffuse manner, the absorptivities of the cavities whose surfaces are either diffuse- or specular reflectors were theoretically determined by Sparrow and co-workers [141, 142, 143]. The directional emissivity and reflectivity of a specular, gray or isothermal groove were analyzed by Perlmutter and Howell [65, 120] in detail. A general method of analysis based on images of surfaces was described. It was shown that the directional radiant properties strongly depend on the shape of the local macroscopic surface structure which can be controlled by proper design of these surfaces. A perfect emitter which possesses very high emissivity in a desired direction was designed from grooved surfaces with specular walls with a reflectivity of one and a black base (see fig. 3.12). The directional emissivity of such grooved surfaces is represented in figure 3.13. Hollands [64] showed that a v-corrugated specular surface is directionally selective. The directional absorptivity and emissivity of such surface as well as a method of choosing the best angle of opening for a particular solar energy design was presented.

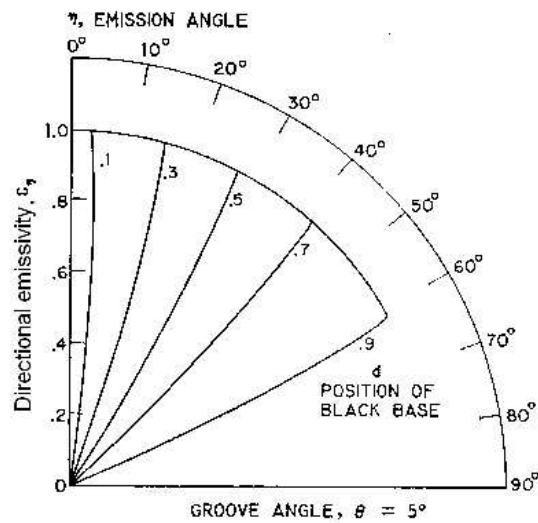


Fig. 3.13. Directional emissivity of the grooved surface with non-dimensional distance d from the bottom of the groove as the parameter obtained by Perlmutter and Howell [120].

A variety of surfaces with different geometries and surface finishes were investigated by Clausen and Neu [28] for their use of directionally dependent radiation properties and application to the thermal and visual design of space vehicles. The directional absorptivity and reflectivity of such surfaces were measured and compared with the analytically predicted values. Black and co-worker [13, 14] experimentally and analytically studied and optimized the directional emission from specially prepared v-groove and rectangular cavities. It was found that a v-groove with flat black base and specular reflecting sides is a directional cavity, which emits a large percentage of its energy in the near normal directions. Similarly, a rectangular groove with black sides and specular reflecting base is a directional cavity with a large percentage of its emitted energy leaving at grazing angles. An optimum depth and an optimum opening angle of the v-groove and of the rectangular groove were determined with an image technique where an emission pattern exists with the strongest collimation of emitted energy. Demont et al. [33] experimentally and theoretically studied the emissivity of v-shaped and other groove geometries (e.g. conical, cylindrical and hemispherical shaped cavities) on opaque materials. Strongly directional properties were observed in some surface conditions. For example, studies on triangular grooves or rectangular grooves show that these cavities have complementary actions. The first type increases emission in the direction normal ($\vartheta = 0^\circ$) to the surface, while the second type increases the emission towards the tangential direction ($\vartheta = 90^\circ$) when the reflection is specular. So a \surd -groove, which associates both of these grooves should have an important apparent emissivity whatever emission angle (ϑ) is

considered. It was suggested that the emissivity of a material may be almost tripled by a \surd -grooving as shown for the case of stainless steel (304 L) in figure 3.14 . The fabrication of superficial cavities of various forms and dimensions modifies the directional spectral emissivities or absorptivities. They are usually increased compared to those of optically smooth material. The gain in these properties depends on the material, the type of cavities, as well as the wavelength and the direction of the emitted or incident radiation. Calculations based on a geometric optics model were in close agreement with experimental results for variously shaped grooves when the characteristic dimension of the cavity is larger than the wavelength of radiation. But when the characteristic dimension is close to the wavelength of the radiation, a clear discrepancy appeared between the measured and calculated results. This discrepancy cannot be ascribed merely to the invalidity of geometrical optics model. However, it was observed that the measured emissivities were always greater than those calculated from the proposed models.

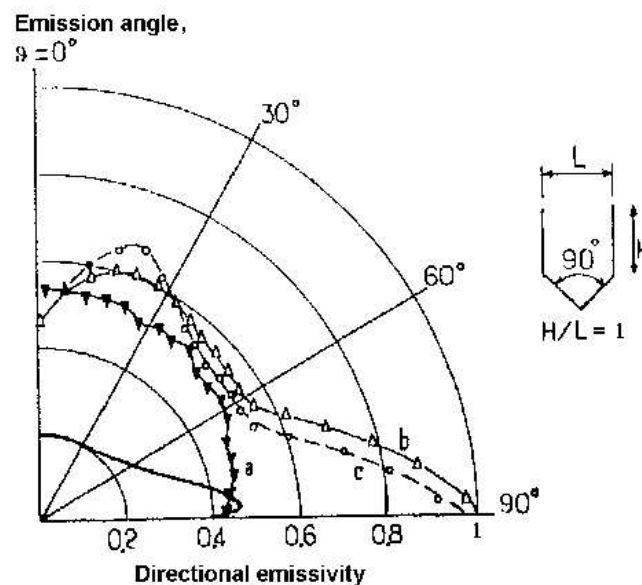


Fig 3.14. Directional emissivity of a \surd -groove with emission angle as the parameter. The directional spectral emissivity of stainless steel (304 L) measured at temperature , $T = 773 \text{ K}$ and wavelength, $\lambda = 5 \mu\text{m}$, is given by the solid curve. Dotted curves a, b, and c are obtained from the calculated values with the assumptions (a) isotropic emission and diffuse isotropic reflection, (b) isotropic emission and specular reflection and (c) anisotropic emission and specular reflection, respectively.

For non-uniform temperature of the walls O'Brien and Heckert [113] numerically determined the effective emissivity of a v-grooved blackbody cavity with both specular- and diffuse reflecting walls. It was reported that the effect of relatively large wall temperature gradients on the effective emissivity is small for both specular- and diffuse reflecting walls.

Mekhortsev et al. [107] presented the results of computer modeling of temperature distributions and effective emissivities of reference blackbody cavities with both triangular and trapezoidal profiles covering a temperature range from 100 K to 900 K. A finite element method was applied to calculate temperature distributions and an effective emissivity simulation was realized by a Monte Carlo method. Zhimin [165] proposed the approximate solution of an integral equation describing the radiative heat transfer in both isothermal and non-isothermal diffuse rectilinear grooves with a triangular shape and obtained the dependences of total directional, normal and hemispherical emissivities on several critical parameters. An effective emissivity modeling was performed by Prokhorov et al. [122] for concentric isothermal and non-isothermal grooves of trapezoidal and triangular profile with mixed specular-diffuse reflection for various viewing conditions. It was shown that a temperature drop towards the peak of a groove might lead to a substantially decreased effective emissivity.

3.2.3 Periodic Microstructured Surfaces

Both measurements and theoretical models for the investigation of radiative properties of regular surface macrostructures were based on the assumption that the geometric scale of the radiating surfaces is much larger than the wavelength of radiation. This was a natural assumption given by the available methods for fabricating the radiating surface structures at the time of the investigation. The planar photolithographic and other manufacturing technologies like chemical etching that have evolved in the microelectronics industry now make it possible to study the radiative properties in the region where the geometric scale of the radiating surfaces is on the order of the wavelength of radiation. The surface containing these small-scale structures will be referred to as periodic microstructured surfaces.

Recently, spectral control of thermal radiation has been focused on as an application of micromachining techniques. This method is expected to be applicable in various thermal systems, since electromagnetic interactions at a microstructured surface are receiving considerable attention. Up to now, several authors have demonstrated spectral control of the emissivity by means of periodic microstructures and some of the most recent works will be discussed here.

Hesketh et al. [58, 60, 61, 62] extensively reported the directional and polarized spectral emissivity from one-dimensional heavily doped lamellar silicon surfaces with rectangular microstructure geometries. Selective thermal emission by electromagnetic

standing waves was observed in microgrooves with repeat distances and depths of the grooves varied from 10 μm to 22 μm and from 0.7 μm to 44 μm , respectively. The measurements were carried out at temperatures of 300 $^{\circ}\text{C}$ and 400 $^{\circ}\text{C}$ and the experimental results were compared with data calculated by a geometric optics model. This research on the emission properties was extended by Wang and Zemel [156, 157, 158] to the case where the silicon is a dielectric material. Several theoretical models, for example Bloch-wave, coupled-mode, effective medium and waveguide methods, were examined. The results from the periodic micromachined undoped silicon surfaces indicate that although these methods provide guidance for the prediction of the emission properties, none of the models yields a complete solution.

Cohn et al. [29] systematically studied modal reflection from microcontoured nickel surfaces with one-dimensional sinusoidal and triangular profiles, and for chrome and doped silicon samples with rectangular profiles. The experimental results were compared with rigorous calculations based on the electromagnetic theory and extinction theory [37, 38, 97]. Good agreement was observed between the experimental findings and the theoretical predictions qualitatively and quantitatively (see figures 3.15-3.19). Polarized directional spectral reflectivity and emissivity of a silicon carbide (SiC) one dimensional grating was studied experimentally and theoretically by Gall et al. [47] in the wavelength region between 10 μm and 11.5 μm . It was shown that the existence of peaks of the emitted monochromatic radiation in particular angular directions implies that, due to surface waves, the thermally excited field is partially coherent along the interface.

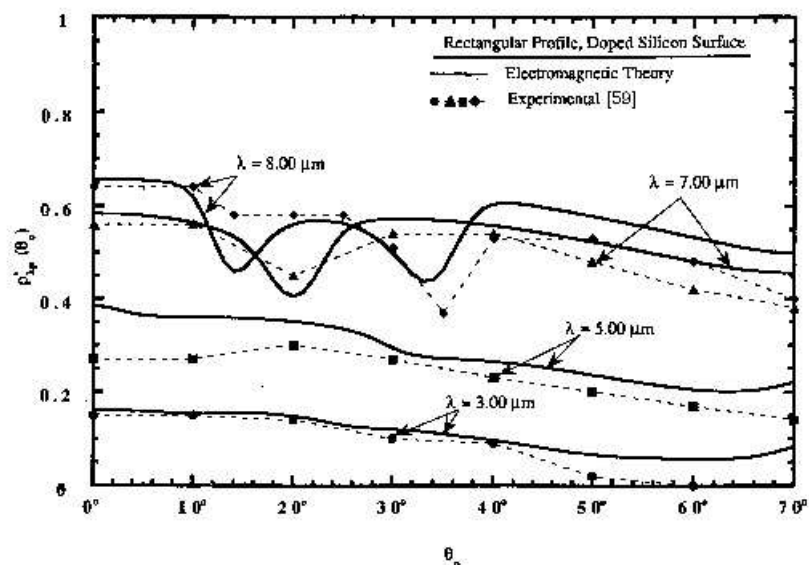


Fig. 3.15 P-polarized directional hemispherical reflectivity as a function of incident angle for a microstructured doped silicon surface with a rectangular profile (period = 10.0 μm , depth = 0.7 μm and width = 6.3 μm) reported by Cohn et al. [29].

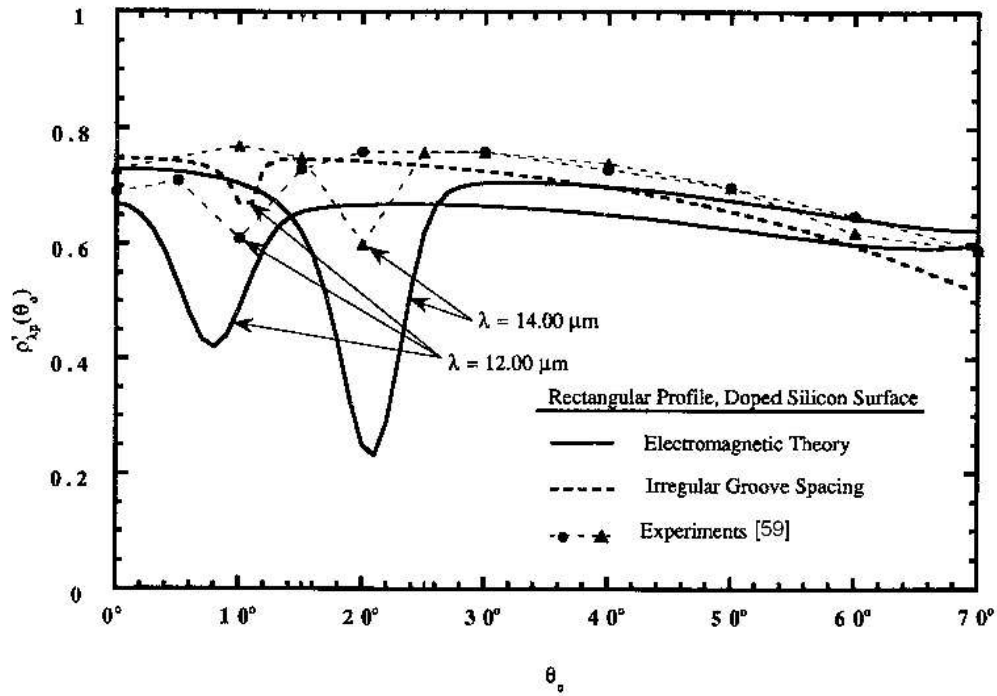


Fig. 3.16. P-polarized directional hemispherical reflectivity as a function of incident angle for a microstructured doped silicon surface with a rectangular profile (period = 10.0 μm , depth = 1.5 μm and width = 7.3 μm) reported by Cohn et al. [29].

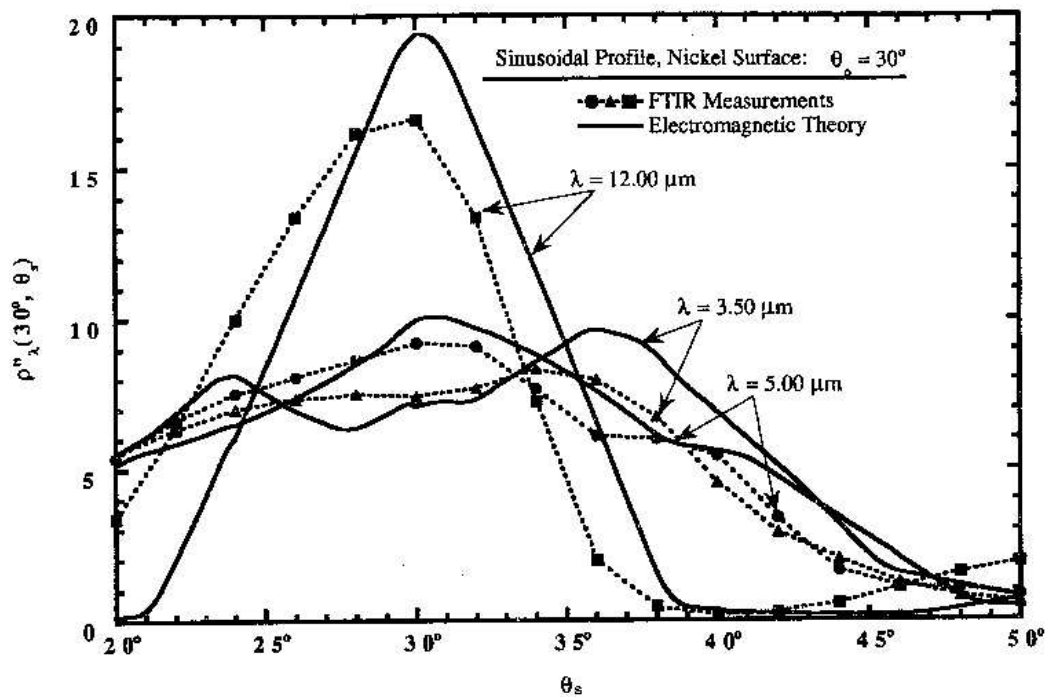


Fig. 3.17. Comparison between electromagnetic theory and experimental results as a function of scattering angle (θ_s) and incident wavelength for a nickel surface with a sinusoidal profile reported by Cohn et al. [29].

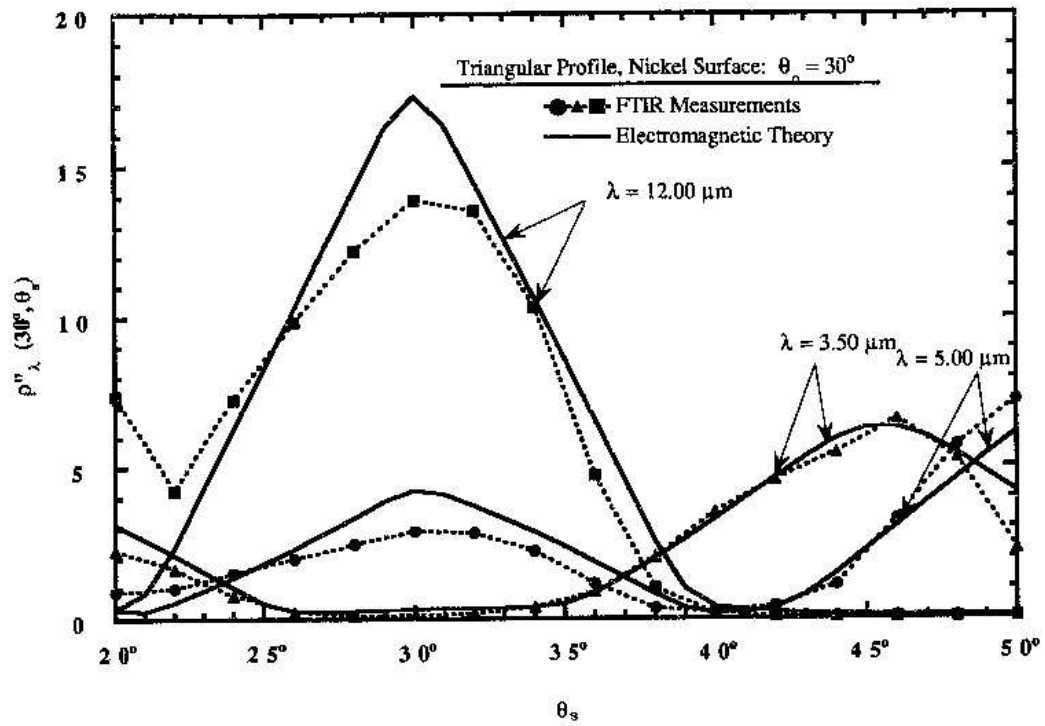


Fig. 3.18. Comparison between electromagnetic theory and experimental results as a function of scattering angle (θ_s) and incident wavelength for a nickel surface with a triangular profile reported by Cohn et al. [29].

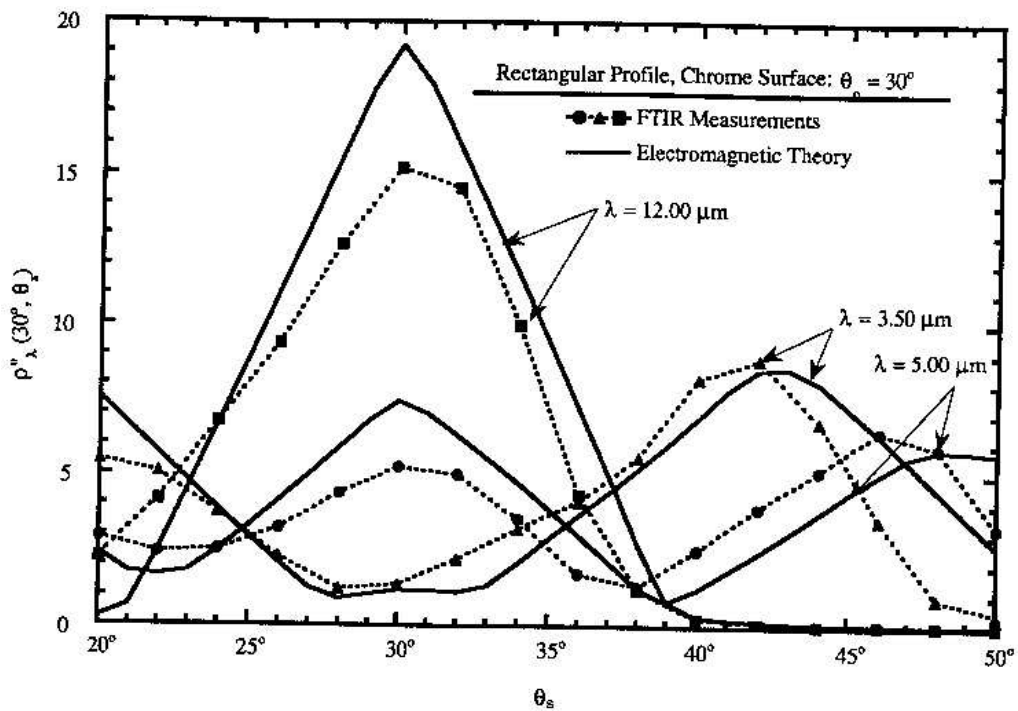


Fig. 3.19. Comparison between electromagnetic theory and experimental results as a function of scattering angle (θ_s) and incident wavelength for a chrome surface with a rectangular profile reported by Cohn et al. [29].

Tang and Buckious [147] reported detailed results on reflection from two dimensional metallic square grooved surfaces with repeat distances and surface heights ranging from 10 μm to 30 μm and from 1.6 μm to 20 μm , respectively. The detailed feature of thermal emissivity from microstructured surfaces was demonstrated experimentally as well as analytically. The possibility of controlling spectral reflectivity and thereby spectral emissivity from periodic microstructured metallic surfaces was shown, although the incident wavelength is restricted to the midinfrared range (2 μm -12 μm). A simulation study of selective emission from the tungsten surface with periodic microstructures was presented by Heinzl et al. [42, 55, 56] using the coupled wave theory. It was demonstrated that thermal radiation from microstructured tungsten surfaces can be utilized for fabricating thermophotovoltaic selective emitters.

As high temperature applications (e.g. thermophotovoltaic generation of electricity), Sai et al. [129, 130, 131] investigated the resonance effect between the emissive fields and two-dimensional periodic microstructured metal surfaces in the near infrared region. Numerical calculations based on rigorous coupled-wave analysis were also performed to obtain the optimum configuration of surface microstructures with rectangular and hexagonal cavities. It was confirmed that the surface microstructure can be applied to the control of the spectral emission from high-temperature resistive materials made of a single crystal.

For the infrared wavelength region between 3 μm and 25 μm , Maruyama et al. [98] performed measurements of polarized directional emission spectra, which reveal that the thermal emission from a two dimensional microcavity shows a isotropic and random polarization character. It was found that the surface microcavity structure made on low-emissivity material surface is very efficient to control the thermal radiation and the dominant peaks of the emission spectra can be explained by a simple cavity resonator model. Puscasu et al. [124] demonstrated an enhancement of the emitted radiation from frequency selective surfaces consisting of aluminium patches on silicon substrates in the infrared wavelength region from 3 μm to 15 μm . It was shown that the resonant wavelength can be tuned by a proper choice of the array design parameters for the particular application. By using the near-field coherence properties of thermal sources [21, 136], Greffet et al. [50] made theoretical calculations and experimental measurements, which demonstrate that it is indeed possible to build an infrared antenna (see figure 3.20) by properly designing a microstructure on a polar material such as glass, silicon carbide (SiC), and semiconductors. Two types of thermal sources were designed: first, a thermal source exhibiting a high degree of spatial coherence, which radiates infrared light in a narrow solid angle when it is heated, and its emission

spectrum depends on the direction of observation, i.e. its emission at a given wavelength is highly directional as shown in figure 3.21. Second, a partially coherent source radiating quasi-monochromatic infrared light isotropically at a single wavelength for all observation angles, i.e. its emission at a given wavelength is not directional. It was confirmed that thermal emission of radiation by surfaces may be controlled in order to produce new types of infrared sources. All materials supporting surface waves can be used, including glass. One can imagine a modification of the Green house effect of glass by changing the absorption of the glass with the microstructured surface. Instead of being reflective, the glass will be more absorptive and the heat isolation with the green house effect will be improved to some extent.

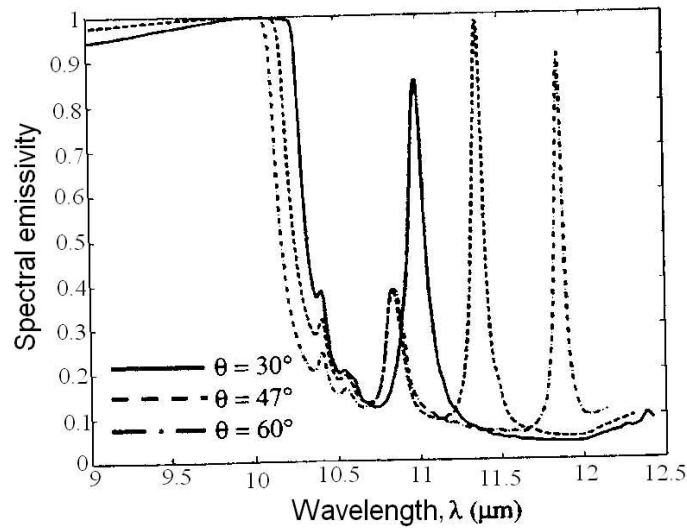


Fig. 3.20. Theoretical spectral emissivity for different angles of observation (θ) for a silicon carbide (SiC) grating with period = 6.25 μm , height = 0.285 μm , volume filling factor = 0.5 obtained by Greffet et al. [50].

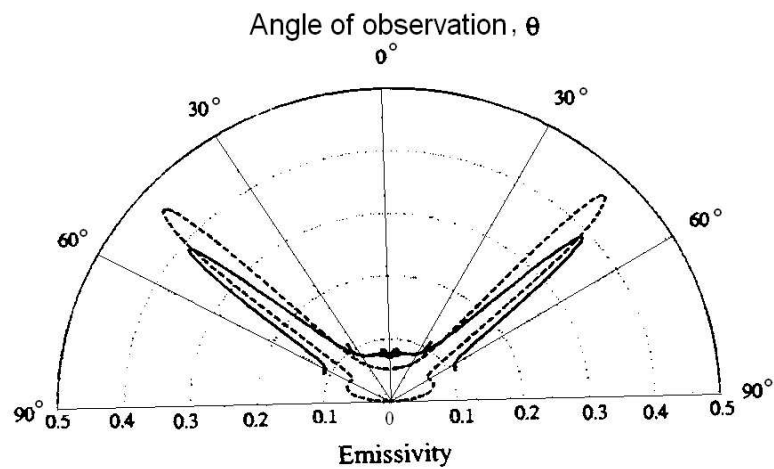


Fig. 3.21. Emissivity of a silicon carbide (SiC) grating for the wavelength, $\lambda = 11.36 \mu\text{m}$. Solid curve was obtained from experimental data and dash curve was obtained from theoretical calculation by Greffet et al. [50].

Within the visible spectral range, Zou et al. [166] investigated the effects of two-dimensional etched holes on the optical properties of micromachined polycrystalline silicon reflective surfaces (mirrors). It was found that when the dimension of etched holes increases, an increasing portion of the incident power will be diffracted and transmitted due to etched holes, leading to decreasing reflectivity of surface micromachined mirrors. Similarly, Jaecklin et al. [69] studied mechanical and optical properties of surface-micromachined mirrors in single crystalline silicon, polycrystalline silicon and aluminium. Foley [44] presented recent technological advances in the field of replicated, microstructured plastic optics and their applications in display optics. It was noted that new processes such as high precision molding, new materials such as high temperature thermoplastics, and new optical elements such as moth-eye antireflective microstructure and one-piece imaging screens provide optical designers and systems engineers with new degrees of freedom and flexibility in display applications.

Lin et al. [43, 82] demonstrated spectral control of emissivity by means of periodic microstructures on three-dimensional photonic crystals. It was shown that the absence of electromagnetic modes in a certain wavelength range suppresses the thermal emission, while in the pass bands high thermal emission is observed.

The analysis of optical properties of surfaces with microstructures is still a difficult problem. Yet, despite the large amount of work in this field, it is worth mentioning that most of the reported works deal with the study of the reflectivity. Although there is a simple relation between emissivity and reflectivity of an opaque material given by Kirchhoff's law, there is still a lack of detailed analysis of the emission processes in the framework of electromagnetic theory.

4 Modelling of Emission from Regular Surface Structures

As discussed in the foregoing chapters there are two types of emitting regular surface structures differing in the physical dimensions of the structural pattern. One are the regular surface macrostructures whose physical dimensions are much greater than the wavelength of the radiation, and the other are periodic surface microstructures having dimensions in the order of the wavelength of the radiation. These suppositions are generally assumed for the calculation and measurement of the radiative properties such as emissivity or reflectivity for the respective surface structures. For the prediction of radiative properties from the macrostructured surfaces a geometric optic approximation may be applied [33, 143]. This purely geometric model cannot include spectral features due to interference effects observed on the microstructured surfaces. There is also no spectral dependence, other than that which arises from the particular surface. An exact solution to the rigorous quantification of the directional and spectral radiative properties of microstructured surfaces has been recently obtained by the use of electromagnetic scattering theory [37, 38, 97]. Thus, analytical modelling of radiative properties of regular surface structures can be classified into two broad categories: exact models derived from electromagnetic theory and approximate models developed by simplifications (e.g., geometric optic model). A short discussion about these models and about the classical optical grating theory will be presented in the following sections.

4.1 Geometric Optic Model

There are two models of the geometric optic approximation, namely the specular and the diffuse approximate model. The first model assumes that the walls of the surface cavity are specularly reflecting whereas the second model assumes that all reflecting surfaces are diffuse. When the surfaces of the cavity are diffuse reflectors, the radiative heat exchange within the cavity is described by several simultaneous integral equations with many independent physical parameters. A complete set of solutions to this problem is a very formidable computational task. Therefore, the calculation of the emission from a regular macrostructured surface with rectangular grooves will be presented below by using the specular geometric optic model of Sparrow and Jonsson [143].

The specular geometric optic model, also termed ray tracing, traces the energy incident on a macrostructured surface throughout its interaction with the surface until it leaves the surface, thereby including multiple reflection from various surface elements. The number of

surface interactions typically increases with the surface cavity depth as shown in figure 4.1. Each surface interaction is modelled as a reflection from a locally optically smooth surface (Fresnel's approximation, section 2.4). Therefore, in the limit of a plane surface, the specular geometric optic approximate model reduces to the Fresnel's approximation since only a single reflection from the surface occurs. Since the specular geometric optic approximation is computationally less expensive than the exact solution obtained by the use of electromagnetic theory, the geometric parameter domain for an accurate prediction of the radiative properties of the macrostructured surface by this approximate model is important to be known.

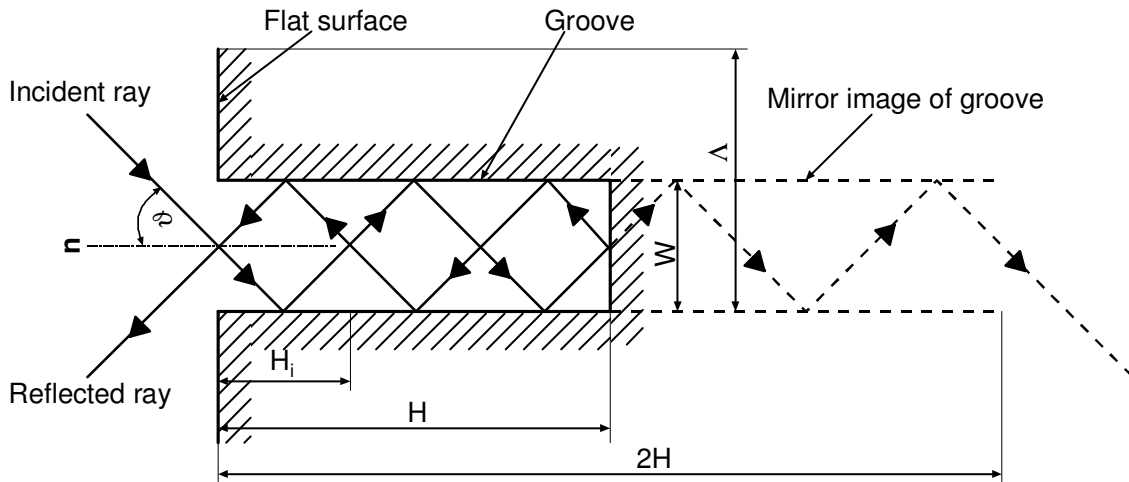


Fig. 4.1 Incoming collimated set of parallel rays in a specular rectangular cavity of a macrostructured surface.

The specular geometric optic model considers a macrostructured surface composed of many alternating flat surfaces and rectangular grooves as shown in figure 4.1. The emission properties of the flat surfaces can be found from measurements on a smooth surface of the same material. Hence, the cavity model developed here is for the grooves themselves. The emissivity of the macrostructured surface is then the sum of the emissivities of the smooth flat surfaces and rectangular grooves, in proportion to their areas. Kirchhoff's law states that the directional spectral emissivity is equal to the directional spectral absorptivity of a surface. The directional spectral absorptivity is easier to calculate for this geometry than the directional spectral emissivity. Therefore, a collimated set of parallel rays incident on a specular rectangular cavity of the macrostructured surface at an angle θ is considered to determine the directional spectral absorptivity (see figure 4.1). It is shown how a single collimated ray enters the cavity, is reflected by the walls, and then emerges back from the opening of the cavity. A mirror image of the cavity as formed in the base surface is also shown at the right by the dashed lines. For the moment, it is assumed that the base surface is removed and that the

ray can move freely through a virtual cavity of depth $2H$. Then, figure 4.1 demonstrates that the reflection pattern in the dashed or image portion of this virtual cavity is the same as that which occurs in the actual rectangular cavity after the ray has been reflected from the base surface. Thus, the number of surface contacts which a ray experiences within the actual cavity is equal to the number of the surface contacts experienced in the virtual cavity with depth $2H$ open at both ends, plus one additional surface contact caused by reflection at the base.

A depth of the cavity wall, which is directly illuminated by the incoming ray bundle, is denoted by H_i . Due to the specular reflections the ray bundle moves deeper into the cavity advancing a distance H_i with each reflection. The number of surface contacts n made by the ray bundle with the cavity sidewalls is determined as

$$n = \text{INT} \left[\frac{2H}{H_i} \right] \quad (4.1)$$

where INT means take the integer value of the expression in bracket. An additional surface contact is made with the base surface. When a ray bundle experiences $(n + 1)$ contacts with a surface of absorptivity α , the fraction of its radiant power, which is thus absorbed, is given by the expression [143]

$$\frac{d^3\Phi_{n+1}^{abs}}{d^3\Phi_t^{in}} = 1 - (1 - \alpha)^{n+1} \quad (4.2)$$

where $d^3\Phi_{n+1}^{abs}$ and $d^3\Phi_t^{in}$ are the locally absorbed radiant power after $(n + 1)$ surface contacts (reflections) of the ray bundle with the walls of the cavity and the total incoming radiant power incident into the cavity, respectively.

In addition to the $(n + 1)$ surface contacts, the ray bundle makes a final contact with the surface just before leaving the cavity. This final contact occurs over a depth equal to $(2H - nH_i)$. Since the radiant power incident on this segment of surface is equal to the fraction $(1 - \alpha)^{n+1} [(2H - nH_i)/H_i]$ of the incoming ray bundle, the fraction of this power that is absorbed can be expressed as

$$\frac{d^3\Phi_i^{abs}}{d^3\Phi_t^{in}} = \alpha(1 - \alpha)^{n+1} \left[\frac{(2H - nH_i)}{H_i} \right]. \quad (4.3)$$

By adding the expressions (4.2) and (4.3) and doing some mathematical operations we get

$$\alpha_{cav} = \frac{d^3\Phi_t^{abs}}{d^3\Phi_t^{in}} = 1 - (1 - \alpha)^{n+1} \left[1 - \alpha \left(2 \frac{H}{H_i} - n \right) \right] \quad (4.4)$$

where $d^3\Phi_t^{abs}$ is the total absorbed radiant power by the cavity. Equation (4.4) gives the fraction of the incoming radiant power which is absorbed by all surface contacts, i.e. the ratio of the total absorbed radiant power by the cavity to the total incoming radiant power into the cavity, which is precisely equal to the absorptivity of the rectangular cavity, α_{cav} . The geometry of the rectangular cavity yields

$$W = H_i \tan \vartheta. \quad (4.5)$$

With the help of equation (4.5) the directional spectral emissivity, which is by Kirchhoff's law equal to the directional spectral absorptivity, can be calculated from equation (4.4) for the rectangular cavity as the function of the angle of incidence of radiation entering the cavity, geometric parameters of the cavity, and the absorptivity of the smooth flat surface α :

$$\varepsilon'_{cav} = \alpha'_{cav} = 1 - (1 - \alpha)^{n+1} \left[1 - \alpha \left(\frac{2H}{W} \tan \vartheta - n \right) \right] \quad (4.6)$$

where H , W and n are the depth of the rectangular cavity, the width of the cavity (groove) and number of the surface contacts made by the ray bundle with the cavity sidewalls respectively. From equation (4.6) it is clear that a given cavity (i.e., given H/W) absorbs radiant power more effectively when the parallel rays enter the cavity at a large angle of incidence ϑ . This is because such rays undergo a greater number of specular reflections than do rays which enter the cavity at a small angle of incidence. Additionally, for rays entering the cavity at a given angle of incidence, the amount of radiant power absorbed increases steadily as the cavity depth increases.

The directional spectral emissivity of a macrostructured surface ε'_λ is then determined by summing the directional spectral emissivity of the flat surface and that of the rectangular cavity in proportion to their projected areas, as follows:

$$\varepsilon'_\lambda = \frac{(\Lambda - W)}{\Lambda} \varepsilon'_f + \frac{W}{\Lambda} \varepsilon'_{cav} \quad (4.7)$$

where ε'_f and ε'_{cav} are the directional spectral emissivities of the flat surface and of the rectangular grooved cavity respectively, and Λ is the repeat distance or period of the macrostructure.

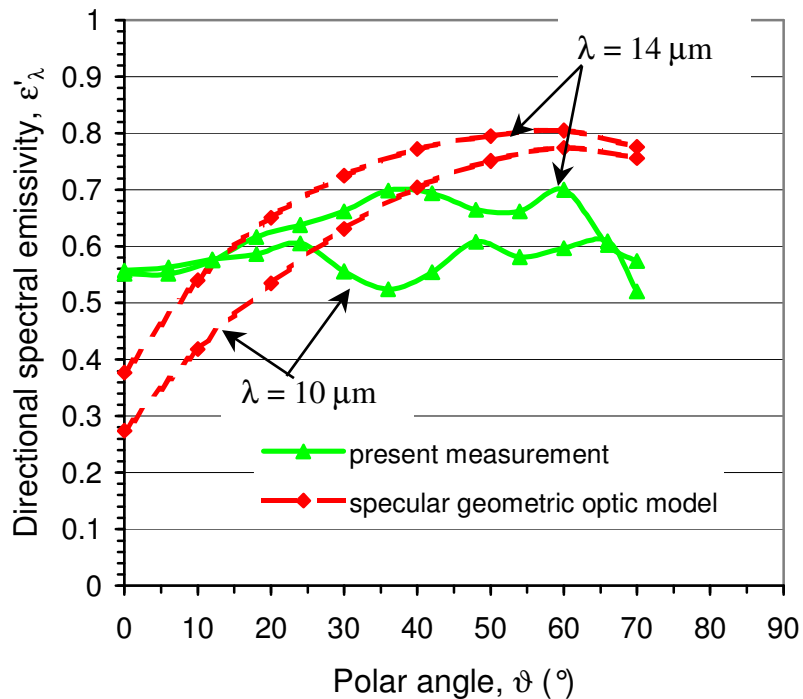


Fig. 4.2. Calculated and measured directional spectral emissivities of the microstructured undoped silicon surface with deep microgrooves, $H = 21.4 \mu\text{m}$ for the wavelengths of radiation, $\lambda = 10 \mu\text{m}$ and $\lambda = 14 \mu\text{m}$.

In order to analyse the usefulness of the geometric optical model on the microstructured surfaces, the directional spectral emissivity of the microstructured undoped silicon surface investigated in this work is calculated by using above equations (4.6) and (4.7). The measured values of the directional spectral emissivity of the smooth undoped silicon surface (see appendix A table A.10) are taken for the directional spectral absorptivity of the cavity surface α . The directional spectral emissivity values calculated for the microstructured silicon surface with the groove depth, $21.4 \mu\text{m}$ for the wavelengths of radiation, $\lambda = 10 \mu\text{m}$ and $\lambda = 14 \mu\text{m}$ are presented in figure 4.2 with the measured values in the present experiment. As already expected, the calculated and measured values are not in good agreement to each

other quantitatively. However, they have more or less a similar trend. The emission peaks due to interference effects as seen in the measured values of microstructured silicon surface with the groove depth, $H = 21.4 \mu\text{m}$ are not found in the calculated values by using the specular geometric optic model for the same groove depth. This implies that the specular geometric optic model is not suitable to interpret the emissivity values of the microstructured surface. However, it provides a base of comparison for the experimental emissivity data measured on the microstructured surfaces.

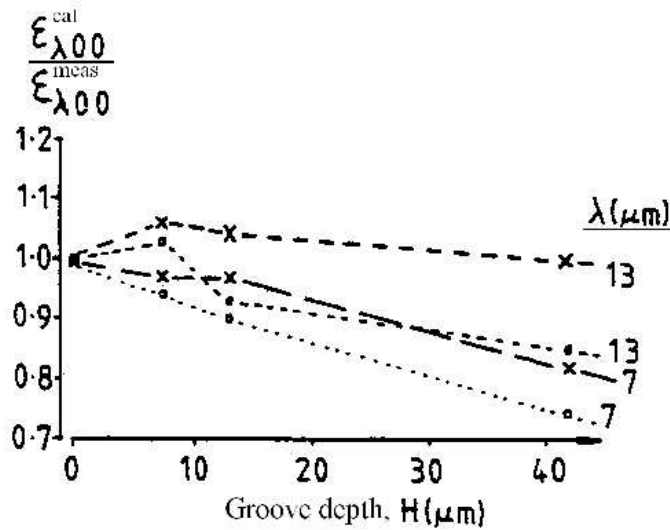


Fig. 4.3. Ratio of calculated to measured normal spectral emissivity of doped microstructured silicon surface versus groove depth (H) with the wavelength of radiation as the parameter. Curves with x denote calculated values obtained by diffuse geometric optic model and curves with o denote calculated values obtained by using specular geometric optic model as reported by Hesketh [59].

The diffuse geometric optic model is based on the assumption that all reflecting surfaces of the rectangular cavity are diffuse. A good description about this model is to be found in reference [59, 143]. Recently, Hesketh [59] performed a detailed analysis of the diffuse and specular geometric models and their usefulness to interpret the directional spectral emissivity data of heavily doped microstructured silicon surfaces. He confirmed that both geometric optic models do not provide exact solutions for the microstructured surface with dimensions in the order of the wavelength of the radiation as shown in figure 4.3. His measured and calculated data using the specular geometric optic model for directional spectral emissivity of doped silicon are presented in figures 4.8 and 4.9 (see section 4.3).

4.2 Electromagnetic Theory

Rigorous calculation of the radiative properties of periodic micromachined surfaces with structure in the order of the wavelength of radiation generally requires a complete consideration of the electromagnetic theory. Recent advances in electromagnetic scattering predictions based on the extinction theorem [159] and Green's theorem [145] provide an exact solution to surface scattering analysis [22, 97, 112, 133]. This is because integral equation methods for electromagnetic theory cover all ranges of the surface slope, height and wavelength of the radiation and there is no theoretical limitation on the geometry, nor on the dielectric properties of the surface. The directional distribution of scattered energy is a function of the material surface through the optical constants as well as the surface parameters, the wavelength and angle of incidence of the incoming radiation. This will be discussed in classical optical grating theory (see section 4.3). However, grating theory fails to predict the magnitude of the scattered energy which is important for predicting the radiative properties of the surface being considered. The geometry of the microstructured surface plays an important role in determining the magnitude of the scattered radiation energy distribution by the use of electromagnetic theory. The exact integral equations have been developed for both two-dimensional perfectly conducting and dielectric microstructured surfaces by Dimenna and Buckius [38] which will be presented in this section.

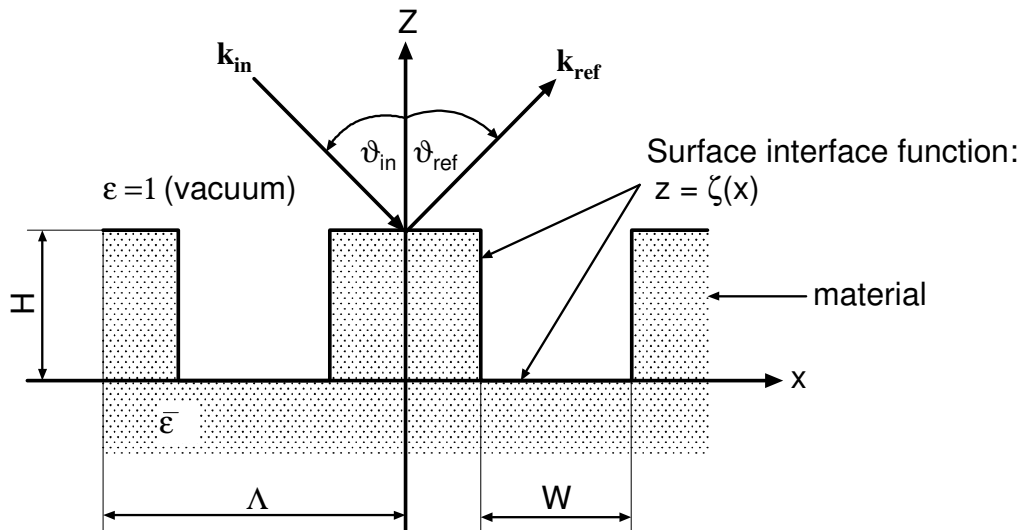


Fig. 4.4. Schematic of the surface cross section defining parameters for surfaces with rectangular profile.

The calculation of radiation properties of a microstructured surface using the electromagnetic theory needs three steps: the first step is the generation of the surface profile,

the second step is the solution to the integral equations of scattering for the prescribed surface, and the last step is the calculation of the thermal radiation properties. The governing equations require the solution to a set of integral equations for the electric and magnetic field. This solution is developed from the extinction theorem and Maxwell's equations. The bi-directional reflectivity is then calculated by integrating the solutions of the integral equations for each surface profile directly. The regular or periodic surface profiles are generated as algebraic functions of the desired geometry as shown for example in figure 4.4.

A brief overview for the analytical determination of the radiative properties of such surface profiles is provided here and a complete formulation of the governing equations for the surface scattering is presented in reference [38, 97]. The governing electromagnetic equations in Helmholtz form are derived from the Maxwell's equations [145]. The p-polarized field is given by

$$\mathbf{E}(x,z,t) = (E_x(x,z), 0, E_z(x,z))\exp(-i\omega t) \quad (4.8)$$

and

$$\mathbf{H}(x,z,t) = (0, H_y(x,z), 0)\exp(-i\omega t) \quad (4.9)$$

where $\mathbf{H}(x,z,t)$ is the magnetic field intensity vector, $\mathbf{E}(x,z,t)$ is the electric field intensity vector, ω is the angular frequency and t is the time. The components of each field in the x-, y- and z- axes are denoted by the subscripts x, y, and z. Similarly, the s-polarized field is given by

$$\mathbf{E}(x,z,t) = (0, E_y(x,z), 0)\exp(-i\omega t) \quad (4.10)$$

and

$$\mathbf{H}(x,z,t) = (H_x(x,z), 0, H_z(x,z))\exp(-i\omega t) \quad (4.11)$$

With Green's theorem and the jump boundary conditions, integral equations for the radiation scattering from surfaces are derived. With the help of additional coordinates (x', z') , the Green's function for the two-dimensional Helmholtz equation referring to a line source can be expressed in terms of the Hankel function of the first kind and zeroth order. In the vacuum region above the surface $z > \zeta(x)$ (i.e., surface interface function), the integral equations expressed in terms of the coordinates x and z for the p-polarized case are [97]

$$H_y^>(x, z) = H(x)_0 + \int_{-\infty}^{\infty} \left[A_0(x, z; x', z') H(x') - B_0(x, z; x', z') L(x') \right]_{z'=\zeta(x')} dx' \quad (4.12)$$

and for the material region below the surface, $z < \zeta(x)$,

$$H_y^<(x, z) = - \int_{-\infty}^{\infty} \left[A_\varepsilon(x, z; x', z') H(x') - \bar{\varepsilon} B_\varepsilon(x, z; x', z') L(x') \right]_{z'=\zeta(x')} dx' \quad (4.13)$$

Similarly, the corresponding integral equations for the s-polarized field are

$$E_y^>(x, z) = E(x)_0 + \int_{-\infty}^{\infty} \left[A_0(x, z; x', z') E(x') - B_0(x, z; x', z') F(x') \right]_{z'=\zeta(x')} dx' \quad (4.14)$$

and

$$E_y^<(x, z) = - \int_{-\infty}^{\infty} \left[A_\varepsilon(x, z; x', z') E(x') - B_\varepsilon(x, z; x', z') F(x') \right]_{z'=\zeta(x')} dx' \quad (4.15)$$

Here $A_i(x, z; x', z')$ and $B_i(x, z; x', z')$ ($i = 0$ for perfectly conducting and $i = \varepsilon$ for general material properties) are functions of Green's function and its derivative (see reference [97]). $A_0(x, z; x', z')$ and $B_0(x, z; x', z')$ are obtained by setting the value of the complex relative dielectric constant, $\bar{\varepsilon} = 1$ in $A_\varepsilon(x, z; x', z')$ and $B_\varepsilon(x, z; x', z')$, respectively. In these equations, the limit as z goes to $\zeta(x)$ has been used to yield the following definitions [97]:

$$H(x)_0 = H_y^>(x, z)_0 \Big|_{z=\zeta(x)} \quad (4.16)$$

and

$$E(x)_0 = E_y^>(x, z)_0 \Big|_{z=\zeta(x)} \quad (4.17)$$

where $H(x)_0$ and $E(x)_0$ are the prescribed incident fields. The unknowns in equations (4.12) and (4.13) are $H(x')$ and $L(x')$ for the p-polarized case, and in the equations (4.14) and (4.15), they are $E(x')$ and $F(x')$ for the s-polarized case. $L(x')$ is related to derivative of magnetic field $H(x')$ normal to the surface, and $F(x')$ is related to the derivative of electric field $E(x')$ normal to the surface, as

$$L(x') = \left(-\zeta'(x') \frac{\partial}{\partial x'} + \frac{\partial}{\partial z'} \right) H_y^>(x', z') \Big|_{z'=\zeta(x')} \quad (4.18)$$

and

$$F(x') = \left(-\zeta'(x') \frac{\partial}{\partial x'} + \frac{\partial}{\partial z'} \right) E_y^>(x', z') \Big|_{z'=\zeta(x')}. \quad (4.19)$$

After evaluating the magnitude of the incident power flow with the help of the Poynting power theorem [145], the results are substituted into equation (2.17) to obtain the desired relation for the bi-directional reflectivity of the p-polarized field as

$$\rho_{\lambda,p}''(\vartheta_{in}, \vartheta_{ref}) = \frac{1}{8\pi} \frac{1}{L_x \cos \vartheta_{ref} \cos \vartheta_{in}} \left| r_p(\vartheta_{ref}) \right|^2 \quad (4.20)$$

and, similarly, for the bi-directional reflectivity of the s-polarized field

$$\rho_{\lambda,s}''(\vartheta_{in}, \vartheta_{ref}) = \frac{1}{8\pi} \frac{1}{L_x \cos \vartheta_{ref} \cos \vartheta_{in}} \left| r_s(\vartheta_{ref}) \right|^2 \quad (4.21)$$

where the scattering reflection functions for p-polarized and s-polarized fields are given by the expressions [97]

$$r_p(\vartheta_{ref}) = \int_{-\infty}^{\infty} \exp\{-ik_0(x' \sin \vartheta_{ref} + \zeta(x') \cos \vartheta_{ref})\} [ik_0(\zeta'(x') \sin \vartheta_{ref} - \cos \vartheta_{ref}) H(x') - L(x')] dx' \quad (4.22)$$

and

$$r_s(\vartheta_{ref}) = \int_{-\infty}^{\infty} \exp\{-ik_0(x' \sin \vartheta_{ref} + \zeta(x') \cos \vartheta_{ref})\} [ik_0(\zeta'(x') \sin \vartheta_{ref} - \cos \vartheta_{ref}) E(x') - F(x')] dx' \quad (4.23)$$

respectively, and L_x is the finite surface length. ϑ_{in} and ϑ_{ref} are the angle of incidence and angle of reflection or scattering of the radiation respectively. $\zeta(x)$ and $k_0 = 2\pi/\lambda$ are the surface interface function and the magnitude of the wave vector (\mathbf{k}_{in}) of the incident radiation respectively.

For unpolarized reflection, a simple arithmetic average of equations (4.20) and (4.21) has to be taken. The unpolarized equations for bi-directional reflectivity are then integrated over all angles of scattering or reflection ϑ_{ref} to obtain unpolarized directional hemispherical reflectivity using equation (2.18):

$$\rho'_\lambda(\vartheta_{in}) = \int_{\Omega_{ref}} \rho''_\lambda(\vartheta_{in}, \vartheta_{ref}) \cos \vartheta_{ref} d\Omega_{ref} \quad (4.24)$$

The other surface properties, emissivity and absorptivity, are determined from Kirchhoff's law and conservation of energy on the surface interface. The directional emissivity for perfectly opaque surface is found by subtracting the directional hemispherical reflectivity from unity with the help of equation (2.28):

$$\varepsilon'_\lambda(\vartheta_{in}) = 1 - \rho'_\lambda(\vartheta_{in}) \quad (4.25)$$

It is very computationally intensive to solve the above multiple coupled integral equations. A numerical method was used to solve these equations given by the electromagnetic theory formulation [22, 37, 38, 97, 112, 133]. The results of directional emissivity obtained by Dimenna and Buckius [37] for different geometries of silicon surface are presented as an example in figure 4.5. Accurate solutions were obtained by using a quadrature scheme. The integral equations were discretized over the intervals of interest within the surface length so that the integral equations reduce to a set of algebraic equations in matrix form. The matrix elements were provided by Maradudin et al. [97]. Solving the system and finding the unknown values was a large project although it was carried out by using a powerful computer like Cray Y-MP. To circumvent these difficulties, various surface scattering approximations were developed [148], one of them is geometric optics approximate model described in the last section 4.1. As mentioned earlier, it is worthwhile to note that such approximations provide accurate solutions for the surface whose dimensions are much greater than the wavelength, but they fail to predict the exact results for the surface with the dimensions in the order of the wavelength of the radiation. However, they provide a base of comparison for the experimental emissivity data measured on the microstructured surfaces.

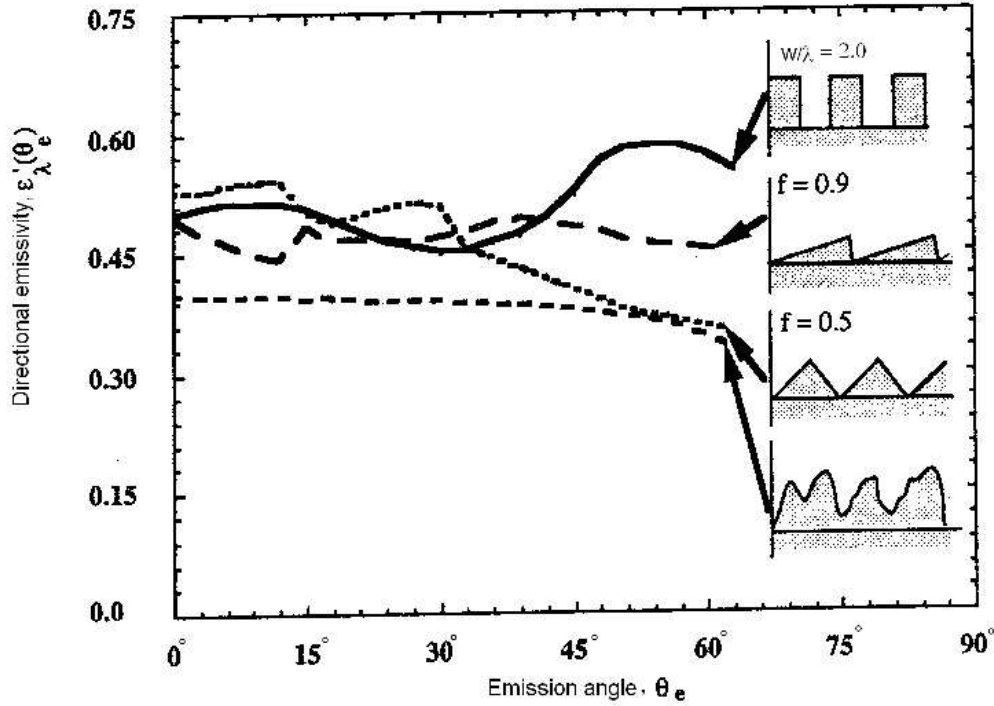


Fig. 4.5. Directional emissivity of different geometries with optical properties of silicon ($n = 2.0$, $k = 4.0$) and the same surface parameters ($\Lambda/\lambda = 4.0$, $H/\lambda = 2.0$). The fraction of the triangular domain locating the peak is denoted by f , and the width of the rectangular cavity is W/λ . The random rough surface at the bottom represents one of the 100 surface realizations as reported by Dimenna and Buckius [37].

4.3 Classical Optical Grating Theory

It is well known that the radiative properties of a surface are highly dependent on the surface profile. Unlike smooth surfaces and random rough surfaces, which exhibit a continuous reflection distribution, periodic structures act as a diffraction grating. The function of a diffraction grating is to interact with an electromagnetic wave in such a way that it generates a series of further waves, travelling in different directions which are dependent upon the wavelength. Because of this interaction, energy is scattered into discrete angular directions, known as diffraction orders or modes. The amount of energy and the angular directions depend on the relationship among the incident wavelengths and surface geometric parameters, such as repeat distance or period of the grooved surface. To obtain this relationship, let us consider a source of waves incident at an angle ϑ_{in} on a periodic structured surface and diffracted at an angle ϑ_{dif} as shown in figure 4.6.

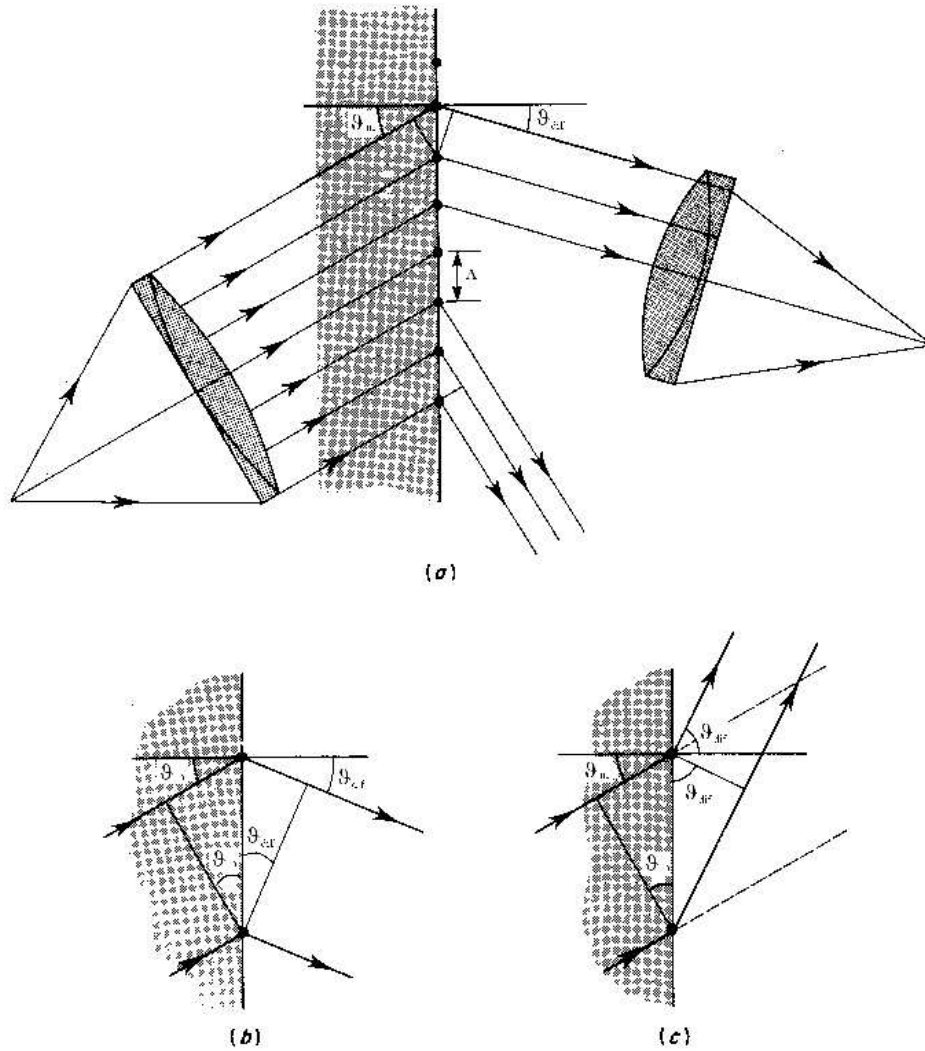


Figure 4.6. Nomenclature for the general grating equation.

In figure 4.6 each groove is represented as a point for the sake of simplicity. In the case of the periodic surface structures, the magnitude of the contribution from each source will depend upon the form of the groove, but it will be equal for each groove. The condition that a diffracted order should exist is that the contributions from each groove should all be in phase, or rather out of phase by an integral number of 2π radians. This means that the difference in path from the source to the focussed image via successive grating grooves should be equal to a whole number of wavelengths. In order words, referring to the figure 4.6

$$\Lambda \sin \vartheta_m \pm \Lambda \sin \vartheta_{dif} = m\lambda \quad (4.26)$$

where m is an integer known as the order number. This equation is valid for the case $\vartheta_{dif} < \vartheta_m$ and it is often called “the grating equation”. It provides a very simple expression for

the angular positions of the modes. However, it fails to predict the absolute magnitude of the scattered or reflected radiant energy, for which the electromagnetic theory is required (chapter 4.2).

The precise form of the grating equation (4.26) depends upon the choice of sign convention for the angles of incidence and diffraction. If a convention is adopted that angles have the same sign when they are on the same side as the grating normal and opposite sign when the rays cross over the normal, then the diffraction angle (ϑ_{dif}) as shown in figure 4.6 (b) is positive and positive sign is taken in equation (4.26). Similarly, for the case where the diffraction angle (ϑ_{dif}) lies in the opposite side of the grating normal as shown in figure 4.6 (c), then ϑ_{dif} is negative and negative sign is taken in equation (4.26).

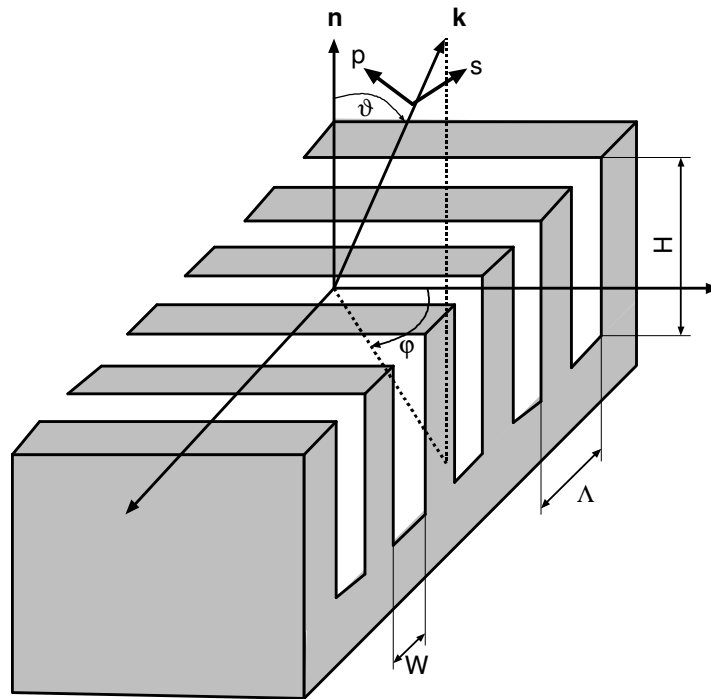


Fig. 4.7. Schematic diagram of a periodic surface microstructure with geometrical parameters, and the p- and s-polarizations of emission wave vector \mathbf{k} .

Diffraction science has received much attention since the discovery by Wood [160] in experiments on reflection gratings. The interaction of a p-polarized electromagnetic wave with metallic diffraction gratings under an azimuthal angle $\varphi = 90^\circ$ (reference line lies in the direction of microgrooves, see figure 4.7) gives rise to rapid bright and dark variations in the reflectivity spectrum which was termed ‘singular anomalies’. These variations are probably caused by some type of resonant interaction between the light diffracted from different grating

lines and correspond with the onset or disappearance of particular spectral diffraction orders. The first and simplest explanation of the anomalies was given by Rayleigh in 1907, who suggested that they occur when an order “passes off over the grating horizon” [67]. That is, when the angle of diffraction (ϑ_{dif}) is 90° and the order moves over the grating surface. The wavelength which is grazing the surface is called Rayleigh wavelength (λ_R). This wavelength can be calculated from the grating equation (4.26) rewriting it for the case $\vartheta_{\text{dif}} > \vartheta_{\text{in}}$ and putting the diffraction angle, $\vartheta_{\text{dif}} = 90^\circ$. This wavelength depends on the polar incident angle (ϑ_{in}) and on the grating repeat distance or period (Λ) as:

$$\lambda_R = \frac{\Lambda}{m} [1 \pm \sin \vartheta_{\text{in}}] \quad (4.27)$$

where m is an integer. At the Rayleigh wavelength, there is a discontinuity in the number of orders that are allowed to propagate. The energy in the order which passes off has to be redistributed among the other orders and this accounts for the sudden fluctuations of the efficiency of these orders. This explanation was successful in describing the position of many of the anomalies described by Wood, but not of all observed Wood’s anomalies.

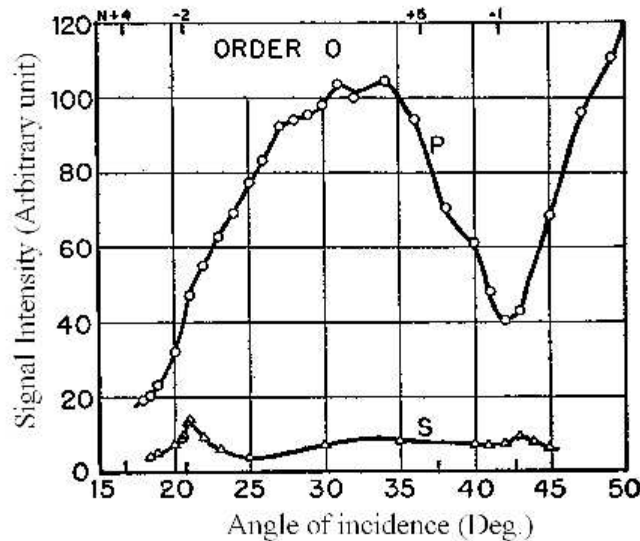


Fig 4.8. Anomalies for metallic grating (C2) measured by Palmer [117] using monochromatic light with wavelength, $\lambda = 0.5461 \mu\text{m}$. Symbol P denotes p- polarization and S denotes s- polarization.

Palmer [117] and Hessel et al. [63] presented a surface reactance explanation for the Wood’s anomalies suggesting that in some cases the position of the anomaly depends upon

the material of which the grating surface was made. It was demonstrated in the case of metallic gratings that the strong anomalies in the p-polarization and the weak anomalies in the s-polarization are due to the excitation of the leaky electromagnetic waves travelling along the surface (i.e., surface plasmon) with the azimuthal angle $\varphi = 90^\circ$ supported by the grating (see figure 4.8). This results in an additional mechanism for loss, thus increasing the absorption and thereby increasing the emission [67, 106]. This mechanism related to the excitation of the surface plasmons through the coupling of the electromagnetic radiation with the grating is described in the following.

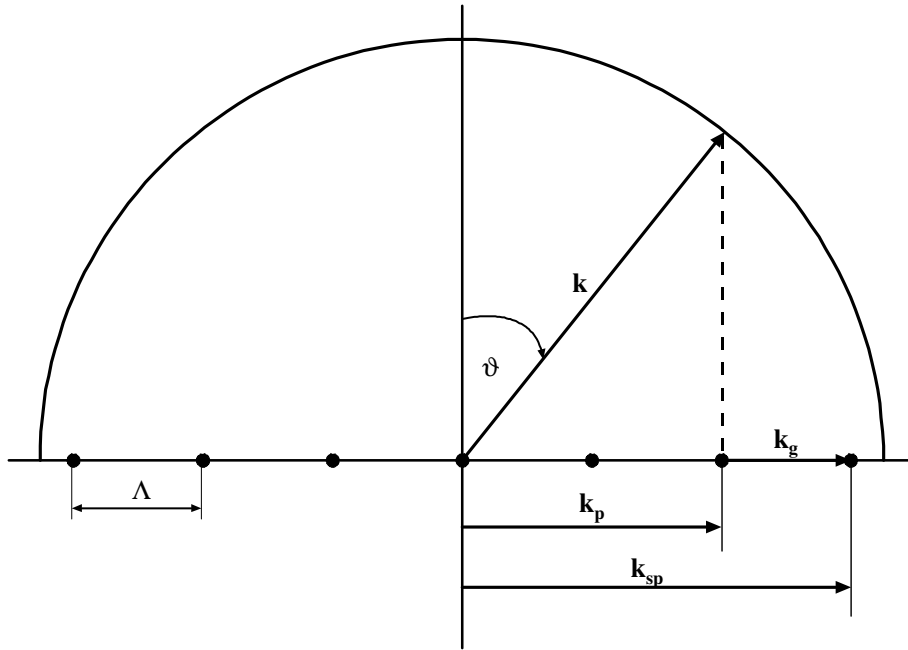


Fig. 4.9. Vector diagram for the coupling of energy into surface plasmons in a grating. black circles denote the grooves.

The collective oscillations of the free (conduction) electrons at the surface of a metal can be described as a series of waves. These are longitudinal electromagnetic waves similar to sound waves propagating in the surface of the metal. These waves are called surface plasma oscillations and may be thought of either as waves or in quantum mechanical terms as surface plasmons. The magnitude of the surface plasmon wave vector \mathbf{k}_{sp} (see figure 4.9) is given by [150]

$$\mathbf{k}_{sp} = \frac{\omega}{c} \sqrt{\left[\frac{\epsilon_{re}(\lambda)}{1 + \epsilon_{re}(\lambda)} \right]} \quad (4.28)$$

where $\varepsilon_r(\lambda)$ is the real part of the complex dielectric constant of the material. This surface wave \mathbf{k}_{sp} exists typically at metal surfaces where the real part of the dielectric constant is smaller than -1 . It is possible to couple energy into these waves from an electric field oscillating parallel to the surface of the metal. If the surface is perfectly smooth then no coupling takes place, but if the surface is rough then there will be local vibrations (oscillations) in the electric field and it is possible to couple energy into the surface plasma oscillations from the field associated with electromagnetic radiation which is being emitted by the metal surface. The extent to which the coupling will occur depends upon the roughness of the surface.

A microstructured surface can be regarded as a regular form of roughness, so it is perhaps reasonable to expect that similar effects would be observed on periodic microstructured surfaces (i.e., gratings). Furthermore, a microstructured surface or a grating acts in such a way that it adds to the momentum of a photon a quantum of momentum that is proportional to the groove density. This “grating momentum” can also be taken into account when considering the coupling between the electromagnetic radiation and the surface plasmons in the grating. The condition for this coupling may be illustrated with the help of a vector diagram shown in figure 4.9. The condition for the coupling is given by

$$\mathbf{k}_p + \mathbf{k}_g = \mathbf{k}_{sp} \quad (4.29)$$

where $k_p = k \sin \vartheta$ is the magnitude of the horizontal component of the wave vector \mathbf{k} of the emitted radiation. The magnitude of the wave vector \mathbf{k} of the emitted radiation can be written as the function of the wavelength as

$$k = \frac{2\pi}{\lambda} \quad (4.30)$$

In figure 4.9, \mathbf{k}_g is the grating effective wave vector or in short the grating vector, and its magnitude is a function of the grating geometry as [67, 106]:

$$k_g = \frac{m2\pi}{\Lambda} \quad (4.31)$$

Here m is the integer and Λ is the repeat distance or period of the microgrooves, which are denoted by black points in figure 4.9.

By using equations (4.28), (4.30) and (4.31), equation (4.29) can be expressed in an alternative form to obtain a relation among the polar angle of emission (ϑ), the repeat distance of the grating, the real part of the complex dielectric constant of the material and the wavelength of the radiation:

$$\sin \vartheta = \sqrt{\left[\frac{\epsilon_{re}(\lambda)}{1 + \epsilon_{re}(\lambda)} \right]} - \frac{m\lambda}{\Lambda} \quad (4.32)$$

Equation (4.32) is very useful because it enables to calculate from a known value of the repeat distance or period (Λ) of the grating and the optical constants of the material roughly where an anomaly would be expected to be observed. However, it can only be regarded as a first approximation because it takes no account of the depth or the shape of the grooves and this is nowhere more important than in the region of an anomaly.

In the experiments of Hesketh et al. [58] on the emission properties of highly doped silicon gratings, standing electromagnetic wave modes (organ pipe like modes) in the depth and the slot width of the grating were identified. Wood's anomalies were observed in the shallow gratings and related to the excitation of surface plasmons through coupling with the grating vector [58, 59, 60, 61, 62]. It was suggested that those anomalies which did not fit the Rayleigh's explanation might be due to some resonance effect within the grooves themselves. The results of the directional spectral emissivity for the doped microstructured silicon surface obtained by Hesketh et al. [60] are represented in figures 4.10 and 4.11 for different microgrooves at azimuthal angles $\varphi = 90^\circ$ and $\varphi = 0^\circ$ respectively.

Emission anomalies for dielectric gratings were first described by Palmer and Evering for the azimuthal angle $\varphi = 90^\circ$ [118]. They demonstrated that there is also the surface wave propagation in the dielectric grating as in the case of the metal grating. It was shown that Rayleigh's criterion as given in equation (4.27) for grating anomalies applies for both p- and s-polarizations.

Wang and Zemel [156, 157, 158] studied the emission properties of undoped silicon gratings which are largely dielectric material. It was demonstrated that emission anomalies exist in dielectric silicon gratings with characteristic dimensions close to the emitted

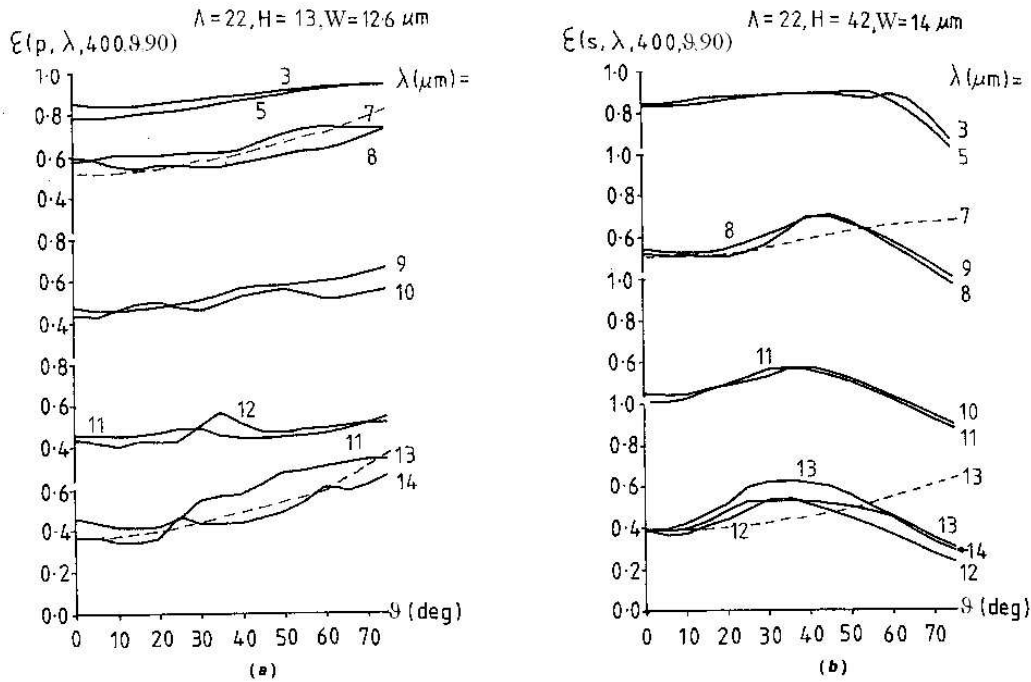


Fig. 4.10. Directional spectral polarized emissivity of doped silicon microgrooves at surface temperature 400 °C and azimuthal angle $\phi = 90^\circ$, as a function of polar angle (θ) with wavelength as the parameter. The solid lines are experimental data and dash lines are calculated data by using the specular geometric optic model. (a) p-polarized radiation (b) s-polarized radiation, as obtained by Hesketh et al. [60].

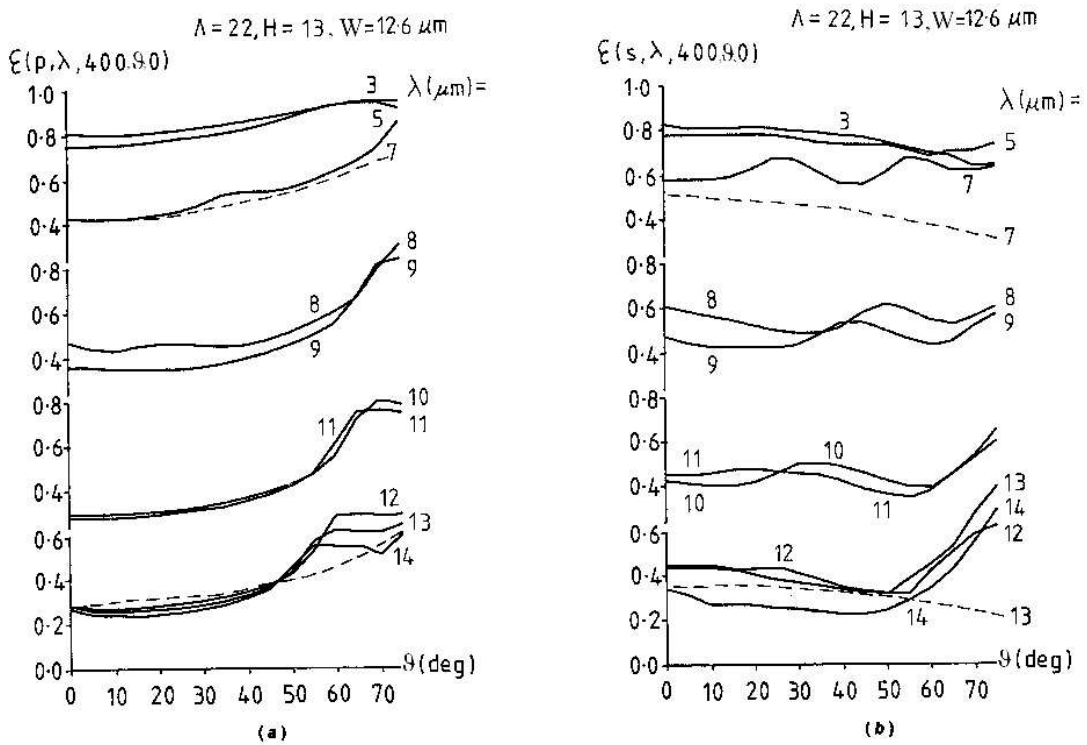


Fig. 4.11. Directional spectral polarized emissivity of doped silicon microgrooves at surface temperature 400 °C and azimuthal angle $\phi = 0^\circ$, as a function of polar angle (θ) with wavelength as the parameter. The solid lines are experimental data and dash lines are calculated data by using the specular geometric optic model. (a) p-polarized radiation (b) s-polarized radiation, as obtained by Hesketh et al. [60].

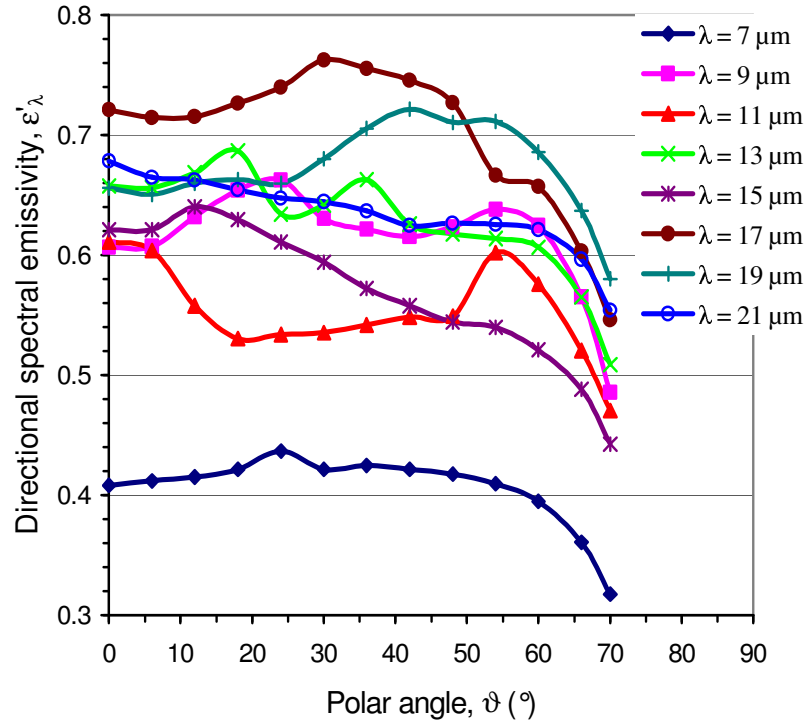
wavelengths and that Rayleigh's criterion for grating anomalies applies for both p- and s-polarizations. Rayleigh's criterion (i.e., $\vartheta_{dif} = 90^\circ$) is given as

$$\sin \vartheta_{in} = \left| 1 - \frac{m\lambda}{\Lambda} \right| \quad (4.33)$$

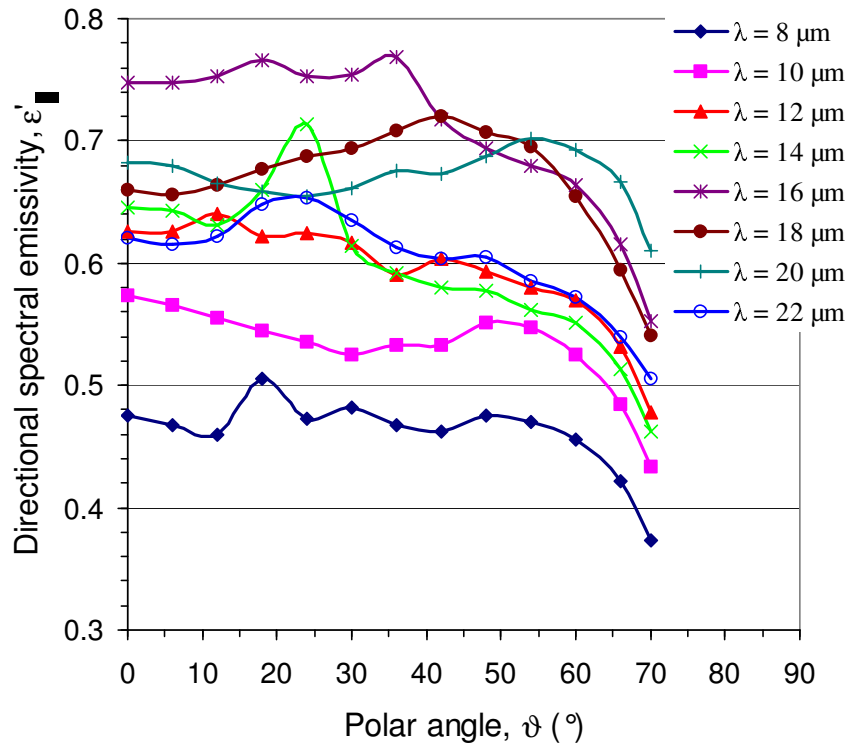
for azimuthal angles $\varphi = 90^\circ$ and the absolute value is taken because the angle of incident ϑ_{in} is always positive. Equation (4.33) can also be approximated for the polar angle (ϑ) of the emitted radiation instead of the angle of the incident radiation (ϑ_{in}) in the grating by putting the average value of the real part of the dielectric constant for the undoped silicon, $\epsilon_{re} \cong 11.72$ for the wavelength range $4 \mu\text{m} < \lambda < 60 \mu\text{m}$ [5] into the equation (4.32), although this equation is valid for the metallic gratings where the real part of the dielectric constant is smaller than -1. This fact implies that one obtains the same relation (i.e., equation (4.33)) between the angle of incident (ϑ_{in}) in the grating or the polar angle of emission (ϑ) and the repeat distance of the grating (Λ) by considering either the Rayleigh's criterion for grating anomalies or the existence of the surface plasmon wave on the regular microstructured undoped silicon surface like on the metal surfaces.

As the present investigation is on the undoped silicon, which is a dielectric material, equation (4.33) will be used in the interpretation of the directional spectral emissivity data at the azimuthal angle $\varphi = 90^\circ$ in chapter 9.

The directional spectral emissivity data of doped silicon microgrooves for different groove depths measured in the present work are tabulated in appendix A and graphically presented in appendix B. The measurement results obtained for the microgrooves with period, $\Lambda = 10 \mu\text{m}$, width, $W = 6.5 \mu\text{m}$ and depth, $H = 11.2 \mu\text{m}$ for the azimuthal angle $\varphi = 90^\circ$ are shown in figure 4.12. Pronounced emission peaks are seen on the emissivity curves. This implies that the surface geometry interacts with the electromagnetic wave radiated by the microstructured surface if the dimensions of the grooves are in the order of the wavelength of the radiation. Calculated polar angles of spectral emissivity maxima (peaks) by using equation (4.33) and that measured in the present work when azimuthal angle, $\varphi = 90^\circ$ for undoped silicon microgrooves with period, $\Lambda = 10 \mu\text{m}$, width, $W = 6.5 \mu\text{m}$ and depth, $H = 11.2 \mu\text{m}$ are given in table 4.1. There is close agreement between calculated and measured values considering the polar angle resolution of 6° .



(a)



(b)

Fig. 4.12. Directional spectral emissivity of a microgrooved undoped silicon surface with the wavelength of radiation as parameter at an azimuthal angle, $\phi = 90^\circ$ for the microgrooves with period, $\Lambda = 10 \mu\text{m}$, width, $W = 6.5 \mu\text{m}$ and depth, $H = 11.2 \mu\text{m}$ ($T = 200 \text{ }^\circ\text{C}$). (a) odd values of wavelength (b) even values of wavelength.

Table 4.1. Calculated and measured polar angles of spectral emissivity maxima (peaks) at an azimuthal angle, $\varphi = 90^\circ$ for undoped silicon microgrooves with period, $\Lambda = 10 \mu\text{m}$, width, $W = 6.5 \mu\text{m}$ and depth, $H = 11.2 \mu\text{m}$ in the present work ($T = 200 \text{ }^\circ\text{C}$). The symbol ‘-’ denotes no peak is observed.

$\lambda / \mu\text{m}$	m (order)	$\vartheta_{\text{cal.}}$ (deg)	$\vartheta_{\text{meas.}}$ (deg)
7	1	17.4	-
	2	23.6	24
8	1	11.5	18
	2	36.8	30
9	1	5.7	-
	2	53.1	54
10	1	0	0
11	1	5.7	-
12	1	11.5	12
13	1	17.4	18
14	1	23.6	24
15	1	30	-
16	1	36.8	36

5 Principle and Methods of Measurement of Emissivity

In this chapter, different measurement procedures for the emissivity of technical solid surfaces are introduced and their advantages and disadvantages are discussed.

There are different methods for the measurement of the emissivity of a technical surface, but the selection of a proper and accurate method depends on many factors, such as the state of aggregation of the substance, the temperature interval and the emissive properties to be measured. The emissive properties of a surface are generally classified in four different quantities taking in account the emission direction and the range of wavelength of the radiation (see section 2.1.2). For example, directional or hemispherical and spectral or total emissivities can be measured. There are mainly two methods of measurement of emissive quantities which are known as the calorimetric and the radiometric technique. The principle of measurement by using these techniques will be explained in the following sections.

5.1 Calorimetric Measurement Technique

The calorimetric techniques of emissivity measurement are based on the principle that for a system in a steady state, the electrical power supplied to heat the sample is equal to the heat flow from the sample to its surroundings (energy balance principle). By using this method only the hemispherical total emissivity of the sample can be measured. Figure 5.1 gives a schematic representation of the calorimetric technique for the emissivity measurement.

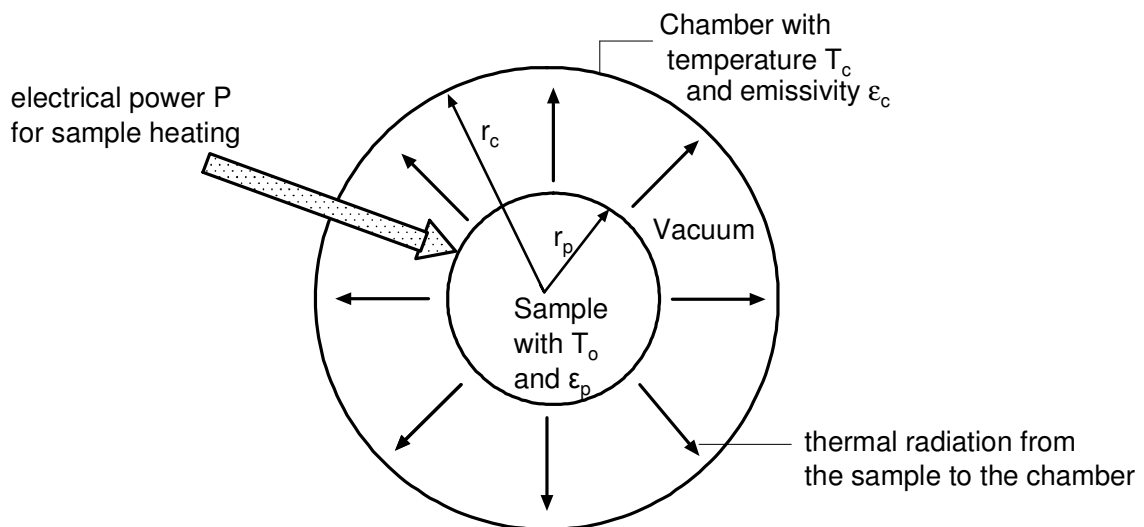


Fig. 5.1 Schematic representation of the layout of a calorimetric technique.

A sample with an unknown hemispherical total emissivity ε_p is placed inside a spherical chamber which is evacuated. The vacuum chamber has a known hemispherical total emissivity value ε_c and is being kept at constant uniform temperature T_c with the help of a thermostat. The sample is heated with a known electrical power P and has constant uniform temperature T_0 after the system has reached the steady state. In this condition the electrical power P supplied to heat the sample is equal to the heat flow \dot{Q}_p from the sample to its surroundings (vacuum chamber) caused by the temperature gradient between the sample and the chamber. Because of the evacuated space between the sample and the chamber, there is no heat transfer due to free convection, and therefore, radiation and possibly some conduction are the only possible heat transfer mechanism between them.

For the radiative exchange in a hollow enclosure with two zones the radiant heat flow \dot{Q}_p from the sample to the chamber is calculated from the equation [6] (when conduction is neglected)

$$\dot{Q}_p = P = \varepsilon A_p \sigma (T_0^4 - T_c^4) + \dot{Q}_{loss} \quad (5.1)$$

where ε and σ are the radiative exchange factor and Stefan-Boltzmann constant respectively. A_p is the surface area of the sample with radius r_p and it is equal to $4\pi r_p^2$ for a spherical sample and $2\pi r_p (r_p + h)$ for a cylindrical sample. \dot{Q}_{loss} is the heat loss due to the conduction heat transfer through the electrical wires and the sample holding devices. Because the sample is completely enclosed by the vacuum chamber, the radiative exchange factor is given by the simple relation [6]

$$\frac{1}{\varepsilon} = \frac{1}{\varepsilon_p} + \frac{A_p}{A_c} \left(\frac{1}{\varepsilon_c} - 1 \right) \quad (5.2)$$

where $A_c = 4\pi r_c^2$ is the surface area of the spherical chamber with a radius r_c . After substituting equation (5.2) in equation (5.1) and doing some mathematical manipulations, we get the required relation for the hemispherical total emissivity of the sample

$$\varepsilon_p = \frac{P}{A_p \sigma (T_0^4 - T_c^4) - P(1/\varepsilon_c - 1) A_p / A_c} \quad (5.3)$$

For a cylindrical sample with radius r_p and height h , equation (5.3) can be expressed in an alternative form as the function of the geometrical parameters:

$$\varepsilon_p = \frac{P}{2\pi\sigma r_p (r_p + h)(T_0^4 - T_c^4) - P(1/\varepsilon_c - 1)[r_p(r_p + h)/2r_c^2]} \quad (5.4)$$

By using equation (5.4) the hemispherical total emissivity ε_p of the cylindrical sample can easily be determined when all the quantities at right hand side of the equation are known through the experimental measurements.

The advantage of this calorimetric technique is the direct determination of hemispherical total emissivity of the sample. Its disadvantage is the requirement of the vacuum condition and therefore, the need of long temperature setting time. The heat loss \dot{Q}_{loss} due to the conduction heat transfer through the electrical wires and the sample holding devices is determined by calibration measurements. The measurement error is estimated to be nearly 8%. A problem is the measurement of the sample surface temperature T_0 as described in chapter 6.

5.2 Radiometric Measurement Technique

In the infrared wavelength range radiometric techniques are preferably used for the measurement of the directional spectral emissivity. This most popular technique is based on the comparison of the spectral intensity of radiation from a sample surface to that from a reference body. Normally, a blackbody is taken as the reference body because its spectral intensity of radiation is well known from the Planck's law of radiation, equation (2.1). Such a blackbody can be realized approximately by a special cylindrical cavity for the practical purpose. In this technique the temperature of the cylindrical cavity must be equal to the temperature of the sample surface being measured. The directional spectral emissivity can hereby be determined either directly or indirectly by measuring the reflectivity of the sample. In the following sections these two methods are described in detail.

5.2.1 Indirect Determination of Emissivity

With the indirect method the directional spectral emissivity is determined by measuring the directional hemispherical spectral reflectivity first and then using the Kirchhoff's law of radiation in combination with the radiative energy balance on the sample

surface. The later states that the sum of the directional spectral emissivity, reflectivity, and transmissivity of a sample is unity, equation (2.27). This can be also expressed formally as

$$\varepsilon'_\lambda(\lambda, \vartheta, \varphi, T) = 1 - [\rho'_\lambda(\lambda, \vartheta, \varphi, T) + \tau'_\lambda(\lambda, \vartheta, \varphi, T)]. \quad (5.5)$$

Equation (5.5) implies that the directional spectral emissivity $\varepsilon'_\lambda(\lambda, \vartheta, \varphi, T)$ is composed of the directional hemispherical spectral reflectivity $\rho'_\lambda(\lambda, \vartheta, \varphi, T)$ and the directional spectral transmissivity $\tau'_\lambda(\lambda, \vartheta, \varphi, T)$. For the thermal radiation in case of an opaque sample the directional spectral transmissivity can be taken as zero. Then the equation (5.5) can be rewritten as

$$\varepsilon'_\lambda(\lambda, \vartheta, \varphi, T) = 1 - \rho'_\lambda(\lambda, \vartheta, \varphi, T). \quad (5.6)$$

Equation (5.6) shows that the directional spectral emissivity of a sample can be determined if the directional hemispherical spectral reflectivity of the sample is known. The directional hemispherical spectral reflectivity is defined as the radiation flow reflected into all directions divided by the incident radiation flow from one direction. Another directional reflectivity is useful when one is concerned with the reflected intensity into one direction resulting from incident radiation flow from all directions. It is known as the hemispherical directional spectral reflectivity. For the measurement of this hemispherical directional spectral reflectivity Brandenberg [16] proposed a method in which an Ulbricht sphere was used. Figure 5.2 schematically represents the reflectivity measurement with the help of the Ulbricht sphere. Since the incident intensity is uniform over all incident directions, the reciprocity relation for directional spectral reflectivity can be used in the Ulbricht sphere. The reciprocity relation states that the hemispherical directional spectral reflectivity of a sample is equal to the directional hemispherical spectral reflectivity if the incident intensity is uniform over all incident directions [138]. From this relation the required value of the directional hemispherical spectral reflectivity in equation (5.6) is obtained to get the directional spectral emissivity of the sample indirectly.

As shown in figure 5.2 the radiation beam from an infrared source enters the Ulbricht-sphere through an inlet after passing through an aperture and strikes a point on the inner wall of the sphere. The radiation beam is reflected diffusely so that there is an uniform radiation field inside the sphere. The sample is placed in the centre of the Ulbricht-sphere and reflects

the radiation beam striking its surface. The reflected beam from the sample surface can be registered with the help of a detector placed outside the sphere after passing through an outlet opening. In an ideal case, the measurement of the reflected radiation flux can be done at any angle between 0° and 90° by tilting the sample at a required angular position.

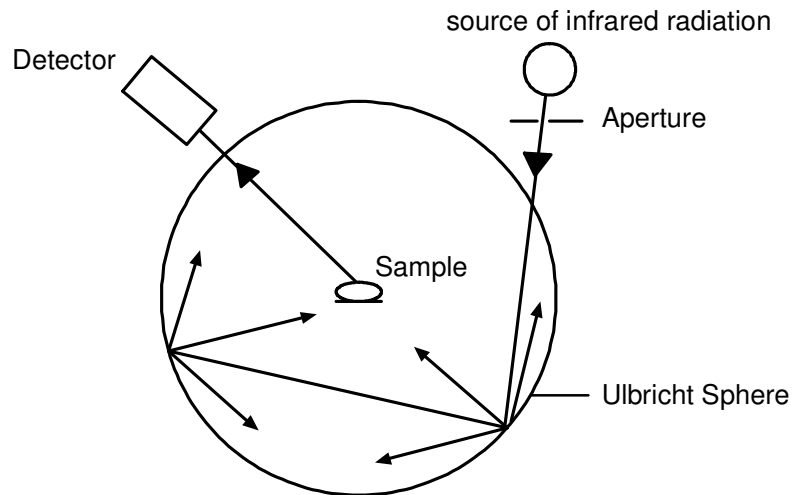


Fig. 5.2 Schematic representation of the Ulbricht-Sphere for the measurement of the hemispherical directional spectral reflectivity.

In this method there is no need of vacuum condition. But the optical system is very complex and operation of the apparatus is not easy. The temperature of the sample is equal to the room temperature and the hemispherical directional spectral reflectivity can be measured only between the angle of radiation 15° and 88° . The inner wall of the Ulbricht-sphere must have a small known value of emissivity.

5.2.2 Direct Determination of Emissivity

The direct method of the determination of the directional spectral emissivity is based on parallel measurements of the directional spectral intensity of radiation from a sample surface and that from a blackbody cavity with the same temperature as the sample surface in vacuum. In the following the principle of the measurement of the directional spectral emissivity will be described with the help of an experimental set up developed by Labuhn [79].

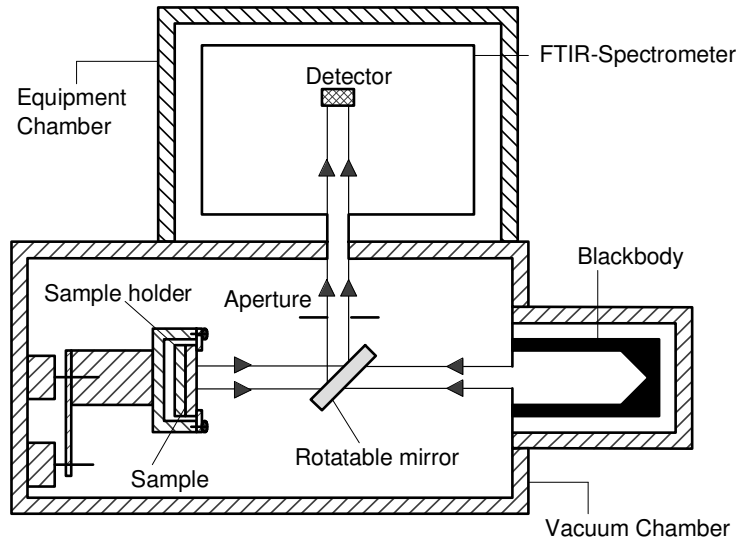


Fig. 5.3 Arrangement of the sample, blackbody and detector inside the vacuum chamber for the measurement of the directional total emissivity.

In the arrangement as shown in figure 5.3 a rotatable mirror is moved between two positions, one position seeing the sample and other position seeing the blackbody so that the detector can alternatively receive the radiation from either of them. In the same way the sample can also be rotated at different angles from the detector axis. The possible angle of rotation of the sample in this arrangement is limited from 0° to 70° . The sample fastened on a holder and the blackbody are surrounded by an evacuated black chamber whose temperature is controlled by a thermostated system as the detector of a FTIR-spectrometer located inside an equipment chamber. Because both the sample holder and the blackbody are made of copper with high conductivity, their temperatures can be measured very precisely by using the platinum resistance thermometers Pt 100 with four wire technique. The true temperature of the sample surface is unknown because there is a loss of heat due to radiation from the sample surface. Therefore, true temperature of the sample surface is theoretically determined with the help of the energy balance equation (see chapter 6).

The directional spectral emissivity is measured in two stages for each particular temperature. First, the background emission intensity, $L_{\lambda,a}$, from optical parts of the FTIR-spectrometer is determined by the calibration measurements. Then, the emission intensity of the sample, $L_{\lambda,s}$, at different polar and azimuthal angles (ϑ, φ) , and the emission intensity of the blackbody cavity, $L_{\lambda,b}$, at the same temperature T as the sample are measured one after another. The directional spectral emissivity $\varepsilon'_\lambda(\lambda, \vartheta, \varphi, T)$ of the sample is then calculated as:

$$\varepsilon'_\lambda(\lambda, \vartheta, \varphi, T) = \frac{L_{\lambda,s}(\lambda, \vartheta, \varphi, T) - L_{\lambda,a}(\lambda, T)}{L_{\lambda,b}(\lambda, T) - L_{\lambda,a}(\lambda, T)} \quad (5.7)$$

The directional total emissivity $\varepsilon'(\vartheta, \varphi, T)$ as defined by equation (2.7) for different emission angles can be calculated theoretically from the measured directional spectral emissivity $\varepsilon'_\lambda(\lambda, \vartheta, \varphi, T)$ using the simple relation:

$$\varepsilon'(\vartheta, \varphi, T) = \frac{\int_{\lambda=0}^{\infty} \varepsilon'_\lambda(\lambda, \vartheta, \varphi, T) L_{\lambda,b}(\lambda, T) d\lambda}{\int_{\lambda=0}^{\infty} L_{\lambda,b}(\lambda, T) d\lambda} \quad (5.8)$$

where $L_{\lambda,b}(\lambda, T)$ is spectral radiance of a blackbody given by the Planck's law of radiation as

$$L_{\lambda,b}(\lambda, T) = \frac{C_1}{\pi \lambda^5 (e^{C_2/\lambda T} - 1)} \quad (5.9)$$

where C_1 and C_2 are called first and second constants of radiation and have the values $3.742 \times 10^{-4} \text{ W}\mu\text{m}^2$ and $1.439 \times 10^4 \mu\text{mK}$ respectively. Because of the limited spectral sensitivity of the detector, the integration with respect to the wavelength in equation (5.8) cannot be done up to infinity in the practice. By the use of DTGS (deuterated triglycine sulphate) detector the directional spectral emissivity can be measured in spectral range from $4 \mu\text{m}$ to $25 \mu\text{m}$. Therefore, equation (5.8) is approximated by the following equation

$$\varepsilon'(\vartheta, \varphi, T) = \frac{\int_{\lambda=4}^{25} \varepsilon'_\lambda(\lambda, \vartheta, \varphi, T) L_{\lambda,b}(\lambda, T) d\lambda}{\int_{\lambda=4}^{25} L_{\lambda,b}(\lambda, T) d\lambda} \quad (5.10)$$

The radiance that is not accounted for is nearly 1% of the total radiance below $4 \mu\text{m}$ and 6% above $25 \mu\text{m}$ for the surface temperature $150 \text{ }^\circ\text{C}$. This is one of the possible errors in the measurement of the directional spectral emissivity by using the radiometric technique.

Assuming symmetrical distribution of the radiative properties over the surface, i.e. the spectral emissivity of the sample being independent of the azimuthal angle φ , the

hemispherical total emissivity can be obtained from the directional total emissivity by integration over all emission angles as

$$\varepsilon(T) = \int_{\vartheta=0}^{\pi/2} \varepsilon'(\vartheta, T) \sin 2\vartheta \, d\vartheta. \quad (2.13)$$

Good results for the directional total emissivity and therefore for the hemispherical total emissivity can be achieved if directional spectral emissivity values are measured at as many different polar angles ϑ as possible between 0° and 90° . Because of geometrical constraints of the experimental set up the directional spectral emissivity could be measured only at polar angles up to 70° . The values of directional spectral emissivity at polar angles 70° up to 90° were obtained by extrapolation with the help of a polynomial curve fitted to the measured values by the least square method.

In the present work the experimental set up developed by Labuhn [79] is used with some modifications. The FTIR-spectrometer is calibrated so that the directional spectral emissivity data can be obtained for the extended infrared wavelength range $4 \mu\text{m} \leq \lambda \leq 25 \mu\text{m}$ instead of $4 \mu\text{m} \leq \lambda \leq 20 \mu\text{m}$. The sample chamber is sealed with additional measures to get better vacuum below 2 Pascal instead 5 Pascal. To get the exact angular position of the sample and mirror their movements are controlled by using a recent graphical program package “Labview”. The exact determination of the temperature of the sample surface plays a vital role for the accurate measurement of the directional spectral emissivity. In this work, more emphasis is therefore given to the exact determination of the surface temperature of the sample. The surface temperature is calculated by using energy balance equations. A simulation of the temperature distribution on the sample surface is also carried out by using finite-element method (FEM). A third way is measuring the surface temperature of the sample with an infrared thermo-camera. For this purpose a Zink Selenide window is constructed on the front side of the sample chamber to observe the sample surface by thermo-camera. These three procedures for the determination of the surface temperature of the sample will be explained in the next chapter.

6 Numerical Simulation and Calculation of Sample Surface Temperature

The exact determination of the sample surface temperature is especially important in the measurement of the radiative properties of technical surfaces. As explained they rely on a comparison between the spectral radiance from a sample surface and that from a blackbody at exactly the same temperature. If the temperature of the sample surface differs from the blackbody temperature in just a small amount, the measured radiance of the blackbody at the wrong temperature may introduce a high percentage of error in the spectral emissivity of the sample surface. This is because the radiance based measurement signal is proportional to the fourth power of the surface temperature. For example, for the detector temperature 285.15 K, the error $\Delta T = 0.5$ K in the measurement of the sample surface temperature $T = 371.95$ K yields an error of nearly 1% in the measured emissivity of the sample surface. The effect of errors in the temperature measurement upon the uncertainty of the emissivity will be analysed in section 6.4.

Temperature measurement by using the thermocouples may introduce errors of several Kelvin in the worst case, because of a possibly non-uniform temperature distribution in the sample due to heat loss from the surface by radiation. Furthermore, a contact sensor may introduce errors in the measurement of radiative properties due to the possible radiative heat exchange between the material of the contact sensor and the sample surface. It is therefore not suitable to measure the surface temperature of the sample with the help of a contact sensor placed directly on the surface to be measured. In the case of mechanically machinable samples, contact sensors can be inserted just below the sample surface (e.g. 1 mm below the surface) with a cost of negligible error in the temperature measurement if the sample has good thermal conductivity (e.g., copper, aluminium). But this cannot be done for the temperature measurement of hardly machinable materials such as glass, which have poor thermal conductivity. Therefore, instead of the temperature measurement with contact sensors, a theoretical estimation of the surface temperature of the sample is performed by using energy balance equations. A simulation of the temperature distribution on the sample surface is also carried out with the help of finite-element method (FEM). A third way is measuring the surface temperature of the sample with an infrared thermo-camera. These three ways for the exact determination of the surface temperature of the sample are described in the following sections.

6.1 Theoretical Estimation of Temperature of Sample Surface

A theoretical estimation of the surface temperature of a sample is based on the local energy balance for the sample. In a steady state the flow of heat flux from the back of the sample to its surface is equal to the loss of heat flux from the sample surface to its environment by means of conduction, free convection and radiation heat transfer processes.

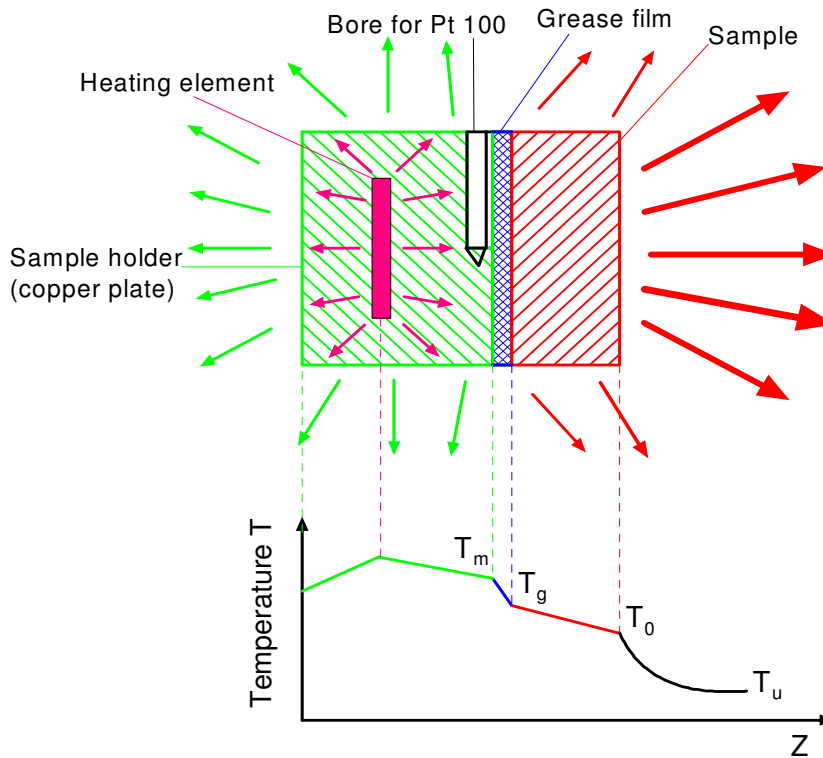


Fig. 6.1. Schematic representation of heat transfer through the sample holder and sample with temperature gradients.

Figure 6.1 illustrates a heat flow model of the real sample holder consisting of three-material layer, namely the copper plate (sample holder), a grease film and the sample. The temperature gradients arising from heat conduction, free convection and radiation in the copper made sample holder and the sample are shown in the same schematic representation. The joint between the copper plate and the back of the sample consists of temperature stabilized vacuum grease, e.g. Lithelen, which guarantees a good conduction of heat between the sample holder and the sample. The contact layer of the grease film should be uniform and its thickness can be determined by weighing. The sample is fastened to the sample holder by using three stainless steel bolts with Teflon nuts (diameter, $d = 8$ mm, length, $l = 20$ mm) having very poor thermal conductivity, $\lambda = 0.26$ W/mK (see figure 6.3). Since there are only point contacts on the circumference between the sample holder and the Teflon nuts, the loss

of heat through these three nuts by thermal conduction can be estimated for the maximum temperature difference $\Delta T = 200$ K as: $\dot{Q} = 3\lambda(\Delta T/l)(\pi d^2/4) = 0.4$ W. This heat flow from three Teflon nuts is taken as negligible in comparison to the electrical power, $P = 32.5$ W supplied to the system.

The temperature T_m at the interface between the copper plate and the grease film is measured by means of a calibrated platinum resistance thermometer (Pt 100) with four wire technique. The temperature at the interface between the grease film and the back of the sample is denoted by T_g (see fig. 6.1). The surface temperature of the sample is T_0 , which is to be calculated, and T_u is the temperature of the sample chamber environment. The balance equation of local energy flux can be written for the sample surface, that means, in a steady state the flow of heat flux \dot{q}_e from the back of the sample to its surface must be equal to the loss of heat flux \dot{q}_a from the sample surface to the chamber environment:

$$\dot{q}_e = \dot{q}_a . \quad (6.1)$$

The heat transfer from the back of the sample to its surface takes place only by means of conduction assuming that the heat loss from the peripheral area of the sample is negligible. This assumption may be taken, because the thickness of the sample ($\delta = 0.6 - 5.0$ mm) is very small in comparison to its diameter ($d = 150.0$ mm). For example, in case of a $\delta = 0.6$ mm thick aluminium sample with the surface temperature 200 °C and the atmospheric air temperature 22 °C, the total heat loss (i.e., $\dot{Q}_s = \alpha_{rs} \Delta T \pi d \delta$) due to the convection and radiation processes from the circumference is 0.26% of that from the surface of the sample (i.e., $\dot{Q}_0 = \alpha_{r0} \Delta T \pi d^2 / 4$). If the sample thickness is $\delta = 5$ mm, then this quantity becomes 2.1%. Let us consider that the sample has the thickness δ_p and the constant thermal conductivity λ_p , then the heat flux \dot{q}_e through the sample from its backside to the surface is given by

$$\dot{q}_e = \lambda_p \frac{T_g - T_0}{\delta_p} \quad (6.2)$$

In this equation, the grease temperature T_g on the back of the sample is unknown. To replace this unknown quantity with the known measured temperature T_m of the copper plate,

we calculate the heat flux in the grease film which must be equal to the heat flux \dot{q}_e in the sample:

$$\dot{q}_e = \lambda_g \frac{T_m - T_g}{\delta_g} \quad (6.3)$$

where λ_g and δ_g are the thermal conductivity and the thickness of the grease film, respectively. Eliminating the temperature T_g from the equations (6.2) and (6.3), we get the heat flux through the sample as

$$\dot{q}_e = \frac{(T_m - T_0)}{\left(\frac{\delta_p}{\lambda_p} + \frac{\delta_g}{\lambda_g} \right)}. \quad (6.4)$$

The heat flux \dot{q}_a from the sample surface to the chamber environment composes of the heat flux due to the free convection- and radiation heat transfer processes and can be expressed as

$$\dot{q}_a = (\alpha_c + \alpha_r)(T_0 - T_u) = \alpha_t(T_0 - T_u) \quad (6.5)$$

where α_t is the total heat transfer coefficient which consists of both the convective heat transfer coefficient α_c and the radiative heat transfer coefficient α_r . The heat transfer coefficients are taken as mean values over the sample surface.

The radiative heat transfer coefficient α_r is approximately described by the heat transfer from the sample surface to the chamber environment at temperature T_u by radiation as

$$\alpha_r = \varepsilon_p \sigma \frac{(T_0^4 - T_u^4)}{(T_0 - T_u)} \quad (6.6)$$

where ε_p is the hemispherical total emissivity of the sample surface and σ is the Stefan-Boltzmann constant. Equation (6.6) is valid for a case where the vacuum chamber completely encloses the sample surface and where the surface area of the vacuum chamber is much larger than that of the sample surface.

The mean convective heat transfer coefficient α_c can be determined by considering the heat transfer through free convection from the sample surface to the chamber environment, i.e. air. This mean convective heat transfer coefficient can easily be calculated with the help of the dimensionless quantity mean Nusselt-number Nu_m as:

$$\alpha_c = \frac{\lambda_a}{L} Nu_m \quad (6.7)$$

where λ_a is the thermal conductivity of the air and L is the characteristic length of the heat transfer surface; here the diameter d of the cylindrical sample. Churchill and Chu [26] have derived empirically an equation to calculate the mean Nusselt-number for the laminar free convection from a vertical plate of the height L given by:

$$Nu_m = 0.68 + \frac{0.67 Ra^{1/4}}{\left[1 + (0.492/Pr)^{9/16}\right]^{4/9}} \quad (6.8)$$

where Ra and Pr are the well known dimensionless quantities Rayleigh-number and Prandtl-number, respectively. The Rayleigh-number can be expressed as the product of Grashof-number and Prandtl-number. The Grashof-number is defined by the following expression:

$$Gr = \frac{gL^3 \beta (T_0 - T_u)}{\nu^2} \quad (6.9)$$

where g is the acceleration due to gravity, β is the thermal expansion coefficient of air, ν is the kinematic viscosity of air and T_u is the temperature of the chamber environment (air). For sake of simplicity, air can be regarded as an ideal gas and therefore, its thermal expansion coefficient can be taken as the reciprocal air temperature ($\beta = 1/T_u$). The Prandtl-number gives information about the fluid characteristics and is defined as the ratio of the kinematic viscosity ν to the thermal diffusivity a of the fluid:

$$\text{Pr} = \frac{\nu}{a} \quad (6.10)$$

Using equations (6.9) and (6.10), the Rayleigh-number can be calculated as

$$\text{Ra} = \text{Gr} \cdot \text{Pr} = \frac{gL^3 \beta (T_0 - T_u)}{\nu a}. \quad (6.11)$$

Now, the mean Nusselt-number can be calculated with the help of above equations (6.8)-(6.11) using the diameter d of the cylindrical sample surface for the characteristic length L . Then, putting equation (6.6) and (6.7) in equation (6.5), the heat flux flow \dot{q}_a from the sample surface to the chamber environment can be written in the following form:

$$\dot{q}_a = \frac{\lambda_a}{d} \text{Nu}_m (T_0 - T_u) + \varepsilon_p \sigma (T_0^4 - T_u^4). \quad (6.12)$$

Substituting equations (6.4) and (6.12) in equation (6.1), we get a polynomial of fourth order determining the required sample surface temperature T_0

$$\frac{(T_m - T_0)}{(\delta_p/\lambda_p + \delta_g/\lambda_g)} = \frac{\lambda_a}{d} \text{Nu}_m (T_0 - T_u) + \varepsilon_p \sigma (T_0^4 - T_u^4). \quad (6.13)$$

After doing some mathematical manipulation in equation (6.13), it can be reduced in the following form:

$$T_0^4 + AT_0 + B = 0 \quad (6.14)$$

where A and B are auxiliary coefficients with the values

$$A = \frac{1/(\delta_p/\lambda_p + \delta_g/\lambda_g) + \lambda_a \text{Nu}_m/d}{\varepsilon_p \sigma} \quad (6.15)$$

$$B = - \left[\frac{T_m / (\delta_p / \lambda_p + \delta_g / \lambda_g) + \lambda_a Nu_m T_u / d}{\varepsilon_p \sigma} + T_u^4 \right]. \quad (6.16)$$

Equation (6.14) can be solved analytically for the surface temperature of the sample T_0 when the coefficients A and B are known and constant [19]:

$$T_0 = \left[\frac{A}{4 \cdot \sqrt{U/2}} - \frac{U}{2} \right]^{1/2} - \sqrt{\frac{U}{2}} \quad (6.17)$$

U is the auxiliary parameter defined by the equation:

$$U = \left[\left(\frac{A}{4} \right)^2 + \sqrt{\left(\frac{A}{4} \right)^4 + \left(-\frac{B}{3} \right)^3} \right]^{1/3} + \left[\left(\frac{A}{4} \right)^2 - \sqrt{\left(\frac{A}{4} \right)^4 + \left(-\frac{B}{3} \right)^3} \right]^{1/3}. \quad (6.18)$$

In equations (6.15) and (6.16), coefficients A and B contain parameters which depend on the surface temperature T_0 of the sample. Therefore, equation (6.17) should be solved iterative with the help of a computer programme beginning with a guess value of the hemispherical total emissivity ε_p of the sample surface at any surface temperature.

The surface temperature T_0 of the sample can be controlled by adjusting the measured temperature T_m of the copper plate to a value implied by equation (6.13)

$$T_m = T_0 + (\delta_p / \lambda_p + \delta_g / \lambda_g) \left[\frac{\lambda_a}{d} Nu_m (T_0 - T_u) + \varepsilon_p \sigma (T_0^4 - T_u^4) \right]. \quad (6.19)$$

In practice, the copper plate is heated up to the calculated temperature T_m which can be held constant with the help of PID (Proportional Integral Differential)-regulator to get the required surface temperature T_0 of the sample.

Equations (6.15), (6.16) and (6.19) can be more simplified if the sample chamber is evacuated. Since free convection heat transfer does not take place in a vacuum and only radiation heat transfer is effective, the terms with the mean Nusselt-number Nu_m may be cancelled out:

$$A = \frac{1/(\delta_p/\lambda_p + \delta_g/\lambda_g)}{\varepsilon_p \sigma} \quad (6.20a)$$

$$B = - \left[\frac{T_m/(\delta_p/\lambda_p + \delta_g/\lambda_g)}{\varepsilon_p \sigma} + T_u^4 \right] \quad (6.20b)$$

$$T_m = T_0 + \varepsilon_p \sigma (\delta_p/\lambda_p + \delta_g/\lambda_g) (T_0^4 - T_u^4) \quad (6.21)$$

In practice, it is difficult to obtain absolute vacuum to avoid free convection heat transfer completely. Therefore, the influence of the residual low air pressure inside the vacuum chamber on free convection heat transfer will briefly be presented in the following section.

6.2 Heat Transfer in Vacuum

In modern usage vacuum is considered to exist in an enclosed space when the pressure of the gaseous environment is lower than atmospheric pressure or has been reduced as much as necessary to prevent the influence of some gas on a process being carried out in that space. The physical quantity used to characterize such a vacuum state is the gas pressure. The pressure exerted by gas molecules on a boundary surface is expressed as the rate of the transfer of the normal component of their momentum divided by the area of the considered boundary.

The heat transfer due to a temperature gradient in a gaseous environment can take place in following three ways:

- I. Heat is transferred by means of energy exchange from the region of high temperature to the region of low temperature by the kinetic motion or direct impact of gas molecules. This mode of heat transfer is called conduction.
- II. Heat transfer takes place as a consequence of the motion of the gas which is set up by buoyancy effects resulting from density differences caused by temperature differences in the gas. This mechanism of heat transfer is known as free or natural convection.
- III. In a perfect vacuum where no gas molecules are present, thermal radiation is the only means of heat transfer. That is, the radiative energy emitted by a body is

transmitted in vacuum in the form of electromagnetic waves according to Maxwell's classical electromagnetic-wave theory [145] or in the form discrete photons according to Planck's hypothesis [121].

In practice, it is difficult to obtain perfect vacuum. Therefore, in such case one should consider the heat transfer by conduction and free convection as well. In order to estimate this heat flow the thermal conductivity of the residual gas in vacuum must be calculated. The thermal conductivity of a gas varies with the temperature and pressure. Wutz et al. [161] have theoretically determined the thermal conductivity of a gas existing between two parallel plates with temperatures T_1 and T_2 separated by a distance d and it is given by the equation:

$$\lambda = \frac{n_m \bar{c}}{2} \frac{C_{m,V}}{N_A} \bar{l} \frac{d}{d + 2\bar{l}(2/a_E - 1)} \quad (6.22)$$

where n_m is the number density, \bar{c} is the mean velocity, and \bar{l} is the mean free path of molecules. $C_{m,V}$ is the molar isochoric heat capacity, $N_A = 6.02214199 \times 10^{23} \text{ mol}^{-1}$ is the Avogadro-constant, and a_E is the accommodation coefficient or accommodation probability. The accommodation coefficient a_E is defined as the ratio of the energy actually transferred between impinging molecules and the surface to the energy which would be transferred if the molecules attained thermal equilibrium with the surface. Its value depends on the type of gas, material, surface condition, and temperature. The values of the accommodation coefficient for several gases in combination with several materials having different surface conditions are tabulated in Berman [11]. The values of the number density (n_m), the mean velocity (\bar{c}) and the mean free path of the molecules (\bar{l}) can be determined with the help of the kinetic theory of gases [161]:

$$n_m = \frac{p}{kT} \quad (6.23a)$$

$$\bar{c} = \sqrt{\frac{8R_m T}{\pi M_m}} \quad (6.23b)$$

$$\bar{l} = \frac{1}{\sqrt{2} n_m 4\pi r^2} = \frac{kT}{\sqrt{2} p 4\pi r^2} \quad (6.23c)$$

where p and T are the pressure and the temperature of the gaseous environment, respectively. $k = 1.3806503 \times 10^{-23}$ J/K is the Boltzmann-constant, and $R_m = 8.314472$ J/(mol K) is the universal gas constant. M_m is the molar mass of the gas. The molecules of the gas are assumed as spheres of the radius r . From equation (6.23c) it is clear that the mean free path of the molecules (\bar{l}) is inversely proportional to the gas pressure (p).

The thermal conductivity of a gas given by equation (6.22) can be expressed as a function of the pressure exerted in a gaseous environment with the help of the relation (6.23a) for the number density of the molecules, as:

$$\lambda = \frac{p\bar{c}}{2kT} \frac{C_{m,v}}{N_A} \bar{l} \frac{d}{d + 2\bar{l}(2/a_E - 1)} \quad (6.24)$$

Equation (6.24) can further be simplified by considering two limiting cases of pressure:

- I. **High pressure:** Since the mean free path of the molecules (\bar{l}) is inversely proportional to the gas pressure, p (see equation 6.23c), at the high pressure exerted in a gaseous environment $d \gg \bar{l}$ is fulfilled and hence $d \gg 2\bar{l}(2/a_E - 1)$ may be assumed. Equation (6.24) then reduces to

$$\lambda = \frac{\bar{c}}{2} \frac{C_{m,v}}{R_m T} \bar{l} \cdot p \quad (6.25)$$

where the relation $R_m = N_A \cdot k$ is used. In the high pressure regime thermal conductivity λ is independent of pressure, since \bar{l} is proportional to $1/p$, see equation (6.23c).

- II. **Low pressure:** At a low pressure exerted in the gaseous environment $d \ll \bar{l}$ is fulfilled (i.e., the gas molecules fly without any impact from one plate to the other plate) and hence $d \ll 2\bar{l}(2/a_E - 1)$ may be assumed, equation (6.24) is simplified to:

$$\lambda = \frac{\bar{c}}{2} \frac{C_{m,v}}{R_m T} \frac{d a_E}{(2 - a_E)} \cdot p \quad (6.26)$$

In the low pressure regime thermal conductivity λ is proportional to pressure.

Equation (6.26) is significant in the case where a perfect vacuum cannot be obtained. The heat flow \dot{Q} by means of conduction from the cylindrical sample surface with diameter D and length l to the gaseous environment can be estimated as:

$$\dot{Q} = \lambda A \frac{\partial T}{\partial z} = \bar{c} \frac{C_{m,v}}{4R_m T} \frac{a_E}{(2 - a_E)} \pi D(2l + D)(T_1 - T_2) \cdot p \quad (6.27)$$

where T_1 and T_2 are the temperature of the cylindrical sample surfaces and that of the chamber walls, respectively. On this basis the heat loss from the sample surface by free convection may be guessed, if d is identified with a thickness of a boundary layer.

At low pressure, atmospheric air can be treated as an ideal gas mixture, so that the pressure dependence of its molar isochoric heat capacity $C_{m,v}$ may be neglected. By using the empirical value of the accommodation coefficient for air $a_E = 0.5$ as given by Govindarajan and Gopal [48], the thermal conductivity of air can be calculated as a function of air pressure with the help of the equation (6.24). Figure 6.2 shows this functional relationship between the thermal conductivity and the air pressure.

It is clear from figure 6.2 that at an air pressure about 1 Pa, a rapid drop of the thermal conductivity takes place and it goes to zero at infinitely small pressures. This means in practice, one should obtain a vacuum lower than 1 Pa to avoid the free convection heat transfer in gaseous environment. The pressure dependence of thermal conductivity correlates with different flow regimes characterized by Knudsen's number K_n [11]:

$$K_n = \frac{\bar{l}}{d} \quad (6.28)$$

where \bar{l} is the mean free path of gas molecules and d is a characteristic dimension of the system accommodating the gas.

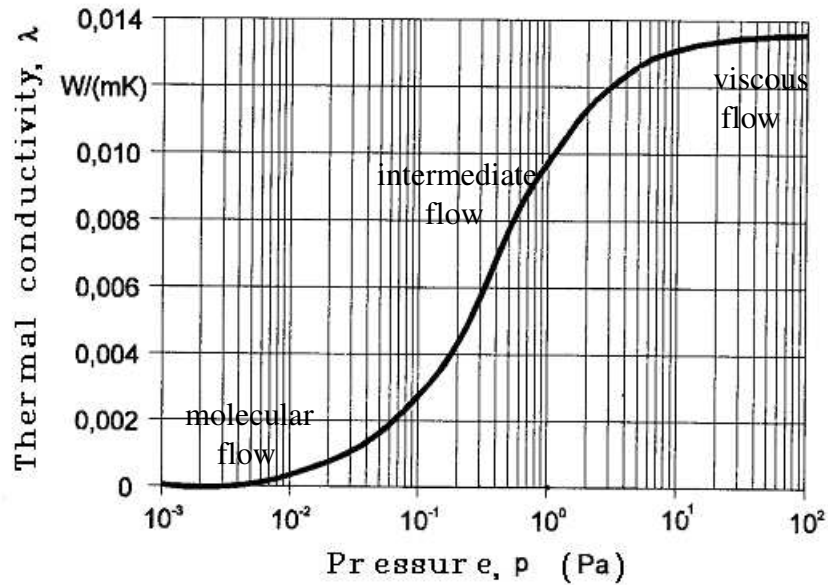


Fig. 6.2. Pressure dependence of thermal conductivity of air.

It is shown in figure 6.2 that in the range of low pressures *molecular flow* conditions prevail (i.e., $K_n > 3$), and intermolecular collisions are rare, compared with molecular collisions with the sample surfaces and walls of the vacuum chamber. The heat transfer is proportional to pressure. As the number density of molecules increases, the flow regime shifts from molecular to that of *transition or intermediate flow* (i.e., $0.01 < K_n < 3$). The mean free path of gas molecules becomes significantly less than the distance separating the sample surfaces from the walls of the vacuum chamber. The proportionality between the heat transfer and pressure observed before is no longer maintained. At still higher pressures the flow regime of gas becomes *viscous* (i.e., $K_n < 0.01$), and thermal conductivity becomes independent of gas pressure. At our experimental set up a vacuum pump allowed pressures down to 2 Pascal for the sample chamber at room temperature and to 3.5 Pascal for the sample chamber cooled at the temperature 12 °C.

6.3 Simulation of Temperature Distribution on Sample Surface by Finite Element Method (FEM)

The measuring surface area of the sample is a circle with a diameter equal to the aperture diameter (max. 40 mm here) used in the present experimental set up (see fig. 8.2) if the measurement of the spectral emissivity is performed normal to the sample surface. But when the sample is rotated at different polar angles for the measurement of the directional spectral emissivity, the image of a circular aperture seems to be an elliptical image on the

sample surface. The large diameter of this elliptical image covers almost all the sample surface depending on the increasing polar angle, ϑ (i.e., large diameter of ellipse = diameter of aperture/ $\cos\vartheta$), and this large diameter must be smaller than the diameter of the sample surface (150 mm). Therefore, for the accurate measurement of the directional spectral emissivity not only the exact determination of the temperature of a sample surface, but also the uniform distribution of the temperature over the entire sample surface is significant. To confirm the isothermal condition of the sample surface, a numerical simulation of the temperature distribution on the sample surface was performed with the help of a finite element method (FEM). The numerical calculations solving the heat conduction equation for the system composed of the sample and sample holder were carried out by using the program package Ansys version 6.1 on the application server of the Helmut-Schmidt University, Federal Armed Forces University Hamburg.

In this work, the directional spectral emissivities of different kinds of samples are measured in respect to their thermal conductivities and surface conditions. They are, for example, borosilicate glass as a bad conductor, silicon as a semiconductor and sand blasted aluminium as a good conductor. The isothermal condition for the temperature distribution of a good conductor is better realized than that of a bad conductor. Therefore, borosilicate glass (B 270) as the bad conductor is chosen for the brief description of the FEM calculations although results of this simulation are given for all samples. The geometrical parameters (see figure 6.3), material properties and the boundary conditions required for the FEM calculations of the sample temperature distribution are listed in table 6.1.

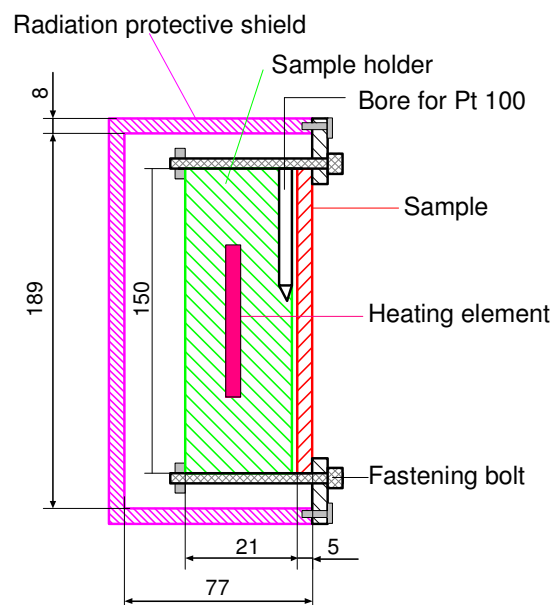


Fig. 6.3. Schematic representation of sample holder with radiation protective shield.

Table 6.1. Geometrical parameters, material properties and thermal boundary conditions for the calculation of the temperature distribution of sample surface (glass B 270) with the help of finite element method (FEM).

<u>Geometrical parameters (see figure 6.3)</u>	
Diameter of cylindrical sample and sample holder: $d = 150$ mm	
Thickness of cylindrical sample holder (copper plate coated with chromium): $\delta_{cu} = 21$ mm	
Thickness of cylindrical sample (glass B 270): $\delta_p = 5$ mm	
Internal diameter of radiation protective shield: $D_i = 189$ mm	
Length of radiation protective shield: $L = 77$ mm	
<u>Material properties</u>	
Thermal conductivity of pure copper [152]: $\lambda_{cu} = 401$ W/mK	
Thermal conductivity of sample (glass B 270): $\lambda_p = 1.01$ W/mK	
Hemispherical total emissivity of polished chromium: $\mathcal{E}_{cr} = 0.071$	
Hemispherical total emissivity of radiation protective shield made of stainless steel: $\mathcal{E}_{ss} = 0.15$	
Hemispherical total emissivity of glass B 270: $\mathcal{E}_p = 0.85$	
Hemispherical total emissivity of chamber walls painted with Nextel-Velvet coating 811-21: $\mathcal{E}_c = 0.94$	
<u>Thermal boundary conditions</u>	
Radiative heat transfer coefficient for sample holder at $T_m = 375.85$ K: $\alpha_{r,cr} = 0.58$ W/m ² K for $T_u = 314.45$ K	
Radiative heat transfer coefficient for sample surface at $T_0 = 371.95$ K: $\alpha_{r,p} = 10.62$ W/m ² K for $T_u = 285.15$ K	
Constant heat flux used for sample heating system to get temperature, $T_m = 375.85$ K: $\dot{q} = 1783.22$ W/m ²	

For the calculations of the sample surface temperatures by a finite element method, the heat exchange by radiation between the sample holder coated with chromium and the radiation protective shield made of stainless steel on one hand, and on the other hand the heat exchange between the sample surface and the walls of the vacuum chamber painted with Nextel-velvet-coating 81-21 has to be taken into account.

The radiative heat transfer coefficient from a body 1 at temperature T_1 to a body 2 at temperature T_2 can be estimated by using the relation from VDI-Wärmeatlas [152]

$$\alpha_r = \varepsilon_{1,2} \sigma \frac{T_1^4 - T_2^4}{T_1 - T_2} \quad (6.29)$$

where $\varepsilon_{1,2}$ is the radiative exchange factor. It is given for a body 1 completely enclosed by the body 2 (i.e., view factor $F_{1-2} = 1$) as

$$\frac{1}{\varepsilon_{1,2}} = \frac{1}{\varepsilon_1} + \frac{A_1}{A_2} \left(\frac{1}{\varepsilon_2} - 1 \right) \quad (6.30)$$

where ε_1 and ε_2 are the hemispherical total emissivities of the body 1 and body 2, respectively. A_1 and A_2 are the surface areas of the body 1 and body 2 participating in the radiative heat exchange.

If the surface area of the body 2 is much larger than that of the body 1 (i.e., $A_2 \gg A_1$), it follows from equation (6.30) that $\varepsilon_{1,2} = \varepsilon_1$. This means the large body 2 appears like a black body to the small body 1. This principle can be used for the heat exchange between the sample surface and the walls of the vacuum chamber, which has a much larger surface area than that of sample surface. So that radiative exchange factor for this case may be taken as the hemispherical total emissivity of the sample surface as given in table 6.1. The radiative exchange factor for the radiative heat exchange between the sample holder and the radiation protective shield is calculated as $\varepsilon_{1,2} = 0,062$ by using equation (6.30). Then, the radiative heat transfer coefficients, $\alpha_{r,cr}$ for the chrome coated sample holder and $\alpha_{r,p}$ for the sample surface are calculated by using the equation (6.29). These values are listed in table 6.1.

A result of the numerical simulation of the glass B 270 surface as the bad conductor is presented in figure 6.4 in order to confirm the uniformity of the temperature distribution. From this figure it is clear that the temperature of the sample surface is uniform over almost all the surface area except on the edges of the sample surface. Because out of 150 mm only maximum 117 mm ($= 40/\cos 70^\circ$) diameter of the sample surface is used when it is rotated at polar angle 70° to measure the directional spectral emissivity, this non-uniformity in the temperature distribution on the edges of the sample surface does not introduce a

significant error in the measurements. The measurement of the directional spectral emissivity at the polar angle 75° is not possible, because the large diameter of the ellipse at the polar angle 75° becomes $154.55 \text{ mm} (= 40/\cos 75^\circ)$ which is greater than the diameter of the sample (150 mm). This is the reason why the measurement of the directional spectral emissivity is limited up to the polar angle 70° by the use of the experimental set up presented in this work. However, the measurement of the directional spectral emissivity can be realized up to the polar angle 75° by using an aperture having a diameter of less than 35 mm. But one should keep it in mind that the decrease of the aperture diameter results in reducing the radiative energy from the sample surface and the blackbody radiator passing to the detector.

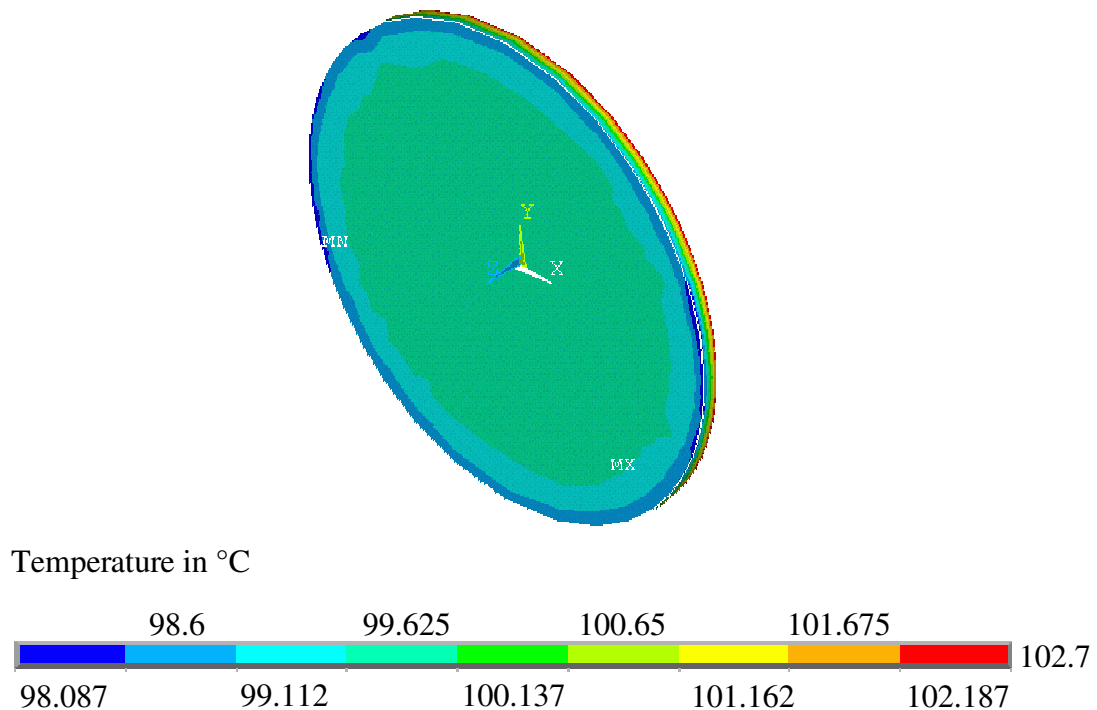


Fig. 6.4. Simulated temperature distribution of the surface of a glass B 270 sample by using finite element method (FEM).

In figures 6.5 and 6.6 the results of numerical simulation obtained by the use of finite element method are presented for the surface temperature distribution of the smooth undoped silicon and the sandblasted pure aluminium respectively. From these figures it is demonstrated that the isothermal condition of the surface temperature distribution of the silicon and the aluminium is better than that of the glass sample. The geometrical parameters and common material properties required for the FEM calculations of these samples can be taken from

table 6.1. The specific material properties and thermal boundary conditions calculated by using equations (6.29) and (6.30) are listed in table 6.2.

Table 6.2. Material properties and thermal boundary conditions for the calculation of the temperature distribution of smooth undoped silicon and sandblasted aluminium with the help of finite element method (FEM).

<u>Smooth undoped Silicon</u>	
Thickness of cylindrical sample:	$\delta_p = 0.6 \text{ mm}$
Thermal conductivity:	$\lambda_p = 82 \text{ W/mK}$
Hemispherical total emissivity:	$\epsilon_p = 0.32$
Radiative heat transfer coefficient for sample holder at $T_m = 473.15 \text{ K}$:	$\alpha_{r,cr} = 1.01 \text{ W/m}^2\text{K}$ for $T_u = 351.15 \text{ K}$
Radiative heat transfer coefficient for sample surface at $T_0 = 472.25 \text{ K}$:	$\alpha_{r,p} = 4.18 \text{ W/m}^2\text{K}$ for $T_u = 285.15 \text{ K}$
Constant heat flux used for sample heating system to get temperature, $T_m = 473.15 \text{ K}$:	$\dot{q} = 3580.02 \text{ W/m}^2$
<u>Pure sandblasted Aluminium</u>	
Thickness of cylindrical sample:	$\delta_p = 5 \text{ mm}$
Thermal conductivity:	$\lambda_p = 236 \text{ W/mK}$
Hemispherical total emissivity:	$\epsilon_p = 0.27$
Radiative heat transfer coefficient for sample holder at $T_m = 374.17 \text{ K}$:	$\alpha_{r,cr} = 0.578 \text{ W/m}^2\text{K}$ for $T_u = 314.45 \text{ K}$
Radiative heat transfer coefficient for sample surface at $T_0 = 374.05 \text{ K}$:	$\alpha_{r,p} = 2.23 \text{ W/m}^2\text{K}$ for $T_u = 285.15 \text{ K}$
Constant heat flux used for sample heating system to get temperature, $T_m = 374.17 \text{ K}$:	$\dot{q} = 1310.12 \text{ W/m}^2$

In table 6.3 the surface temperatures of three different samples, glass B 270, smooth undoped silicon and sandblasted pure aluminium are given for the comparison of the results obtained by two calculation methods, namely the energy balance method and the finite element method. The results obtained by two independent methods are in close agreement with maximum temperature difference of $0.825 \text{ }^\circ\text{C}$ in case of the bad conductor glass B 270.

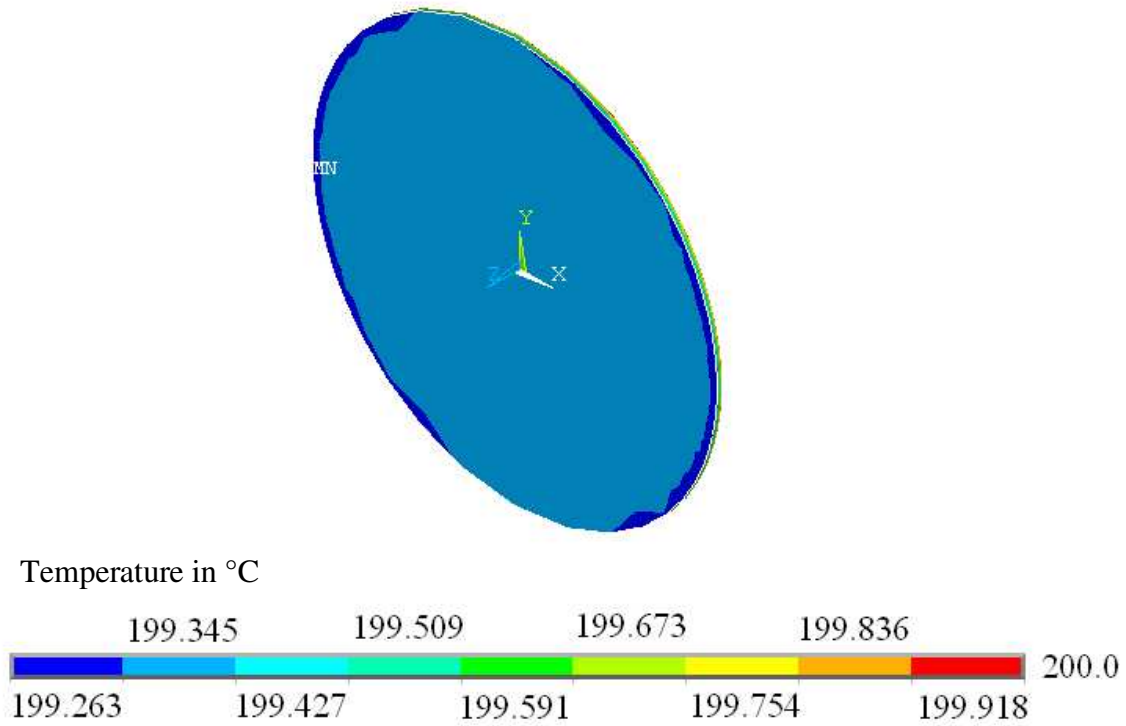


Fig. 6.5. Simulated temperature distribution of the surface of a smooth undoped silicon wafer by using finite element method (FEM).

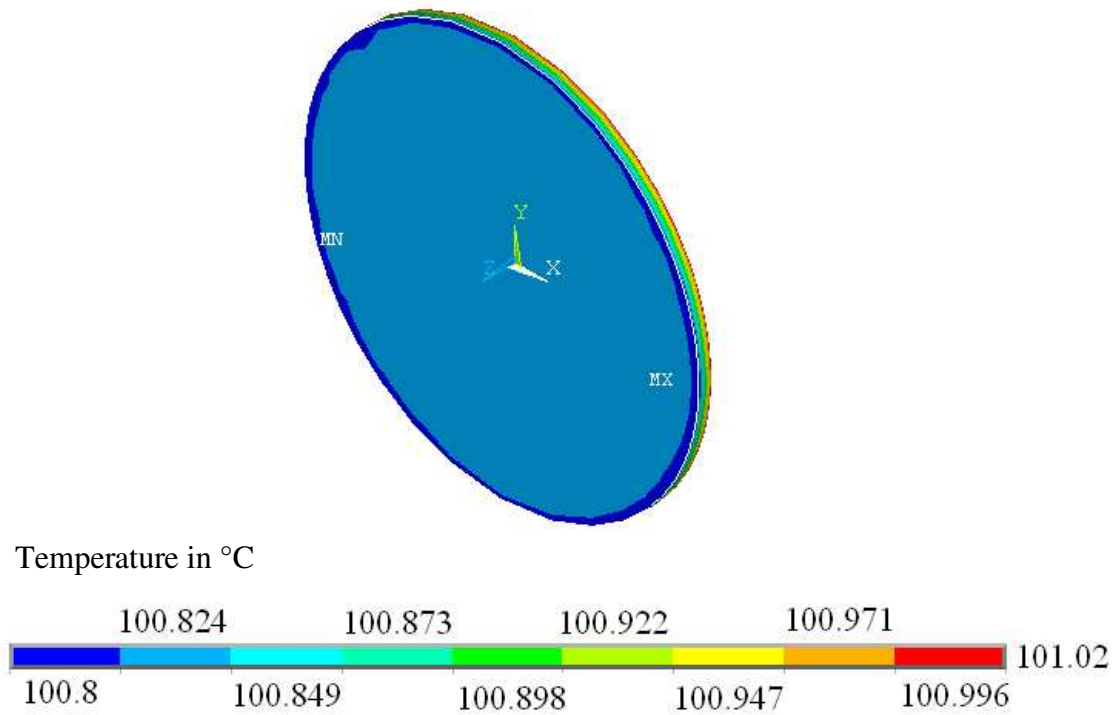


Fig. 6.6. Simulated temperature distribution of the surface of a sandblasted pure aluminium sample by using finite element method (FEM).

Table 6.3. Comparison of the sample surface temperatures obtained by energy balance method and finite element method for three different samples.

Sample	Surface temperature calculated by “Energy balance method”	Surface temperature calculated by “Finite element method”	Temperature difference
Glass B 270	98.8 °C	99.625 °C	0.825 °C
Smooth Silicon	199.1 °C	199.345 °C	0.245 °C
Sandblasted Aluminium	100.9 °C	100.824 °C	0.076 °C

It should be mentioned that in the FEM calculations no adjustment of the radiative heat transfer coefficients α_r to the resulting surface temperatures has been made. Actually, the heat loss at the cold margins of the sample would be smaller than in the centre. The uniformity of the real temperature distribution should therefore be better than calculated. On the other hand, an uniform heat flux at the back side of the sample was assumed.

6.4 Surface Temperature Measurement with an Infrared Thermo-camera

In sections 6.1 and 6.3 it has been demonstrated that the surface temperature of a sample can be calculated by using an energy balance and the finite element method. Another way of determination of the sample surface temperature without using contact sensors is measuring this temperature with an infrared thermo-camera. The IR (infrared)-camera measures and images the emitted infrared radiation from the sample surface. The fact that radiation is a function of sample surface temperature makes it possible for the camera to calculate and display this temperature if the emissivity of the surface is known. For this purpose, the experimental set up (see chapter 8) is modified in a such manner that the measurement of the sample surface temperature with an IR-camera is possible without disturbing the vacuum in the sample chamber. The constructive layout for this is shown in figure 6.7.

As shown in figure 6.7, a 3 mm thick Zinc Selenide (ZnSe)-window is placed inside a vacuum flange with o-ring (not drawn in the figure) on the front side of the sample chamber. This ZnSe-window acts as a seal element for the vacuum and at the same time it allows to pass the infrared radiation from the sample surface to the infrared thermo-camera. The IR- camera used in this work is AGEMA Thermovision 570, which can be operated in the

spectral range from $7.5\ \mu\text{m}$ to $13\ \mu\text{m}$. The radiation from the sample surface must be directed normal to the camera objective. For this purpose, a geometrical calculation is performed to find a suitable position for the IR-camera on the front side of the sample chamber. The position of the IR-camera is obtained at an angle of 54° at which there are no any perturbations on the path of the radiation from the sample surface to the camera (see figure 6.7). The sample is also rotated at the polar angle of 54° so that the radiation from its surface falls normal to the camera objective. With the total emissivity of the sample surface in the normal direction as an input value the IR-camera calculates the desired surface temperature.

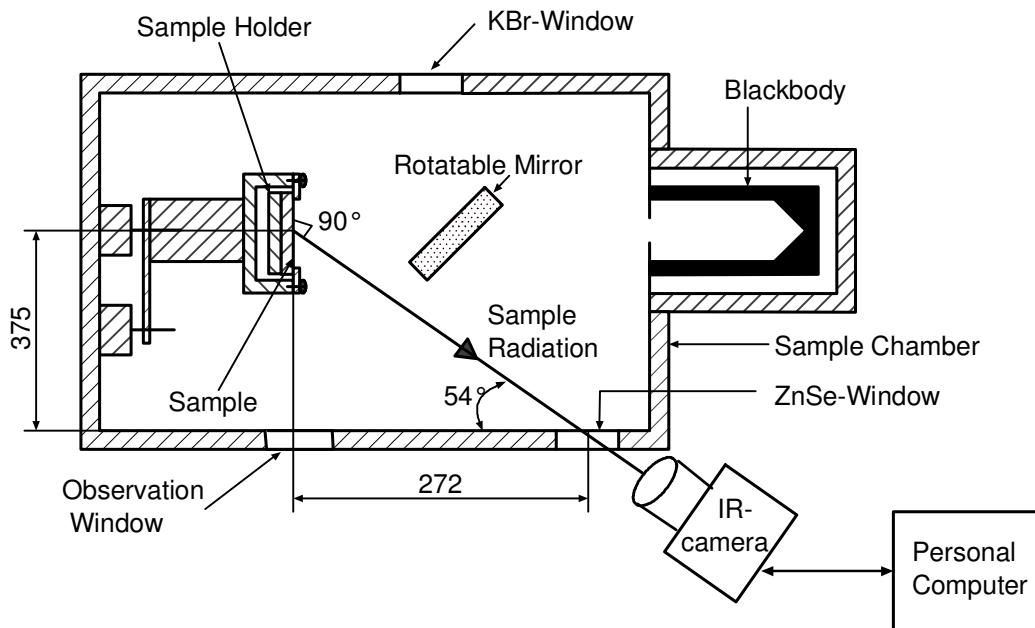


Fig. 6.7. Constructive lay out of the system overview with infrared thermo-camera for the surface temperature measurement of a sample.

The results are provided by the IR-camera as a high resolution colour image, which can be analysed either in the field by using the real-time measurement functions built into the camera, or in a personal computer by using the IRwin Report software (ThermaCAMTM Researcher 2000). Therefore, a personal computer is connected to the IR-camera through a removable PC-Card on which it is possible to capture and store the images to document the sample under inspection.

The IR-camera is easy to use and is operated by using a few buttons, which are conveniently placed on the camera allowing fingertip control of major functions. Also a built-in menu system gives easy access to use camera software for increased functionality. The radiation measured by the camera does not only depend on the sample surface temperature, but is of course a function of its emissivity as well. Radiation also originates from the

surroundings and is reflected by the sample surface. The radiation from the object and the reflected radiation will be influenced by the absorption of the atmosphere inside and outside the sample chamber. Although the sample chamber is evacuated in this work, the short distance outside the sample chamber is in the atmosphere and has some effect on the temperature measurement. Similarly, the effect of the Zinc Selenide window placed in between the sample and the camera must be considered because of its non-full transparency (i.e., only 77%) in the spectral range 7.5 μm - 13 μm .

To measure the sample surface temperature accurately, it is therefore necessary to compensate for the effects of a number of different radiation sources. This is done automatically by the thermo-camera. However, the following object parameters must be supplied for the camera.

I. Emissivity

The most important object parameter to set correctly is the directional total emissivity of the object (sample) being investigated. This is because the emissivity is a function of the object's surface temperature. In this work, however, the emissivity of the sample surface is unknown at the beginning. So that the emissivity value must be guessed at first and then it has to be corrected by an iterative method.

II. Ambient Temperature

The ambient temperature is the average temperature of the surroundings (e.g. other bodies and the air around the object being investigated). This parameter is used to compensate for the radiation reflected in the object, which can reach the camera. If the emissivity of the object is low and the object surface temperature is relatively close to that of the ambient, it will be important to set and compensate for the ambient temperature correctly.

III. Atmospheric Temperature

The atmospheric temperature is the average temperature of the atmospheric air between the object and the camera. The air between the object and the camera absorbs some of the radiation passing through and adds some radiation due to its own temperature. This parameter is therefore used to compensate for the radiation emitted from the atmosphere (air) between the camera and the object, which can

reach the camera and disturbs the measurements. If the emissivity of the object is low, the distance between the object and the camera is very long and the object surface temperature is relatively close to that of the atmosphere, it will be important to set and compensate for the atmospheric temperature correctly.

IV. Distance

The distance is the space between the object and the front lens of the camera. This parameter is used to correct for the fact that radiation is being absorbed between the object and the camera and the fact that that transmissivity drops with the distance. Since the sample chamber is evacuated and nearly 0.5 m space of the total distance of 0.6 m lies in vacuum, the remaining space of 0.1 m lying in the atmosphere is taken as the set value in the present experiment.

V. Relative Humidity

The IR-camera can also compensate for the fact that the transmissivity is dependent on the relative humidity of the atmospheric air (i.e., the H₂O content). To do this the relative humidity is set to the correct value. The relative humidity value between 0% and 99% is used in the calculation of the computed transmission of air. For short distances and normal humidity the relative humidity can normally be left at a default value of 50%.

VI. Transmission

The transmission is the transmissivity of the atmosphere between the object and the camera. There are two options to set the transmission of the atmosphere, namely the computed transmission and the estimated transmission. The program will attempt to compute the transmission of the atmosphere based on the data about its temperature, relative humidity and the distance between the camera and the object being investigated. This value is known as the computed transmission of the atmosphere.

If the space between the object and the camera contains not only air but also a transparent body, the transmission of the space must be estimated by the user. This value is dominated by the transmissivity of the transparent body lying between the object and the camera and is called the estimated transmission of the atmosphere. For example, in this work the transmissivity of the Zink Selenide window (i.e.,

0.77 at the spectral range $7.5 \mu\text{m} - 13\mu\text{m}$) is set as the value of the estimated transmission.

As mentioned above, these object parameters describe the physical properties of the body of interest, its environment and the atmosphere between the object (sample) and camera. The influence of these object parameters on the radiation received by the camera is illustrated in figure 6.8.

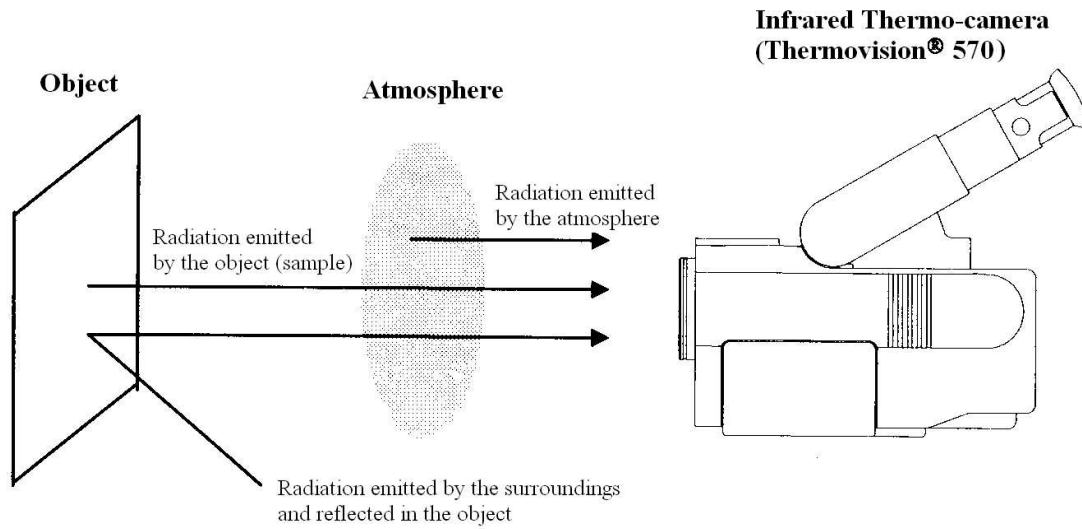


Fig. 6.8. Contributions to the radiation flux received by the IR-camera depending on the object parameters.

In the following, two examples of measuring the surface temperature of an aluminium plate coated with Nextel-Velvet-Coating 811-21 and of a smooth undoped silicon wafer by using the IR-camera are presented. These examples are used for temperature calibration. The object parameters that are to be set for the camera to calculate the surface temperatures are given in table 6.4.

In figure 6.9 an image of the surface temperature of the aluminium sample coated with Nextel-Velvet-Coating 811-21 as measured with the IR-camera is presented. As shown in the temperature scale on the right of this figure, the maximum surface temperature is 89°C , which is exactly equal to that calculated by energy balance method theoretically. Along the two lines LI01 and LI02 drawn horizontally and vertically on the surface the uniformity of the surface temperature distribution is examined. As shown in figure 6.10 these two lines are not exactly isothermals, and there is maximum 3 K temperature difference along the length of each line. This confirms that the uniformity of the surface temperature is not so good. This might be explained by the fact that the irregular thickness of the black coating over the aluminium plate leads to the different temperatures on the surface.

Table 6.4. Object parameters set for the IR-camera for measuring the surface temperatures of the aluminium sample coated with Nextel-Velvet-Coating 811-21 and the sample of smooth undoped silicon.

Object Parameter	Nextel-Velvet-Coating 811-21	Smooth Undoped Silicon
Emissivity	0.96	0.32
Distance (m)	0.1	0.1
Ambient temperature (°C)	40.7	79.6
Atmospheric temperature (°C)	24.0	24.0
Transmission	0.77	0.77
Relative Humidity (%)	40	40

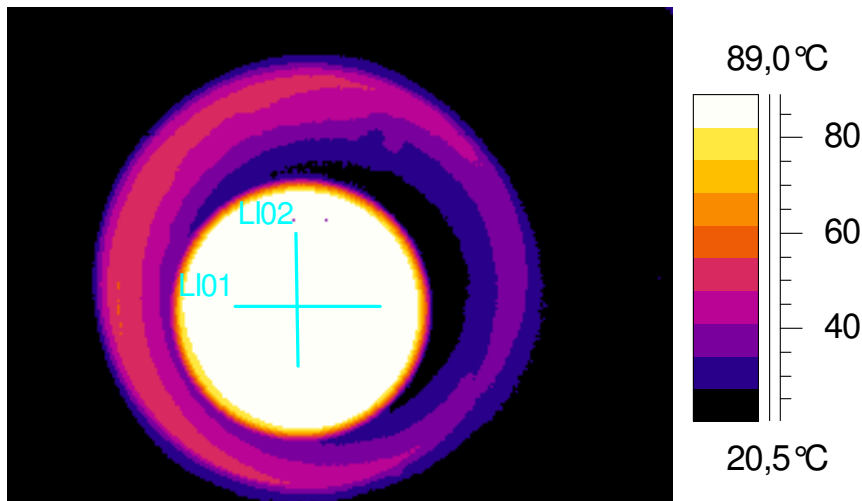


Fig. 6.9. Image of surface temperature of the aluminium sample coated with Nextel-Velvet-Coating 811-21 as measured with the IR-camera.

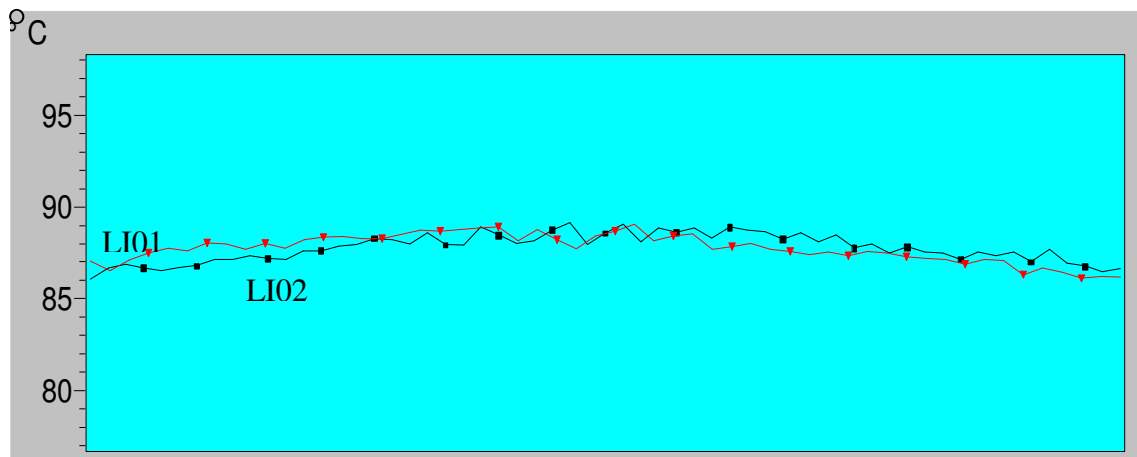


Fig. 6.10. Temperature distribution of the aluminium sample coated with Nextel-Velvet-Coating 811-21 along the lines LI01 and LI02 drawn on the surface.

An image of the surface temperature of the smooth undoped silicon wafer measured with the IR-camera is presented in figure 6.11. As shown in the temperature scale on the right of this figure, the maximum surface temperature is 206.6 °C whereas that theoretically calculated by energy balance method is 207 °C. The temperature distribution over the silicon surface is clearly non-uniform as seen in two different colours. To analyse this in detail, two lines LI01 and LI02 are drawn horizontally and vertically on the surface. As shown in figure 6.12 these two lines are not isothermals, and there is maximum 10 K temperature difference along the length of each line. This confirms that the uniformity of the surface temperature of the silicon wafer is quite bad. This behaviour is not understood.

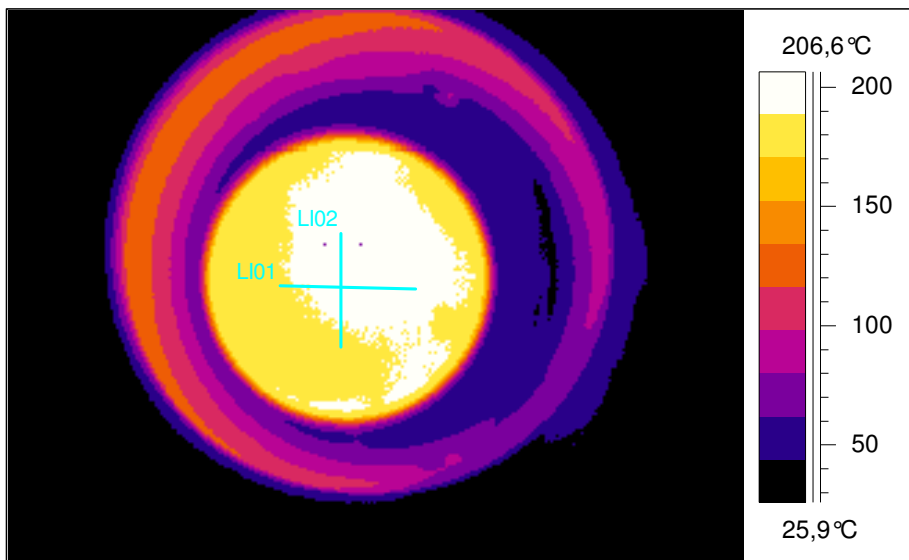


Fig. 6.11. Image of surface temperature of the smooth undoped silicon wafer as measured with the IR-camera.

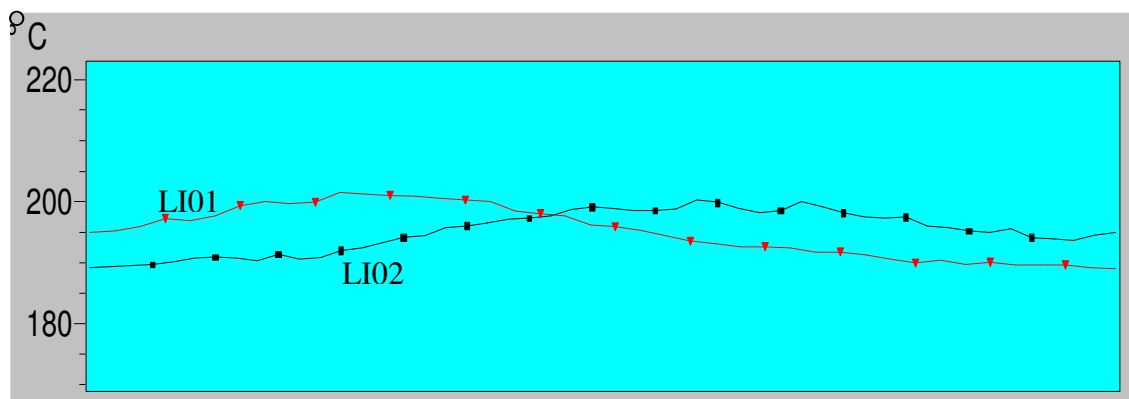


Fig. 6.12. Temperature distribution of the smooth undoped silicon wafer along the lines LI01 and LI02 drawn on the surface.

Finally, it is concluded that measuring the surface temperature with an IR-camera is an additional method to compare the result with that obtained by a different method, e.g. the energy balance method, but for the accurate measurement of the surface temperature with the IR-camera many parameters like the object parameters must be determined very accurately, because they influence the camera temperature reading severely.

6.5 Effect of Temperature Measurement Errors on Emissivity

In this work, the temperature of the sample holder is directly measured by using the platinum resistance sensor (Pt 100). This thermometer with diameter 2 mm is inserted into a hole, which is drilled at 1 mm below the surface of the sample holder (copper plate, see figure 6.3). But the temperature of the sample surface is theoretically estimated by using energy balance equations (see section 6.1) and numerically calculated with the help of finite element method (see section 6.3). As mentioned earlier, the exact determination of the surface temperature of the sample and its uniformity over the surface have direct effects upon the uncertainty of the emissivity measurement. In this work, the hemispherical total emissivity of some smooth surfaces are calculated by the energy balance method as well as by the radiometric method. In the radiometric method the measured directional spectral emissivity is integrated over all wavelengths and all directions to get the hemispherical total emissivity (see equation 2.11). Then the hemispherical total emissivity obtained from two different methods are compared. As in the energy balance method the temperatures and total electrical power P required to heat the sample at steady state is measured experimentally, the effect of errors in the temperature measurement upon the uncertainty of the emissivity measurement is analysed in this section assuming that the electrical power P is measured without error.

The radiative heat flux \dot{q} ($= P/A$) from the sample surface at temperature T_1 to its environment having temperature T_2 and a surface area much larger than that of the sample is calculated by using the relation [152]

$$\dot{q} = \varepsilon_p \sigma (T_1^4 - T_2^4). \quad (6.31)$$

From equation (6.31) it is clear that the heat flux depends on the fourth power of the sample surface temperature. This means a small error in the temperature measurement of the sample surface may introduce large error in the heat flux and consequently in the measurement of the emissivity ε_p of the sample surface.

The uncertainty or error, $\Delta\varepsilon_p$, in the hemispherical total emissivity of the sample surface due to the error, ΔT_1 , in the temperature measurement of the sample surface can be calculated by the differentiation of equation (6.31) and is given by the expression

$$\frac{\Delta\varepsilon_p}{\varepsilon_p} = \left| \frac{4T_1^4}{(T_1^4 - T_2^4)} \right| \frac{\Delta T_1}{T_1} \quad (6.32)$$

For the sample chamber temperature $T_2 = 285.15$ K and the error $\Delta T_1 = 0.5$ K in the measurement of the sample surface temperature $T_1 = 371.95$ K, the error in the measured emissivity of the sample surface ($\Delta\varepsilon_p/\varepsilon_p$) becomes 0.82% from equation (6.32).

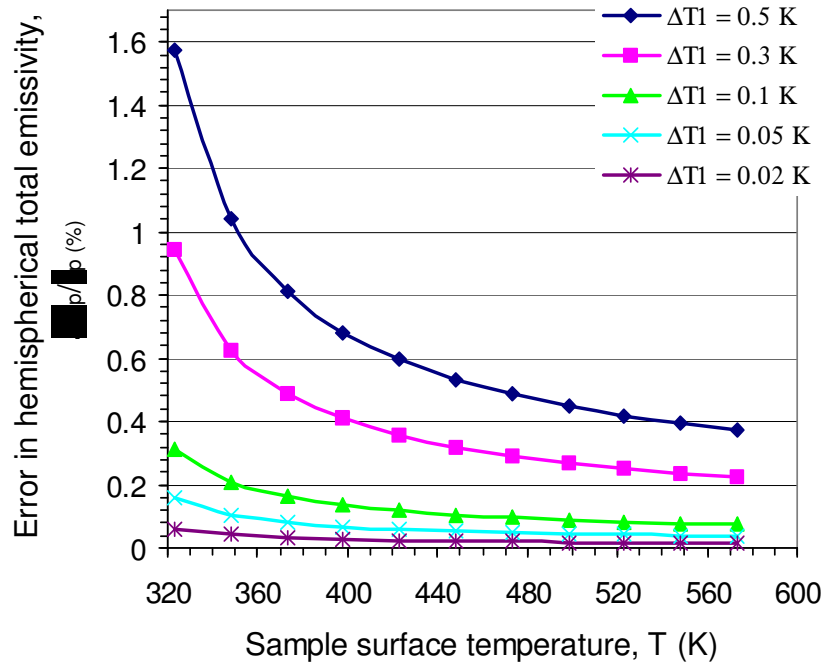


Fig. 6.13. Calculated error in hemispherical total emissivity due to an uncertainty in the sample surface temperature measurement for sample chamber temperature $T_2 = 285.15$ K.

Figure 6.13 shows the trend of the error in the measured hemispherical total emissivity ($\Delta\varepsilon_p/\varepsilon_p$) in percentage due to the different values of error in the surface temperature measurement of a sample for different surface temperatures. It is observed that the error in hemispherical total emissivity becomes larger for the increasing error in the sample temperature measurement. But in the case of large difference between the temperatures of sample surface and the sample chamber ($T_1 - T_2$), this influence in uncertainty of hemispherical total emissivity ($\Delta\varepsilon_p/\varepsilon_p$) is less significant.

7 Understanding of FTIR-Spectroscopy

The purpose of this chapter is to introduce the fundamental concepts of Fourier Transform Infrared (FTIR) spectroscopy. Infrared spectroscopy is the study of the interaction of infrared light with matter. Light is composed of electric and magnetic sine waves which are in planes perpendicular to each other, and the light wave moves through space in a direction perpendicular to the electric and magnetic field vectors. Different kinds of light can be denoted by a quantity called wavelength of the light. But nowadays, wavenumber is the unit typically used in infrared spectroscopy to denote different kinds of light. The wavenumber of a light wave is the reciprocal of the wavelength.

All objects in the universe at a temperature above absolute zero send out infrared radiation. When infrared radiation interacts with matter it can be absorbed, causing the chemical bonds in the material to vibrate. Chemical structural fragments within molecules tend to absorb infrared radiation in the same wavenumber range regardless of the structure of the rest of the molecule that the fragment is in. This means there is a correlation between the wavenumbers at which a molecule absorbs infrared radiation and its structure. This correlation allows the structure of unknown molecules to be identified from the molecule's infrared spectrum which makes infrared spectroscopy a useful chemical analysis tool. In addition to chemical structures, infrared spectrum can provide quantitative information as well, such as emission of the infrared radiation from thermally excited molecules in a sample.

A plot of measured infrared radiation intensity versus wavenumber is known as an infrared spectrum. An instrument used to obtain an infrared spectrum is called an infrared spectrometer. There are several kinds of instruments used to obtain infrared spectra; the most popular among them is the Fourier Transform Infrared (FTIR) spectrometer. In the following sections a detailed description about the FTIR-spectrometer will be given with its advantages and limitations.

7.1 The FTIR-Spectrometer

The FTIR (Fourier Transform Infrared)-spectrometer is a sensor technology based on the two-beam type interferometer originally designed by Michelson in 1891. The Michelson interferometer is a device that divides a beam of radiation into two distinct paths and then recombines the two beams after introducing a difference of length in the two paths. Under these conditions, interference between the beams can occur. The interference creates variations in the output beam intensity as the difference in the path length changes. The

intensity variations of the output beam can be measured with a detector as a function of the path difference.

The simplest form Michelson interferometer is shown in the figure 7.1. It consists of two mutually perpendicular plane mirrors M1 and M2, one of which is mounted so that it can be moved along an axis perpendicular to its plane surface. This movable mirror M2 is normally moved at constant velocity or could be moved and held at equally spaced points for fixed, short time periods and then rapidly stepped between points. A beam splitter BS is located between the fixed mirror M1 and the movable mirror M2 at an equal distance L . The beam splitter divides the input beam of radiation from a source S into two beams. That is, the input beam is partially reflected to the fixed mirror and partially transmitted to the movable mirror. After the beams return to the beam splitter at O , they interfere and are again partially reflected and partially transmitted. Because of the effect of interference, the intensity of each beam, one passing to the detector D through the sample Sa and the other returning to the source S , depends on the difference of path lengths $2x$ (where x is the displacement of the movable mirror) in the two arms of the interferometer. The variation in the intensity of the beams seen by the detector is a function of the path difference and a graph or plot of this intensity (after being amplified by an amplifier A) is known as an interferogram $I(x)$. After mathematical manipulation with the help of a Fourier transform (FT)- computer, the interferogram ultimately provides the desired spectral information in a Fourier Transform Infrared (FTIR)- spectrometer.

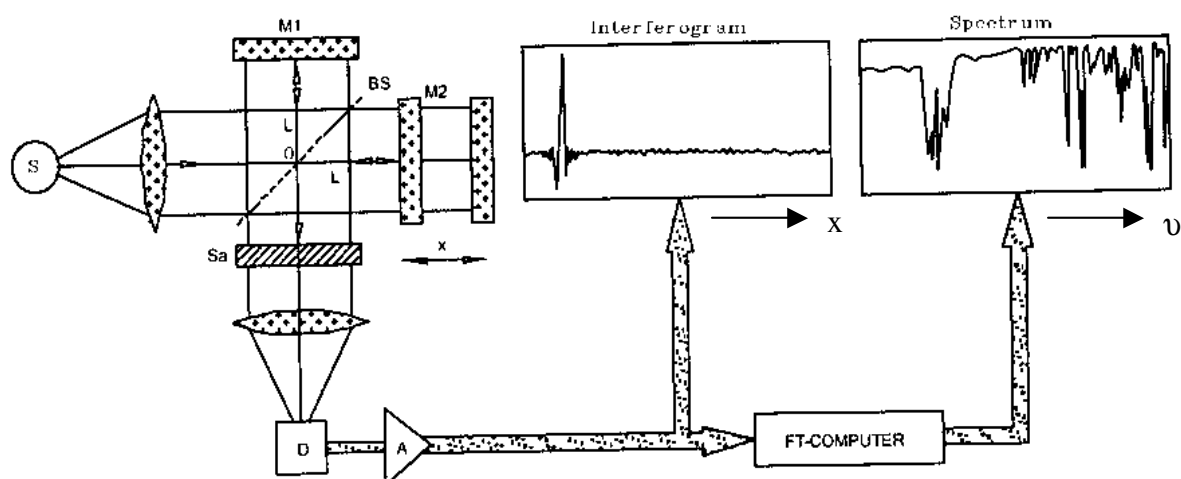


Fig. 7.1. Schematic representation of a Michelson interferometer in connection with FTIR-Method.

First an ideal situation is considered where a source of pure monochromatic radiation produces an infinitely narrow and perfectly collimated beam with the wavelength λ . When the fixed and movable mirrors are equidistant from beam splitter (i.e., zero path difference), then the two beams travel the same distances through the same materials are exactly in phase after they recombine at beam splitter. At this point, the beams interfere constructively and the intensity signal of the beam passing to the detector is the sum of the intensity signals of the two beams passing to the fixed and movable mirrors. Therefore, all the light from the source reaches the detector at this path difference (retardation). This condition of constructive interference again exists if the displacement of the movable mirror is an even number multiple of one-half wavelength.

If the movable mirror is displaced a distance which is exactly an odd number multiple of one-half wavelength, then destructive interference takes place. Because the beams are 180° out of phase on recombination at the beam splitter, no light passes to the detector. This pattern of constructive-destructive interference repeats as the mirror moves further.

By moving the mirror, the signal at the detector varies sinusoidally, a maximum being registered each time when the path difference is an integral multiple of wavelength. The intensity signal of the beam at the detector, measured as a function of path difference x , is given by the symbol $I(x)$ which is generally referred to as interferogram and it is proportional to the radiant energy which is striking the detector. The intensity signal at any point where $x = n\lambda$ (where n is an integer) is equal to the intensity or radiance of the source $L(\nu)$. At other values of x , the intensity signal of the beam at the detector or interferogram is given by the expression:

$$I(x) = \frac{1}{2} L(\nu) \{1 + \cos(2\pi\nu x)\} \quad (7.1)$$

where ν is the wavenumber of the radiation defined as the reciprocal of the wavelength λ . $I(x)$ is the interferogram from a monochromatic source measured with an ideal interferometer and it is the signal we are interested in. Equation (7.1) shows that the interferogram for a monochromatic source is a cosine function of constant amplitude and a single wave number or frequency. It can also be seen that the interferogram contains a constant component equal to $L(\nu)/2$ and a modulated component equal to $\{L(\nu)/2\}\cos(2\pi\nu x)$. But only the modulated component is important in spectrometric measurements which is generally referred to as the

interferogram $I(x)$. The interferogram from a monochromatic source measured with an ideal interferometer is therefore given by the equation

$$I(x) = \frac{1}{2} L(\nu) \cos(2\pi\nu x) \quad (7.2)$$

In practice, several factors affect the magnitude of the signal measured at the detector. For example, the beam splitter efficiency, detector response and amplifier characteristics. That is why the amplitude of the interferogram as observed after detection and amplification is proportional not only to the intensity of the source, but also to these factors. In this non-ideal case, above equation (7.2) can be modified by a single wavenumber-dependent correction factor, $F(\nu)$, to yield

$$I(x) = F(\nu) L(\nu) \cos(2\pi\nu x) \quad (7.3)$$

The above description shows how the interferometer modulates each wavelength into an unique harmonic function of frequency and performing the Fourier transformation of a measured interferogram (equation 7.3) is not a big problem. However, if the source is not monochromatic and emits radiation with a continuous spectrum, the interferogram is the resultant of the interferograms corresponding to each wavenumber. Therefore, it is more complex and a digital computer is usually required to do the Fourier transformation. For such a polychromatic source the interferogram can be represented by the integral:

$$I(x) = \int_0^{\infty} F(\nu) L(\nu) \cos(2\pi\nu x) d\nu \quad (7.4)$$

which is one-half of a cosine Fourier transform pair, the other being

$$L(\nu) = \frac{2}{F(\nu)} \int_{-\infty}^{\infty} I(x) \cos(2\pi\nu x) dx \quad (7.5)$$

Because $I(x)$ is an even function, equation (7.5) may be rewritten as

$$L_v(\nu) = \frac{4}{F(\nu)} \int_0^{\infty} I(x) \cos(2\pi\nu x) dx \quad (7.6)$$

Equations (7.4) and (7.6) show that the complete spectrum from 0 to ∞ (cm^{-1}) can be theoretically measured at infinitely high resolution. However, in order to achieve this the moving mirror of the interferometer has to be scanned an infinitely long distance varying from 0 to ∞ which is not possible to do in practice. Therefore, the signal must be digitized at finite sampling intervals. This effect of measuring the signal over a limited retardation (path difference) is to cause the spectrum to have a finite resolution. Further details about the FTIR-spectrometer are to be found in Bell [10].

7.1.1 Advantages and Disadvantages of FTIR-Spectrometer

To understand the advantages of FTIR-spectrometer, and how it has become the predominant tool of obtaining infrared spectra, the performance of FTIR-spectrometer must be compared to the type of infrared instruments that came before it. These instruments were called dispersive instruments or conventional grating infrared spectrometers. The FTIR-spectrometer has some significant advantages in comparison to dispersive grating infrared spectrometers. But some problems can also arise in FTIR-spectrometers because of the complicated mathematical procedures in the Fourier Transformation. In the following sections brief explanations will be given about some advantages and disadvantages of FTIR-spectrometer.

I. Advantages:

(i) Jaquinot- or Throughput-Advantage:

The circular apertures used in FTIR-spectrometers have a larger area than the linear slits used in conventional grating spectrometers. FTIR-spectrometers therefore enable higher throughput of radiation. This fact is called the Jaquinot or throughput advantage.

(ii) Multiplex- or Fellget-Advantage:

In conventional grating spectrometers the spectrum is measured directly by recording the intensity at different monochromator settings for a wavenumber one after the other. But in a FTIR-spectrometer, the complete spectrum originating from an infrared source of radiation is used so that all frequencies impinge simultaneously on the detector due to which the

possible distortion in the source spectrum can be prevented. This advantage is known as multiplex or Fellgett advantage of the FTIR-spectrometers.

(iii) Connes-Advantage:

The position of the movable mirror in interferometer of FTIR-spectrometer is determined with the help of the wavelength of a laser beam which is constant and known exactly. This accounts for achieving high accuracy in the measurement of the optical path difference between fixed and movable mirror and high wavenumber accuracy can therefore be achieved in the calculation of the spectrum. This accounts for the so-called Connes advantage.

(iv) Measurement Time:

The measuring time in FTIR-spectrometer is the time needed for the movable mirror to travel over a distance proportional to the desired resolution. Because of the very fast movement of the mirror, complete interferogram and then spectra can be measured in fractions of a second. This small time of measurement is essential for tracking processes which are changeable with time, for example in chemical reactions.

(v) Resolution:

The resolution of a grating spectrometer is improved by the reduction of the slit size through which the radiation passes. But the intensity of the radiation is decreased by the use of a small sized slit. The maximum resolving power of grating spectrometers are therefore limited by the slit size. In FTIR-spectrometers, higher resolution than in grating spectrometers can be achieved by increasing the length of the measured interferogram by taking more sampling points or by zero filling.

II: Disadvantages:

(i) Digitalization or Picket-Fence-Effect:

In the FTIR-spectroscopy, the measured interferogram and the spectrum calculated from it have been digitalized. The picket-fence effect occurs when the interferogram contains frequencies which do not coincide with the frequency sample points. If a frequency component lies exactly halfway between two sample points, incorrect signal reduction can occur. Then one seems to be viewing the true spectrum through a picket-fence, thereby clipping those spectral contributions lying between the sampling points, in other words

'behind the pickets'. This so-called picket-fence effect can be overcome by adding zeros to the end of the interferogram. This procedure is known as zero filling (see section 7.2).

(ii) Finite Length of Interferogram or Leakage-Effect:

The truncation of the interferogram at a finite optical path difference can cause disturbance in the line shape of the calculated spectrum. This effect is known as leakage-effect and the proper mathematical term to describe the effect of truncating the interferogram on the spectra is convolution. The solution to the problem of leakage is to truncate the interferogram so that there are no or very few side lobes on the spectral line. This method of the truncation of the interferogram is known as apodisation (see section 7.2).

(iii) Aliasing:

Another possible source of error due to using a digitized version of a continuous interferogram is aliasing. The discrete Fourier transformation (DFT) yields not just a single spectrum but rather the spectrum plus its mirror image. This means that a DFT of an n -point interferogram yields only $n/2$ meaningful output points. The remaining $n/2$ points are superfluous and therefore have to be discarded. This replication of the original spectrum and its mirror image on the wavenumber axis is termed aliasing. This effect can be removed by using filters which are transparent only for the radiation with the required wavenumber interval (i.e., no overlapping occurs with a wavenumber smaller than folding wavenumber).

(iv) High Computational Expense:

In FTIR-spectrometers, the evaluation of the measured data requires a high computational expense as compared to grating spectrometers. But by the use of the computers these days this disadvantage is not much interesting.

A detailed explanation on the advantages and disadvantages of the FTIR-spectrometers can be found in Griffiths and Haseth [53].

7.1.2 Calibration Formula for FTIR-Spectrometer

In this section a procedure to calibrate a Fourier transform infrared (FTIR)-spectrometer is presented. A blackbody source at two different temperatures is used to eliminate errors in the calibration. Calibration of Fourier transform infrared spectrometers is essential in all cases for which emission spectra are measured and physical parameters are to be calculated from the spectra. Such examples are: contactless temperature measurement

[149], measurement of spectral emissivity of technical surfaces and determination of concentrations of the various gases that are contained in the exhaust gas of industrial smoke stacks or aircrafts.

A FTIR- spectrometer operating in emission mode (i.e., the infrared radiation source built in the spectrometer is switched off and the sample emission is used as the infrared source) is used to measure many spectral points of the object radiance. These equipments do not provide spectra in absolute and physically meaningful units. The result of a measurement with a FTIR- spectrometer is therefore a spectrum in instrument dependent units called arbitrary units. In order to obtain a connection to the actual spectral radiance, it is necessary to calibrate the measured spectrum.

For the calibration of a measured spectrum one should know the influences on the radiation that passes from the investigated surface to the detector of the FTIR- spectrometer. Figure 7.2 visualizes the influences on the radiation. The detector receives not only radiation from the sample surface to be investigated, but radiation emitted by parts of the instrument itself passes through the interferometer as well. These two components are influenced by the atmosphere (e.g. moisture, carbon dioxide in air), the optical components of the spectrometer (e.g. lenses, mirrors, beam splitter, detector) and its electronics (e.g. filters, amplifiers).

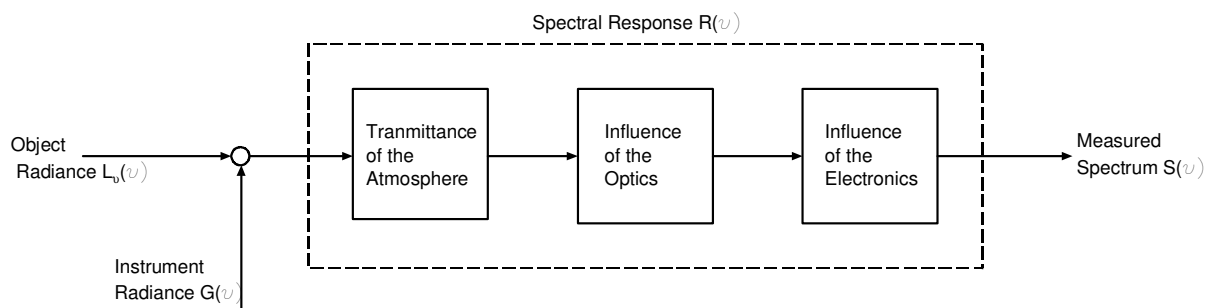


Fig.7.2 Block diagram of the mathematical model describing the calibration procedure of a spectrum measured by a FTIR-Spectrometer.

As explained above, fundamental to every calibration procedure is a mathematical model that describes the spectrum provided by the FTIR- spectrometer as a function of the radiation that enters the spectrometer and this model must contain all the components which influence the radiation. Thus, many parameters are required for the model equations. The values of these parameters cannot be calculated theoretically. That is why it is the task of a calibration procedure to determine all these parameters of the model. This can be achieved by

taking spectra of one or more sources of well known radiation and by applying the appropriate data evaluation.

Blackbody radiators are usually used as calibration sources for the calibration of a FTIR-spectrometer that is sensitive in the thermal infrared region of the electromagnetic spectrum. The radiation of a black surface is given by Planck's law in wave number formulation:

$$L_v(\nu, T) = \frac{c_1 \nu^3}{e^{(c_2 \nu / T)} - 1} \quad (7.7)$$

where $L_v(\nu, T)$ is the spectral radiance emitted by the surface ($\text{W}/\text{cm}^2 \text{srm}^{-1}$), $\nu = 1/\lambda$ is the wavenumber (cm^{-1}), T is the surface temperature (K), $c_1 = 1.191062 \times 10^{-12} \text{ Wcm}^2$ is the first radiation constant, $c_2 = 1.438786 \text{ cmK}$ is the second radiation constant.

The mathematical model that describes a radiance spectrum measured by a FTIR - spectrometer which receives radiation from a sample surface as visualized in fig. 7.2 is given by the expression [84]

$$S(\nu) = R(\nu)[L_v(\nu) + G(\nu)] \quad (7.8)$$

where $S(\nu)$ is the measured spectrum that is obtained from the spectrometer, $L_v(\nu)$ is the spectral radiance of the sample surface, $R(\nu)$ is the spectral response of the spectrometer which is composed of the transmissivity of the atmosphere, influence of the optics and influence of the electronics, and $G(\nu)$ is the spectral radiance of the spectrometer's inner parts.

In order to obtain the spectral radiance that is emitted by the investigated object, the instrument functions $R(\nu)$ and $G(\nu)$ must be known. Then the calibrated spectrum i.e., the actual spectral radiance can be calculated from the measured spectrum $S(\nu)$ using the following relation:

$$L_v(\nu) = \frac{S(\nu)}{R(\nu)} - G(\nu) \quad (7.9)$$

The task of the calibration procedure is the determination of the unknown functions $R(\nu)$ and $G(\nu)$. Therefore, it is necessary to measure spectra $S(\nu)$ of radiation sources of known spectral radiances $L_\nu(\nu)$. As the spectral radiance of a blackbody can be determined by using the Planck's law, equation (7.7), one should have to take the spectra $S_1(\nu)$ and $S_2(\nu)$ of a blackbody at different temperatures T_1 and T_2 , and solve them for the unknown functions. Rewriting equation (7.8) for the temperatures T_1 and T_2 :

$$S_1(\nu) = R(\nu)[L_{\nu_1}(\nu) + G(\nu)] \quad (7.10)$$

$$S_2(\nu) = R(\nu)[L_{\nu_2}(\nu) + G(\nu)] \quad (7.11)$$

where $L_{\nu_1}(\nu)$ and $L_{\nu_2}(\nu)$ are the spectral radiance of a blackbody at temperatures T_1 and T_2 respectively. Solving equations (7.9) and (7.10) for the unknown functions $R(\nu)$ and $G(\nu)$, we get the required relations:

$$R(\nu) = \frac{S_1(\nu) - S_2(\nu)}{L_{\nu_1}(\nu) - L_{\nu_2}(\nu)} \quad (7.12)$$

$$G(\nu) = \frac{S_1(\nu)}{R(\nu)} - L_{\nu_1}(\nu) \quad (7.13)$$

Since an FTIR-spectrometer provides a discrete spectrum, the calibration procedure must determine the two parameters $R(\nu_i)$ and $G(\nu_i)$ for each discrete wavenumber ν_i where i represent n spectral elements. Therefore, the equations (7.8)-(7.13) are valid for every wavenumber ν_i , but for the sake of simplicity the index i of ν_i is omitted in these equations.

It must be emphasized that the instrument functions $R(\nu)$ and $G(\nu)$ depend on the distance between the spectrometer and the calibration source. The model assumes that this distance is part of the spectrometer and thus it is never changed. If the object under investigation is at a greater distance than the calibration source, the influence of the additional path, which not only absorbs but also emits radiation, is usually not negligible.

7.2 Method of Conversion of Interferogram to Spectrum

As discussed earlier, the calculation of a spectrum from an interferogram is theoretically a Fourier transformation. But in practice some additional steps are necessary for the conversion of the interferogram to a spectrum, because the interferograms are digitalized, confined and cannot be measured symmetrically referring to the centerburst (i.e., position of zero displacement, $x = 0$). The calculation of the spectrum to get the directional spectral emissivity of a sample from the measured interferogram requires the following steps, which are presented schematically in figure 7.3.

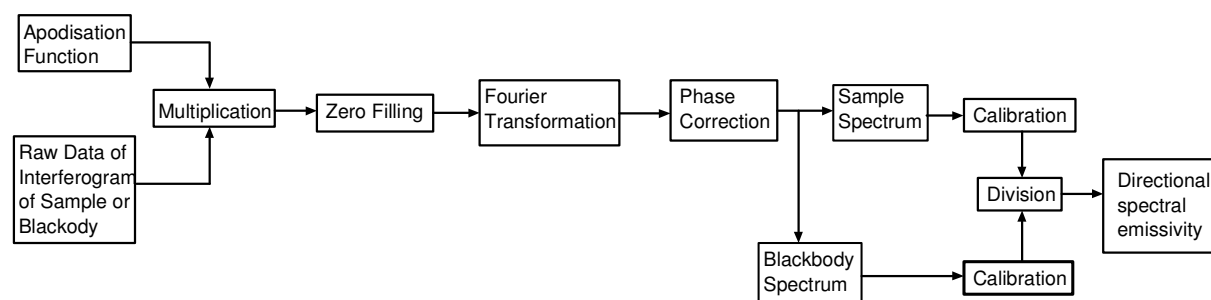


Fig. 7.3 Schematic diagram of the calculation of a sample or a blackbody spectrum from raw data of interferogram to get the directional spectral emissivity of a sample.

I. Apodisation

The measured interferogram is finite and terminates at its ends abruptly. This results in a disturbance (side lobes) on the line shape of the spectrum calculated from it. In other words, due to the truncation of the interferogram at finite optical path difference numerous additional peaks called side lobes or feet are generated on the spectral line shape besides a main maximum peak as shown in figure 7.4 (top right). The analytical form of the instrument line shape (ILS) corresponding to a boxcar truncation (i.e., Fourier transform of boxcar function) is the well-known sinc function (i.e., $\text{sinc}(x) = \sin(x)/x$). The side lobes of the sinc function cause a leakage of the spectral intensity, i.e. the intensity is not strictly localized but contributes also to these side lobes. As the side lobes do not correspond to actually measured information but rather represent an artifact due to the abrupt truncation, it is desirable to reduce their amplitude. The process which attenuates these artificial side lobes in the spectral domain is known as apodisation.

The aim of the apodisation procedure is to find a cut off or apodisation function which provides fewer side lobes than the sinc function after multiplying the interferogram by it. Numerous such functions exist, e.g. triangular, trapezoidal, Happ-Genzel and Blackmann-

Harris functions etc (see figure 7.4). As side lobe suppression always causes main maximum broadening, achievement of good results from apodisation is only possible at the cost of resolution. Therefore, the selection of a suitable apodisation function depends on what one is aiming at. As the instrument line shape (ILS) produced by the Blackmann-Harris function provides nearly the same width at half height (WHH) as the other functions, but at the same time, the highest side lobe suppression and is furthermore nearly zero at the interval ends (see right bottom figure 7.4), it can be considered as a better apodisation function than the other ones.

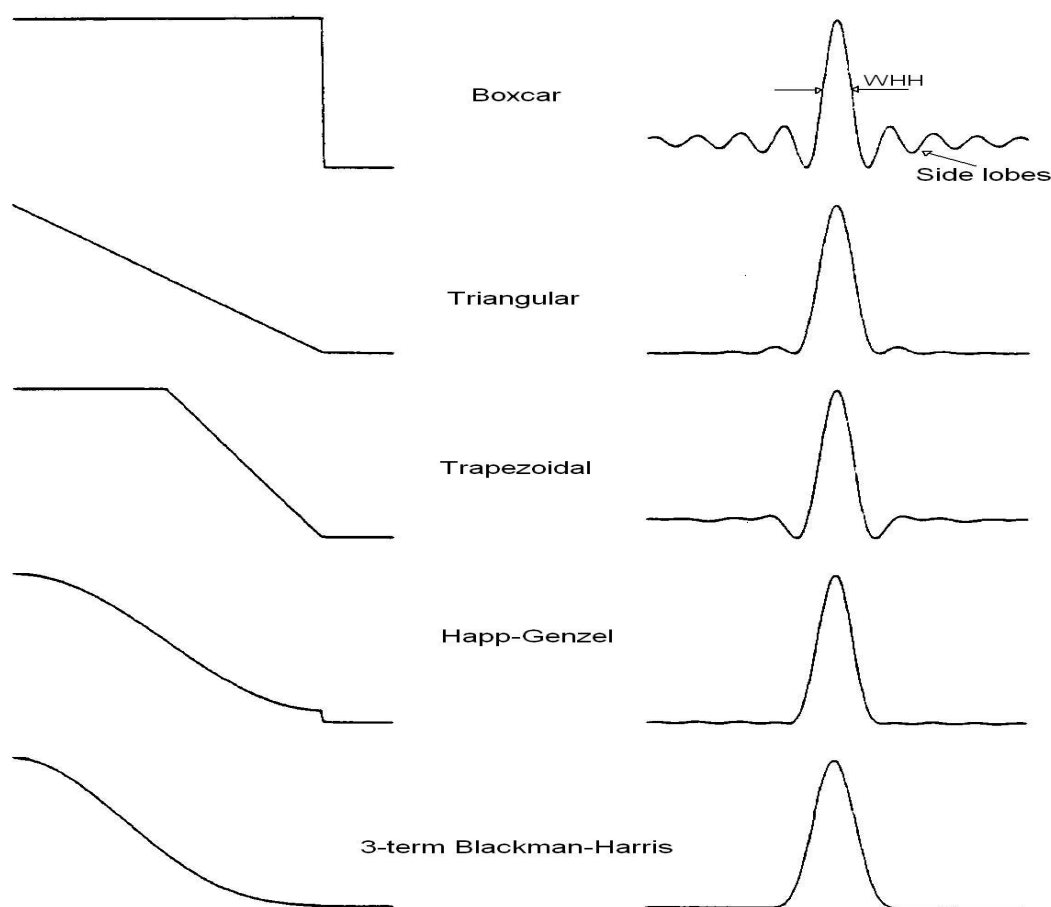


Fig. 7.4. Different types of apodisation functions (left) and their instrumental line shapes (ILS) after corresponding Fourier transformations (right) plotted together with the boxcar truncation on the top.

II. Zerofilling

The problem of the picket-fence effect described in section 7.1.1 is less extreme than stated if the spectral components are broad enough to be spread over several sampling positions. In other words, a smoother plot of the spectrum can result when the size of the interferogram is expanded by adding zeros to its end thereby increasing the number of points

per wave number in the spectrum. Thus, this procedure which is known as zero filling has the effect of interpolating the spectrum and reducing the picket-fence error. Because those zeros which are added to the interferogram contain no informations, the resolution of the spectrum is not increased by the procedure of zero filling. Normally, one should always at least double the original interferogram size for practical measurements by zero filling it, i.e. the zero filling factor (ZFF) of two should be chosen.

It should be noted that zero filling does not introduce any errors, because the instrumental line shape is not changed. It is therefore superior to polynomial interpolation procedures working in the spectral domain.

III. Fourier Transformation

The measured interferograms are digital. The digitized interferogram must be converted into a spectrum by means of a mathematical operation called Fourier transformation (FT). Generally, the Fourier transformation determines the frequency components making up a continuous waveform. However, if the interferogram (waveform) is sampled and consists of discrete, equidistant points, the discrete version of the Fourier transformation (DFT) has to be used.

Because of its high computing expense the discrete Fourier transformation (DFT) is seldom used in practice. Instead a number of so-called fast Fourier transformations (FFT) are in use, the most common of which is the Cooley-Tukey numerical algorithm (consult reference [53]). The aim of these fast Fourier transformations is to reduce the number of complex mathematical operations, leading to a saving of computing time.

IV. Phase Correction

The measured interferogram mostly is not symmetric about the centerburst (i.e., $x = 0$). Due to this reason the result of the Fourier transformation of an interferogram generally is a complex spectrum rather than a real spectrum. In other words, the spectrum after the Fourier transformation composes of a purely real part and a purely imaginary part. Equivalently, the complex spectrum can also be represented by the product of the true amplitude spectrum and the complex exponential containing the wavenumber-dependent phase. The process of extraction of this true amplitude spectrum from the complex output of the Fourier transformation is known as phase correction. This can be performed either by calculating the square root of the power spectrum (i.e., product of the complex spectrum and its conjugate spectrum) or by multiplication of the complex spectrum by the inverse of the phase

exponential and taking the real part of the result. This procedure is known as ‘multiplicative phase correction’ or the Mertz method, and the other method of phase correction called Forman method is mathematically equivalent to the Mertz method, but it is performed in the interferogram domain. More details about the Mertz and Forman methods of phase correction are to be found in Griffiths and Haseth [53].

V. Calibration and Division by a Blackbody Spectrum

After doing the phase correction the sample spectrum is free of the phase error. A similar procedure is carried out with a blackbody interferogram to get blackbody spectrum without the phase error. The last mathematical operation to be performed is the calibration of these two spectra (see section 7.1.2) and the division of the calibrated sample spectrum by the calibrated blackbody spectrum to get the directional spectral emissivity of the sample.

In this chapter, a brief description is given on how the raw data gained from the FTIR-spectrometer is processed to get a spectrum and then the directional spectral emissivity of a sample. Herres and Groenholz [57] is referred for more details about the understanding of the FTIR-spectroscopy data processing.

7.3 Correction of Reflection of Radiation from Surroundings

It is well known that every surface which has the temperature above 0 K emits electromagnetic radiation. This radiation is represented by Planck’s law given in equation (7.7) multiplied by a wavenumber and temperature dependent surface emissivity.

All the radiation proceeding from a sample surface is not only the emitted one. Moreover, radiation from the surroundings is reflected at or possibly passes through the sample. The radiance of the thermal emission from the sample surface near ambient or lower temperatures is so small that the background radiation emitted by the surroundings seriously affects the accuracy of the emissive measurement. A fraction of the background radiation reflected at the sample surface can increase the apparent radiance of the sample and cause misinterpretation of the emissivity value. Therefore, a correction of the reflection of the background radiation from the surroundings has to be performed. This will be done in the followings.

Assuming a homogeneous temperature distribution in the surroundings and having all surfaces inside the chamber painted with black paint ($\epsilon=0.94$), the surroundings can be regarded as a blackbody with ambient temperature T_u (i.e., temperature of the chamber wall)

and emissivity close to $\varepsilon = 1$. This may be assumed because the surface area of the chamber walls is much larger than the sample surface area and the sample is completely enclosed by the chamber walls from all sides. This means the chamber walls appear like a blackbody to the sample [152]. Then using equation (7.7) the radiance (spectral intensity) of the surroundings is given by

$$L_{v,u}(v, T_u) = \frac{c_1 v^3}{e^{(c_2 v/T_u)} - 1}. \quad (7.14)$$

The fraction of radiation of the surroundings being reflected at the sample surface can be obtained by using the directional hemispherical spectral reflectivity $\rho'_v(v, \vartheta, \varphi, T_o)$ of the sample. Taking the assumption of incident radiation from the surroundings being homogeneous, the spectral radiance $L_{v,u}^{ref}$ of the reflected radiation from the sample surface is calculated as

$$L_{v,u}^{ref}(v, \vartheta_{ref}, \varphi_{ref}, T_o, T_u) = \rho'_v(v, \vartheta_{ref}, \varphi_{ref}, T_o) L_{v,u}(v, T_u) \quad (7.15)$$

where T_o is the surface temperature of the sample, ϑ_{ref} is the polar angle and φ_{ref} is the azimuthal angle of the reflection. Since the incident radiance is assumed to be uniform over all incident directions, the reciprocity relation for directional spectral reflectivity can be used. The reciprocity relation states that the hemispherical directional spectral reflectivity of a sample is equal to the directional hemispherical spectral reflectivity for the same angles (ϑ, φ) and $(\vartheta_{ref}, \varphi_{ref})$ for the incident and reflected radiation respectively (see section 2.1.4). Using this reciprocity relation, equation (7.15) can equivalently be expressed as the function of the directional hemispherical spectral reflectivity $\rho'_v(v, \vartheta, \varphi, T_o)$:

$$L_{v,u}^{ref}(v, \vartheta_{ref}, \varphi_{ref}, T_o, T_u) = \rho'_v(v, \vartheta, \varphi, T_o) L_{v,u}(v, T) \quad (7.16)$$

If the sample is perfectly opaque (i.e., the directional spectral transmissivity of the sample, $\tau'_v(v, \vartheta, \varphi, T_o) = 0$), the rest of the radiant power is absorbed. As given in section 2.1.3, the absorbed part of the radiant power can be calculated by using the directional spectral absorptivity $\alpha'_v(v, \vartheta, \varphi, T_o)$:

$$d^3\Phi_{\nu,u}^{abs}(\nu, \vartheta, \varphi, T_o, T_u) = \alpha'_\nu(\nu, \vartheta, \varphi, T_o) L_{\nu,u}(\nu, T_u) dA \cos \vartheta d\Omega d\nu \quad (7.17)$$

From the energy balance for an opaque body (i.e., $\tau'_\nu(\nu, \vartheta, \varphi, T_o) = 0$), the sum of the reflected and absorbed part of the radiant power is equal to the incident radiant power to the sample surface from the surroundings which yields (see section 2.1.7):

$$\alpha'_\nu(\nu, \vartheta, \varphi, T_o) + \rho'_\nu(\nu, \vartheta, \varphi, T_o) = 1 \quad (7.18)$$

Thus, the total radiance received by an instrument measuring the radiance of a sample surface can be represented as following relation:

$$L_\nu(\nu, \vartheta, \varphi, T_o, T_u) = \frac{\varepsilon'_\nu(\nu, \vartheta, \varphi, T_o) c_1 \nu^3}{e^{(c_2\nu/T_o)} - 1} + \rho'_\nu(\nu, \vartheta, \varphi, T_o) \frac{c_1 \nu^3}{e^{(c_2\nu/T_u)} - 1} \quad (7.19)$$

where $\varepsilon'_\nu(\nu, \vartheta, \varphi, T_o)$ is the directional spectral emissivity of the sample surface at surface temperature T_o . By putting the well known Kirchoff's law of the directional spectral quantities for a surface:

$$\alpha'_\nu(\nu, \vartheta, \varphi, T_o) = \varepsilon'_\nu(\nu, \vartheta, \varphi, T_o) \quad (7.20)$$

into equation (7.18), equation (7.19) can be simplified as

$$L_\nu(\nu, \vartheta, \varphi, T_o, T_u) = \frac{\varepsilon'_\nu(\nu, \vartheta, \varphi, T_o) c_1 \nu^3}{e^{(c_2\nu/T_o)} - 1} + [1 - \varepsilon'_\nu(\nu, \vartheta, \varphi, T_o)] \frac{c_1 \nu^3}{e^{(c_2\nu/T_u)} - 1}. \quad (7.21)$$

The corrected hemispherical spectral emissivity $\varepsilon'_\nu(\nu, \vartheta, \varphi, T_o)$ of the sample surface can be obtained by solving equation (7.21):

$$\varepsilon'_\nu(\nu, \vartheta, \varphi, T_o) = \frac{\frac{L_\nu(\nu, \vartheta, \varphi, T_o, T_u)}{c_1 \nu^3} [e^{(c_2\nu/T_u)} - 1] - 1}{\frac{e^{(c_2\nu/T_u)} - 1}{e^{(c_2\nu/T_o)} - 1} - 1} \quad (7.22)$$

However, this approach for the correction of reflection of the radiance from the surroundings is not always sufficiently accurate in practice, because the assumption of a homogeneous spectral radiance of the surroundings does not necessarily hold true in the actual apparatus.

8 Measurement of Directional Spectral Emissivity

In this chapter the experimental set up with different components used for the measurement of directional spectral emissivity of technical solid surfaces is explained in detail. The fabrication procedure of the microstructured silicon surfaces used as one specific sample is also briefly presented.

8.1 Experimental Set up

For the measurement of the directional spectral emissivity of technical solid surfaces an experimental set up is introduced in this section. Different components used in the experimental installation are presented with the description of their operations. Figure 8.1a illustrates the spatial arrangement and the connection of all the components used in the present experiment, a photo of the experimental set up is presented in figure 8.1b.

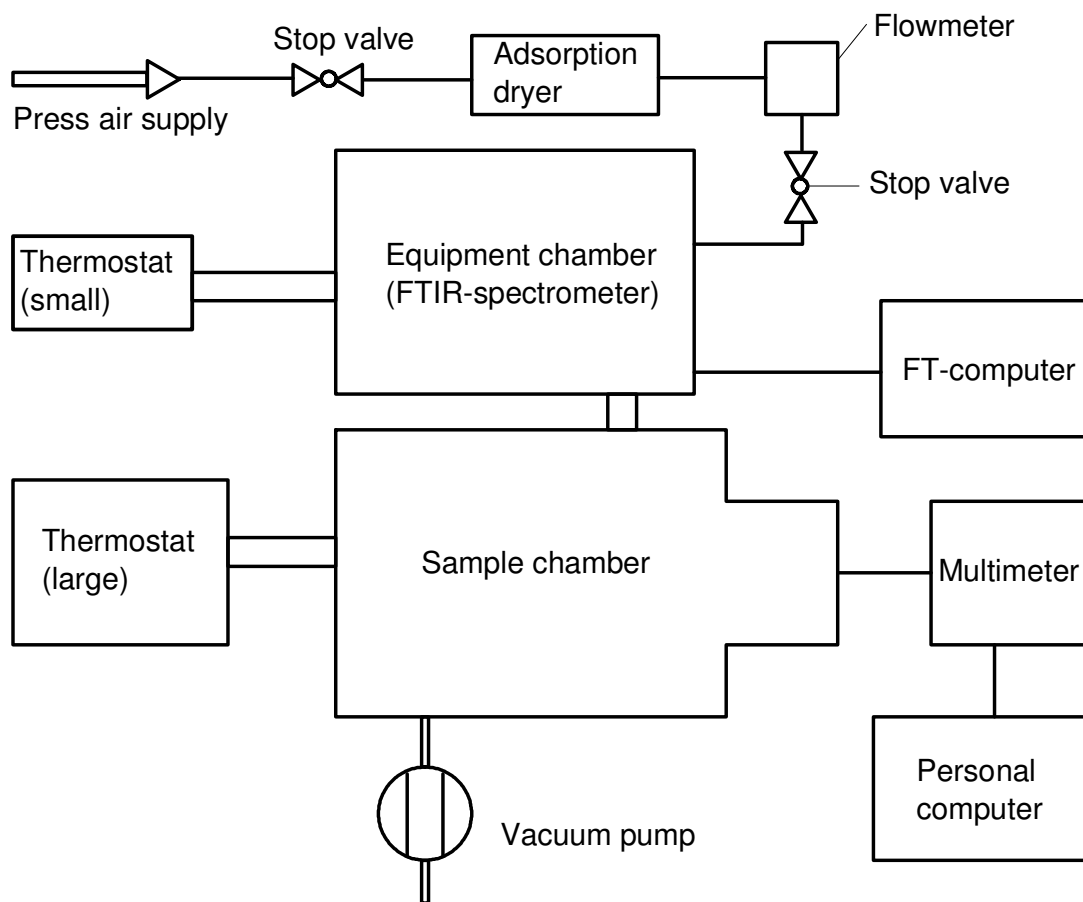


Fig.8.1a. Spatial arrangement and the connection of the components used in the present experiment.

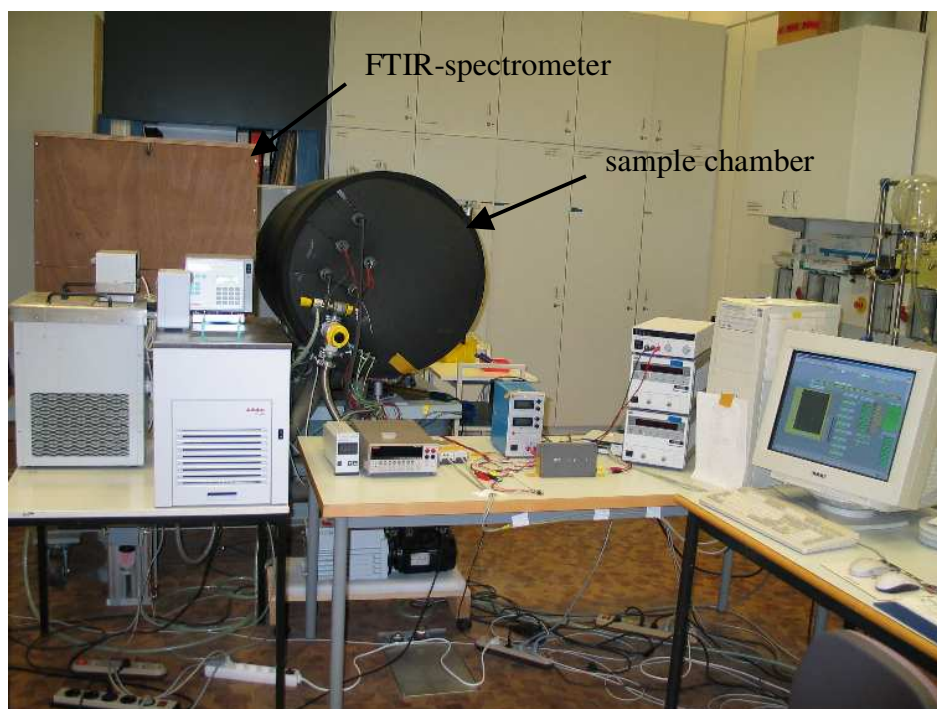


Fig. 8.1b. Photo of experimental set up.

The evacuated sample chamber encloses different components, for example, a sample holder (copper plate), a cylindrical cavity as a blackbody radiator, and a rotatable plain mirror attachment between them. The equipment chamber contains a Fourier transform infrared spectrometer type EQUINOX 55 manufactured by Bruker Optik GmbH. For an external source of radiation this equipment has an inlet window, to which the sample chamber is connected with the help of a pipe. Through this connection the radiation from the sample surface and the blackbody radiator alternatively passes to the detector of the FTIR-spectrometer instead of the radiation from the internal infrared source normally used in an FTIR-spectrometer (see figure 7.1). This FTIR-spectrometer can measure the radiation intensity in the wavelength range between 0.8 and 27 μm , although in between one has to change the different beam splitters and detectors. The sample chamber is evacuated below 3.5 Pa with the help of a vacuum pump. The sample chamber and the equipment chamber are kept at a same constant temperature of 12 $^{\circ}\text{C}$ (optimum temperature at which the deuterated triglycine sulfate “DTGS”- detector has a high sensitivity [79]) by using two different thermostats, so that no radiative heat transfer takes place between chamber walls and the detector. The spectrometer is purged with dry and carbon dioxide free air to remove the carbon dioxide and the water moisture remaining inside it. To make it free from the moisture and carbon dioxide the pressurized air from the compressor is first sent to the adsorption dryer and then to the flowmeter to control its flow rate before it enters the spectrometer. A Fourier

transform (FT)- computer is connected to the FTIR-Spectrometer for the Fourier transformation of the raw data supplied by the spectrometer. The temperature measurement of the sample surface and the blackbody radiator is carried out by the use of calibrated platinum resistance thermometers Pt-100 connected to a multimeter which is remotely controlled with the help of a program written in graphical software package “Lab View” installed on a personal computer. More details of the sample chamber with different components are given in the next section.

8.1.1 Sample Chamber in connection with FTIR-Spectrometer

The schematic representation of the sample chamber with different components in connection with the FTIR- spectrometer is shown in figure 8.2. Due to its high spectral resolution and signal to noise ratio as well as high speed of spectrum measurement, the FTIR- spectrometer is becoming a suitable tool in the field of emission spectroscopy. For this reason it is used in this work.

The inner walls of the sample chamber are painted with black lacquer (Nextel-Velvet-Coating 811-21) with the hemispherical total emissivity of 0.94, so that the radiation striking the chamber walls from the heated components is reflected in small amounts only. Other components, for example, parts of the sample holder attachment which are near to the electrical heater are made from stainless steel with low emissivity value. Their surfaces and the outer surface of the blackbody radiator are coated with polished chromium to reduce surface emissivity.

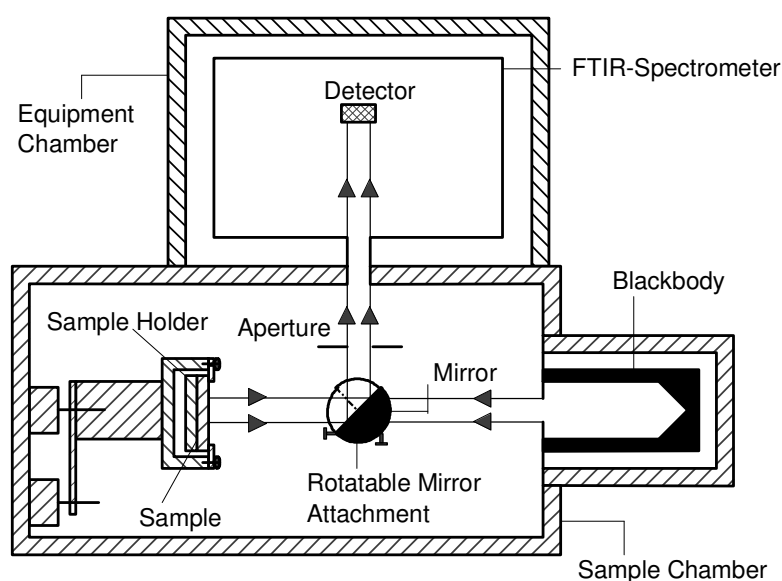


Fig. 8.2 Schematic representation of the sample chamber with different components in connection with FTIR-spectrometer.

The adjustment of the optical axes between the detector and the sources of radiation is performed in every sample change with the help of an auto-collimation telescope, so that the maximum amount of radiation from the source can reach the detector. A rotatable mirror attachment is installed in the sample chamber at equidistance from the sample surface and the opening of the reference blackbody. The rotatable mirror is used to switch between the sample radiation and the blackbody radiation as an input signal for the FTIR-spectrometer. This also guarantees the same optical path length for both sources of radiation while passing from the sources to the detector. The rotatable mirror attachment can be rotated at an angle $\pm 90^\circ$ so that the plain mirror receives and diverts the radiation from the sample surface and the blackbody radiator alternatively to the detector. An aperture is placed between the spectrometer and the mirror attachment in order to cover the same measuring area of the radiation from the sample surface as well as from the blackbody radiator to the detector.

To study the directional characteristics of the radiation of the sample surface, the sample positioning attachment has to be rotated between two axes, i.e., the polar and the azimuthal angle. This is realized with the help of the DC-bar armatured motors in combination with the line coded absolute rotation transducers. The speed of rotation of the DC motors is controlled with the help of variable DC voltage sources from the output channels of the multi function data acquisition card of National Instrument.

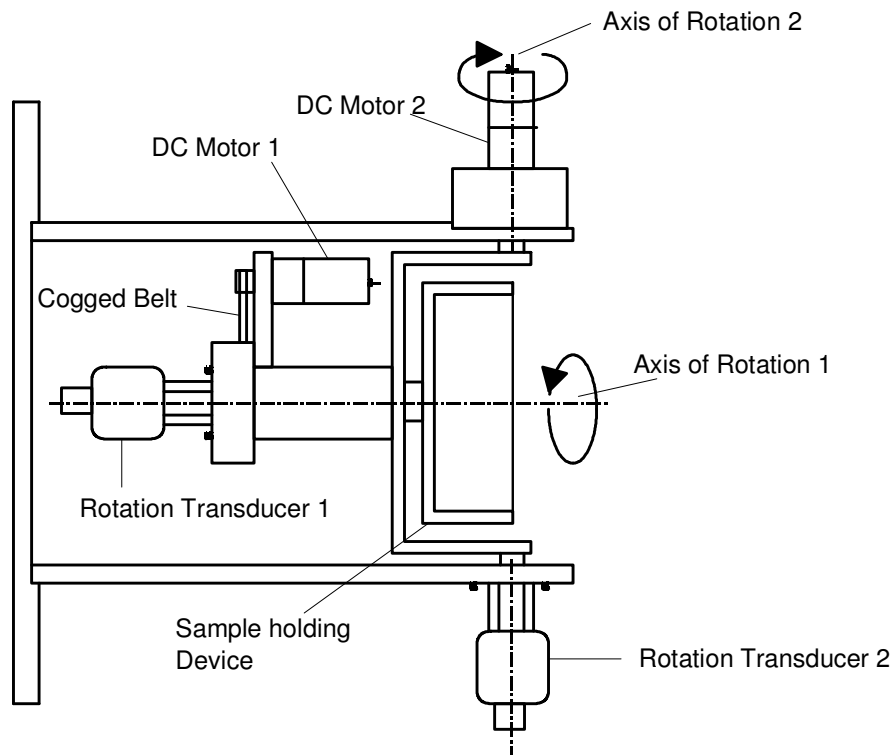


Fig. 8.3a. Layout of the sample positioning attachment

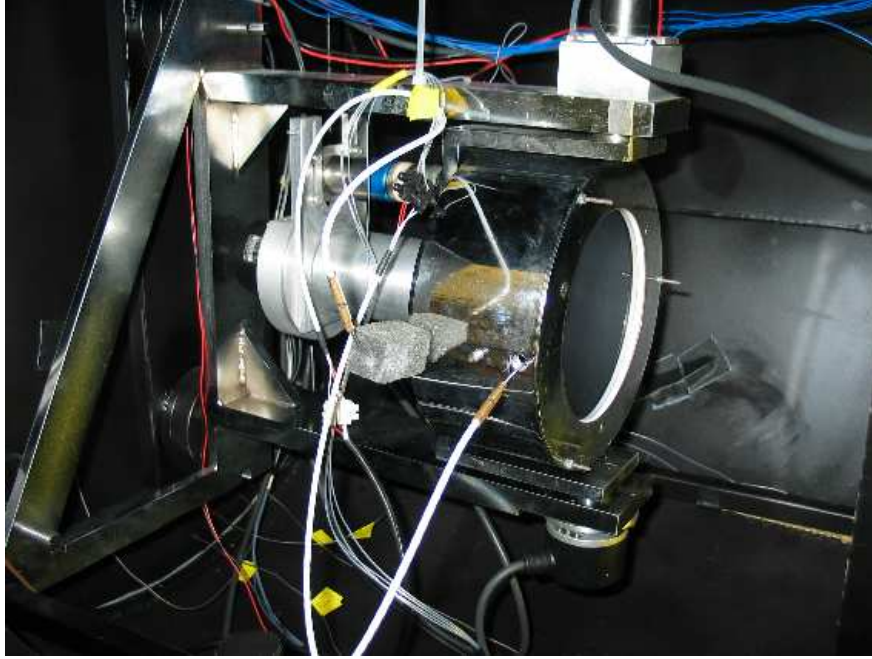


Fig. 8.3b. Photo of the sample positioning attachment.

Figure 8.3a and 8.3b show the layout and photo for the control mechanism of the rotating axes of the sample positioning attachment, respectively. The main function of the sample positioning attachment is to bring the sample to different desired polar and azimuthal angles. The DC motor 1 enables the movement of the sample holding device and thereby the sample at the axis of rotation 1 so that the sample can be rotated at a desired azimuthal angle. A cogged belt is used for the transmission of angular momentum between the motor 1 and the sample holder. The DC motor 2 drives the sample at the axis of rotation 2 through a clutch so that the sample can be moved at one fixed desired polar angle. In order to confirm the position (combination of polar and azimuthal angles) of the sample both axes of rotation 1 and 2 are connected with two rotation transducers 1 and 2, respectively. The control of the movement of the motors occurs by reading the signal pulses from the respective rotation transducer with the help of a computer program written in the graphical software package “Lab View”. The rotation transducer used in this work contains a graduation with 2048 lines on the transducer disc. That means the rotation transducer gives 2048 analog signal pulses per revolution, i.e., the resolution of the position of the sample (angle of rotation per pulse) is calculated as

$$R = \frac{360^\circ}{2048} = 0.17578^\circ = 10.55' \quad (8.1)$$

The computer program compares the actual number of analog signal pulses with the number of pulses for a particular angle of rotation set in the program, whereas the first one is the input from the rotation transducer. This actual number of analog signal pulses is counted by the use of the pulse counter of a multi function data acquisition card. When the actual value of the pulse coincides the set value, the DC voltage feeded to the DC-motor from the analog output of the data acquisition card automatically cuts off. The sample takes the position defined by the set value of the analog signal pulses.

8.1.2 Sample Heating System

For the exact determination of the directional spectral emissivity of a sample surface at one particular temperature, its value should be constant and uniform along the surface. Figure 8.4 illustrates the constructive layout and the assembly of the sample heating system used in present work for this achievement.

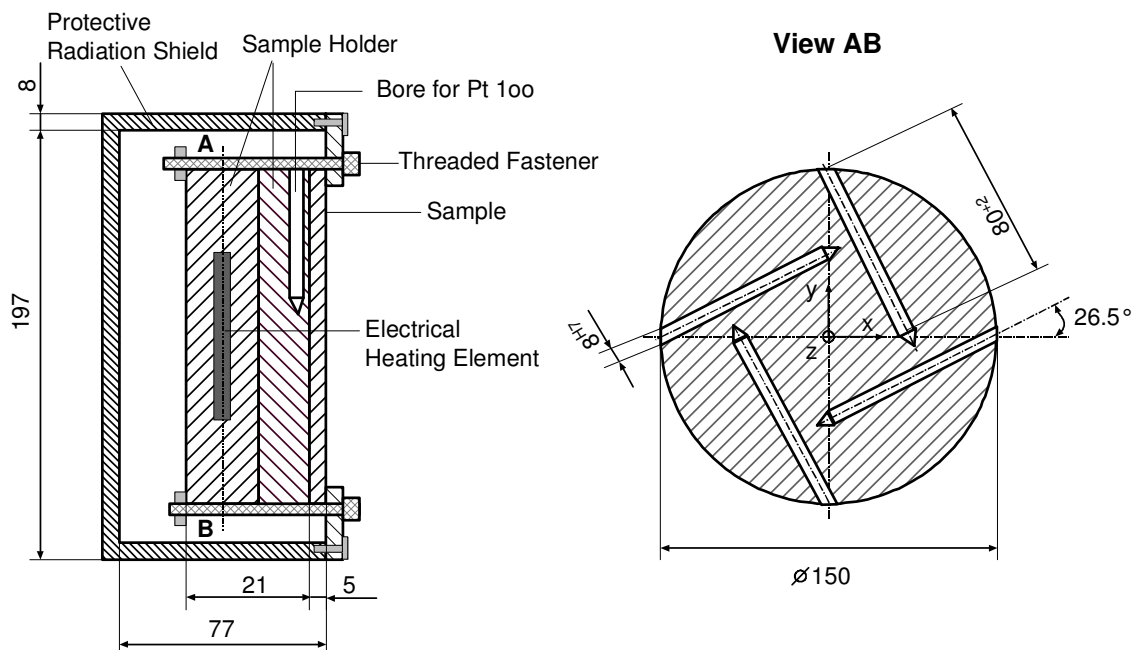


Fig. 8.4 Construction of the sample heating system with some important physical dimensions.

The sample heating system consists of three circular plates with diameter 150 mm namely one sample plate, two copper plates, the rear one with electrical heating elements, and a protective radiation shield of stainless steel. The copper plate just behind the sample acts as the sample holder. A bore is drilled in this sample holder at 1 mm below its contact surface with the sample plate for inserting the calibrated platinum resistance thermometer Pt 100. The

In order to realize a very close approximation to a blackbody, there are mainly two points that have to be considered during constructive design of such blackbody radiator in the laboratory. Firstly, one should try to get an effective emissivity of the opening of the blackbody nearly unity (as the emissivity of a theoretical blackbody) and secondly, the isothermal condition of the walls of the blackbody should be maintained. For this purpose a cavity is manufactured from a copper cylinder which is a very good conductor of heat. V-shaped grooves with a profile angle 60° are cut in the inner walls of the copper cylinder in order to increase the effective emissivity. In addition, a black lacquer (Trader name: Nextel-Velvet-Coating 811-21) with the total emissivity value $\mathcal{E} = 0.94$ is coated on these V-shaped grooves. According to Psarouthakis [123] the effective emissivity, ε_{eff} of the surfaces with V-shaped grooves in the isothermal condition can be determined from following relation

$$\frac{1}{\varepsilon_{eff}} = 1 + \left(\frac{1}{\mathcal{E}} - 1 \right) \sin \frac{\Theta}{2} \quad (8.2)$$

where \mathcal{E} is the total emissivity of the black lacquer and Θ is the profile angle of the V-shaped grooves. Substituting the emissivity value of the black lacquer and the profile angle of the grooves in equation (8.2), the effective emissivity of the internal surface of the blackbody cavity can be increased to $\varepsilon_{eff} = 0.969$.

Bauer [8] has proposed another constructive method of further increasing the total emissivity of the opening of a blackbody cavity. With a sufficiently small opening to the cavity only a very little of the original incident beam entering the cavity will be able to leave it. The condition of complete absorption of the entering beam is fulfilled to a high degree if the radius of the opening of the blackbody cavity is much smaller than the length of the cavity and its end-surface is taper (conical in shape). According to Bauer the emissivity of the opening of such a blackbody cavity ε_{bc} can be calculated by using the expression

$$\varepsilon_{bc} = 1 - \frac{1 - \varepsilon_{eff}}{1 + \left(\frac{l}{r} \right)^2} \quad (8.3)$$

where ε_{eff} is the effective emissivity of the internal surface of the cavity, l is the length of the cavity and r is the radius of the opening of the cavity. Putting their values $\varepsilon_{eff} = 0.969$, $l = 120$

mm and $r = 22.5$ mm in equation (8.3) for the blackbody cavity used in the present work, the total emissivity of its opening can be obtained as $\varepsilon_{bc} = 0.9989$.

The blackbody cavity is uniformly heated with the help of a high power electrical heating coil. Spiral grooves for placing the electrical heating coil are cut in equal distances to obtain uniform heating over all the surface. Thus, the electrical heating coil wraps the cavity in spiral form and covers the back- and circumferential surfaces of the cavity. This blackbody cavity is inserted into another hollow copper cylinder to protect it from the radiation of the surroundings. In order to reduce the heat loss due to the radiation, the cylinder surfaces are coated with chromium and polished to reduce the value of total emissivity. The temperature of the cavity is measured with the help of two calibrated platinum resistance thermometers Pt 100 placed in two parallel holes as shown in figure 8.6. These holes are drilled in two sides of the copper cylinder (blackbody radiator) so that one can observe the uniformity of the temperature distribution along the two different surfaces. The difference of the temperatures measured by two calibrated Pt 100 thermometers at these two places is $\Delta T < 0.1$ K.

8.2 Fabrication of Microstructured Silicon Surfaces

The microstructured silicon surfaces used in this work have been manufactured by the Fraunhofer Institut für Siliziumtechnologie (ISIT). The monocrystalline undoped silicon wafers with crystal orientation (100) are employed in the experiments. The index numbers in the bracket (hkl) are called the *Miller indices* in crystallography. They are multiples of the reciprocal intercepts of a plane with the x , y and z coordinate axes and are used to specify the orientations of planes for a crystal structure. The crystal orientation (100) means that this particular plane parallels the y and z axes while intersecting the x axis at lattice parameter a of a unit cell as shown in figure 8.7.

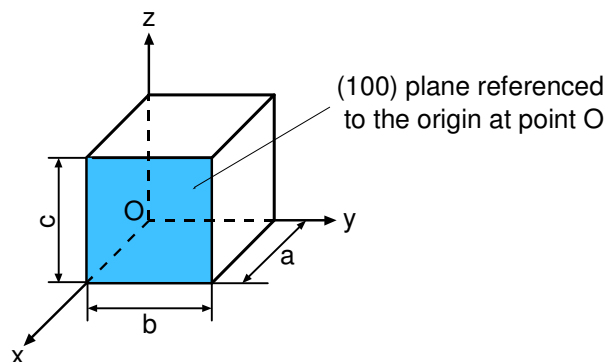


Fig. 8.7. A unit cell with x , y , and z coordinate axes, showing axial lengths a , b , and c as lattice parameters and plane (100) referenced to the origin at point O .

The silicon wafers are circular in shape with a diameter of 150 mm and are 0.6 mm thick. One side of the wafer is polished and the other side is flat with clean and smooth condition. The microgrooves of different depths are etched into the polished side. The depth of the microgrooves are controlled by the etch time. Silicon is chosen as the sample because it is well known that highly crystallographically preferential etching can be performed with the help of a number of simple chemical etchers.

The photos of rectangular microstructured silicon surfaces taken with the help of a scanning electron microscope (REM: Rasterelektronenmikroskop) as supplied by ISIT are shown in figure 8.8. These photos show the top view and the side view of the rectangular microstructured surfaces with a set of microgrooves. In the top view the grey area is the unetched flat part of the silicon wafer and the black area is the base of the groove. The rectangular shaped microgrooves are clearly seen in the side view. The parallel sides of the grooves are (100) planes.

The dimensions of the microgrooves exhibit a systematic error. According to the manufacturer the etch depths possess an accuracy of $\pm 2\%$. The flank angle of the etched structures is better than 88° . The smoothness of the grooves with respect to the wafer diameter is $\pm 5\%$. The sidewall variation is 70-80 nm. The lithography used in the manufacturing process is Süss MA 150. The dry etching processes consist of (i) SiO₂ Hardmask - Lam 590 RIE System, CF₄ (ii) Silicon Trench – Alcatel ICP System, SF₆/C₄F₈ Process and (iii) Photo resistance discharge – Matrix, O₂ Plasma [71].

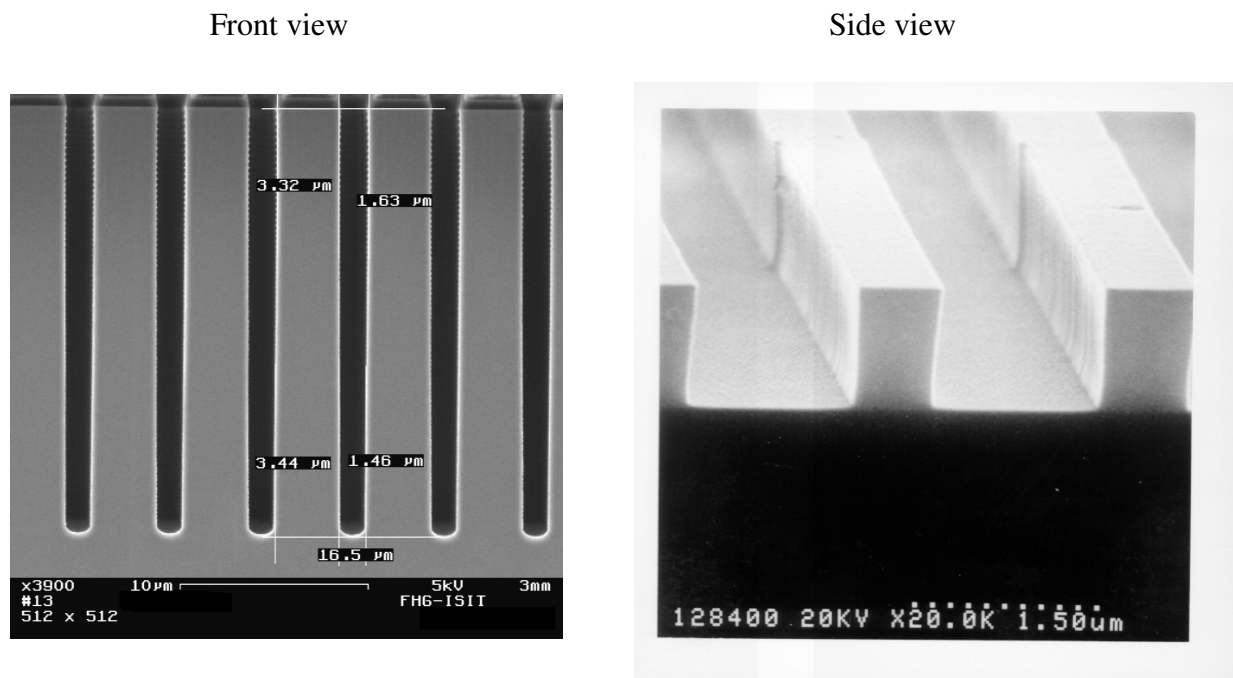


Fig. 8.8. Photo of rectangular microstructured silicon surfaces taken with the help of a scanning electron microscope (REM: Rasterelektronenmikroskop) as supplied by ISIT.

The desired period (Λ) and the width (W) of all the microgrooves are the same and have the values 10 μm and 6.5 μm respectively. The depths (H) of the microgrooves are different for each microstructured silicon wafer. A period is the sum of a groove width and the width of an unetched flat part (bridge) lying near the groove. The silicon wafers are numbered according to the desired dimensions of the microgrooves as follows:

1. Period (Λ) = 10 μm , width (W) = 6.5 μm , Depth (H) = 1 μm
2. Period (Λ) = 10 μm , width (W) = 6.5 μm , Depth (H) = 3 μm
3. Period (Λ) = 10 μm , width (W) = 6.5 μm , Depth (H) = 10 μm
4. Period (Λ) = 10 μm , width (W) = 6.5 μm , Depth (H) = 22 μm
9. Period (Λ) = 10 μm , width (W) = 6.5 μm , Depth (H) = 34 μm

Table 8.1. Actual dimensions of the etched microstructures of the silicon wafers with five different etch depths.

Wafer no.	Depth center(μm)	Depth edge(μm)	Groove width center (μm)	Groove width edge (μm)	Bridge width center (μm)	Bridge width edge (μm)
1	1.0	1.0	6.25	6.3	3.75	3.7
2	3.4	3.3	6.25	6.3	3.75	3.7
3	11.2	11.0	6.25	6.3	3.75	3.7
4	21.4	21.0	6.3	6.4	3.7	3.6
9	34.2	33.7	6.7	6.5	3.3	3.5

The actual dimensions of the etched microstructures of the silicon wafers are determined by the use of white light interferometer. The measuring accuracy of this method is better than ± 50 nm. The actual dimensions of the etched microgrooves measured are given in the table 8.1 [71].

9 Results and Discussion

In this chapter results of the directional spectral emissivity measured with the help of the experimental set up described in chapter eight are presented and discussed. Before starting the measurement of the directional spectral emissivity of periodic microstructured silicon surfaces, the emissivity measuring equipment is first of all calibrated and the results are validated with those of samples whose directional spectral emissivities are well known in literature. Of course, a reference emissivity standard would be a right choice for the validation of the results, but to the best of our knowledge, there are no such emissivity standards available for the validation. We found only reflectance standards, which were not useful for this work. In addition to the blackbody described earlier, the samples used for the validation are: Nextel-Velvet-Coating 811-21, borosilicate glass B 270, sand blasted aluminium and smooth undoped silicon whose directional spectral emissivities have been investigated earlier by several research groups. The calibration parameters or instruments functions $R(\nu)$ and $G(\nu)$ calculated in section 7.1.2 are determined experimentally for each discrete wavenumber.

9.1 Calibration Parameters

As mentioned in section 7.1.2, the instrument functions $R(\nu)$ and $G(\nu)$ are used as calibration parameters to obtain the measured spectra in radiance units, which were originally in instrument dependent arbitrary units. Moreover, these instrument functions consider emitted and absorbed parts of the radiative energy by the inner parts of the spectrometer and the influence of the optical path environments (i.e., moisture and carbon dioxide etc.) on the radiation. To determine these instrument functions for each discrete wavenumber, the blackbody radiator positioned in the sample chamber is used. For this purpose the blackbody cavity is heated to any two different temperatures, such as 100 °C and 200 °C, and the intensity spectra of the blackbody are measured at these temperatures separately. The theoretical spectral radiances of the blackbody radiator at these two temperatures are calculated by using Planck's law (equation 7.7). From these theoretical values of spectral radiance of the blackbody at different wavenumbers and from the intensity spectra measured at the same temperatures and the wavenumbers, the calibrating parameters or instruments functions for each discrete wavenumber can be obtained as described in section 7.1.2. These instrument functions, also called spectral response $R(\nu)$ and instrument radiance $G(\nu)$, are presented in figures 9.1 and 9.2, respectively.

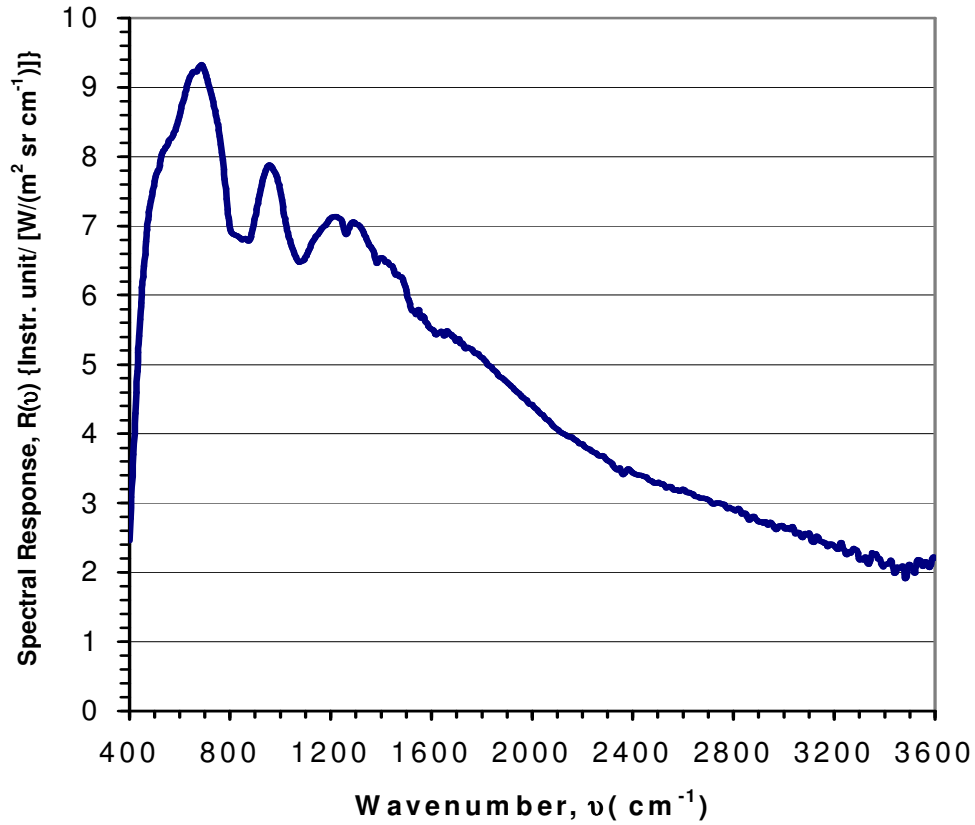


Figure 9.1 Spectral response $R(\nu)$ obtained from theoretical spectral radiances and measured spectra of a blackbody radiator at temperatures 100°C and 200°C .

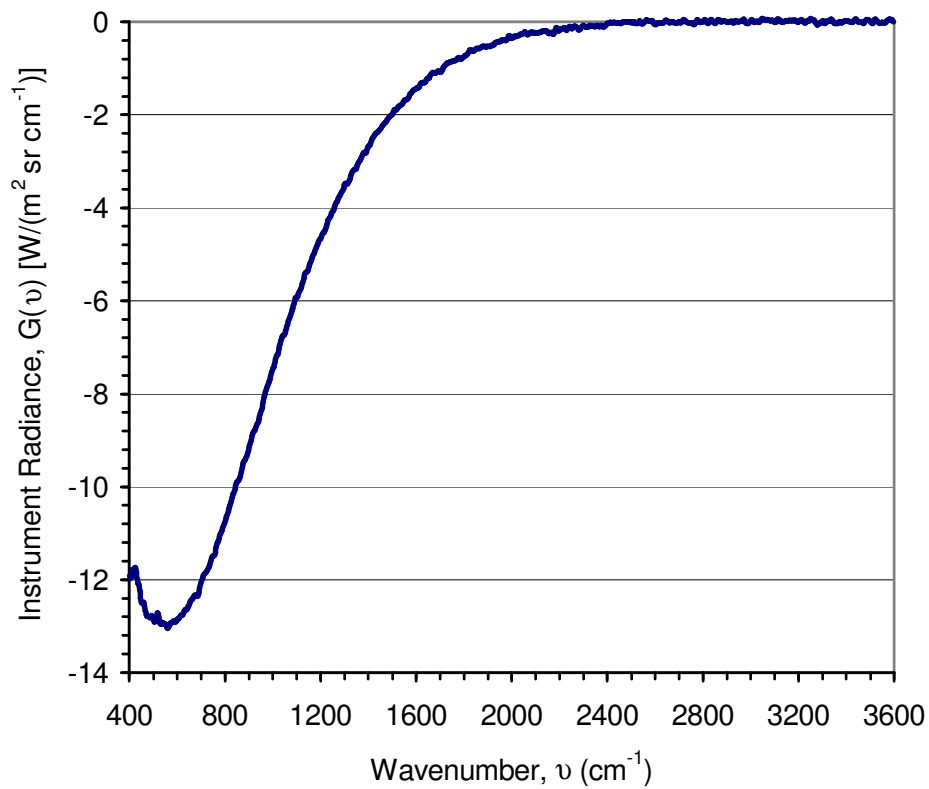


Figure 9.2. Instrument radiance $G(\nu)$ obtained from theoretical spectral radiances and measured spectra of a blackbody radiator at temperatures 100°C and 200°C .

The influence of the path that the radiation must pass through from the calibration source (blackbody radiator) to the detector and the radiation from the inner parts of the spectrometer can be observed in figures 9.1 and 9.2. In particular, the strong absorptions of the radiative energy by the beam splitter (KBr) in the spectral regions 830 cm^{-1} and 1180 cm^{-1} lead to a drastic decrease in sensitivity (see figure 9.1). Since the calibration is performed with a blackbody radiator placed in a vacuum chamber and the spectrometer is purged by dry and CO_2 filtered press air, which is then free of carbon dioxide and moisture, the absorptions due to CO_2 and H_2O are not observed in the above figures.

9.2 Spectral Emissivity of Blackbody Cavity

It is well known that the spectral emissivity of an ideal blackbody is unity, which is independent of the wavelength of the radiation. But in practice, it is very difficult to realize such an ideal blackbody. In this work a cylindrical cavity is used as the technical realization of the blackbody radiator whose theoretical total emissivity is 0.9989 (see chapter 8). Before determining the spectral emissivity of the blackbody cavity, the spectrum from the blackbody cavity is calibrated with the help of calibration parameters $R(\nu)$ and $G(\nu)$ (see section 9.1).

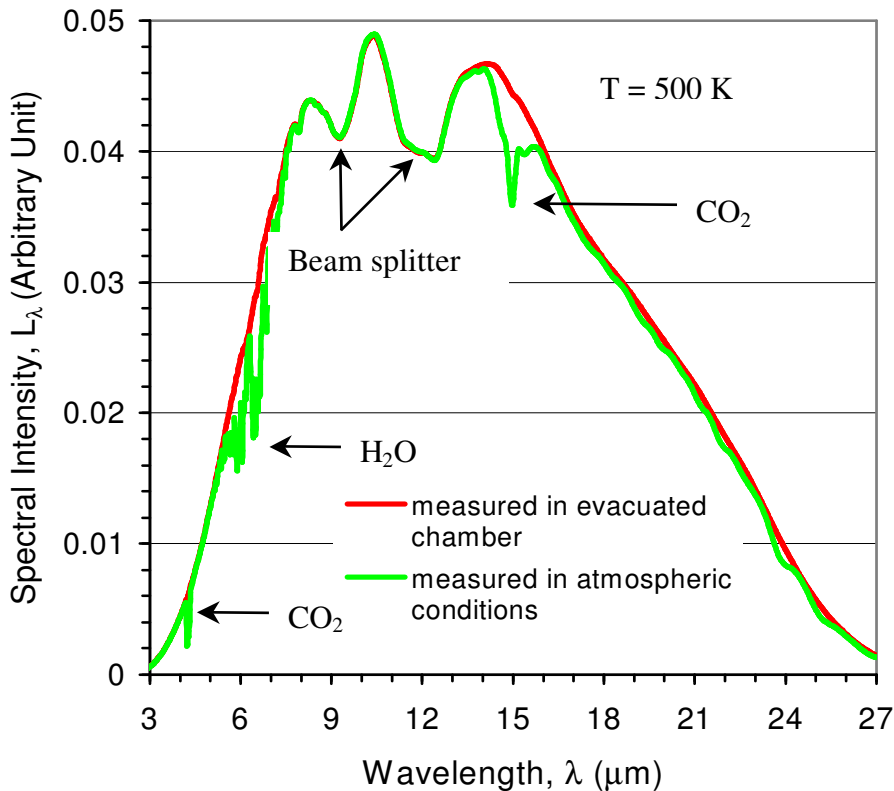


Fig. 9.3. Spectral intensity distribution (in arbitrary unit) of the blackbody cavity at temperature 500 K measured in evacuated sample chamber and in atmospheric conditions.

In figure 9.3 the spectral intensity (spectral radiance) of the blackbody cavity at a temperature of 500 K measured in the evacuated sample chamber and under atmospheric conditions is presented. In this figure, the spectrum measured in the evacuated sample chamber with the purged spectrometer containing only dry air is free of absorption bands due to moisture and carbon dioxide, but exhibits the strong absorptions by the beam splitter inside the spectrometer. On the other hand, the spectrum measured under atmospheric conditions shows the strong absorption bands of the carbon dioxide (at wavelengths, $\lambda = 4.25 \mu\text{m}$ and $15.0 \mu\text{m}$) and water (at $\lambda = 6.25 \mu\text{m}$) also, even though the optical path through the gas is only 1.5 m.

The strong absorptions in the spectral regions $8.47 \mu\text{m}$ and $12.05 \mu\text{m}$ by the beam splitter (KBr) cannot be removed by experimental attempts. But these absorptions can of course be eliminated by the use of calibration parameters as shown in figures 9.1 and 9.2. The mathematical procedure for this is already described in chapter 7. In figure 9.4, the measured and calibrated spectral radiance of the blackbody cavity is compared with the theoretical spectral radiance of the blackbody radiator (i.e., $\epsilon = 0.9989$) calculated with the help of Planck's law of radiation. These two curves show the good coincidence of the theoretical and measured values of the spectral radiance of the blackbody radiator. After the calibration of the measured spectrum of the blackbody cavity its intensity spectrum is in the unit of spectral radiance and free of all the absorptions.

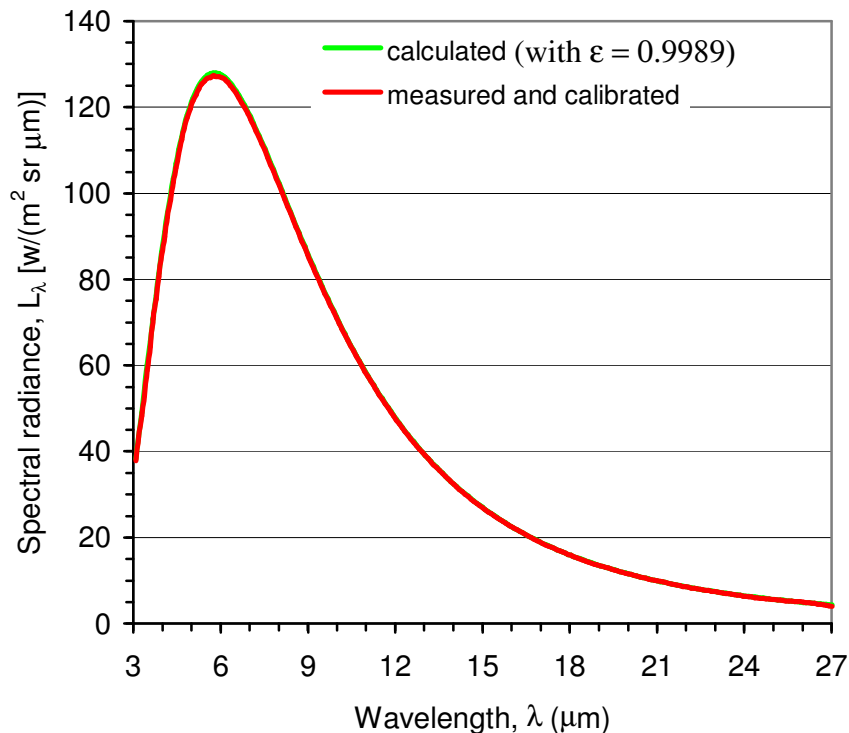


Fig. 9.4. Measured spectral radiance of the blackbody cavity after calibration and the calculated spectral radiance of the theoretical blackbody at temperature 500 K.

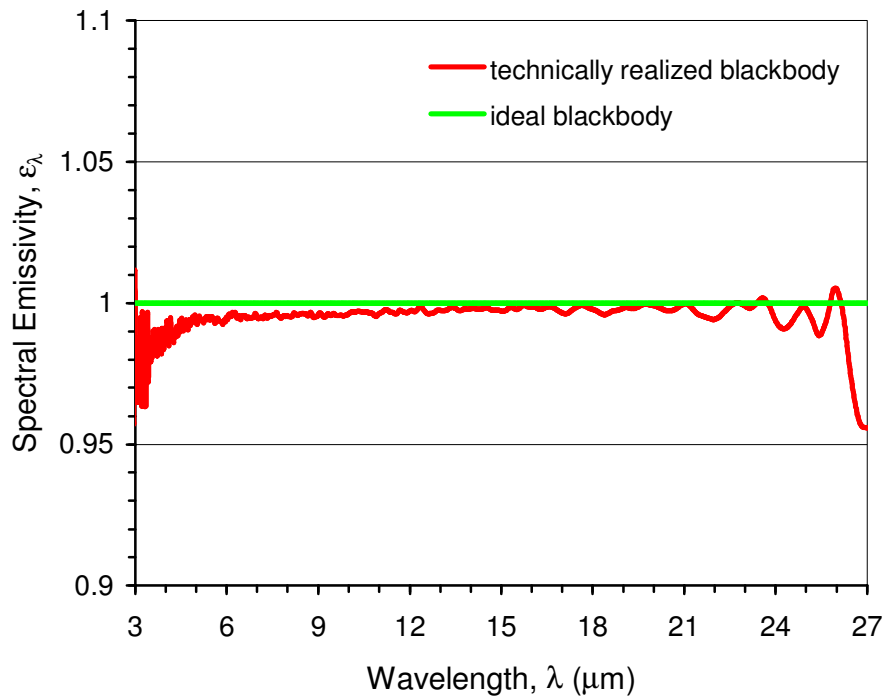


Fig. 9.5. Spectral emissivity of the technically realized blackbody cavity measured at 500 K and that of an ideal blackbody.

The measured spectral emissivity of the blackbody cavity used in this work is presented in the figure 9.5. In this figure the emissivity curve of an ideal blackbody, which is unity and constant in the whole spectral range, is also drawn for comparison. The measured spectral emissivity of the technically realized blackbody is nearly constant with respect to the wavelength of the radiation and approaches to the emissivity curve of an ideal blackbody. The relative deviation of the spectral emissivity in most of the spectral range is less than 1% from the ideal value. This deviation is high in the spectral range below 4 μm and above 25 μm due to the present noises with high amplitude in the spectrum.

9.3 Validation of Results of Emissivity Measurement

In this section, results of the measurement of directional spectral emissivities of some sample surfaces are presented for the purpose of validation. The sample surfaces are chosen in regard to the availability of their emissivity values in literature. The advantage would be to have emissivity values as many as possible, depending on the material types and the surface conditions.

9.3.1 Nextel-Velvet-Coating 811-21

In order to validate the directional spectral emissivity results obtained in this work, the spectral emissivity of black paint with the trading name *Nextel-Velvet-Coating 811-21* applied on an aluminium plate is measured at different emission angles from 0° to 70° . The selected black paint has been provided by MANKIEWICZ GEBR. & CO. and its physical properties are well characterized. Because its directional spectral emissivity values at different temperatures have already been investigated experimentally by different authors [68, 78, 90] in detail, it is taken as a reference material for validation of the results of the emissivity measurement.

In the present work, a smooth surface of aluminium plate with a diameter of 150 mm and a thickness of 5 mm is coated with Nextel-Velvet-Coating 811-21 with the help of a spraying pistol so that the thickness of the coating can be achieved almost uniform over the surface. The average thickness of the coating is 0.15 mm. The backside of the plate is polished and a thin layer of heat conducting grease is applied between this aluminium plate and the sample holder plate of copper to insure good heat conduction between them. The directional spectral emissivity of Nextel-Velvet-Coating 811-21 is measured at three different temperatures: 92.5°C , 123.5°C and 148°C . The values of the directional spectral emissivity are presented in appendix A (table A.1).

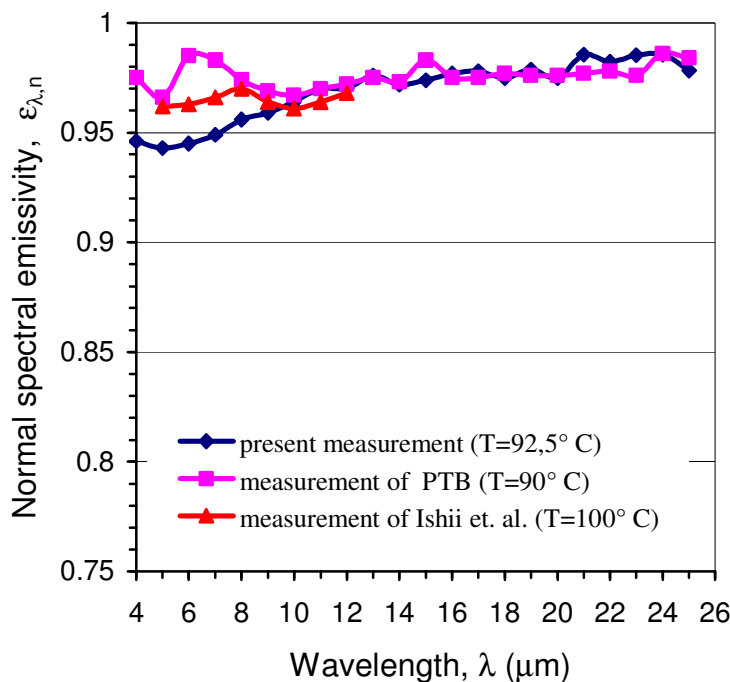


Fig. 9.6. Normal spectral emissivity of Nextel-Velvet-Coating 811-21 measured normal to radiating surface.

Figure 9.6 presents the normal spectral emissivity of the Nextel-Velvet-Coating 811-21 measured at temperature 92.5 °C in the present experiment along with the data of measurements by other authors [68, 90]. It is clear from this graph that the normal spectral emissivity is almost constant at wavelengths between 8 μm and 25 μm and its value increases slightly with the wavelengths between 4 μm and 8 μm . This trend of dependence of the normal spectral emissivity with the wavelength of the radiation agrees with both the results reported by PTB (Physikalisch-Technische Bundesanstalt) [90] and Ishii et al. [68] in the wavelength range 8 μm to 25 μm , but the present results are closer to the results of Ishii et al. than that of PTB in the wavelength range 4 μm to 8 μm .

The directional total emissivity $\varepsilon'(\vartheta, T)$ at different emission angles can be calculated from the measured directional spectral emissivity $\varepsilon'_\lambda(\lambda, \vartheta, T)$ at respective angles by integration using the simple relation given in section 5.2.2 (equation 5.10). The calculated values of directional total emissivity from the measured directional spectral emissivities at different temperatures are given in appendix A (table A.4).

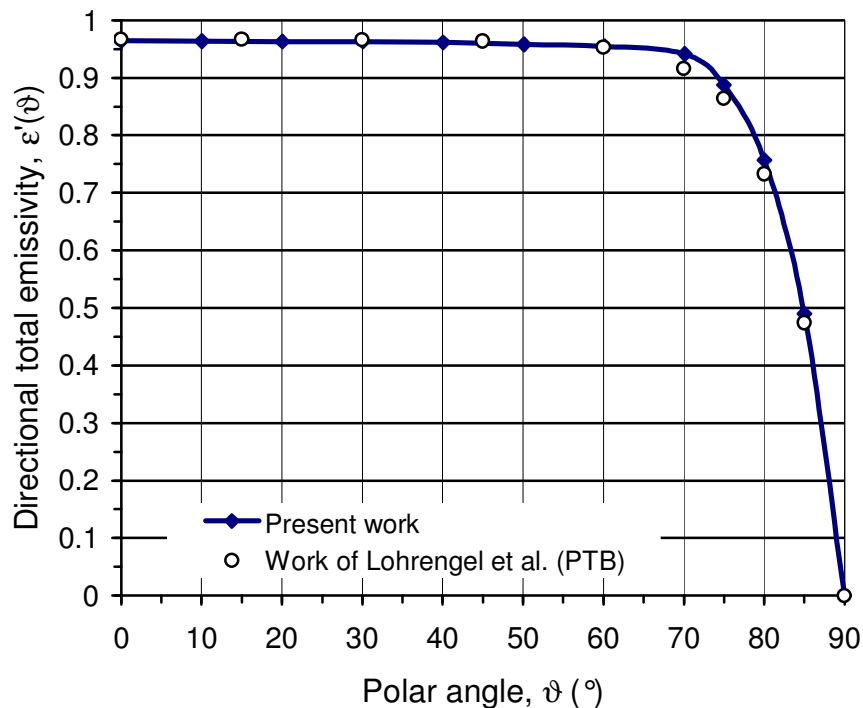


Fig. 9.7. Directional total emissivity of Nextel-Velvet-Coating 811-21 measured at different emission angles.

Figure 9.7 graphically shows the directional total emissivity of the Nextel-Velvet-Coating 811-21 at different emission angles measured in the present experiment and the same quantity measured by Lohrengel et al. [90]. The solid curve is the result of the present study at

temperature 92.5 °C and the values denoted by the circles are reported in reference [90] for temperature 90 °C. A comparison between these two curves yields that the results obtained from two different instruments are in good agreement with each other over all the angles of emission. Similarly, good coincidence is found for the normal total emissivity of Nextel-Velvet-Coating 811-21 measured at an angle normal to the radiating surface in this work and that measured by Lohrengel et al. [90] and Kwor et al. [78] as represented in figure 9.8.

By making the assumption that the emissivity of the Nextel-Velvet-Coating 811-21 is independent of the azimuthal angle, the hemispherical total emissivity can be obtained from the directional total emissivity by integration over all emission angles (polar angles) using equation (2.13). Good results for the directional total emissivity and therefore, for the hemispherical total emissivity will be achieved if directional spectral emissivity values are measured at as many different angles as possible between 0° and 90°. Because of geometrical constraints, the directional spectral emissivity can be measured at angles up to 70° by the use of the present experimental set up. The values of the directional spectral emissivity at angles between 70° and 90° are obtained by the use of an extrapolation principle, i.e., a suitable polynomial curve is fitted to the measured values.

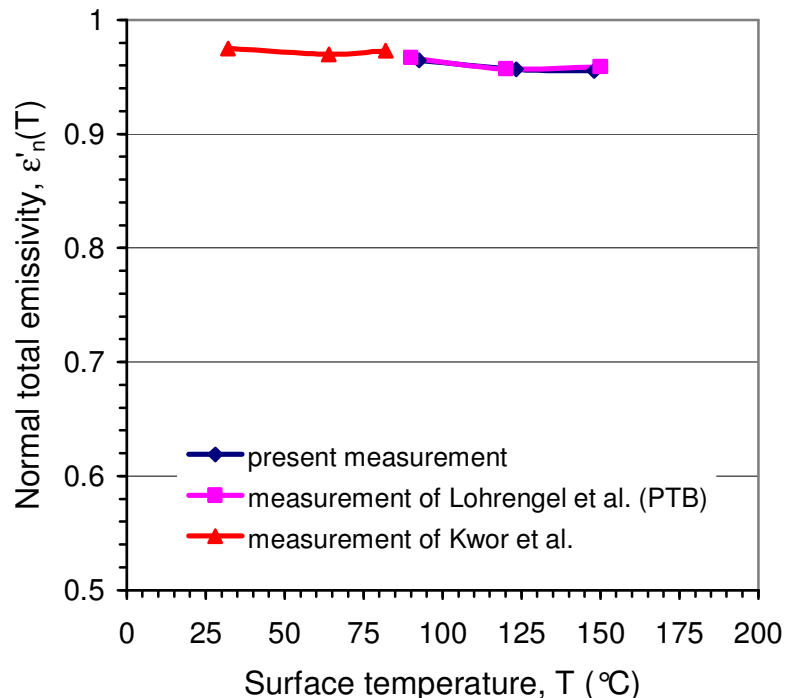


Fig. 9.8. Normal total emissivity of Nextel-Velvet-Coating 811-21 at different surface temperatures calculated in present work and that obtained by Lohrengel et al. [90] and by Kwor et al. [78].

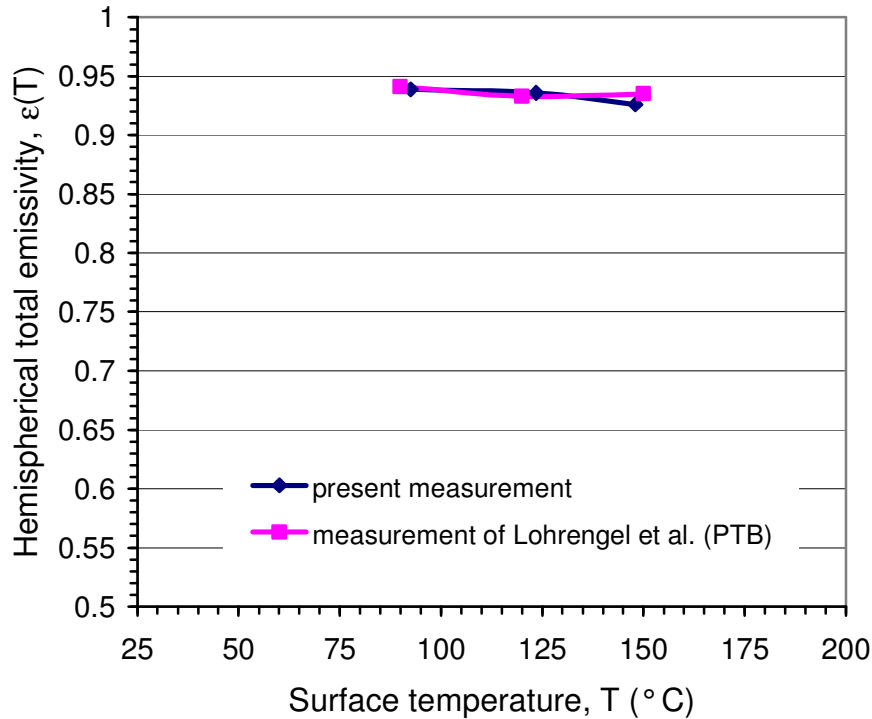


Fig. 9.9. Hemispherical total emissivity of Nextel-Velvet-Coating 811-21 at different surface temperatures calculated in present work and that obtained by Lohrengel et al. [90].

The hemispherical total emissivities of Nextel-Velvet-Coating 811-21 at different surface temperatures are calculated from the values of directional total emissivities. The hemispherical total emissivities are tabulated in appendix A (table A.5) and are graphically presented in figure 9.9 with the values obtained by Lohrengel et al. [90]. As shown in this figure, the values of the hemispherical total emissivity of the Nextel-Velvet Coating 811-21 at different temperatures obtained in the present work almost agree with that measured by Lohrengel et al. [90]. The hemispherical total emissivity of the investigated surface is more or less consistent in the temperature range at which the measurements are performed.

9.3.2 Borosilicate Glass B 270

For the validation of the directional spectral emissivity results obtained in this work, the spectral emissivity of a borosilicate glass with the trading name *B 270 Superwite* is measured at different polar angles from 0° to 70° . The selected borosilicate glass has been manufactured by SCHOTT DESAG AG, Deutsche Spezialglas and its physical properties are well characterized.

Table 9.1. Chemical composition of the borosilicate glass used in the present experiment and that used in [151].

Chemical composition in %	SiO ₂	B ₂ O ₃	Na ₂ O	K ₂ O	Al ₂ O ₃	BaO	CaO	Sb ₂ O ₃	MgO
Glass used in Touloukian [151]	74.7	9.6	6.9		5.7	2.2	0.9	-	-
Glass used in present work	71.1	-	7.5	8.4	-	1.6	10.7	0.5	0.2

The directional spectral emissivity of the borosilicate glass B 270 with the thickness of 5 mm is measured at the surface temperature 98.8 °C. The temperature distribution on the glass surface is numerically calculated by the use of finite element method (FEM). The result of the FEM simulation is already presented in figure 6.3. This figure confirms the uniformity of the temperature distribution on the glass surface, although the thermal conductivity of glass is very poor ($\lambda = 1.01$ W/mK). The non-transparency of the glass with the thickness of 5 mm is confirmed by measuring two spectra of its surface radiation. Firstly, the spectrum of the glass surface is measured without painting its rear surface. Secondly, the spectrum is measured after painting its rear surface with the black lacquer (Nextel-Velvet-Coating 811-21). Figure 9.10 shows both spectra measured in the same thermal conditions have almost the same spectral

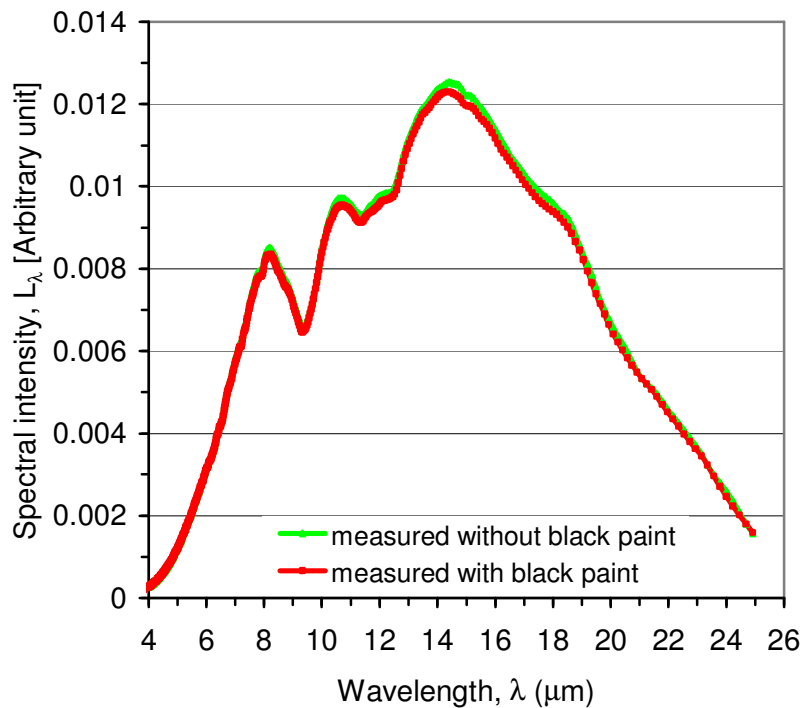


Fig. 9.10. Two different spectra of glass B 270 surface with and without black paint on its rear surface measured at the temperature 102.7 °C of the sample holder.

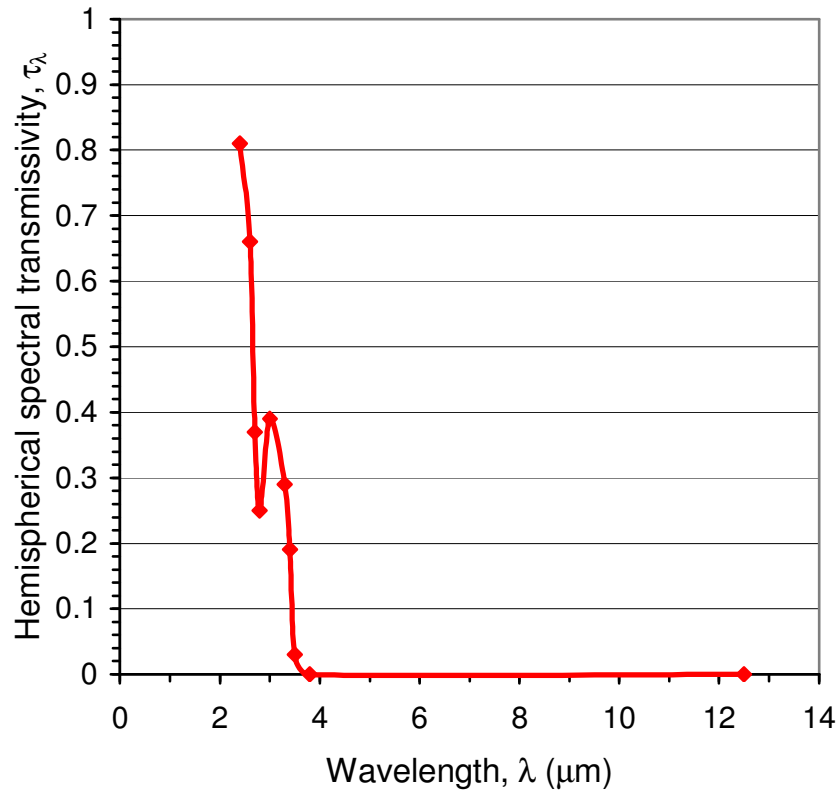


Fig. 9.11. Hemispherical spectral transmissivity of borosilicate glass at the surface temperature 537.85 °C as reported by Touloukian [151].

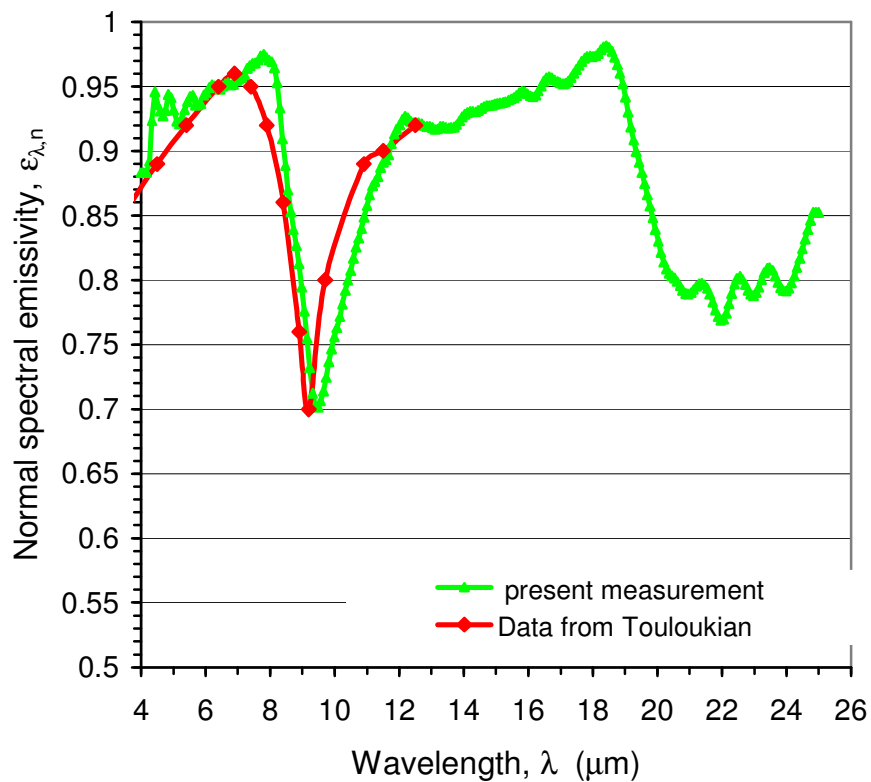


Fig. 9.12. Normal spectral emissivity of the borosilicate glass measured in the present work and the values for the surface temperature 537.85 °C given by Touloukian [151].

intensity. The spectral intensity of the glass surface with black paint on the backside is expected higher than that without painting if the glass sample would have been transparent, but a reverse effect is observed at some spectral range. The reason is the decrease of the glass surface temperature due to the presence of the poor conducting black paint between the sample and the sample holder. This confirms the non-transparency of the glass used in the present experiment. For the additional confirmation of non-transparency, the hemispherical spectral transmissivity of the borosilicate glass with thickness 3.17 mm is presented in figure 9.11 as reported by Touloukian [151]. This diagram shows the hemispherical spectral transmissivity of the borosilicate glass is zero in the spectral regions $\lambda = 3.8 \mu\text{m}$ onwards.

The normal spectral emissivity of the borosilicate glass measured in this work is presented in figure 9.12 together with the values given in Touloukian [151]. The two curves have same trend, but the peak position of an absorption band near $\lambda = 9 \mu\text{m}$ is not exactly at the same wavelength. This might be because of a small difference in the chemical composition of the borosilicate glass used in the present experiment to that used in [151] as given in table 9.1.

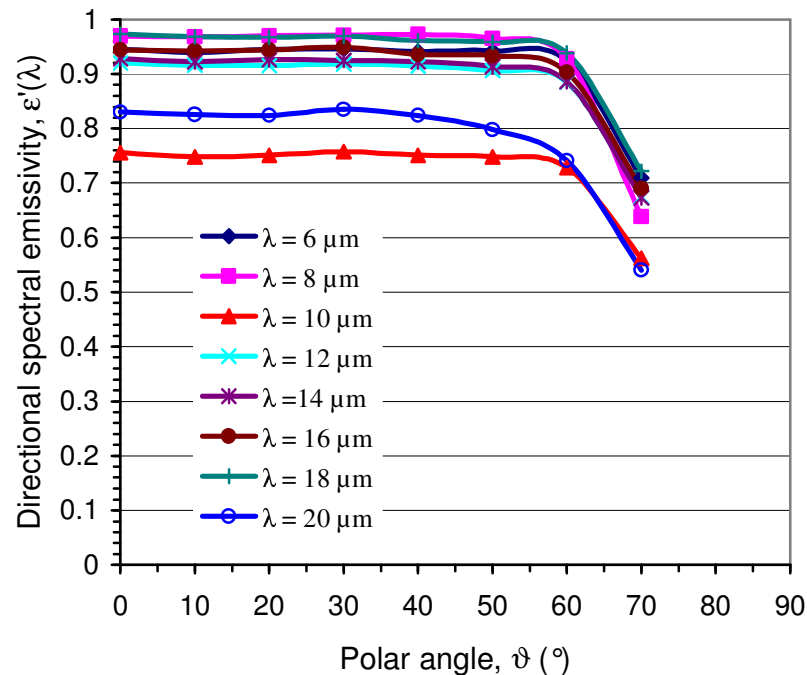


Fig. 9.13. Directional spectral emissivity of the borosilicate glass B 270 measured at the temperature 98.8 °C.

The directional spectral emissivity of the borosilicate glass B 270 measured at the surface temperature 98.8 °C for different emission angles is presented in figure 9.13. The directional total emissivity at different emission angles can be calculated from the measured directional spectral emissivity at the respective angles by integration using equation (5.10). A

comparison of the directional total emissivity of borosilicate glass at different emission angles measured in the present experiment at the temperature 98.8 °C and the same quantity measured by Lohrengel and Tingwaldt [88] at the temperature 85 °C is presented in Figure 9.14. This comparison of directional total emissivity measured in the present work with the measured values given in reference [88] and with the calculated values by using Fresnel's equation tells that the results obtained from three different methods are in good agreement with each other over all the angles of emission. The optical constants used for this calculation are taken from reference [86]. Although the borosilicate glass used by Lohrengel and Tingwaldt [88] is glass B 260, it is the same as glass B 270 because the name has been replaced according to the manufacturer SCHOTT DESAG AG, Deutsche Spezialglas.

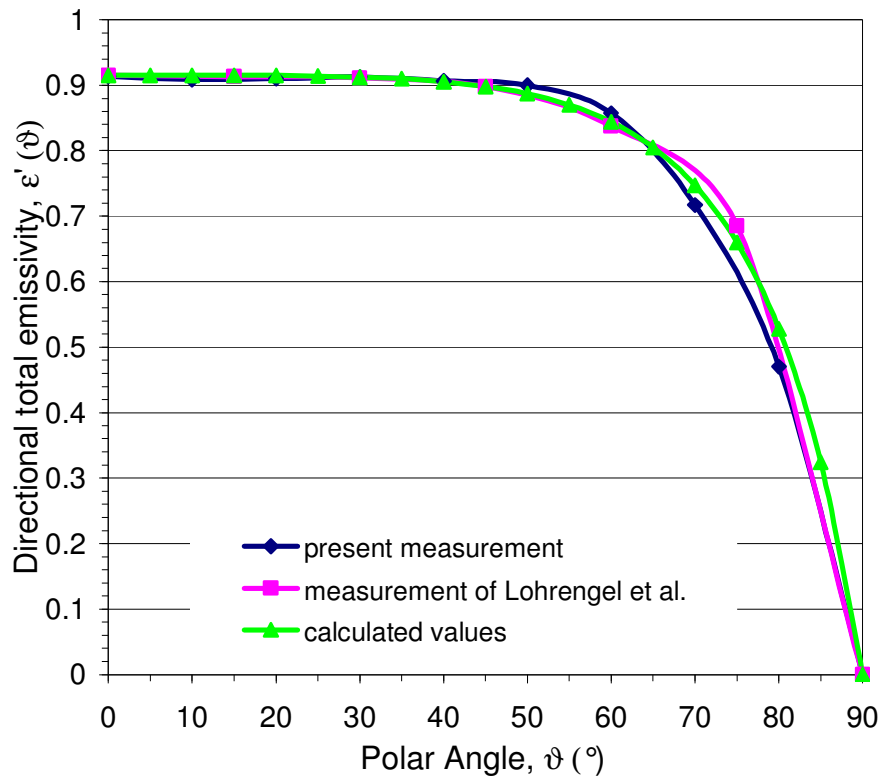


Fig. 9.14. Directional total emissivity of the borosilicate glass B 270 measured in present work and that measured by Lohrengel et al. [88]. The calculated values of the directional total emissivity by using the Fresnel's equation [86] are also presented.

The hemispherical total emissivity can be determined from the directional total emissivity values by integration over all emission angles (polar angles) using equation (2.13). The value of hemispherical total emissivity so obtained in the present work is $\varepsilon = 0.843$ whereas that reported in reference [88] is $\varepsilon = 0.858$. The hemispherical total emissivity

calculated by using the values of directional total emissivity obtained from Fresnel's equation is $\varepsilon = 0.85$. These three values are very close to each other.

9.3.3 Sand Blasted Aluminium

A further sample used for the validation of the emissivity results obtained in this work is sand blasted high-purity (99.99%) aluminium, usually termed 1199 alloy. The polished front surface of the 5 mm thick aluminium plate is sand blasted by the corundum of corn size 0.5 mm - 0.8 mm and the back surface is lapped. The contact surface between the sample and the sample holder is smeared with heat conducting grease in order to achieve good heat conduction between them.

The directional spectral emissivity of the sand blasted aluminium measured at the surface temperature 374 K is presented in figure 9.15 as function of the emission angles between 0° and 70° with the wavelength of radiation as parameter. The directional spectral emissivity increases slightly with the increase in polar angle up to 60° and then decreases. This behaviour conforms more or less to that of electrically good conducting metals, whose directional spectral emissivity, according to the electromagnetic theory, depends on the polar angle ϑ and the optical constants n and k of the material (see equations (2.46)-(2.50)). The directional spectral emissivity increases with the increase in the polar angle and it takes a maximum value at polar angles larger than 80° . As the optical constants n and k depend on the wavelength of radiation λ (see equations (2.32) and (2.33)), this also applies to the directional spectral emissivity. At large wavelengths, the directional spectral emissivity of metals decreases with increasing wavelength λ [6, 15]. This is also seen in the present measurement (see fig. 9.16).

For the comparison of the directional spectral emissivity values measured in this work with the values available in reference [151], the directional spectral emissivity at the emission angle 25° is represented in figure 9.16. It is clear from this graph that the values of emissivity measured in this work at the surface temperature 374 K are in good agreement with those values given by Touloukian [151] for the surface temperature 306 K.

The directional total emissivity is calculated from the measured directional spectral emissivity at different emission angles by using equation (2.9). The directional total emissivity values of the sand blasted aluminium plate at different emission angles calculated in present work at temperature 374 K are presented in appendix A (table A.9).

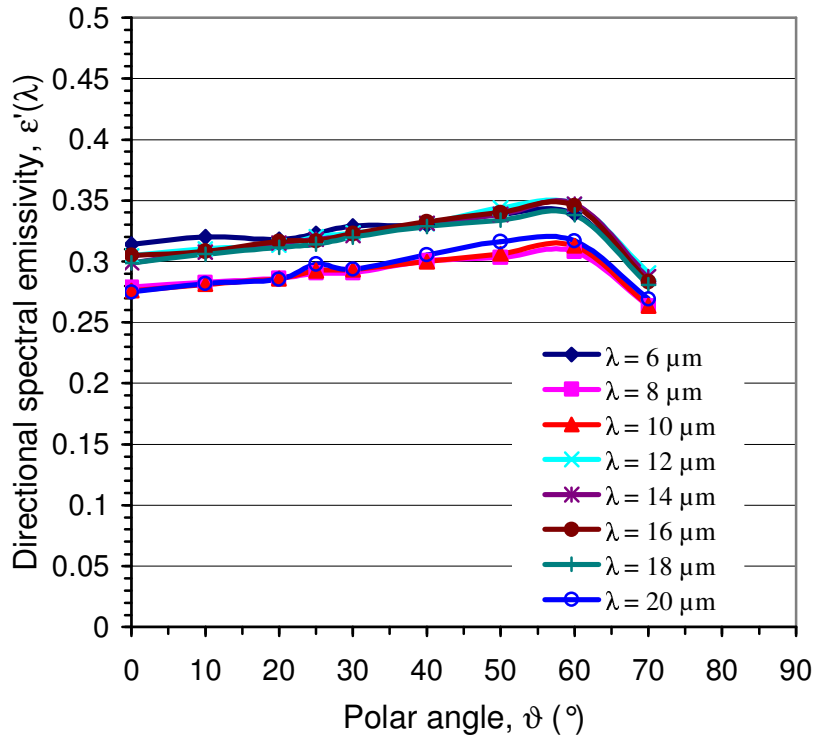


Fig. 9.15. Directional spectral emissivity of the sand blasted aluminium measured at surface temperature 374 K.

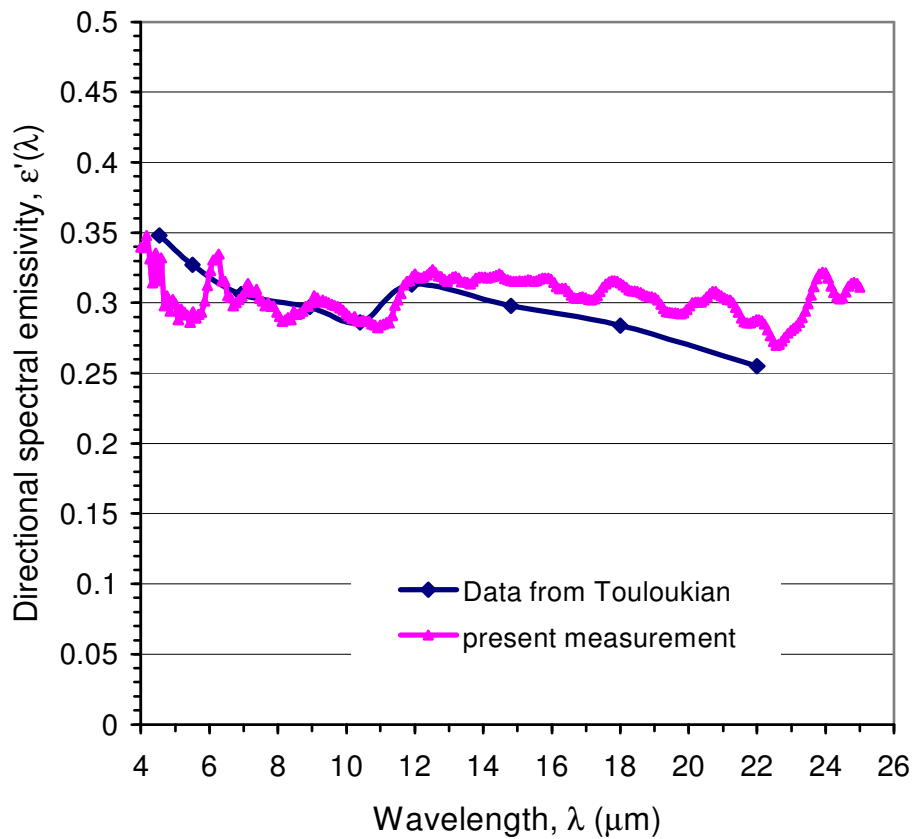


Fig. 9.16. Directional spectral emissivity of sand blasted aluminium measured at a radiating angle of 25° .

The hemispherical total emissivity is determined from the directional total emissivity values through integration over all emission angles from 0° to 90° by using equation (2.13). As the measurement of the directional spectral emissivity is possible at the emission angles between 0° and 70° in this work, the values of the directional total emissivity at emission angle between 70° and 90° are determined by the use of an extrapolation method. The value of the hemispherical total emissivity for the sand blasted aluminium plate obtained by integration using equation (5.10) according to the radiometric method is $\varepsilon = 0.29$ at the surface temperature 374 K. The same quantity obtained by the use of the energy balance method is $\varepsilon = 0.27$. These values of emissivity determined by two independent methods are close to each other.

9.3.4 Smooth Undoped Silicon

The directional spectral emissivity of a monocrystalline undoped silicon wafer with a diameter of 150 mm and a thickness of 0.6 mm is measured to validate the results of emissivity measurements obtained in this work and to compare the results between smooth and microstructured silicon surfaces. The orientation of the silicon crystal is (100) as described in section 8.2 and the wafer surface is polished. The temperature distribution of the sample surface is calculated by the use of FEM method as explained in section 6.3.

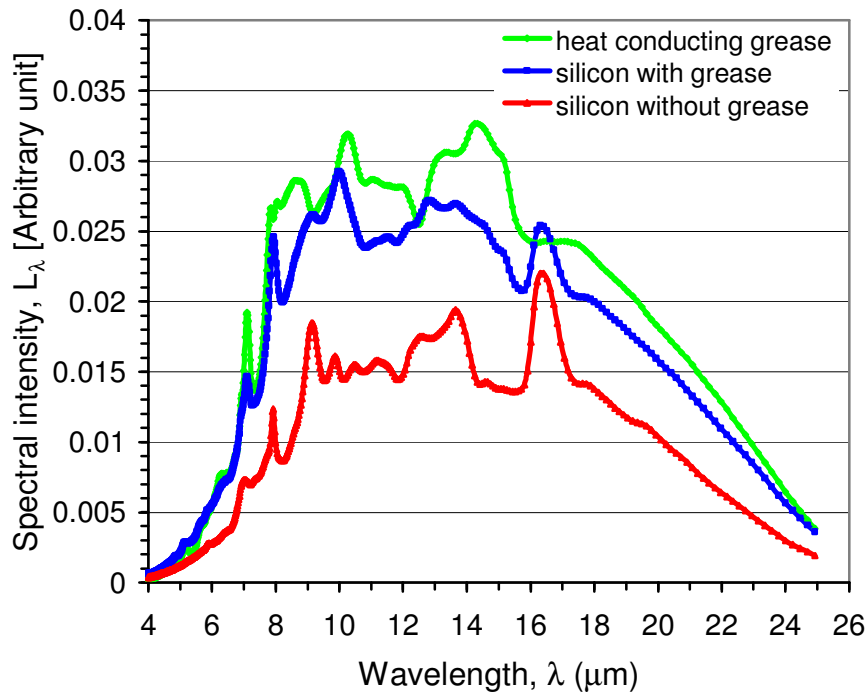


Fig. 9.17. Spectra of the silicon wafer measured with and without the heat conducting grease on its backside at temperature 199.1 °C. A spectrum of the heat conducting grease is also presented at temperature 175.6 °C of the sample holder.

The transparency of the sample with respect to radiation is confirmed by taking two spectra with and without heat conducting grease on its rear surface. These spectra are presented in figure 9.17 together with a spectrum of the heat conducting grease layer, which is smeared on the sample holder plate. Although its temperature (175.6 °C) is lower than that of silicon wafer (199.1 °C), the spectrum of the heat conducting grease exhibits higher spectral intensity than the silicon surface. As observed in the figure 9.17, the spectral intensity of the radiation from the silicon surface with heat conducting grease on its backside is much higher than that of the silicon surface without grease. This fact indicates that the silicon wafer with a thickness of 0.6 mm is transparent within the measured range of wavelengths of the radiation. The same argument can be concluded from the figure 9.18 where normal spectral transmissivity of silicon wafer is seen not to be zero at all the spectral range from 1.21 μm to 12 μm as reported by Touloukian [151]. Therefore, the use of heat conducting grease on the contact surface between sample and sample holder is avoided and the sample is in direct contact to the sample holder made of copper.

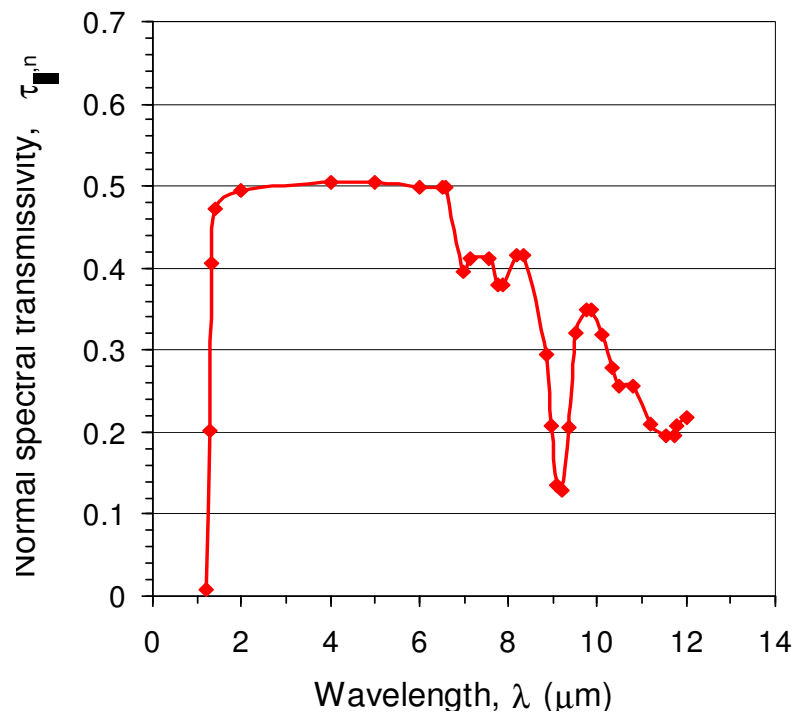


Fig. 9.18. Normal spectral transmissivity of silicon wafer at the surface temperature 200 °C as reported by Touloukian [151].

Since the hemispherical total emissivity of a polished copper surface at a surface temperature of 500 K is very low, $\varepsilon = 0.031$ [132], the error of the emissivity measurement

due to the transparency of the sample is taken to be negligible. The normal spectral emissivity of the polished copper surface as a function of the wavelength of radiation is also presented in figure 9.19 [151]. From this figure it can be inferred that the normal spectral emissivity of the polished copper at the wavelengths $\lambda = 5 \mu\text{m}$ onwards is constant having the value $\epsilon = 0.02$.

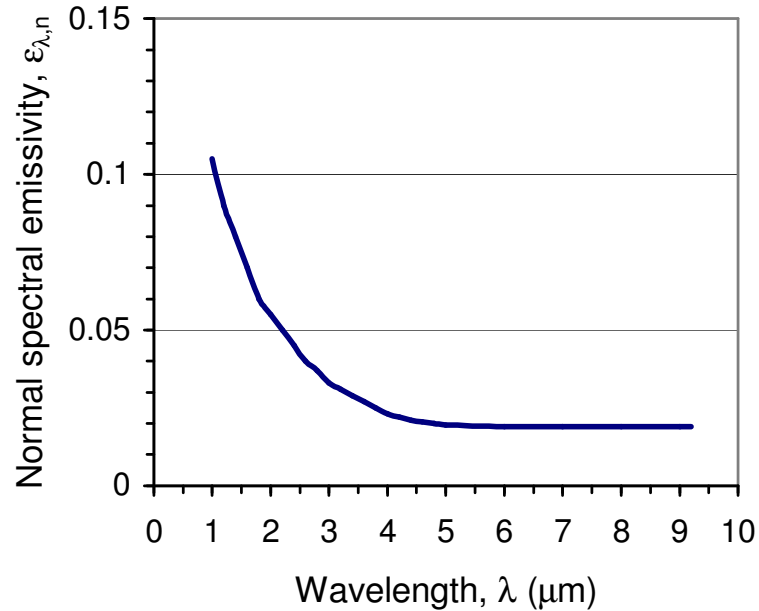


Fig. 9.19. Normal spectral emissivity of polished copper at the surface temperature 294.26 K as reported by Touloukian [151].

The normal spectral emissivity of the silicon wafer is measured at the temperature 199.1 °C and compared with the results of other authors [134, 144] as shown in figure 9.20. The values of the normal spectral emissivity obtained in this work are in close agreement with those values measured by Stierwalt et al. [144] at the temperature 200 °C and by Sato [134] at the temperature 269.85 °C.

The directional spectral emissivities of the undoped silicon wafer measured at different polar angles between 0° and 70° are presented in figure 9.21. The directional total emissivity is calculated from the measured directional spectral emissivity at different emission angles by using equation (5.10). The directional total emissivity values of the undoped silicon wafer at different emission angles calculated in present work at the temperature 199.1 °C are tabulated in appendix A (table A.12).

The hemispherical total emissivity is determined from the directional total emissivity values through integration over all emission angles from 0° to 90° by using equation (2.13). As the measurement of the directional spectral emissivity is possible only for the emission angles between 0° and 70°, the values of the directional total emissivity at emission angle

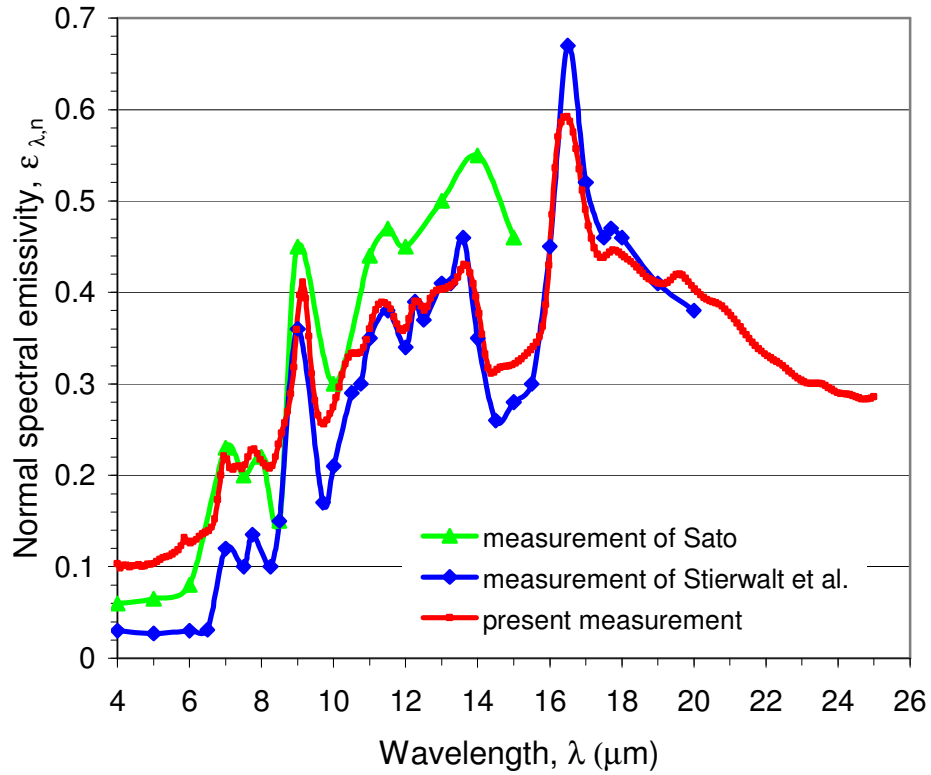


Fig. 9.20. Normal spectral emissivity of the monocrystalline undoped silicon wafer measured at an angle normal to the radiating surface.

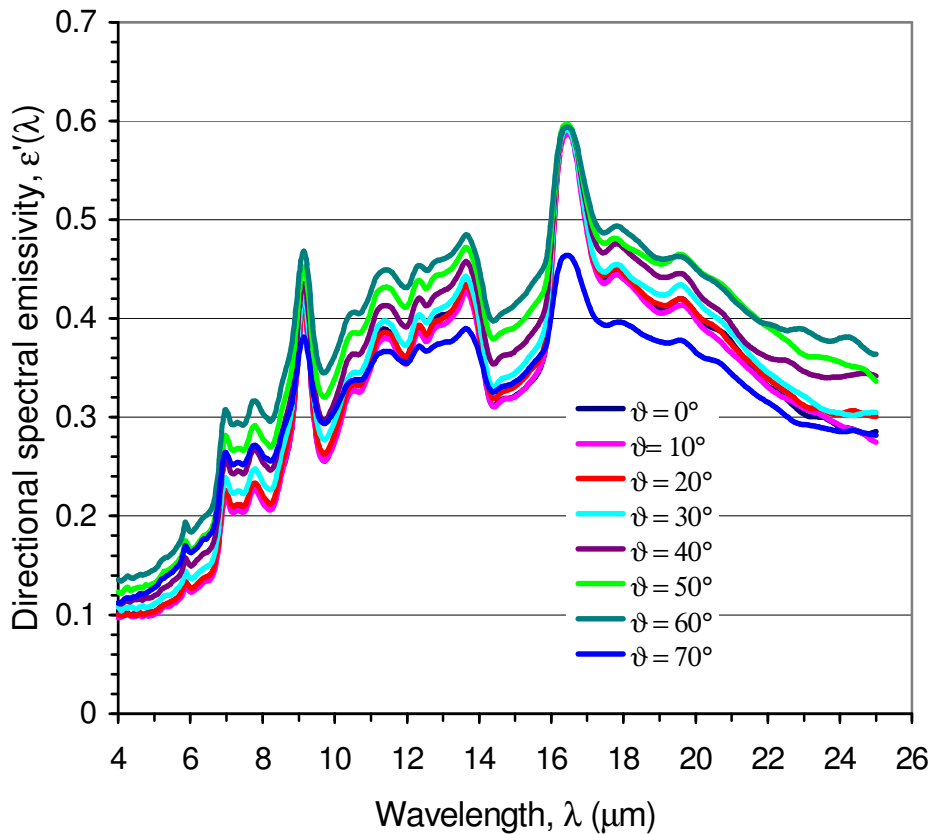


Fig. 9.21. Directional spectral emissivity of the undoped silicon wafer measured at temperature 199.1 °C.

between 70° and 90° are found by the use of the extrapolation method. In this method a suitable polynomial curve is fitted to the measured values of the directional total emissivity. A polynomial function of order six is suited for the extrapolation. The value of hemispherical total emissivity obtained for the undoped silicon wafer in the present work is $\varepsilon = 0.27$ by the radiometric method and $\varepsilon = 0.32$ by the energy balance method at the surface temperature 199.1°C .

9.4 Periodic Microstructured Silicon Surfaces

As described earlier, for sake of simplicity the radiative energy transfer in engineering science is often described with the help of hemispherical and over the total range of wavelengths integrated quantities of radiative properties of a surface. But for the detailed description of radiative energy transfer spectral and directional radiative surface properties are required. Therefore, the measurement of the directional spectral quantities of surface properties such as emissivity of technical solid surfaces is very essential. In foregoing section the measurements of the directional spectral emissivities of undoped silicon wafer and some other materials with smooth or normal surface conditions have been treated.

In this section measurements on periodic microstructured silicon surfaces are dealt with. Recent developments in the field of micromachining have made it possible to manufacture periodic microstructures with the size of light wavelengths (micrometer). At such surfaces interference effects are expected to arise due to electromagnetic radiant interactions. The resonance between the electromagnetic field and periodic microstructures offers one of the most promising ways to vary optical properties artificially. In order to study these effects the directional spectral emissivities of periodic microstructured undoped silicon surfaces are measured and presented in this section.

The directional spectral emissivity data presented in this section refer to periodic microstructured undoped silicon surfaces with the fixed repeat distance or period (Λ) $10\ \mu\text{m}$ and the groove width (W) $6.5\ \mu\text{m}$. The depth (H) of the groove is varied to five different values: $1\ \mu\text{m}$, $3.4\ \mu\text{m}$, $11.2\ \mu\text{m}$, $21.4\ \mu\text{m}$ and $34.2\ \mu\text{m}$. The measurements are performed for the different polar angles $\vartheta = 0^\circ$ to 70° in steps of 6° and for two azimuthal angles $\varphi = 0^\circ$ and 90° for all the microgrooves. Additionally, two measurements on the microgrooves with depth $H = 21.4\ \mu\text{m}$ are performed at the azimuthal angles $\varphi = 30^\circ$ and 60° in order to analyse the azimuthal angle dependence of the directional spectral emissivity of the microgrooves. The measurements are done at a surface temperature of 200°C .

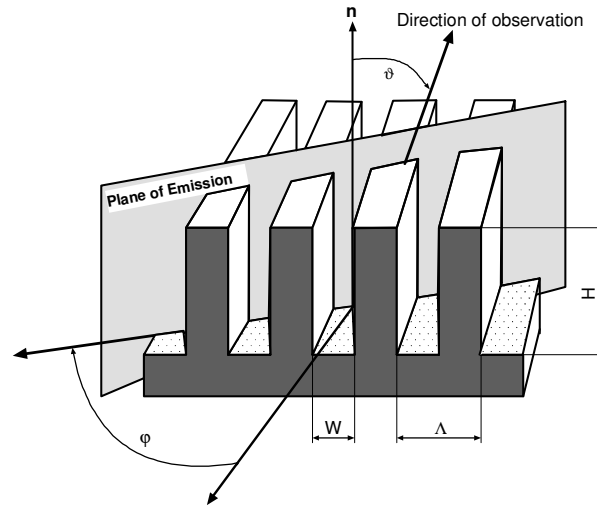


Fig. 9.22. Schematic drawing of the microgrooves showing different physical parameters.

A schematic drawing of the microgrooves showing the repeat distance or period (Λ), groove width (W), groove depth (H), polar angle (ϑ), azimuthal angle (φ), and direction of observation is given in figure 9.22. The measurements of the directional spectral emissivities of the smooth silicon surface and of the microstructured silicon surfaces will enable a better comparative study of the emission properties of these two different surface conditions of the same material.

9.4.1 Normal Spectral Emissivity

The directional spectral emissivity measured at the polar angle $\vartheta = 0^\circ$ is also known as the normal spectral emissivity. For the microstructured surfaces the normal spectral emissivity data are presented for five different depths of the grooves for both azimuthal angles $\varphi = 0^\circ$ and 90° . The rotation of the sample about two azimuthal angles has two effects: one is to exchange the direction of the grooves (horizontal to vertical and vice versa) and the other is to observe adjacent areas of the sample for analysing the interference effects.

The normal spectral emissivity measured for the deep microgrooves with depth $H = 21.4 \mu\text{m}$ on an undoped silicon surface at both azimuthal angles $\varphi = 0^\circ$ and 90° is presented in figure 9.23. The curves show that the emissivity data for whole spectral range measured at these two azimuthal angles coincide with each other. This indicates a very good sample uniformity and repeatable data of measurements. The measurement data of the microgrooves for five different groove depths are given in appendix A (table A.13-A.22).

The normal spectral emissivity data obtained for two types of microgrooves, namely shallow microgrooves (depth $H = 1 \mu\text{m}$ and $3.4 \mu\text{m}$) and deep microgrooves

(depth $H = 11.2 \mu\text{m}$, $21.4 \mu\text{m}$ and $34.2 \mu\text{m}$) are presented in figures 9.24 and 9.25 respectively. These data are compared with the normal spectral emissivity of the smooth undoped silicon surface (i.e., $H = 0$) given in the same diagrams.

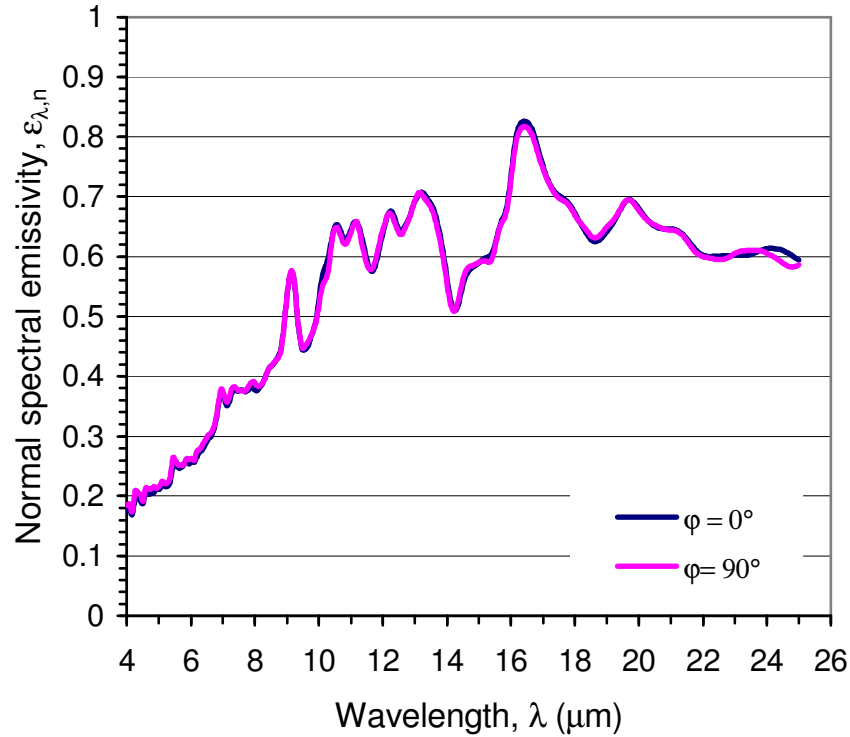


Fig. 9.23. Normal spectral emissivity of microstructured undoped silicon with a groove depth $H = 21.4 \mu\text{m}$ at azimuthal angles $\phi = 0^\circ$ and 90° ($T = 200 \text{ }^\circ\text{C}$).

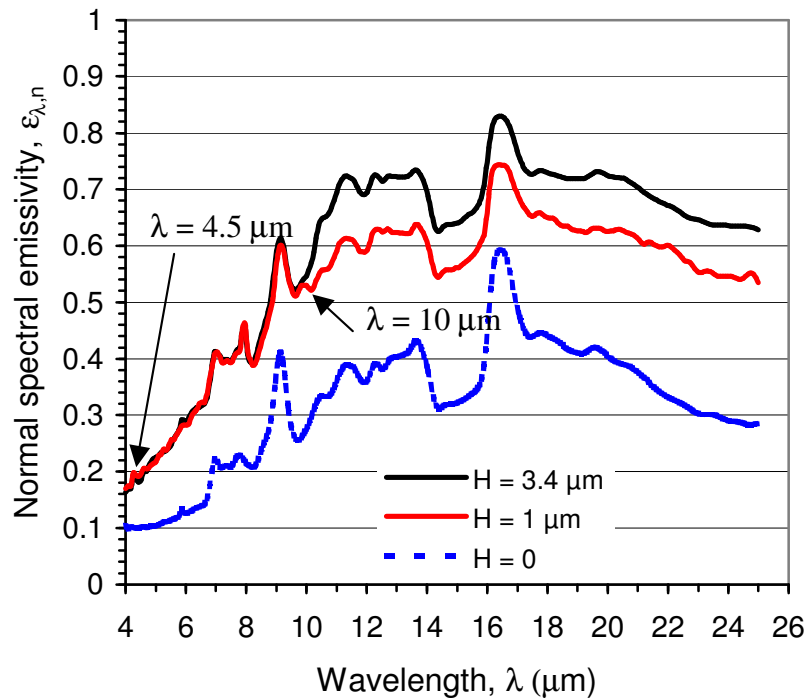


Fig. 9.24. Normal spectral emissivities of shallow microgrooves with depths $H = 3.4 \mu\text{m}$ and $1 \mu\text{m}$ on undoped silicon surface. Depth $H = 0$ indicates the normal spectral emissivity of smooth silicon surface ($T = 200 \text{ }^\circ\text{C}$).

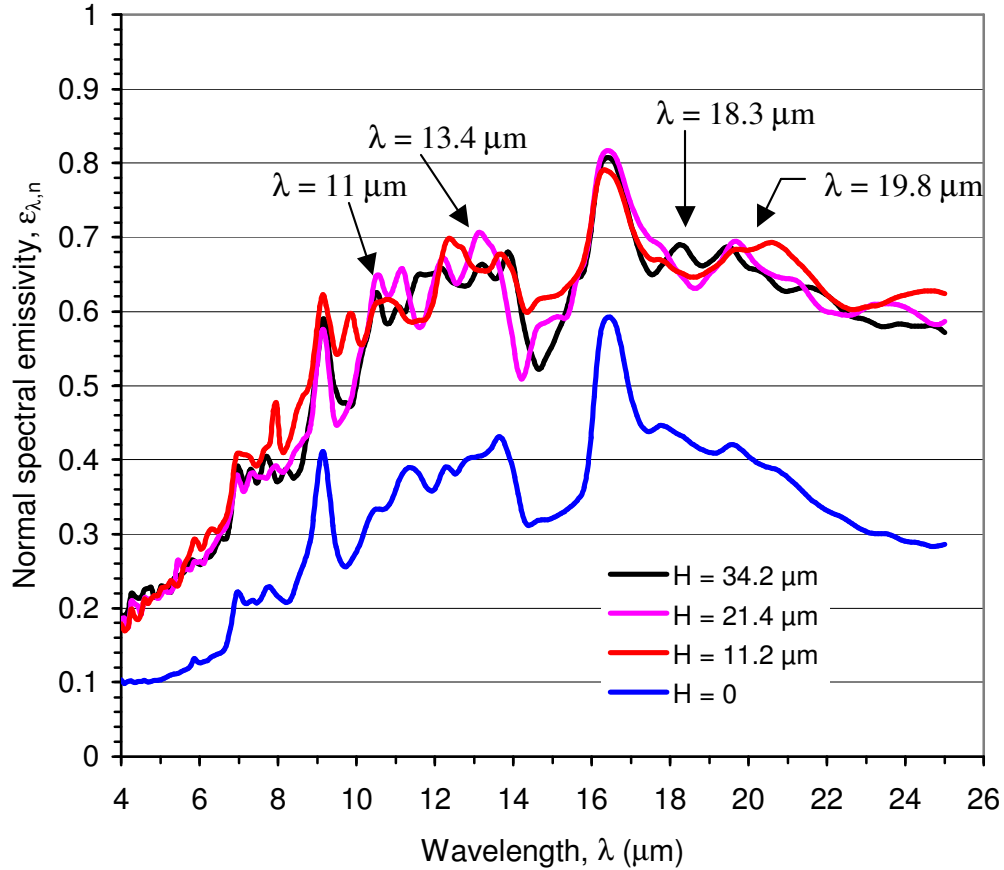


Fig. 9.25. Normal spectral emissivities of deep microgrooves with depths $H = 34.2 \mu\text{m}$, $21.4 \mu\text{m}$ and $11.2 \mu\text{m}$ on undoped silicon surface. Depth $H = 0$ indicates the normal spectral emissivity of smooth silicon surface ($T = 200 \text{ }^\circ\text{C}$).

As shown in figure 9.24, the normal spectral emissivity for the shallow microgrooves is greatly enhanced over that the smooth silicon surface indicated by the depth $H = 0$. As a result the normal total emissivity of shallow microgrooves at all wavelengths is greater than that of the smooth silicon surface. But there are no pronounced spectral peaks to observe except two weak peaks at wavelengths $\lambda = 4.5 \mu\text{m}$ and $10 \mu\text{m}$ as pointed by arrows in the figure 9.24. These maxima are explainable by Wood's anomalies, which may arise due to the onset or disappearance of particular spectral diffraction orders known as Rayleigh wavelengths (see chapter 4). Rayleigh's criterion for grating anomalies i.e., equation (4.33) can therefore be used for the interpretation of these maxima. Rearranging equation (4.33) and substituting $\sin\vartheta_{\text{in}} = \sin 0^\circ = 0$, we get

$$\lambda = \frac{\Lambda}{m} \quad (9.1)$$

Substituting the value of repeat distance or period, $\Lambda = 10 \mu\text{m}$ into equation (9.1) yields for diffraction order $m = 1$, a value of wavelength $\lambda = 10 \mu\text{m}$ and for $m = 2$ the value is $\lambda = 5 \mu\text{m}$. The results are in close agreement with the observed maxima at the wavelengths $\lambda = 4.5 \mu\text{m}$ and $10 \mu\text{m}$.

As in the case of the shallow microgrooves, the normal spectral emissivity for the deep microgrooves is greatly increased over that of the smooth silicon surface indicated by the depth $H = 0$ in figure 9.25. For this reason the normal total emissivity of deep microgrooves at all wavelengths is greater than that of the smooth silicon surface. Contrary to the case of the shallow microgrooves, many pronounced emission peaks have been observed for all deep microgrooves with three different depths. Some of the observed emission peaks are pointed by arrows in figure 9.25. The spectral arrangement of these emission maxima is different for different depths. This feature indicates that the emissivity data depend not only on the repeat distance (Λ) of the microgroove, but also on the depth of the groove (H). The simplest explanation for the maxima is that they arise due to the path difference or standing wave type of interference in the microgrooves [58]. This interference condition for polar angle $\vartheta = 0^\circ$ is given by the relation (see equation (9.4))

$$\lambda = \frac{2H}{m} \quad (9.2)$$

where m is a positive integer.

Table 9.2 Calculated and measured wavelengths where emission maxima of undoped silicon at an azimuthal angle $\varphi = 0^\circ$ and polar angle $\vartheta = 0^\circ$ are observed for the surface temperature $T = 200^\circ\text{C}$.

m (order)	H = 34.2 μm		H = 21.4 μm		H = 11.2 μm	
	$\lambda_{\text{cal.}} (\mu\text{m})$	$\lambda_{\text{meas.}} (\mu\text{m})$	$\lambda_{\text{cal.}} (\mu\text{m})$	$\lambda_{\text{meas.}} (\mu\text{m})$	$\lambda_{\text{cal.}} (\mu\text{m})$	$\lambda_{\text{meas.}} (\mu\text{m})$
1					22.4	20.8
2			21.4	19.8	11.2	11.0
3	22.8	21.8	14.3	13.4	7.5	7.2
4	17.1	18.3	10.7	10.6	5.6	5.9
5	13.7	13.8	8.6	8.1	4.5	4.2
6	11.4	11.0	7.1	7.5		
7	9.7	10.7	6.1	6.8		

The calculated wavelengths ($\lambda_{\text{cal.}}$) from equation (9.2) at which the emission maxima are expected and the measured wavelengths ($\lambda_{\text{meas.}}$) where the emissivity peaks were observed are given in table 9.2. It is clear from this table that there is good agreement between calculated and measured values of the wavelength for the emission maxima. This behaviour demonstrates that the proposed interference condition (i.e., equation 9.2) has its usefulness for the interpretation of the normal spectral emissivity of the deep microgrooves and it provides an additional support for the reasonable data of the normal spectral emissivity measured in this work.

9.4.2 Directional Spectral Emissivity at Azimuthal Angle $\varphi = 0^\circ$

The directional spectral emissivity of the smooth undoped silicon surface has been measured at different polar angles (ϑ) from 0° to 70° and the results were presented in section 9.3.4. It is observed that there is an increase in spectral emissivity at large polar angles resulting in correspondingly more total emissivity at respective polar angles. However, the emissivity is independent of the azimuthal angle. But the microgrooved surface has less symmetrical emitting areas than the smooth surface so that quite different emission characteristics would be expected for measurements taken at two azimuthal angles $\varphi = 0^\circ$ and 90° (i.e., microgrooves are parallel and perpendicular to the direction of observation, see figure 9.22). The spectral emissivity of the microstructured undoped silicon is therefore measured at different polar angles (ϑ) from 0° to 70° and at two azimuthal angles $\varphi = 0^\circ$ and 90° . The directional spectral emissivity data of the microstructured undoped silicon surfaces at an azimuthal angle of $\varphi = 0^\circ$ for the surface temperature $T = 200^\circ\text{C}$ are presented in this section.

The directional spectral emissivity measurements are performed at zero azimuthal angle ($\varphi = 0^\circ$) for five different depths of the microgrooves. The complete data set for different groove depths is given in appendix B (figures B.3, B.5, B.7, B.9, and B.11). The directional spectral emissivity of the microgrooved undoped silicon surface measured at the azimuthal angle $\varphi = 0^\circ$ for the groove depth $H = 34.2\ \mu\text{m}$ with the wavelength of radiation as parameter is discussed in the following.

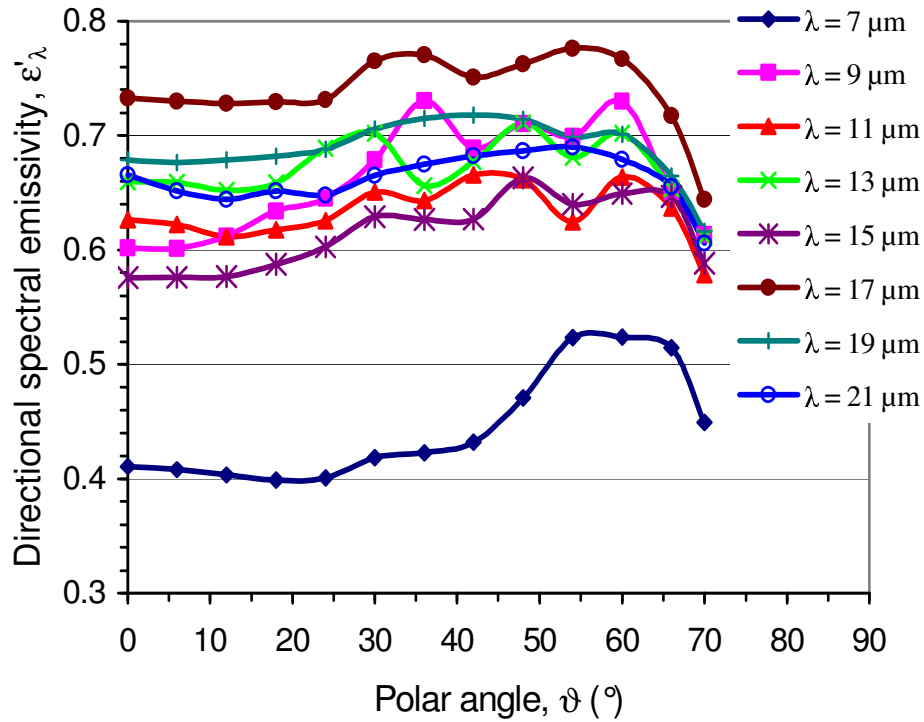


Fig. 9.26a. Directional spectral emissivity of a microgrooved undoped silicon surface with wavelength of radiation as parameter (odd value) measured at an azimuthal angle $\varphi = 0^\circ$ for a groove depth $H = 34.2 \mu\text{m}$ ($T = 200^\circ\text{C}$).

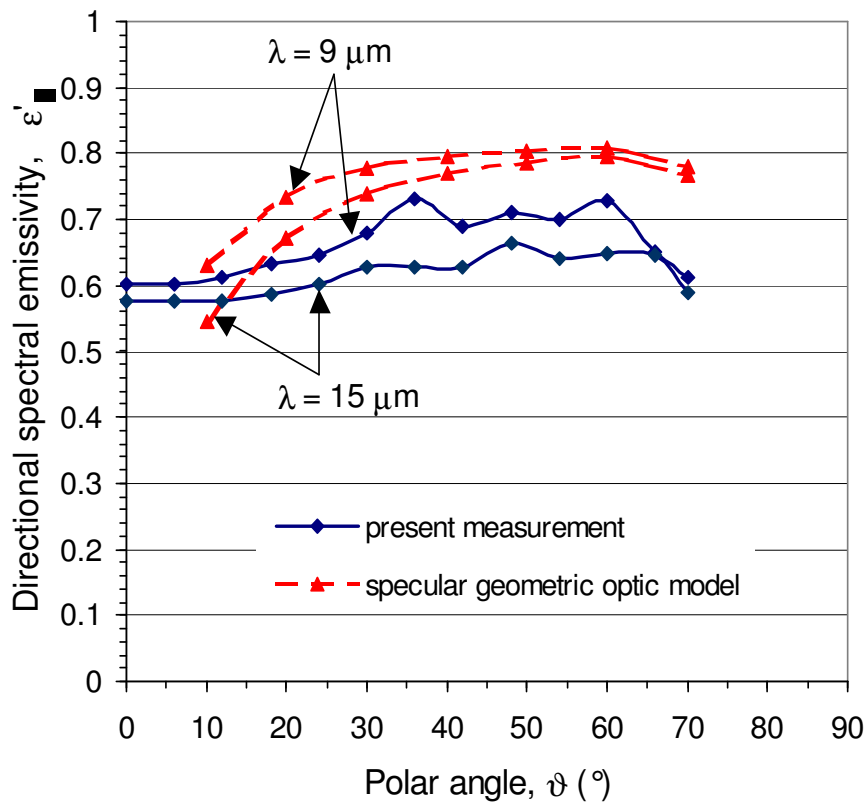


Fig. 9.26b. Comparison of the calculated and measured directional spectral emissivity of a microgrooved undoped silicon surface for the wavelengths of radiation $\lambda = 9 \mu\text{m}$ and $15 \mu\text{m}$ at an azimuthal angle $\varphi = 0^\circ$ for a groove depth $H = 34.2 \mu\text{m}$ ($T = 200^\circ\text{C}$). The dashed lines indicate the values calculated by using the specular geometric optic model (see chapter 4, equations (4.6) and (4.7)).

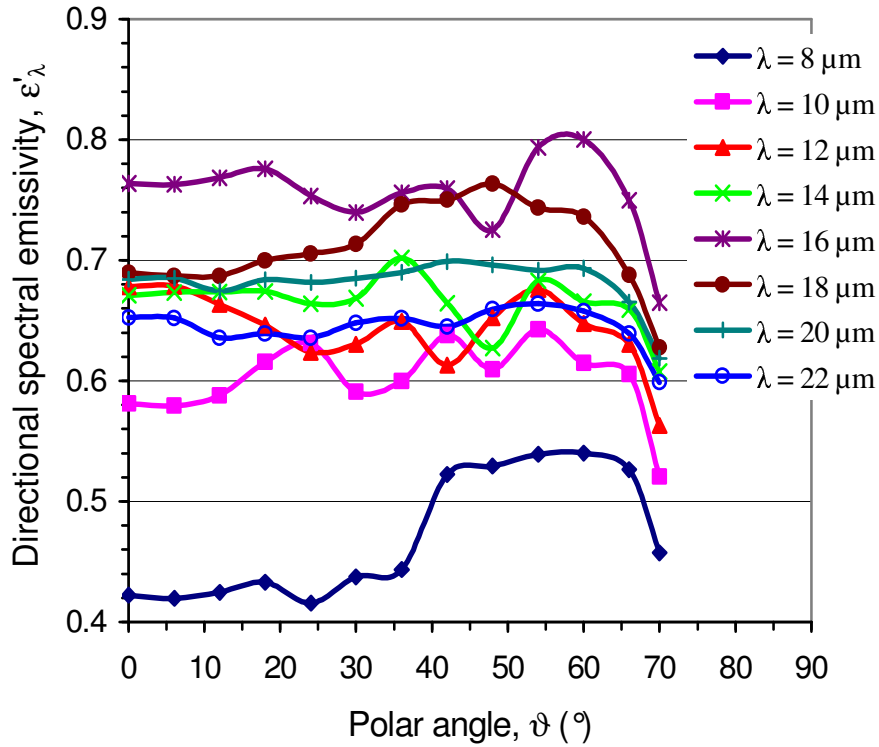


Fig. 9.27a. Directional spectral emissivity of a microgrooved undoped silicon surface with wavelength of radiation as parameter (even value) measured at an azimuthal angle $\phi = 0^\circ$ for a groove depth $H = 34.2 \mu\text{m}$ ($T = 200 \text{ }^\circ\text{C}$).

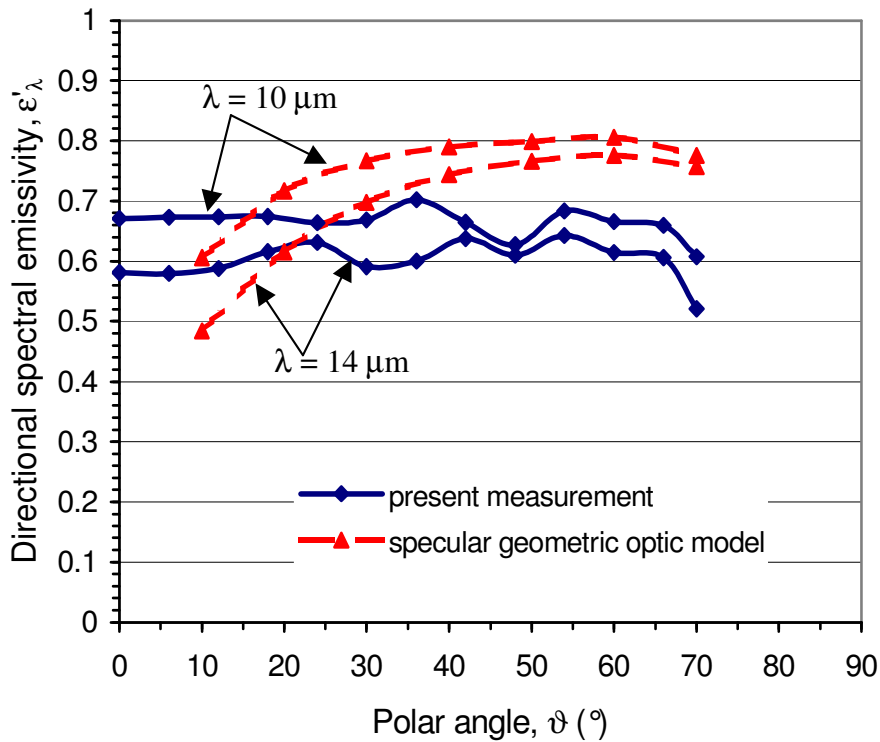


Fig. 9.27b. Comparison of the calculated and measured directional spectral emissivity of a microgrooved undoped silicon surface for the wavelengths of radiation $\lambda = 10 \mu\text{m}$ and $14 \mu\text{m}$ at an azimuthal angle $\phi = 0^\circ$ for a groove depth $H = 34.2 \mu\text{m}$ ($T = 200 \text{ }^\circ\text{C}$). The dashed lines indicate the values calculated by using the specular geometric optic model (see chapter 4, equations (4.6) and (4.7)).

As shown in figures 9.26a and 9.27a several pronounced emissive peaks are observed for microgrooves with depth, $H = 34.2 \mu\text{m}$ at an different polar angles (ϑ), and wavelengths $9 \mu\text{m} \leq \lambda \leq 17 \mu\text{m}$. A few features and some broad maxima are seen at shorter and longer wavelengths. The spacing between emission maxima increases as the wavelength increases. The directional spectral emissivities of the microgrooves as calculated by the specular geometric optic model (see section 4.1) are also presented in figures 9.26b and 9.27b with the measured values for some wavelengths. From these figures it is clear that there is an qualitative agreement in a certain extent between the calculated values (dashed lines) and measured values (solid lines) of the directional spectral emissivity for the same wavelength. But these values are not in accordance with each other quantitatively. This is because the geometric optic model fails to predict the exact results for the microgrooved surface with the dimensions in the order of the wavelength of radiation (see chapter 4). Therefore, the emission peaks due to the interference effects seen in the measured data are not present in the calculated data.

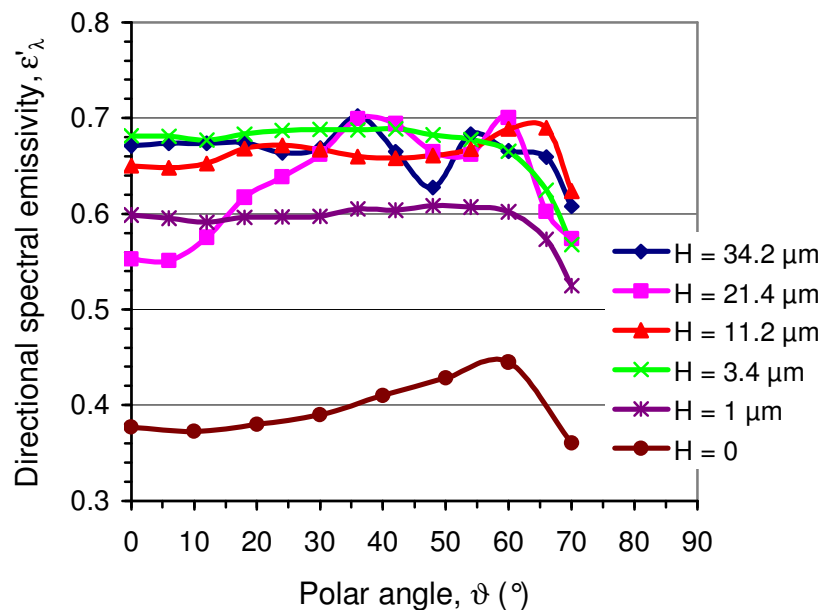


Fig. 9.28. Directional spectral emissivity of undoped silicon microgrooves at a wavelength $\lambda = 14 \mu\text{m}$ with the groove depth (H) as parameter and an azimuthal angle $\phi = 0^\circ$ ($T = 200 \text{ }^\circ\text{C}$).

The directional spectral emissivity at zero azimuthal angle $\phi = 0^\circ$, and a wavelength of radiation $\lambda = 14 \mu\text{m}$ is shown in figure 9.28 for the different microgrooves with depth (H) as parameter. It is observed that the emission peaks for the same wavelength depend on the depth of the microgrooves. The amplitude of the peaks decreases as the depth of the microgrooves decreases. A regular variation of the positions of the peaks with the depth of the

microgrooves is also observed. There are no distinct peaks to be seen for the shallow microgrooves (depth $H = 1 \mu\text{m}$ and $3.4 \mu\text{m}$). The emissivity curves of the shallow microgrooves appear similar to the emissivity curve of the smooth silicon indicated by $H = 0$ in the same diagram. This behavior implies that one might expect a groove depth (H) dependence of the directional spectral emissivity of the microgrooves.

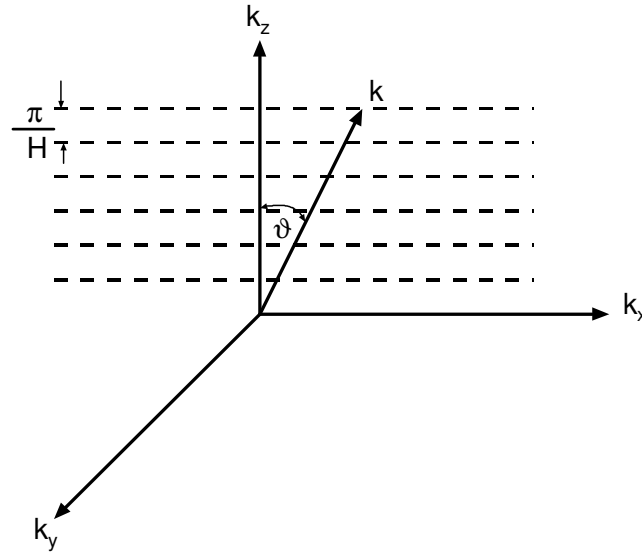


Fig. 9.29. Schematic representation of discrete modes of electric field in the microgroove with depth H .

The directional spectral emissivity data for the azimuthal angle of $\varphi = 0^\circ$ can be interpreted in terms of a coupling of the discrete vertical modes of the electric field with the wave vector of the emitted radiation. The vertical component of the electric field is discrete in the z -direction by the geometry and a continuum of modes exists in the x -direction. This is represented as lines a distance π/H apart along k_z as shown in figure 9.29. The co-ordinate system is fixed with the microgrooves in the x - y plane and the z -axis is perpendicular to it. When the azimuthal angle $\varphi = 0^\circ$, the observations are made in the z - x plane as the polar angle (ϑ) is varied. For the coupling, the z -component k_z of the wave vector \mathbf{k} in the direction of observation must be equal to the distinct values resulting from the allowable wavelengths of standing waves in the microcavity, i.e.:

$$|\mathbf{k}| \cos \vartheta = k_z = \frac{m\pi}{H} \quad (9.3)$$

By using equation (4.30) for expressing the magnitude of the wave vector \mathbf{k} as the function of the wavelength (i.e., $|\mathbf{k}| = 2\pi/\lambda$), equation (9.3) can be written as

$$\cos \vartheta = \frac{m\lambda}{2H} \quad (9.4)$$

where m is a positive integer and ϑ is the polar angle (i.e., angle of observation), at which emission maxima are to be expected.

The position of the maxima calculated by using the equation (9.4) and measured in the present experiment are listed in table 9.3 for the microgroove with depth $H = 34.2 \mu\text{m}$. Good agreement is found between the calculated and the measured values of the polar angle at which the emission maxima appear. This behaviour in both the normal and angular data adds more weight to the validity and usefulness of the proposed wave model, i.e. equation (9.4), for the interpretation of the directional spectral emissivity data measured at the azimuthal angle of $\phi = 0^\circ$. The simplest explanation for the emission peaks is that they may arise from resonances of the vertical standing waves (k_z) in the microgrooves. However, an additional coupling between the adjacent microgrooves cannot be excluded since two neighbouring microgrooves are only $(\Lambda - W) = 10 - 6.5 = 3.5 \mu\text{m}$ apart.

Table 9.3. Calculated and measured polar angle of spectral emissivity maxima for undoped silicon microgrooves with a depth $H = 34.2 \mu\text{m}$ at an azimuthal angle $\phi = 0^\circ$ ($T = 200^\circ\text{C}$). The symbol “-” indicates no peak is observed.

$\lambda / \mu\text{m}$	m (order)	$\vartheta_{\text{cal.}}$ (deg)	$\vartheta_{\text{meas.}}$ (deg)	$\lambda / \mu\text{m}$	m (order)	$\vartheta_{\text{cal.}}$ (deg)	$\vartheta_{\text{meas.}}$ (deg)
7	6	52.1	54	15	4	28.7	30
8	8	20.6	18		3	48.8	48
	4	62.1	60		2	64	66
9	6	37.8	36	16	4	20.6	18
	5	48.8	48		3	45.4	42
	4	58.2	60		2	62.1	60
10	6	28.7	24	17	4	6.2	0
	5	43	42		3	41.8	36
	4	54.2	54		2	60.2	54
11	5	36.5	30	18	3	37.9	-
	4	50	42		2	58.2	48
	3	61.1	60	19	3	33.6	42
12	4	45.4	36		2	56.2	60
	3	58.2	54	20	3	28.7	18
13	4	40.5	48		2	54.2	60
	3	55.2	60	21	3	23	18
14	4	35	36		2	52.1	54
	3	52.1	54	22	3	15.2	18
	2	65.8	-		2	50	54

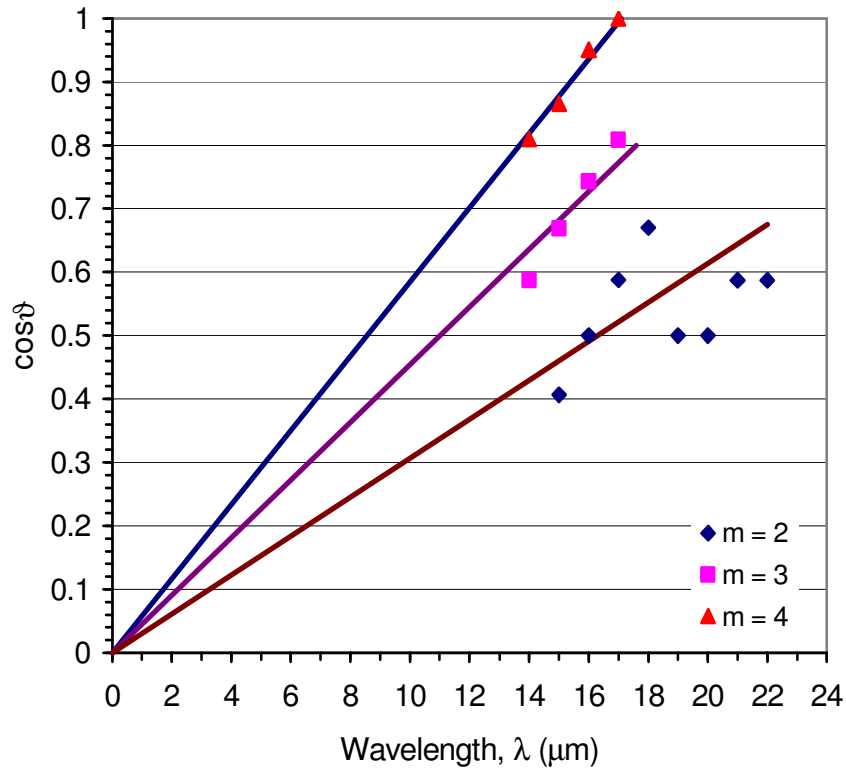


Fig. 9.30. Cosine of polar angle of maximum in directional spectral emissivity of undoped silicon microgrooves with a depth $H = 34.2 \mu\text{m}$ at an azimuthal angle $\phi = 0^\circ$ versus wavelength ($T = 200^\circ\text{C}$).

The wavelengths of radiation for the peak values of the directional spectral emissivity measured at an azimuthal angle $\phi = 0^\circ$ are plotted against $\cos\theta$ as shown in figure 9.30. A straight line fit to the directional spectral emissivity maxima was obtained for each value of m , with a zero intercept. The average calculated groove depth $H = 33.2 \mu\text{m}$ was obtained from the slopes of the lines drawn in figure 9.30 with the slopes $m/2H$ given in equation (9.4) for each value of m . This is in reasonable agreement with the depth of the groove $H = 34.2 \mu\text{m}$ taken for the directional spectral emissivity measurement. This also provides an additional support to the wave model given in equation (9.4) for the interpretation of the directional spectral emissivity data measured at the azimuthal angle of $\phi = 0^\circ$.

9.4.3 Directional Spectral Emissivity at Azimuthal Angle $\phi = 90^\circ$

The directional spectral emissivity data of the microstructured undoped silicon surfaces at the azimuthal angle $\phi = 90^\circ$ are presented in this section. The measurements are performed for five different depths of microgrooves as in the case when the azimuthal angle is $\phi = 0^\circ$. The complete data set for different groove depths is given in appendix B (figures B.2, B.4, B.6, B.8 and B.10). The directional spectral emissivity of the microgrooved undoped

silicon surface with the wavelength of radiation as parameter measured at the azimuthal angle $\varphi = 90^\circ$ for the groove depth $H = 34.2 \mu\text{m}$ is presented and discussed in the following.

Several pronounced emission peaks are observed for microgrooves with depth $H = 34.2 \mu\text{m}$ at different polar angles (ϑ), and the wavelengths $7 \mu\text{m} \leq \lambda \leq 21 \mu\text{m}$ as shown in figures 9.31 and 9.32. The emissivity curves obtained at the azimuthal angle $\varphi = 90^\circ$ show a different behaviour than those obtained at the azimuthal angle $\varphi = 0^\circ$ (section 9.4.2). The emission gradually decreases with the polar angle (ϑ) for all wavelengths, but this decrease in emission is more rapid at larger polar angles. This is because of the shadow effect occurring in the deep microgrooves to the direction of large polar angles so that the detector cannot receive the radiation from the whole area of the grooves (see figure 9.33). A few features and some broad maxima are observed at longer wavelengths. The spacing between emission maxima increases as the wavelength increases. In some cases no wavelength dependence can be read off because the maxima are 10° to 20° wide.

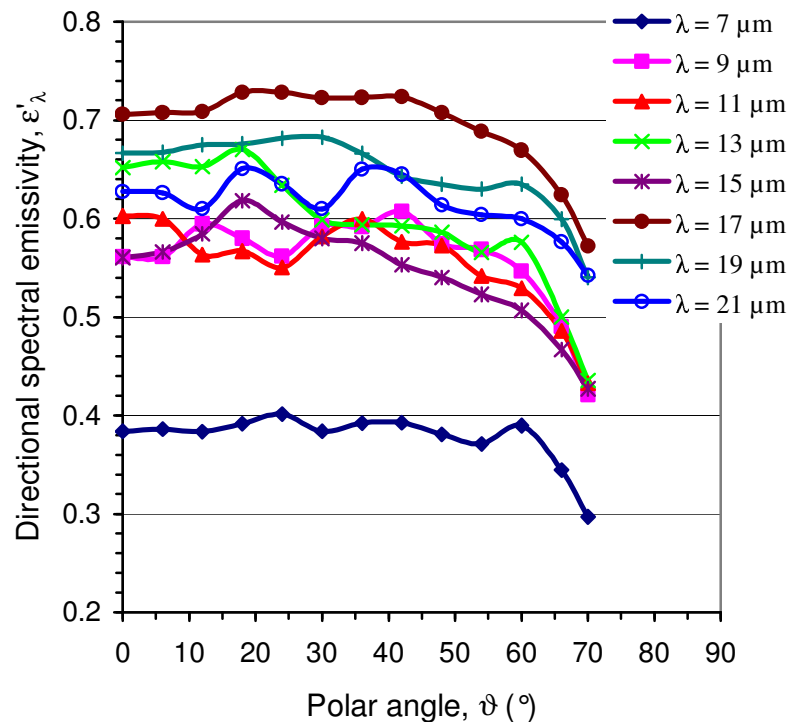


Fig. 9.31. Directional spectral emissivity of a microgrooved undoped silicon surface with the wavelength of radiation as parameter (odd value) at an azimuthal angle of $\varphi = 90^\circ$ for a groove depth $H = 34.2 \mu\text{m}$ ($T = 200^\circ\text{C}$).

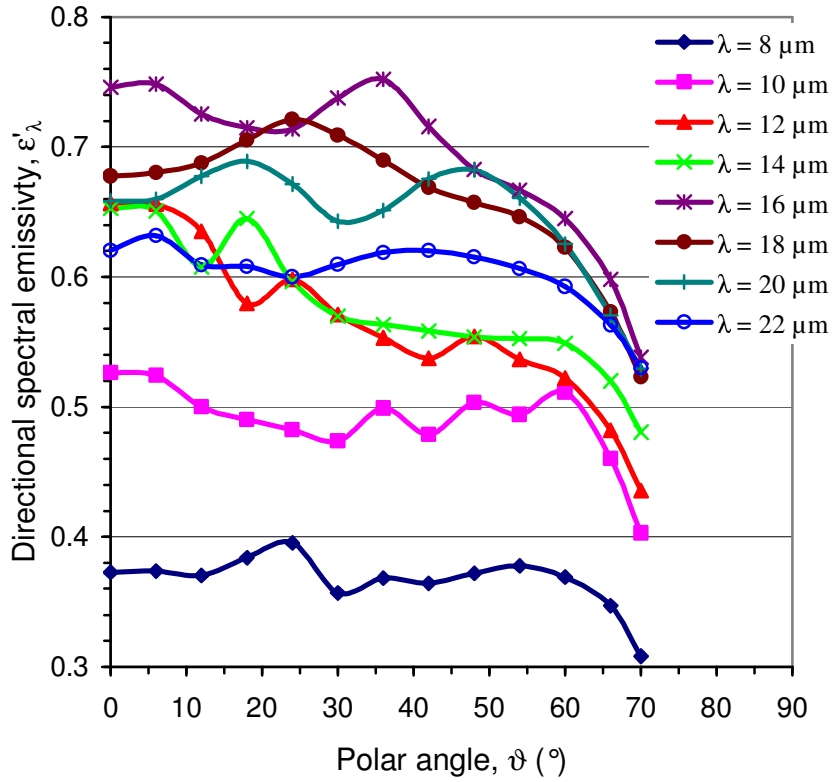


Fig. 9.32. Directional spectral emissivity of a microgrooved undoped silicon surface with the wavelength of radiation as parameter (even value) at an azimuthal angle of $\phi = 90^\circ$ for a groove depth $H = 34.2 \mu\text{m}$ ($T = 200^\circ\text{C}$).

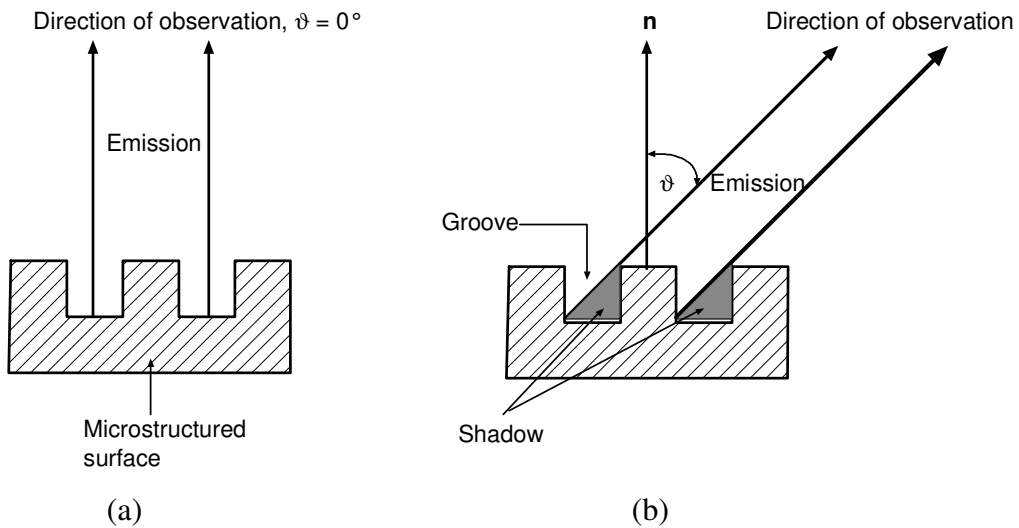


Fig. 9.33. Representation of shadow effect in deep microgrooves to the direction of observation at increasing polar angle (ϑ). (a) no shadow effect occurs when $\vartheta = 0^\circ$ (b) occurrence of shadow effect when $\vartheta > 0^\circ$.

The directional spectral emissivity data for the azimuthal angle of $\varphi = 90^\circ$ can be interpreted in terms of the onset or disappearance of particular spectral diffraction orders known as Rayleigh wavelengths (see chapter 4). Rayleigh's criterion for grating anomalies i.e., equation (4.33), can therefore be used to calculate the polar angles of emission (ϑ), at which the emission maxima are to be expected,

$$\sin \vartheta = \left| 1 - \frac{m\lambda}{\Lambda} \right| \quad (9.5)$$

where Λ is the repeat distance or period of the microgrooves.

The positions of the emission maxima calculated by using the equation (9.5) and measured in the present experiment are listed in table 9.4 for the microgrooves with different depths ($H = 34.2 \mu\text{m}$, $21.4 \mu\text{m}$, $11.2 \mu\text{m}$ and $1 \mu\text{m}$). The agreement between the calculated and the measured values of the polar angles is good considering that the polar angle increments are 6° . As no peaks are observed, the microgroove with depth $H = 3.4 \mu\text{m}$ is not listed in table 9.4.

Table 9.4. Calculated and measured polar angles of spectral emissivity maxima (peaks) for undoped silicon microgrooves with depths $H = 34.2 \mu\text{m}$, $21.4 \mu\text{m}$, $11.2 \mu\text{m}$ and $1 \mu\text{m}$ at an azimuthal angle $\varphi = 90^\circ$ ($T = 200^\circ \text{C}$). The symbol '-' denotes no peak is observed.

$\lambda / \mu\text{m}$	m (order)	$\vartheta_{\text{cal.}}$ (deg)	$\vartheta_{\text{meas.}}$ (deg)			
			H = 34.2 μm	H = 21.4 μm	H = 11.2 μm	H = 1 μm
7	1	17.4	-	-	-	12
	2	23.6	24	24	24	24
8	1	11.5	-	18	18	-
	2	36.8	36	-	30	-
9	1	5.7	12	-	-	0
	2	53.1	-	54	54	48
10	1	0	0	0	0	0
11	1	5.7	-	-	-	0
12	1	11.5	-	-	12	6
13	1	17.4	18	-	18	18
14	1	23.6	-	-	24	24
15	1	30	-	30	-	24
16	1	36.8	36	36	36	30
17	1	44.4	42	48	-	42
18	1	53.1	-	-	-	54
19	1	64.1	60	-	-	60

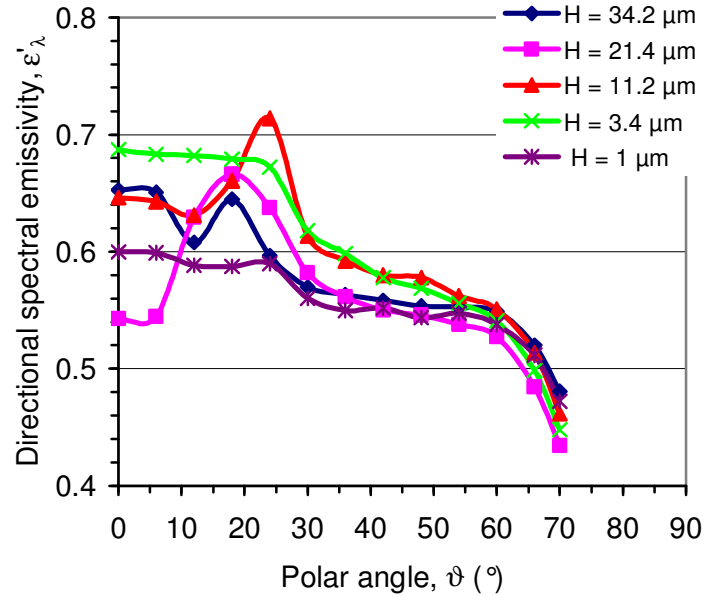


Fig. 9.34. Directional spectral emissivity of undoped silicon microgrooves at the wavelength $\lambda = 14 \mu\text{m}$ with groove depth (H) as parameter and at an azimuthal angle of $\phi = 90^\circ$ ($T = 200^\circ\text{C}$).

In figure 9.34 the directional spectral emissivity at the azimuthal angle of $\phi = 90^\circ$, and the wavelength of the radiation $\lambda = 14 \mu\text{m}$ is shown for the different microgrooves with depth (H) as the parameter. It is observed that the emission peaks for the same wavelength depend to some extent on the depth of the microgrooves. In the deep microgrooves (depth, $H > 4 \mu\text{m}$) the amplitude of the peaks increases as the depth of the microgrooves decreases. There is only one pronounced peak to be seen for each deep microgroove. The angular position of this peak varies with the depth of the microgrooves. A nearly antenna like peak having very large amplitude is observed at the polar angle of $\vartheta = 24^\circ$ for the microgroove with the groove depth $H = 11.2 \mu\text{m}$. This implies that an angular control of the directional spectral emissivity is possible by using the periodic microstructured surface.

Contrary to the deep microgrooves, no distinct peaks are observed in the shallow microgroove with the depth $H = 1 \mu\text{m}$ whereas there are no peaks at all in the shallow microgroove with the depth $H = 3.4 \mu\text{m}$. We have no explanation for this behavior. One might expect not only a groove depth (H), but also a repeat distance (Λ) as well as a width (W) dependence of the directional spectral emissivity of the microgrooves. However, only microgrooves having different groove depths with a fixed repeat distance $\Lambda = 10 \mu\text{m}$ and a fixed width $W = 6.5 \mu\text{m}$ are studied in this work. Therefore, no explanation can be obtained for the repeat distance (period) and width dependence of the directional emissivity of the microgrooves at this stage.

9.4.4 Azimuthal Angle Dependence of Directional Spectral Emissivity

The behavior of the directional spectral emissivity for the high symmetry azimuthal directions of $\varphi = 0^\circ$ and 90° have been established in the foregoing sections 9.4.2 and 9.4.3 respectively. It is now interesting to consider the transition as the azimuthal angle φ is varied over the range from 0° to 90° . For this purpose, two measurements are carried out at the azimuthal angles $\varphi = 30^\circ$ and 60° on the microgrooved silicon surface with the groove period $\Lambda = 10 \mu\text{m}$, width $W = 6.5 \mu\text{m}$ and depth $H = 21.4 \mu\text{m}$. The azimuthal angle dependence of the directional spectral emissivity is plotted in figures 9.36 to 9.39 against the polar angle with wavelength as parameter. All the directional spectral emissivity data measured at the azimuthal angles, $\varphi = 0^\circ, 30^\circ, 60^\circ$ and 90° are shown to illustrate the relevant features.

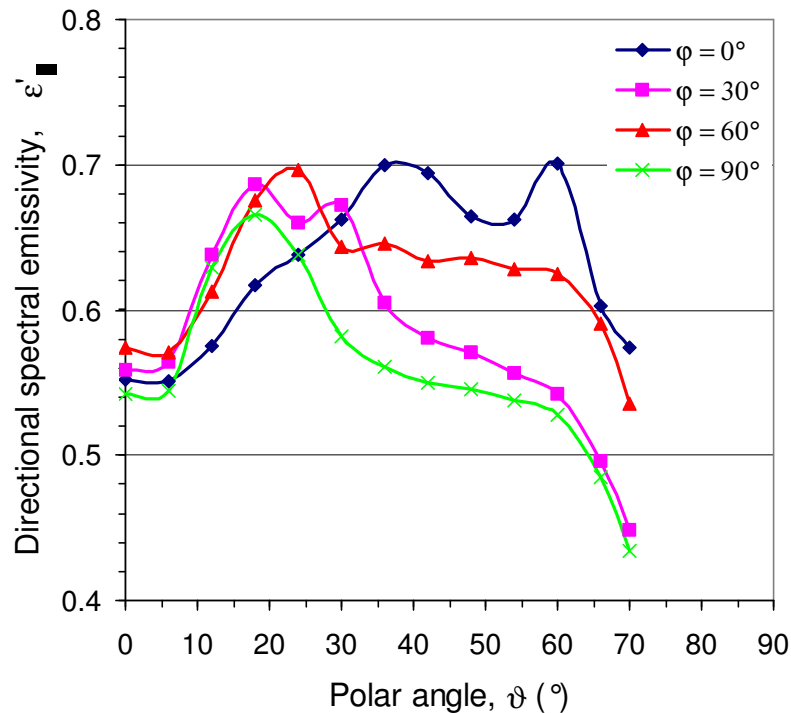


Fig. 9.35. Directional spectral emissivity of the microstructured undoped silicon microgrooves with the depth, $H = 21.4 \mu\text{m}$ at the wavelength, $\lambda = 14 \mu\text{m}$ with the azimuthal angle as parameter.

To do a comparative study among the emissivity data measured at the different azimuthal angles, the directional spectral emissivity of the microgrooves with the depth $H = 21.4 \mu\text{m}$ at the wavelength $\lambda = 14 \mu\text{m}$ is chosen and presented in figure 9.35 for the azimuthal angles $\varphi = 0^\circ, 30^\circ, 60^\circ$ and 90° . In the directional spectral emissivity data measured at the azimuthal angle $\varphi = 0^\circ$, two emission peaks or maxima with high amplitudes are observed.

These are interpreted in terms of a coupling of the discrete vertical modes of the electric field with the wave vector of the emitted radiation as described in section 9.4.2. As the azimuthal angle (φ) advances from zero to higher values, the position of the emission maxima moves to smaller polar angles (see figure 9.35). The number of the emission peaks at a particular wavelength decreases as the azimuthal angle increases. For example out of two emission peaks for the wavelength $\lambda = 14 \mu\text{m}$ the amplitude of the second emission peak at the polar angle $\vartheta = 60^\circ$ becomes smaller as the azimuthal angle (φ) advances from zero to higher values and it vanishes at the azimuthal angle $\varphi = 90^\circ$, resulting in only one peak with the higher amplitude and larger width of 10° to 20° of polar angle. The decrease of the directional spectral emissivity with the larger polar angles is more rapid at higher azimuthal angles as shown in figures 9.36 to 9.39. This behaviour may be due to an enhanced emission within the microgrooves.

As described earlier, the enhancement of the emission within the microgrooves is due to the interaction between the electromagnetic wave and the geometry of the surface with dimensions in the order of the wavelength of radiation. The data of the directional spectral emissivity measured at the azimuthal angle $\varphi = 0^\circ$ can be interpreted in terms of a coupling of the discrete vertical modes of the electric field with the wave vector of the emitted radiation, in which the depth (H) of the microgrooves plays a key role (see section 9.4.2). The emissivity data obtained at the azimuthal angle $\varphi = 90^\circ$ can be interpreted in terms of the onset or disappearance of particular spectral diffraction orders known as Rayleigh wavelengths, which depend on the period (Λ) of the microgrooves (see section 9.4.3). But the behaviour of the directional spectral emissivity for other azimuthal angles ($0^\circ < \varphi < 90^\circ$) except the two high symmetry directions $\varphi = 0^\circ$ and 90° are not interpretable clearly. This is because at the azimuthal directions $0^\circ < \varphi < 90^\circ$, it might also be possible for both above processes to occur at a time. An additional coupling between the adjacent microgrooves cannot also be excluded since two neighbouring microgrooves are only $3.5 \mu\text{m}$ apart. The coupling process may be also influenced by the roughness of the surface of the microgrooves.

In order to understand the process of the enhanced emission within the microgrooves clearly, it is suggested that not only the effect of the depth variation of the microgrooves is to be performed, as done in this work, but also the effects of the variations of the period and of the width of the microgrooves on the emission are to be investigated.

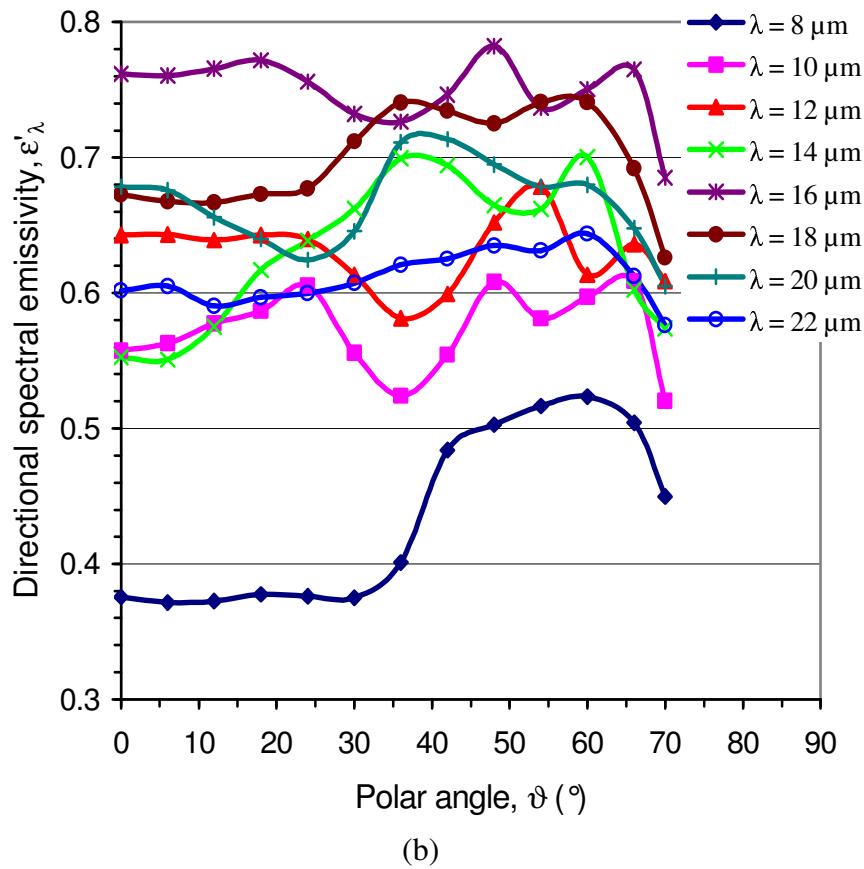
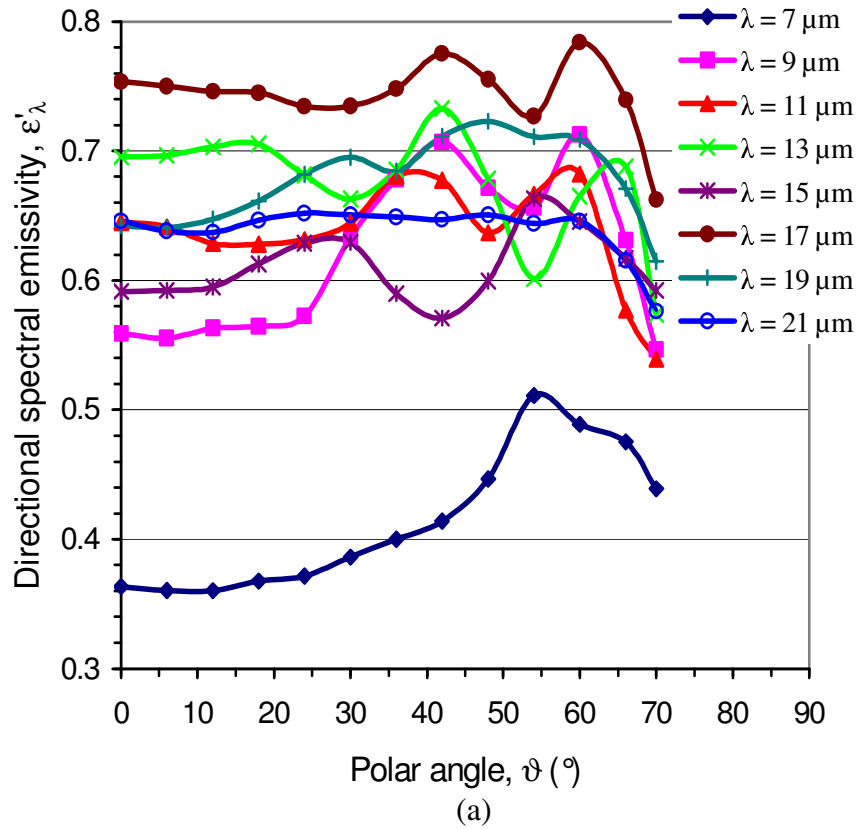
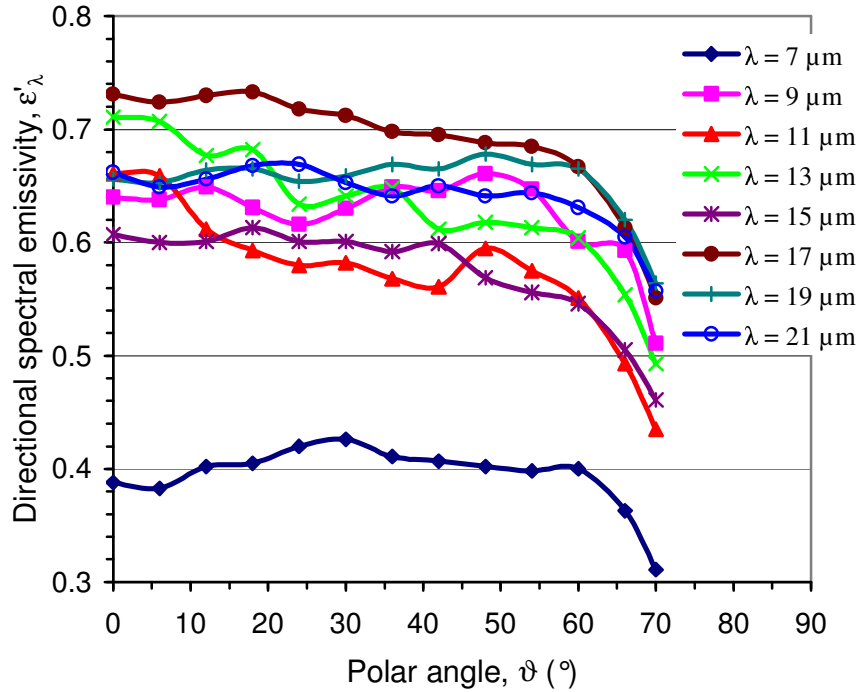
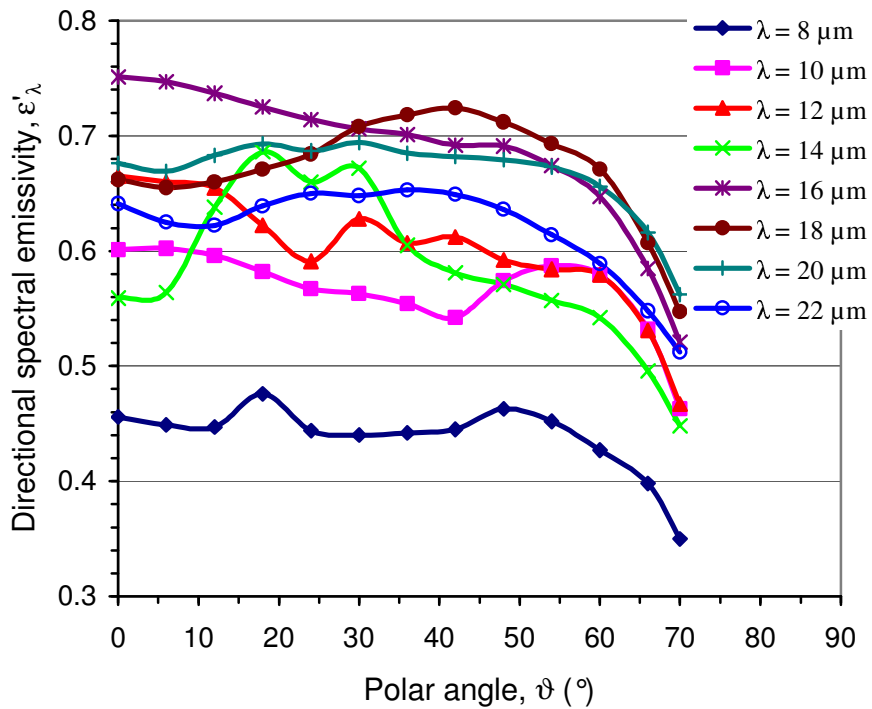


Fig. 9.36. Directional spectral emissivity of a microgrooved undoped silicon surface with the wavelength of radiation as parameter at an azimuthal angle, $\phi = 0^\circ$ for groove depth, $H = 21.4 \mu\text{m}$ ($T = 200^\circ\text{C}$). (a) odd values of wavelength (b) even values of wavelength.

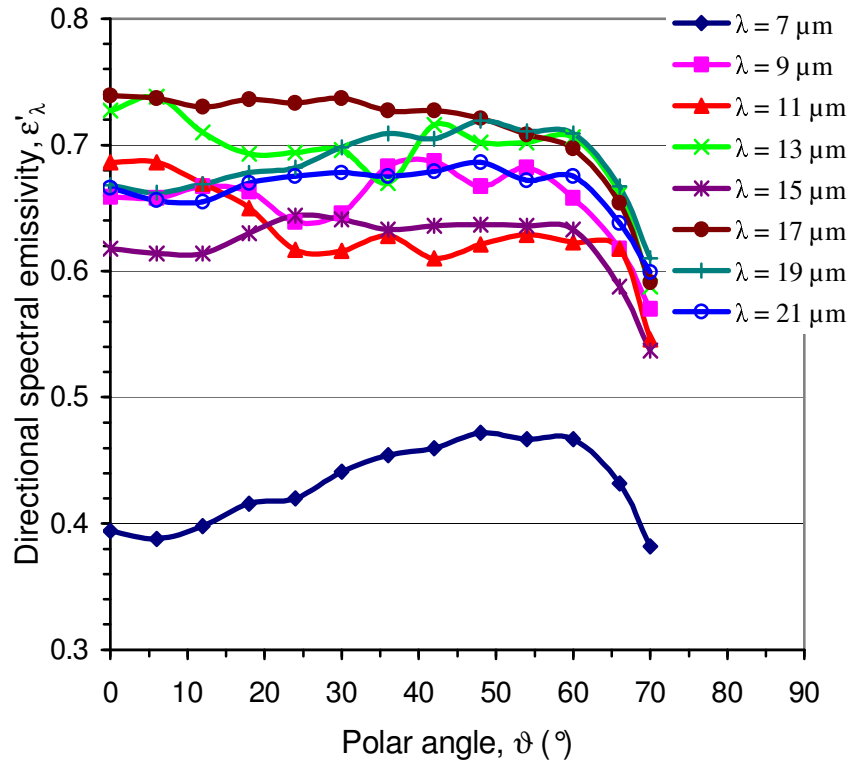


(a)

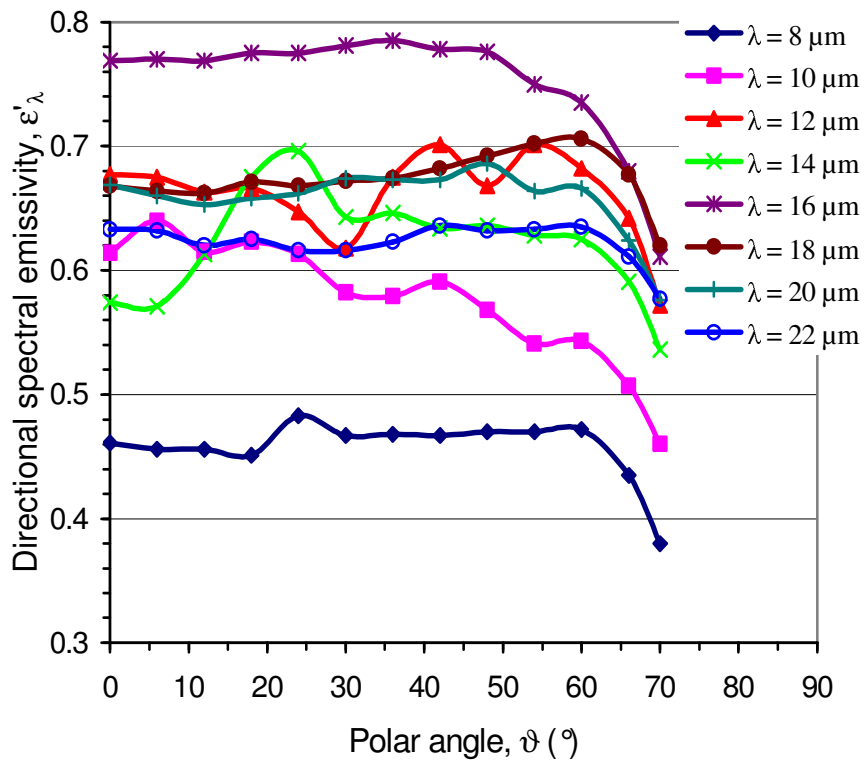


(b)

Fig. 9.37. Directional spectral emissivity of a microgrooved undoped silicon surface with the wavelength of radiation as parameter at an azimuthal angle, $\phi = 30^\circ$ for a groove depth, $H = 21.4 \mu\text{m}$ ($T = 200 \text{ }^\circ\text{C}$). (a) odd values of wavelength (b) even values of wavelength.

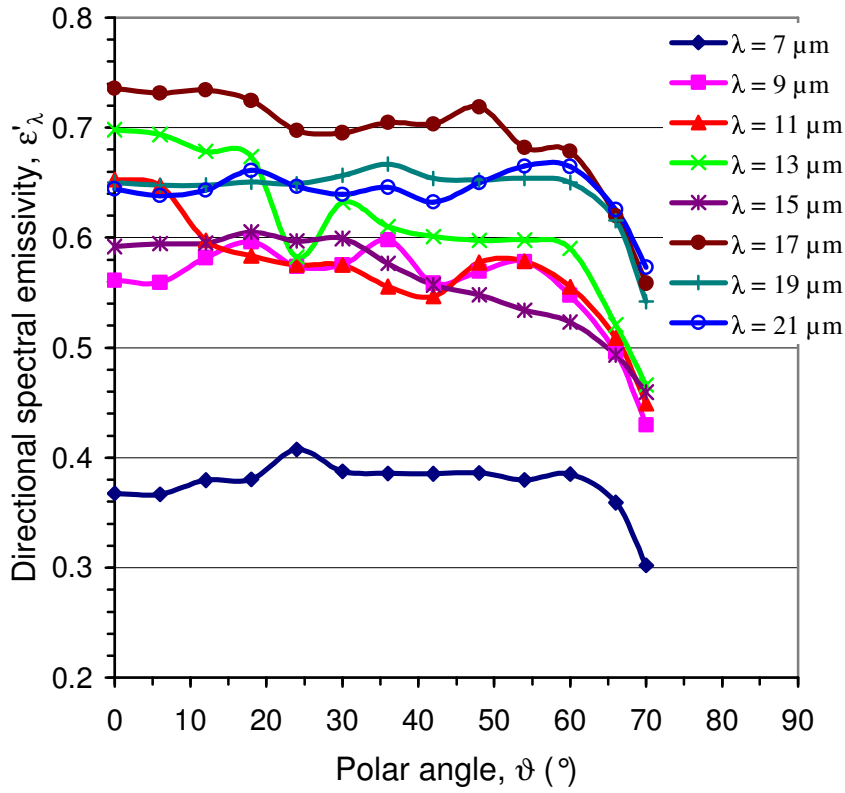


(a)

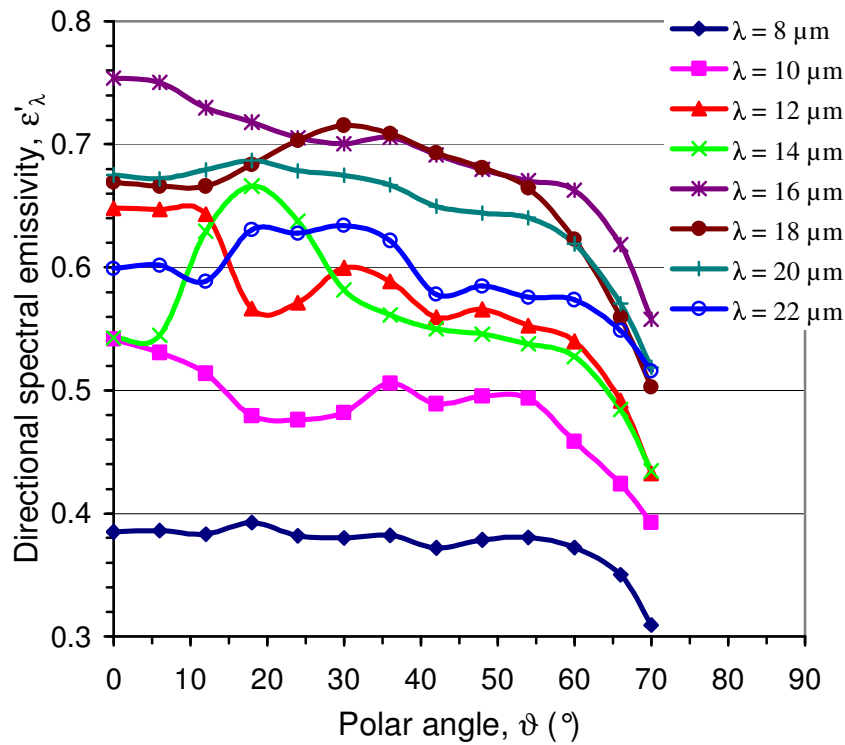


(b)

Fig. 9.38. Directional spectral emissivity of a microgrooved undoped silicon surface with the wavelength of radiation as parameter at an azimuthal angle, $\varphi = 60^\circ$ for a groove depth, $H = 21.4 \mu\text{m}$ ($T = 200^\circ\text{C}$). (a) odd values of wavelength (b) even values of wavelength.



(a)



(b)

Fig. 9.39. Directional spectral emissivity of a microgrooved undoped silicon surface with the wavelength of radiation as parameter at an azimuthal angle, $\phi = 90^\circ$ for a groove depth, $H = 21.4 \mu\text{m}$ ($T = 200 \text{ }^\circ\text{C}$). (a) odd values of wavelength (b) even values of wavelength.

10 Conclusions and Suggestions for Further Works

10.1 Conclusions

By the use of the apparatus presented in this dissertation the directional spectral emissivity of technical solid surfaces with different geometries and coatings can be measured successfully at the sample surface temperature up to 250 °C for polar angles from 0° to 70° and azimuthal angles between 0° and 360°. With the help of a DTGS (deuterated triglycine sulphate) beam splitter useful measurement results can be obtained in the wavelength range from 4 μm to 25 μm. The estimation of the surface temperature of the sample by the use of energy balance equations and the confirmation of a uniform temperature distribution on the sample surface by using finite element method (FEM) have demonstrated the accurate determination of the temperature of the sample surface. The calibration of the Fourier transform infrared (FTIR) spectrometer performed with the help of a technically realized blackbody radiator having an effective emissivity value of 0.9989 has provided the emissivity measurements of the sample without the influence of any optical path influences or background radiation.

The contribution of this work to an understanding of the thermal radiant emission can be divided into two parts. First, measurements of the directional spectral emissivity of some technical solid surfaces with clean smooth surfaces and with periodic microstructured surfaces are delivered. Second, the interpretation of the measured values of the directional spectral emissivity by the use of simple classical models which account for many of the features are offered.

The measurements of the directional spectral emissivity and the derivation of lumped quantities of emissivity of some samples with clean smooth surfaces are carried out in order to validate the results obtained from the apparatus used in this work. The measured values of the emissivities of these samples are in close agreement with the values available in the literature and the emissivities calculated by the Fresnel's equations. The measurement results of the hemispherical total emissivity of the samples obtained simultaneously by using two independent measurement methods, namely the calorimetric method and the radiometric method, have demonstrated the accuracy of the present measurement.

The most interesting features are found in the measurement data of the directional spectral emissivity of the periodic microstructured undoped silicon surface. Contrary to the

case of the smooth silicon surface, regularly spaced maxima over the polar angle are observed in the directional spectral emissivity of the undoped silicon microstructured surface. These arise due to the resonant effect between the electromagnetic field and periodic microstructures. The measurements reported in this work clearly demonstrate that resonances are observed in both azimuthal angles $\varphi = 0^\circ$ and 90° .

The polar angular dependence of the spectral emissivity at azimuthal angle $\varphi = 0^\circ$ shows a noticeable resonant effect. This effect may arise from a coupling of the vertical modes to a radiating wave at angles where the vertical component of the radiation wave vector is equal to the standing wave vector in the vertical direction of the rectangular grooved cavity. At the resonant wavelength, the microgrooves are in effect a more efficient antenna. This effect clearly demonstrates that the electromagnetic radiation interacts strongly with the surface geometry and the directional control of thermal radiation by the surface geometry is possible.

Wood's anomalies are also observed in the directional spectral emissivity at the azimuthal angle, $\varphi = 90^\circ$. The emissivity peaks are clearly discerned with the shallow grooves and become masked by the resonant peaks in the deeper grooves. Like in the p- and s-polarized radiation, these anomalies of the unpolarized radiation may arise from the onset or disappearance of particular spectral diffraction orders known as Rayleigh wavelengths, i.e., they occur when an order passes off over the grating horizon. Present measurement results have demonstrated that the Rayleigh's criterion for the grating anomalies of the p- and s-polarized radiation can also be used for the unpolarized radiation from the microstructured undoped silicon surface.

The azimuthal angle dependence of the directional spectral emissivity is confirmed by measuring the emissivity at four different azimuthal angles, $\varphi = 0^\circ, 30^\circ, 60^\circ$ and 90° . The resonant effect is also observed in the directional spectral emissivity data measured at the azimuthal angles, $\varphi = 30^\circ$ and 60° as in the case of the high symmetry directions, $\varphi = 0^\circ$ and 90° . This effect may be due to an enhanced emission from the microgrooves and in order to understand the process of this enhanced emission, it is suggested that not only the effect of the depth variation of the microgrooves as done in this work, but also the effects of the variations of the period and of the width of the microgrooves on the emission are to be investigated.

For the measurements on microstructured surfaces reported in this work, the emissivity maxima at the resonant condition cannot be predicted by a classical calculation, for example by a geometric optic model. But this may be realized by the use of the rigorous electromagnetic theory qualitatively and quantitatively. The complex numerical calculations

of electromagnetic theory were not performed within the scope of this work. However, present work confirmed that the angular positions of these maxima could be quantitatively compared with those predicted by the use of the existing classical grating theory.

10.2 Further Works

The major problem in the measurement of emission infrared spectra is the low signal-noise ratio resulting from the large background radiation relative to the emission from a sample. One method of increasing the signal (more energy in spectrum) is to collect the emitted radiation over a very large solid angle. This can be achieved by the use of an ellipsoid mirror instead of using simple flat mirror for the reflection of radiation from the sample into the spectrometer. In addition, it is easy to control the sample surface area from which the emission spectrum is taken and therefore, a measurement of emissivity at large zenith angle is also possible by placing the sample at the short focal length and collected radiation is transferred to the long focal length of the ellipsoid mirror [54].

The other method of increasing the signal-noise ratio is to use an MCT (mercury cadmium telluride) detector cooled with liquid nitrogen in the FTIR-spectrometer. Because of its high sensitivity the MCT detector can also receive the weak signal from low emission sample surface, which cannot be detected by DTGS (deuterated triglycine sulphate) detector used in this work. However, the problem of using a MCT detector is the detection of not only the weak radiation from the sample itself, but also the high background radiation resulting from the other parts in the sample- and equipment chambers. To suppress this effect one can cool the sample chamber down to the temperature of the detector so that radiative heat transfer takes place between the detector and the sample only, of course, thereby increasing the cost of the experiment due to the liquid nitrogen cooling facility for the whole sample chamber.

To guarantee the exact determination of sample surface temperature by avoiding the free convection heat transfer between the sample and the chamber environment, the sample chamber should be evacuated up to high vacuum region (10^{-1} - 10^{-6} Pa) which is only possible by the use of a turbo molecular vacuum pump instead of a rotary disc vacuum pump (100 - 10^{-1} Pa) used here. The measurement of the directional spectral emissivity with the help of the presented apparatus can be extended up to the polar angles greater than 70° by decreasing the diameter of the aperture used in the experimental set up. However, it is worthwhile to mention that decreasing the aperture diameter reduces the amount of source radiation passing to the detector, which ultimately causes the low energy in the spectrum.

The direct measurements of the surface temperatures of some samples with an infrared thermocamera could not bring useful results in the present work. Reasonable causes were not found for this behaviour. Therefore, a further effort in the correct use of an infrared thermocamera is suggested for the measurement of the sample surface temperature.

The measurements of the directional spectral emissivity of the microstructured surface have been carried out on undoped silicon only. An extension of the work to other materials is obviously useful to demonstrate the effect of material properties on the angular and spectral control of the radiative properties. The resonant effect may be exploited in further studies of other phenomena such as Raman spectroscopy, photo catalysis, and infrared detectors. These studies would provide additional insight into the process of the enhanced emission from the microstructured surfaces. In order to confirm the results obtained in this work, the measurement of the directional spectral emissivity of a microstructured surface by an other independent measurement technique such as a photo acoustic method would be worthwhile. The effect of microstructured surface on boiling, condensation and viscous forces are important areas for future investigations. Similarly, effect on catalytic chemical reactions and biological systems, for example cell growth, are two further areas still to be explored.

10.3 Applications

The spectral control of the radiative heat transfer by the use of the periodic microstructured surfaces has several applications. Some of them are summarized as follows:

- (i) Infrared detectors with increased sensitivity using the Wood's singularity.
- (ii) Surface enhanced Raman spectroscopy.
- (iii) A high efficiency tungsten filament lamp.
- (iv) Optical matching coating.
- (v) Green house effect.
- (vi) Microstructured plastic optics for display applications.
- (vii) Design of cryogenic systems, solar cells, spacecraft and high temperature heat transfer systems.

Appendix

A Measurement Data for Emissivities

Table A.1. Directional spectral emissivity of Nextel-Velvet-Coating 811-21 measured at temperature 92.5 °C.

Wavelength (λ) in μm	Polar angle (ϑ)							
	0°	10°	20°	30°	40°	50°	60°	70°
4	0.946	0.943	0.939	0.927	0.899	0.931	0.92	0.90
5	0.943	0.943	0.946	0.937	0.932	0.942	0.938	0.929
6	0.948	0.944	0.94	0.949	0.941	0.939	0.935	0.924
7	0.947	0.952	0.95	0.953	0.948	0.942	0.941	0.926
8	0.957	0.959	0.956	0.956	0.953	0.951	0.947	0.933
9	0.959	0.958	0.959	0.958	0.956	0.954	0.949	0.935
10	0.964	0.962	0.963	0.957	0.96	0.956	0.955	0.94
11	0.97	0.971	0.97	0.965	0.968	0.966	0.96	0.947
12	0.97	0.97	0.972	0.966	0.97	0.966	0.961	0.949
13	0.976	0.974	0.974	0.969	0.972	0.971	0.967	0.952
14	0.972	0.973	0.971	0.969	0.969	0.969	0.965	0.949
15	0.974	0.976	0.974	0.969	0.974	0.969	0.966	0.954
16	0.977	0.98	0.976	0.972	0.977	0.971	0.968	0.955
17	0.978	0.978	0.976	0.973	0.974	0.973	0.97	0.954
18	0.975	0.976	0.975	0.971	0.974	0.971	0.966	0.951
19	0.979	0.979	0.978	0.97	0.981	0.973	0.969	0.957
20	0.975	0.979	0.976	0.974	0.975	0.968	0.968	0.953
21	0.985	0.979	0.986	0.969	0.98	0.973	0.973	0.965
22	0.982	0.982	0.979	0.969	0.987	0.973	0.969	0.959
23	0.985	0.988	0.98	0.976	0.984	0.978	0.979	0.967
24	0.986	0.977	0.981	0.968	0.99	0.972	0.976	0.947
25	0.975	0.979	0.967	0.959	0.976	0.951	0.967	0.96

Table A.2. Normal spectral emissivity of Nextel-Velvet-Coating 811-21 measured in present work and that obtained by Lohrengel et al. [90].

Wavelength (λ) in μm	Measured in present work at surface temperature 92.5 °C	Obtained by Lohrengel et al. [90] at surface temperature 90 °C
4	0.946	0.975
5	0.943	0.966
6	0.948	0.985
7	0.947	0.983
8	0.957	0.974
9	0.959	0.969
10	0.964	0.967
11	0.97	0.97
12	0.97	0.972
13	0.976	0.975
14	0.972	0.973
15	0.974	0.983
16	0.977	0.975
17	0.978	0.975
18	0.975	0.977
19	0.979	0.976
20	0.975	0.976
21	0.985	0.977
22	0.982	0.978
23	0.985	0.976
24	0.986	0.986
25	0.975	0.984

Table A.3. Normal total emissivity of Nextel-Velvet-Coating 811-21 at different surface temperatures measured in present work and that obtained by Lohrengel et al. [90] and by Kwor et al. [78].

Present work		Work of Lohrengel et al. [90]		Work of Kwor et al. [78]	
Temperature in °C	Normal total emissivity	Temperature in °C	Normal total emissivity	Temperature in °C	Normal total emissivity
92.5	0.9645	90.0	0.967	32.0	0.975
123.3	0.9567	120.0	0.957	64.0	0.970
148.0	0.9555	150.0	0.959	82.0	0.973

Table A.4. Directional total emissivity of Nextel-Velvet-Coating 811-21 at different sample surface temperatures measured in present experiment and that obtained by Lohrengel et.al. [90].

	Temp. in °C	Polar Angle of emission (ϑ)							
		0°	10°	20°	30°	40°	50°	60°	70°
Present work	92.5	0.9645	0.9638	0.9630	0.9635	0.9616	0.9581	0.9551	0.9415
	123.3	0.9567	0.9597	0.9572	0.9598	0.9571	0.9557	0.9491	0.9401
	148.0	0.9555	0.9537	0.9531	0.9502	0.9489	0.9437	0.9369	0.9202
Work of Lohrengel et al. [90]	Temp. in °C	Polar Angle of emission (ϑ)							
		0°	15°	30°	45°	60°	70°	75°	
	90	0.967	0.967	0.966	0.964	0.953	0.916	0.864	
	120	0.957	0.957	0.957	0.955	0.945	0.912	0.863	
150	0.959	0.959	0.959	0.958	0.948	0.915	0.868		

Table A.5. Hemispherical total emissivity of Nextel-Velvet-Coating 811-21 at different surface temperatures measured in present work and that obtained by Lohrengel et al. [90].

Present work			Work of Lohrengel et al. [90]	
Temperature in °C	Calorimetric method	Radiometric method	Temperature in °C	Radiometric method
92.5	0.935	0.939	90.0	0.941
123.3	0.938	0.936	120.0	0.933
148.0	0.941	0.926	150.0	0.935

Table A.6. Directional spectral emissivity of borosilicate glass B 270 measured at surface temperature 98.8 °C.

Wavelength (λ) in μm	Polar angle (ϑ)							
	0°	10°	20°	30°	40°	50°	60°	70°
4	0.883262	0.926931	0.935892	0.958489	0.935151	0.921817	0.925111	0.654185
5	0.931815	0.926847	0.922664	0.927757	0.922213	0.934858	0.911554	0.6895
6	0.94525	0.939273	0.944736	0.946137	0.94147	0.942303	0.924579	0.709536
7	0.955786	0.953094	0.954414	0.961835	0.954885	0.954094	0.944059	0.735348
8	0.969217	0.968452	0.970024	0.971344	0.972259	0.965289	0.92766	0.638467
9	0.776027	0.768991	0.772927	0.771041	0.758509	0.733897	0.683543	0.481072
10	0.762974	0.753475	0.757489	0.763223	0.75911	0.754385	0.734463	0.567129
11	0.857535	0.842836	0.846411	0.846936	0.843429	0.838461	0.814832	0.621354
12	0.920066	0.916233	0.915424	0.918172	0.914527	0.906391	0.884962	0.674974
13	0.918049	0.907946	0.911218	0.91135	0.907206	0.89836	0.872616	0.662747
14	0.928513	0.922329	0.926156	0.925092	0.922723	0.913702	0.88608	0.672942
15	0.936949	0.934269	0.933398	0.93545	0.930239	0.921229	0.896471	0.681322
16	0.942643	0.941304	0.941693	0.946461	0.935031	0.931288	0.901537	0.688668
17	0.952249	0.954642	0.955305	0.95641	0.946543	0.946582	0.916595	0.696961
18	0.973218	0.968515	0.967289	0.969749	0.961292	0.958044	0.938255	0.722013
19	0.941625	0.928417	0.936199	0.936066	0.927706	0.907659	0.851369	0.606416
20	0.830164	0.82547	0.824177	0.834822	0.823734	0.798235	0.74099	0.540734
21	0.790233	0.765139	0.778781	0.780971	0.778736	0.763226	0.729037	0.543105
22	0.769744	0.768143	0.772244	0.784189	0.757514	0.747269	0.725579	0.548601
23	0.790156	0.792512	0.795122	0.804161	0.779255	0.774536	0.75698	0.565046
24	0.793584	0.83589	0.808635	0.831487	0.798332	0.826882	0.780113	0.600993
25	0.852462	0.79807	0.822564	0.83173	0.852802	0.792054	0.812227	0.593863

Table A.7. Directional total emissivity of borosilicate glass B 270 measured at surface temperature 98.8 °C in present work and that measured by Lohrengel et al. [88] at surface temperature 85 °C. The values of the directional total emissivity at different polar angles calculated with the help of Fresnel's equation are also presented.

Calculated values		Present measurement at temperature, T = 98.8 °C		Measurement of Lohrengel et al. at temperature, T = 85 °C [88]	
Polar angle (ϑ)	Directional total emissivity	Polar angle (ϑ)	Directional total emissivity	Polar angle (ϑ)	Directional total emissivity
0°	0.915	0°	0.9133	0°	0.915
5°	0.915				
10°	0.915	10°	0.9084		
15°	0.915			15°	0.913
20°	0.915	20°	0.9100		
25°	0.914				
30°	0.912	30°	0.9124	30°	0.911
35°	0.910				
40°	0.905	40°	0.9068		
45°	0.898			45°	0.898
50°	0.887	50°	0.9000		
55°	0.870				
60°	0.844	60°	0.8574	60°	0.837
65°	0.805				
70°	0.747	70°	0.7172		
75°	0.660			75°	0.685
80°	0.528				
85°	0.324				
90°	0.000				

Table A.8. Directional spectral emissivity of sand blasted aluminium measured at surface temperature 374 K.

Wavelength (λ) in μm	Polar angle (ϑ)								
	0°	10°	20°	25°	30°	40°	50°	60°	70°
4	0.329464	0.341769	0.29047	0.339695	0.322142	0.328451	0.329596	0.314422	0.281714
5	0.28992	0.293031	0.288453	0.299419	0.286637	0.296769	0.318804	0.312602	0.262175
6	0.314003	0.320126	0.317897	0.323124	0.329008	0.330076	0.338782	0.339025	0.283543
7	0.296217	0.303725	0.306491	0.30822	0.312423	0.316758	0.323398	0.328742	0.275954
8	0.278765	0.282863	0.286291	0.290485	0.290672	0.300305	0.303246	0.308059	0.263458
9	0.289547	0.289818	0.299012	0.304834	0.305848	0.313386	0.31719	0.321704	0.279759
10	0.27432	0.278722	0.2839	0.290756	0.290896	0.299429	0.303666	0.310985	0.262422
11	0.269022	0.275173	0.279988	0.284218	0.287459	0.293032	0.300974	0.305376	0.25593
12	0.304554	0.310351	0.313402	0.320465	0.323203	0.330826	0.343623	0.346606	0.290676
13	0.303535	0.308791	0.313229	0.317191	0.321951	0.327661	0.339802	0.348636	0.287819
14	0.298882	0.307479	0.314998	0.318193	0.321379	0.331282	0.338382	0.347186	0.28752
15	0.301326	0.303607	0.312801	0.315662	0.319356	0.326691	0.338407	0.342604	0.284159
16	0.302522	0.305017	0.312524	0.314452	0.320992	0.330772	0.337709	0.343816	0.281628
17	0.285667	0.292344	0.300099	0.302654	0.308794	0.317702	0.320861	0.323453	0.268691
18	0.298723	0.305972	0.311499	0.314138	0.31998	0.328904	0.333893	0.33822	0.280677
19	0.295398	0.291929	0.299027	0.303693	0.310909	0.309071	0.318261	0.330195	0.2742
20	0.274834	0.281757	0.285349	0.297786	0.293714	0.305425	0.316233	0.31698	0.26914
21	0.286609	0.282763	0.289963	0.303674	0.302409	0.318092	0.322541	0.330685	0.277986
22	0.277485	0.278923	0.296198	0.288181	0.309395	0.304123	0.310683	0.321325	0.270409
23	0.274355	0.268955	0.316296	0.28177	0.28976	0.284419	0.295952	0.320123	0.258974
24	0.285821	0.293207	0.278777	0.317746	0.329522	0.291874	0.31351	0.32617	0.270914
25	0.250544	0.312033	0.266375	0.311202	0.281938	0.270586	0.320643	0.321813	0.225882

Table A.9. Directional total emissivity of sand blasted aluminium measured at the surface temperature 374 K.

Polar angle (ϑ)	0°	10°	20°	25°	30°	40°	50°	60°	70°
Directional total emissivity	0.29	0.295	0.300	0.304	0.307	0.313	0.320	0.326	0.273

Table A.10. Directional spectral emissivity of a smooth undoped silicon wafer measured at the surface temperature 199.1°C.

Wavelength (λ) in μm	Polar angle (ϑ)							
	0°	10°	20°	30°	40°	50°	60°	70°
4	0.10336	0.097072	0.100231	0.108301	0.111607	0.122861	0.135087	0.112242
5	0.10354	0.100823	0.103198	0.111209	0.119666	0.132217	0.146148	0.12768
6	0.125968	0.122694	0.12686	0.136963	0.149736	0.166198	0.18356	0.163113
7	0.217842	0.214152	0.220852	0.233606	0.252934	0.277231	0.303836	0.260469
8	0.213303	0.211087	0.21828	0.231414	0.252375	0.276547	0.301728	0.259622
9	0.396874	0.394642	0.399995	0.409151	0.42305	0.440759	0.457841	0.373055
10	0.274545	0.273999	0.281863	0.294715	0.31472	0.337841	0.361242	0.306093
11	0.360026	0.350651	0.358741	0.371547	0.388905	0.407923	0.427499	0.352343
12	0.361318	0.354948	0.361625	0.37379	0.391959	0.412723	0.431556	0.354709
13	0.403498	0.394285	0.401024	0.411952	0.428321	0.445646	0.460568	0.375581
14	0.376811	0.372639	0.379838	0.389902	0.409873	0.428372	0.444812	0.360308
15	0.322492	0.321524	0.332362	0.346263	0.368301	0.392352	0.415846	0.336909
16	0.485166	0.482211	0.490059	0.496881	0.507778	0.519131	0.527844	0.42035
17	0.490577	0.486444	0.492477	0.494876	0.509779	0.517655	0.526202	0.418743
18	0.441027	0.440272	0.445403	0.450357	0.471399	0.475408	0.489821	0.395611
19	0.410112	0.405789	0.41396	0.424029	0.442015	0.45535	0.460443	0.376421
20	0.403667	0.397921	0.404652	0.418323	0.428082	0.451117	0.449799	0.365114
21	0.374597	0.363691	0.372229	0.384396	0.391732	0.423338	0.419585	0.342625
22	0.330454	0.32926	0.337729	0.344415	0.359974	0.390057	0.393805	0.313865
23	0.302031	0.308124	0.310706	0.32008	0.345371	0.362071	0.387655	0.292138
24	0.289467	0.290534	0.303583	0.303551	0.341379	0.354743	0.380537	0.285595
25	0.285812	0.2748	0.300833	0.304959	0.341886	0.33639	0.363887	0.28209

Table A.11. Normal spectral emissivity of a smooth undoped silicon wafer measured in present work and that measured by Stierwalt et al. [144] and by Sato [134].

Wavelength (λ) in μm	Present Measurement at temperature, $T = 199.1\text{ }^\circ\text{C}$	Measurement of Stierwalt et al. [144] at temperature, $T = 200\text{ }^\circ\text{C}$	Measurement of Sato [134] at temperature, $T = 269.85\text{ }^\circ\text{C}$
4	0.10336	0.03	0.06
5	0.10354	0.027	0.065
6	0.125968	0.03	0.08
7	0.217842	0.12	0.23
8	0.213303	0.11	0.22
9	0.396874	0.36	0.45
10	0.274545	0.21	0.30
11	0.360026	0.35	0.44
12	0.361318	0.34	0.45
13	0.403498	0.41	0.50
14	0.376811	0.35	0.55
15	0.322492	0.28	0.46
16	0.485166	0.45	
17	0.490577	0.52	
18	0.441027	0.46	
19	0.410112	0.41	
20	0.403667	0.38	
21	0.374597		
22	0.330454		
23	0.302031		
24	0.289467		
25	0.285812		

Table A.12. Directional total emissivity of a smooth undoped silicon wafer measured at the surface temperature $199.1\text{ }^\circ\text{C}$.

Polar angle (ϑ)	0°	10°	20°	30°	40°	50°	60°	70°
Directional total emissivity	0.252	0.249	0.255	0.265	0.281	0.300	0.318	0.266

Table A.13. Directional spectral emissivity of a microgrooved undoped silicon surface at an azimuthal angle, $\varphi = 90^\circ$ for a groove depth, $H = 34.2 \mu\text{m}$ ($T = 200 \text{ }^\circ\text{C}$).

Wavelength (λ) in μm	Polar angle, ϑ												
	0°	6°	12°	18°	24°	30°	36°	42°	48°	54°	60°	66°	70°
4.0	0.198	0.192	0.189	0.192	0.197	0.183	0.176	0.188	0.178	0.176	0.175	0.147	0.135
5.012	0.236	0.231	0.228	0.225	0.225	0.217	0.213	0.215	0.225	0.218	0.205	0.181	0.157
6.0241	0.266	0.264	0.26	0.254	0.256	0.262	0.259	0.247	0.244	0.246	0.24	0.23	0.196
7.0361	0.391	0.386	0.383	0.391	0.401	0.384	0.392	0.393	0.381	0.371	0.39	0.344	0.297
8.0482	0.382	0.374	0.37	0.384	0.395	0.357	0.368	0.364	0.372	0.378	0.369	0.347	0.308
9.0602	0.571	0.561	0.594	0.58	0.562	0.593	0.592	0.607	0.574	0.568	0.547	0.49	0.421
10.072	0.537	0.524	0.5	0.49	0.482	0.474	0.499	0.479	0.503	0.494	0.511	0.46	0.403
11.0	0.611	0.6	0.563	0.567	0.55	0.582	0.599	0.576	0.573	0.541	0.529	0.486	0.433
12.096	0.662	0.656	0.635	0.58	0.598	0.571	0.553	0.537	0.554	0.536	0.522	0.482	0.436
13.024	0.66	0.658	0.653	0.67	0.634	0.599	0.593	0.592	0.586	0.565	0.576	0.5	0.436
14.036	0.663	0.651	0.608	0.645	0.597	0.57	0.563	0.558	0.554	0.552	0.549	0.52	0.481
15.048	0.572	0.566	0.585	0.618	0.596	0.58	0.575	0.553	0.54	0.523	0.507	0.467	0.427
16.06	0.754	0.748	0.725	0.715	0.714	0.738	0.752	0.716	0.683	0.667	0.645	0.598	0.538
17.072	0.714	0.708	0.709	0.728	0.728	0.723	0.723	0.724	0.707	0.689	0.669	0.624	0.572
18.0	0.69	0.68	0.688	0.705	0.721	0.709	0.69	0.669	0.657	0.646	0.623	0.573	0.523
19.012	0.678	0.667	0.675	0.676	0.682	0.683	0.666	0.643	0.635	0.63	0.635	0.599	0.54
20.024	0.671	0.66	0.678	0.689	0.671	0.643	0.651	0.675	0.682	0.661	0.625	0.571	0.529
21.036	0.636	0.626	0.61	0.651	0.635	0.61	0.65	0.645	0.614	0.604	0.6	0.576	0.542
22.048	0.633	0.632	0.609	0.608	0.6	0.61	0.619	0.62	0.615	0.606	0.593	0.563	0.53
23.06	0.609	0.595	0.586	0.589	0.582	0.577	0.588	0.595	0.604	0.574	0.539	0.519	0.499
24.072	0.605	0.595	0.581	0.581	0.571	0.566	0.574	0.575	0.59	0.568	0.568	0.544	0.518
25.0	0.60	0.579	0.552	0.574	0.553	0.562	0.561	0.562	0.552	0.542	0.543	0.531	0.507

Table A.14. Directional spectral emissivity of a microgrooved undoped silicon surface at an azimuthal angle, $\varphi = 0^\circ$ for a groove depth, $H = 34.2 \mu\text{m}$ ($T = 200^\circ\text{C}$).

Wavelength (λ) in μm	Polar angle, ϑ												
	0°	6°	12°	18°	24°	30°	36°	42°	48°	54°	60°	66°	70°
4.0	0.175	0.167	0.168	0.169	0.174	0.184	0.181	0.179	0.189	0.194	0.193	0.192	0.158
5.012	0.229	0.222	0.215	0.204	0.204	0.217	0.233	0.232	0.243	0.236	0.242	0.242	0.205
6.0241	0.261	0.267	0.268	0.266	0.271	0.282	0.285	0.284	0.291	0.293	0.333	0.307	0.269
7.0361	0.388	0.408	0.403	0.399	0.401	0.419	0.423	0.432	0.471	0.523	0.524	0.515	0.449
8.0482	0.381	0.42	0.425	0.433	0.416	0.438	0.444	0.523	0.529	0.539	0.54	0.526	0.458
9.0602	0.562	0.602	0.612	0.634	0.645	0.679	0.73	0.689	0.711	0.699	0.73	0.651	0.613
10.072	0.544	0.592	0.603	0.62	0.604	0.571	0.606	0.633	0.607	0.641	0.615	0.596	0.529
11.0	0.613	0.622	0.612	0.618	0.626	0.65	0.643	0.666	0.662	0.625	0.664	0.637	0.578
12.012	0.659	0.679	0.663	0.646	0.624	0.63	0.649	0.613	0.652	0.676	0.648	0.631	0.563
13.024	0.644	0.659	0.652	0.659	0.689	0.702	0.657	0.677	0.711	0.681	0.702	0.654	0.611
14.036	0.663	0.673	0.674	0.674	0.664	0.669	0.702	0.665	0.627	0.683	0.666	0.659	0.608
15.048	0.568	0.576	0.577	0.587	0.603	0.629	0.627	0.627	0.663	0.64	0.65	0.647	0.588
16.06	0.757	0.763	0.769	0.776	0.753	0.74	0.756	0.76	0.725	0.794	0.8	0.75	0.665
17.072	0.723	0.73	0.728	0.729	0.731	0.765	0.77	0.751	0.763	0.776	0.767	0.717	0.644
18.0	0.684	0.687	0.687	0.7	0.706	0.714	0.746	0.75	0.763	0.744	0.736	0.688	0.628
19.012	0.673	0.676	0.679	0.682	0.688	0.705	0.715	0.718	0.714	0.699	0.701	0.665	0.617
20.024	0.67	0.685	0.675	0.684	0.682	0.685	0.69	0.699	0.696	0.692	0.693	0.666	0.619
21.036	0.638	0.652	0.645	0.651	0.648	0.665	0.675	0.682	0.687	0.69	0.679	0.656	0.606
22.048	0.634	0.652	0.636	0.639	0.636	0.648	0.652	0.645	0.659	0.664	0.658	0.639	0.599
23.06	0.605	0.625	0.614	0.623	0.627	0.641	0.637	0.639	0.654	0.641	0.636	0.627	0.582
24.072	0.607	0.628	0.63	0.631	0.616	0.639	0.612	0.615	0.644	0.624	0.636	0.623	0.578
25.0	0.585	0.613	0.615	0.622	0.601	0.617	0.612	0.628	0.647	0.615	0.628	0.619	0.575

Table A.15. Directional spectral emissivity of a microgrooved undoped silicon surface at an azimuthal angle, $\phi = 90^\circ$ for a groove depth, $H = 21.4 \mu\text{m}$ ($T = 200 \text{ }^\circ\text{C}$).

Wavelength (λ) in μm	Polar angle, ϑ												
	0°	6°	12°	18°	24°	30°	36°	42°	48°	54°	60°	66°	70°
4.0	0.184	0.18	0.178	0.181	0.173	0.176	0.178	0.171	0.166	0.168	0.162	0.146	0.126
5.012	0.217	0.22	0.223	0.218	0.213	0.216	0.218	0.215	0.207	0.214	0.212	0.181	0.158
6.0241	0.263	0.26	0.255	0.262	0.258	0.263	0.267	0.253	0.251	0.254	0.242	0.213	0.187
7.0361	0.368	0.367	0.379	0.38	0.407	0.388	0.386	0.385	0.386	0.38	0.385	0.359	0.302
8.0482	0.385	0.386	0.383	0.393	0.382	0.38	0.382	0.372	0.379	0.381	0.372	0.35	0.309
9.0602	0.561	0.559	0.582	0.596	0.574	0.575	0.598	0.559	0.569	0.578	0.547	0.496	0.43
10.072	0.542	0.531	0.514	0.479	0.476	0.482	0.506	0.489	0.495	0.493	0.459	0.424	0.393
11.084	0.653	0.647	0.598	0.584	0.575	0.575	0.556	0.547	0.577	0.579	0.555	0.509	0.449
12.012	0.648	0.647	0.643	0.567	0.571	0.6	0.588	0.56	0.566	0.553	0.54	0.492	0.433
13.024	0.698	0.694	0.678	0.674	0.582	0.632	0.61	0.601	0.598	0.598	0.59	0.521	0.466
14.036	0.543	0.545	0.629	0.666	0.638	0.582	0.561	0.55	0.546	0.538	0.528	0.485	0.434
15.048	0.592	0.595	0.595	0.605	0.597	0.599	0.577	0.557	0.548	0.534	0.523	0.493	0.46
16.06	0.754	0.75	0.73	0.718	0.705	0.701	0.705	0.692	0.679	0.671	0.663	0.618	0.558
17.072	0.736	0.731	0.734	0.725	0.697	0.695	0.704	0.703	0.719	0.682	0.678	0.62	0.558
18.0	0.669	0.666	0.666	0.684	0.703	0.715	0.709	0.693	0.681	0.664	0.623	0.559	0.503
19.012	0.65	0.647	0.648	0.651	0.649	0.656	0.667	0.654	0.652	0.654	0.65	0.615	0.542
20.024	0.675	0.672	0.679	0.687	0.679	0.675	0.667	0.65	0.644	0.64	0.619	0.571	0.519
21.036	0.644	0.638	0.643	0.661	0.647	0.639	0.646	0.632	0.65	0.665	0.665	0.625	0.573
22.048	0.599	0.602	0.589	0.631	0.628	0.634	0.622	0.578	0.585	0.576	0.574	0.549	0.516
23.06	0.607	0.601	0.594	0.591	0.588	0.608	0.61	0.593	0.589	0.58	0.565	0.533	0.498
24.072	0.604	0.611	0.596	0.6	0.591	0.585	0.609	0.594	0.592	0.587	0.58	0.551	0.517
25.0	0.587	0.605	0.575	0.59	0.585	0.573	0.6	0.585	0.598	0.568	0.57	0.547	0.507

Table A.16. Directional spectral emissivity of a microgrooved undoped silicon surface at an azimuthal angle, $\varphi = 0^\circ$ for a groove depth, $H = 21.4 \mu\text{m}$ ($T = 200^\circ\text{C}$).

Wavelength (λ) in μm	Polar angle, ϑ												
	0°	6°	12°	18°	24°	30°	36°	42°	48°	54°	60°	66°	70°
4.0	0.176	0.169	0.173	0.173	0.17	0.173	0.184	0.191	0.188	0.194	0.194	0.184	0.169
5.012	0.211	0.21	0.213	0.22	0.217	0.217	0.218	0.233	0.243	0.24	0.24	0.242	0.209
6.0241	0.258	0.256	0.262	0.258	0.263	0.267	0.275	0.271	0.269	0.292	0.295	0.292	0.261
7.0361	0.363	0.361	0.36	0.368	0.371	0.386	0.4	0.414	0.447	0.511	0.489	0.475	0.439
8.0482	0.376	0.372	0.373	0.378	0.376	0.375	0.401	0.484	0.503	0.517	0.524	0.504	0.45
9.0602	0.559	0.555	0.563	0.564	0.573	0.633	0.678	0.707	0.671	0.656	0.713	0.631	0.546
10.072	0.557	0.563	0.578	0.587	0.605	0.556	0.524	0.554	0.608	0.581	0.597	0.609	0.52
11.0	0.645	0.642	0.628	0.628	0.631	0.644	0.681	0.677	0.637	0.667	0.682	0.577	0.539
12.012	0.643	0.643	0.639	0.643	0.64	0.614	0.581	0.599	0.652	0.678	0.614	0.636	0.609
13.024	0.695	0.697	0.703	0.705	0.681	0.663	0.685	0.733	0.678	0.601	0.665	0.688	0.574
14.036	0.553	0.551	0.575	0.617	0.639	0.662	0.699	0.694	0.665	0.662	0.7	0.602	0.574
15.048	0.591	0.592	0.595	0.613	0.629	0.629	0.59	0.571	0.6	0.663	0.645	0.617	0.592
16.06	0.762	0.76	0.765	0.772	0.756	0.732	0.726	0.746	0.782	0.737	0.75	0.765	0.685
17.072	0.739	0.736	0.732	0.732	0.722	0.723	0.741	0.766	0.744	0.725	0.773	0.727	0.653
18.0	0.673	0.668	0.667	0.673	0.677	0.712	0.74	0.735	0.725	0.741	0.741	0.692	0.626
19.012	0.642	0.641	0.647	0.661	0.682	0.695	0.684	0.711	0.723	0.711	0.709	0.671	0.615
20.024	0.678	0.676	0.656	0.64	0.625	0.645	0.711	0.713	0.695	0.678	0.68	0.648	0.605
21.036	0.646	0.638	0.637	0.646	0.652	0.651	0.649	0.647	0.65	0.644	0.646	0.615	0.576
22.048	0.602	0.605	0.591	0.597	0.6	0.607	0.621	0.625	0.635	0.631	0.644	0.613	0.576
23.06	0.602	0.604	0.609	0.613	0.604	0.609	0.619	0.62	0.622	0.617	0.619	0.584	0.553
24.072	0.614	0.603	0.601	0.604	0.592	0.598	0.605	0.609	0.607	0.605	0.621	0.59	0.562
25.0	0.594	0.584	0.595	0.59	0.582	0.595	0.605	0.606	0.626	0.61	0.633	0.603	0.56

Table A.17. Directional spectral emissivity of a microgrooved undoped silicon surface at an azimuthal angle, $\varphi = 90^\circ$ for a groove depth, $H = 11.2 \mu\text{m}$ ($T = 200 \text{ }^\circ\text{C}$).

Wavelength (λ) in μm	Polar angle, ϑ												
	0°	6°	12°	18°	24°	30°	36°	42°	48°	54°	60°	66°	70°
4.0	0.179	0.178	0.176	0.169	0.173	0.167	0.17	0.166	0.179	0.168	0.163	0.156	0.136
5.012	0.226	0.223	0.219	0.208	0.207	0.208	0.22	0.218	0.204	0.202	0.202	0.198	0.162
6.0241	0.279	0.278	0.29	0.284	0.266	0.269	0.279	0.269	0.259	0.259	0.264	0.248	0.221
7.0361	0.408	0.412	0.415	0.421	0.437	0.422	0.425	0.422	0.418	0.41	0.395	0.361	0.318
8.0482	0.421	0.422	0.416	0.456	0.431	0.434	0.43	0.422	0.437	0.435	0.417	0.384	0.347
9.0602	0.606	0.607	0.632	0.654	0.662	0.63	0.622	0.615	0.623	0.638	0.624	0.565	0.486
10.072	0.556	0.546	0.537	0.536	0.534	0.524	0.531	0.533	0.547	0.545	0.526	0.483	0.436
11.0	0.611	0.604	0.558	0.53	0.534	0.535	0.542	0.548	0.549	0.602	0.576	0.52	0.471
12.012	0.626	0.626	0.64	0.623	0.625	0.617	0.591	0.604	0.593	0.581	0.57	0.532	0.478
13.024	0.657	0.656	0.668	0.687	0.634	0.642	0.663	0.626	0.617	0.614	0.607	0.565	0.509
14.036	0.646	0.643	0.631	0.66	0.714	0.614	0.592	0.58	0.578	0.562	0.551	0.514	0.462
15.048	0.621	0.621	0.64	0.629	0.611	0.594	0.572	0.558	0.544	0.54	0.521	0.488	0.443
16.06	0.748	0.748	0.753	0.766	0.753	0.754	0.769	0.717	0.695	0.68	0.664	0.616	0.552
17.072	0.707	0.702	0.701	0.714	0.727	0.75	0.741	0.735	0.726	0.659	0.647	0.595	0.54
18.0	0.661	0.655	0.664	0.677	0.688	0.694	0.708	0.72	0.707	0.695	0.655	0.594	0.541
19.012	0.656	0.65	0.66	0.663	0.66	0.68	0.705	0.721	0.711	0.711	0.686	0.637	0.58
20.024	0.683	0.68	0.666	0.658	0.655	0.661	0.676	0.674	0.688	0.702	0.693	0.666	0.611
21.036	0.678	0.664	0.662	0.654	0.647	0.644	0.637	0.625	0.627	0.626	0.621	0.596	0.554
22.048	0.621	0.616	0.621	0.649	0.653	0.636	0.613	0.604	0.605	0.585	0.573	0.539	0.505
23.06	0.607	0.6	0.597	0.599	0.611	0.62	0.622	0.612	0.6	0.581	0.572	0.543	0.51
24.072	0.623	0.615	0.625	0.594	0.577	0.585	0.612	0.623	0.603	0.598	0.591	0.559	0.527
25.0	0.624	0.604	0.603	0.583	0.584	0.592	0.616	0.603	0.582	0.594	0.595	0.561	0.533

Table A.18. Directional spectral emissivity of a microgrooved undoped silicon surface at an azimuthal angle, $\varphi = 0^\circ$ for a groove depth, $H = 11.2 \mu\text{m}$ ($T = 200 \text{ }^\circ\text{C}$).

Wavelength (λ) in μm	Polar angle, ϑ												
	0°	6°	12°	18°	24°	30°	36°	42°	48°	54°	60°	66°	70°
4.0	0.179	0.18	0.177	0.173	0.177	0.182	0.197	0.18	0.196	0.207	0.203	0.197	0.157
5.012	0.225	0.223	0.219	0.223	0.221	0.225	0.229	0.226	0.23	0.241	0.239	0.246	0.217
6.0241	0.276	0.275	0.279	0.287	0.293	0.294	0.29	0.296	0.298	0.295	0.307	0.331	0.306
7.0361	0.408	0.405	0.402	0.4	0.404	0.408	0.413	0.423	0.447	0.523	0.583	0.472	0.417
8.0482	0.42	0.416	0.414	0.412	0.408	0.404	0.412	0.506	0.536	0.531	0.549	0.527	0.454
9.0602	0.608	0.604	0.612	0.629	0.665	0.715	0.735	0.726	0.698	0.696	0.718	0.707	0.632
10.072	0.572	0.574	0.59	0.603	0.593	0.586	0.584	0.6	0.632	0.671	0.679	0.609	0.507
11.0	0.61	0.605	0.594	0.594	0.583	0.587	0.598	0.634	0.673	0.675	0.639	0.573	0.512
12.012	0.618	0.617	0.612	0.632	0.655	0.673	0.694	0.684	0.661	0.621	0.604	0.597	0.573
13.024	0.673	0.669	0.657	0.668	0.69	0.714	0.716	0.704	0.675	0.655	0.666	0.698	0.668
14.036	0.65	0.648	0.653	0.668	0.672	0.667	0.66	0.658	0.661	0.668	0.689	0.689	0.624
15.048	0.633	0.629	0.623	0.627	0.633	0.635	0.628	0.633	0.641	0.672	0.696	0.67	0.595
16.06	0.754	0.751	0.75	0.752	0.743	0.737	0.739	0.748	0.769	0.811	0.828	0.777	0.678
17.072	0.721	0.717	0.713	0.711	0.704	0.712	0.722	0.738	0.783	0.807	0.813	0.762	0.677
18.0	0.66	0.657	0.66	0.666	0.668	0.686	0.708	0.761	0.801	0.804	0.794	0.732	0.652
19.012	0.65	0.648	0.658	0.661	0.665	0.672	0.70	0.738	0.736	0.727	0.724	0.683	0.624
20.024	0.693	0.697	0.689	0.694	0.692	0.702	0.717	0.727	0.721	0.73	0.718	0.686	0.627
21.036	0.695	0.683	0.678	0.675	0.668	0.674	0.673	0.657	0.657	0.664	0.656	0.638	0.588
22.048	0.618	0.61	0.602	0.605	0.603	0.617	0.607	0.615	0.628	0.631	0.632	0.621	0.574
23.06	0.599	0.599	0.603	0.611	0.612	0.619	0.611	0.627	0.648	0.636	0.638	0.626	0.581
24.072	0.627	0.623	0.639	0.642	0.629	0.623	0.629	0.642	0.651	0.642	0.652	0.627	0.584
25.0	0.639	0.631	0.654	0.652	0.627	0.627	0.641	0.642	0.629	0.65	0.664	0.644	0.594

Table A.19. Directional spectral emissivity of a microgrooved undoped silicon surface at an azimuthal angle, $\varphi = 90^\circ$ for a groove depth, $H = 3.4 \mu\text{m}$ ($T = 200^\circ\text{C}$).

Wavelength (λ) in μm	Polar angle, ϑ												
	0°	6°	12°	18°	24°	30°	36°	42°	48°	54°	60°	66°	70°
4.0	0.163	0.162	0.169	0.169	0.164	0.175	0.173	0.166	0.167	0.168	0.159	0.147	0.134
5.012	0.225	0.23	0.221	0.209	0.205	0.204	0.193	0.189	0.186	0.191	0.2	0.189	0.167
6.0241	0.289	0.288	0.28	0.28	0.266	0.257	0.256	0.243	0.243	0.246	0.243	0.223	0.195
7.0361	0.41	0.408	0.408	0.41	0.427	0.41	0.414	0.41	0.409	0.404	0.397	0.362	0.313
8.0482	0.406	0.408	0.428	0.44	0.431	0.432	0.432	0.422	0.425	0.423	0.421	0.388	0.34
9.0602	0.603	0.605	0.628	0.63	0.634	0.636	0.641	0.638	0.632	0.628	0.593	0.533	0.462
10.072	0.556	0.546	0.541	0.544	0.544	0.538	0.54	0.533	0.535	0.537	0.533	0.49	0.433
11.0	0.694	0.689	0.628	0.618	0.611	0.612	0.614	0.597	0.588	0.578	0.561	0.512	0.446
12.012	0.695	0.69	0.682	0.631	0.608	0.609	0.615	0.608	0.596	0.579	0.559	0.507	0.447
13.024	0.722	0.717	0.701	0.694	0.638	0.631	0.633	0.625	0.613	0.595	0.576	0.521	0.461
14.036	0.687	0.683	0.682	0.679	0.672	0.618	0.598	0.578	0.569	0.556	0.541	0.499	0.448
15.048	0.641	0.641	0.636	0.642	0.636	0.614	0.576	0.558	0.548	0.533	0.514	0.474	0.432
16.06	0.774	0.771	0.77	0.772	0.763	0.762	0.761	0.719	0.693	0.67	0.65	0.59	0.527
17.072	0.755	0.751	0.755	0.763	0.762	0.769	0.76	0.758	0.749	0.695	0.675	0.611	0.55
18.0	0.729	0.724	0.731	0.741	0.742	0.741	0.74	0.738	0.731	0.735	0.683	0.616	0.555
19.012	0.719	0.715	0.71	0.704	0.701	0.711	0.715	0.704	0.696	0.695	0.685	0.655	0.577
20.024	0.724	0.72	0.709	0.705	0.692	0.692	0.69	0.688	0.682	0.675	0.657	0.62	0.57
21.036	0.701	0.691	0.682	0.683	0.673	0.671	0.659	0.643	0.645	0.636	0.626	0.592	0.545
22.048	0.67	0.665	0.652	0.653	0.643	0.636	0.63	0.62	0.618	0.597	0.586	0.559	0.521
23.06	0.645	0.648	0.641	0.636	0.623	0.614	0.618	0.602	0.602	0.585	0.575	0.543	0.509
24.072	0.635	0.626	0.628	0.614	0.604	0.608	0.613	0.609	0.591	0.577	0.571	0.542	0.507
25.0	0.628	0.608	0.612	0.612	0.602	0.615	0.621	0.589	0.59	0.574	0.581	0.54	0.52

Table A.20. Directional spectral emissivity of a microgrooved undoped silicon surface at an azimuthal angle, $\varphi = 0^\circ$ for a groove depth, $H = 3.4 \mu\text{m}$ ($T = 200^\circ\text{C}$).

Wavelength (λ) in μm	Polar angle, ϑ												
	0°	6°	12°	18°	24°	30°	36°	42°	48°	54°	60°	66°	70°
4.0	0.161	0.159	0.159	0.161	0.169	0.172	0.181	0.191	0.194	0.19	0.203	0.195	0.176
5.012	0.225	0.225	0.224	0.222	0.222	0.222	0.226	0.226	0.224	0.223	0.233	0.256	0.221
6.0241	0.29	0.291	0.291	0.287	0.29	0.285	0.29	0.292	0.287	0.286	0.328	0.33	0.304
7.0361	0.405	0.405	0.398	0.4	0.402	0.403	0.404	0.408	0.482	0.551	0.565	0.523	0.454
8.0482	0.403	0.402	0.398	0.402	0.41	0.418	0.451	0.539	0.541	0.54	0.54	0.505	0.449
9.0602	0.595	0.595	0.596	0.608	0.63	0.693	0.704	0.719	0.738	0.758	0.778	0.747	0.672
10.072	0.562	0.566	0.571	0.583	0.591	0.603	0.619	0.639	0.658	0.675	0.684	0.643	0.568
11.0	0.686	0.687	0.677	0.68	0.687	0.696	0.71	0.722	0.733	0.73	0.719	0.661	0.586
12.012	0.69	0.69	0.679	0.684	0.689	0.696	0.698	0.709	0.705	0.7	0.69	0.636	0.572
13.024	0.72	0.722	0.711	0.715	0.712	0.718	0.723	0.716	0.719	0.704	0.694	0.645	0.582
14.036	0.681	0.681	0.677	0.683	0.687	0.688	0.688	0.688	0.682	0.677	0.665	0.625	0.568
15.048	0.642	0.644	0.64	0.646	0.647	0.647	0.652	0.649	0.649	0.645	0.638	0.599	0.55
16.06	0.772	0.773	0.772	0.776	0.776	0.776	0.775	0.77	0.769	0.758	0.752	0.703	0.641
17.072	0.756	0.754	0.753	0.759	0.758	0.753	0.75	0.751	0.747	0.74	0.737	0.693	0.636
18.0	0.727	0.728	0.727	0.733	0.731	0.732	0.738	0.739	0.738	0.738	0.732	0.692	0.642
19.012	0.718	0.716	0.715	0.72	0.721	0.725	0.734	0.73	0.734	0.739	0.728	0.694	0.644
20.024	0.719	0.719	0.712	0.718	0.72	0.727	0.729	0.727	0.733	0.737	0.728	0.701	0.651
21.036	0.699	0.692	0.683	0.694	0.695	0.694	0.694	0.697	0.712	0.701	0.703	0.677	0.631
22.048	0.665	0.672	0.656	0.663	0.656	0.645	0.655	0.663	0.674	0.66	0.667	0.637	0.599
23.06	0.636	0.643	0.631	0.63	0.618	0.617	0.63	0.642	0.635	0.628	0.641	0.606	0.577
24.072	0.616	0.619	0.605	0.611	0.608	0.606	0.62	0.63	0.618	0.619	0.63	0.59	0.568
25.0	0.591	0.613	0.578	0.593	0.597	0.598	0.613	0.595	0.601	0.602	0.617	0.575	0.56

Table A.21. Directional spectral emissivity of a microgrooved undoped silicon surface at an azimuthal angle, $\varphi = 90^\circ$ for a groove depth, $H = 1 \mu\text{m}$ ($T = 200^\circ\text{C}$).

Wavelength (λ) in μm	Polar angle, ϑ												
	0°	6°	12°	18°	24°	30°	36°	42°	48°	54°	60°	66°	70°
4.0	0.17	0.171	0.17	0.165	0.166	0.169	0.177	0.172	0.169	0.165	0.161	0.15	0.13
5.012	0.217	0.224	0.219	0.217	0.215	0.218	0.198	0.192	0.192	0.187	0.183	0.171	0.15
6.0241	0.282	0.284	0.281	0.276	0.264	0.254	0.25	0.25	0.248	0.246	0.236	0.22	0.196
7.0361	0.412	0.406	0.41	0.401	0.421	0.4	0.404	0.401	0.399	0.399	0.395	0.366	0.32
8.0482	0.414	0.41	0.406	0.416	0.421	0.415	0.415	0.408	0.407	0.404	0.394	0.375	0.326
9.0602	0.586	0.581	0.609	0.607	0.599	0.607	0.601	0.597	0.597	0.592	0.575	0.536	0.472
10.072	0.525	0.521	0.513	0.502	0.502	0.506	0.503	0.495	0.508	0.507	0.501	0.469	0.422
11.0	0.59	0.589	0.546	0.539	0.535	0.542	0.542	0.54	0.538	0.534	0.524	0.494	0.447
12.012	0.592	0.595	0.585	0.555	0.544	0.551	0.55	0.549	0.544	0.541	0.542	0.509	0.465
13.024	0.623	0.625	0.609	0.614	0.581	0.57	0.58	0.571	0.579	0.568	0.557	0.531	0.483
14.036	0.6	0.599	0.588	0.587	0.59	0.56	0.55	0.552	0.544	0.547	0.538	0.511	0.472
15.048	0.561	0.563	0.551	0.558	0.558	0.546	0.526	0.509	0.52	0.511	0.521	0.492	0.459
16.06	0.691	0.692	0.687	0.684	0.684	0.694	0.687	0.673	0.665	0.662	0.654	0.631	0.576
17.072	0.682	0.683	0.678	0.687	0.691	0.678	0.678	0.696	0.675	0.666	0.645	0.627	0.571
18.0	0.65	0.653	0.653	0.655	0.644	0.643	0.652	0.646	0.653	0.66	0.622	0.593	0.547
19.012	0.626	0.626	0.627	0.619	0.621	0.628	0.627	0.624	0.635	0.621	0.631	0.591	0.546
20.024	0.626	0.625	0.613	0.614	0.616	0.616	0.613	0.616	0.626	0.608	0.618	0.582	0.55
21.036	0.61	0.603	0.593	0.596	0.588	0.582	0.587	0.596	0.582	0.584	0.583	0.56	0.529
22.048	0.6	0.61	0.581	0.57	0.563	0.564	0.582	0.574	0.567	0.574	0.56	0.549	0.519
23.06	0.553	0.564	0.544	0.543	0.538	0.553	0.565	0.536	0.546	0.557	0.532	0.525	0.499
24.072	0.546	0.561	0.544	0.551	0.542	0.557	0.549	0.539	0.552	0.551	0.536	0.524	0.49
25.0	0.535	0.567	0.549	0.564	0.543	0.546	0.54	0.528	0.562	0.549	0.537	0.522	0.505

Table A.22. Directional spectral emissivity of a microgrooved undoped silicon surface at an azimuthal angle, $\phi = 0^\circ$ for a groove depth, $H = 1 \mu\text{m}$ ($T = 200^\circ\text{C}$).

Wavelength (λ) in μm	Polar angle, ϑ												
	0°	6°	12°	18°	24°	30°	36°	42°	48°	54°	60°	66°	70°
4.0	0.168	0.172	0.167	0.172	0.175	0.18	0.184	0.196	0.204	0.206	0.211	0.196	0.182
5.012	0.222	0.221	0.221	0.224	0.226	0.232	0.236	0.245	0.248	0.254	0.244	0.22	0.199
6.0241	0.283	0.284	0.282	0.286	0.288	0.294	0.297	0.301	0.302	0.295	0.288	0.269	0.242
7.0361	0.41	0.408	0.406	0.409	0.412	0.416	0.424	0.431	0.468	0.476	0.47	0.442	0.394
8.0482	0.408	0.405	0.405	0.406	0.411	0.412	0.432	0.477	0.481	0.483	0.483	0.456	0.408
9.0602	0.586	0.584	0.582	0.591	0.612	0.652	0.658	0.654	0.654	0.65	0.643	0.602	0.534
10.072	0.525	0.524	0.528	0.535	0.547	0.549	0.559	0.563	0.568	0.565	0.563	0.531	0.477
11.0	0.59	0.586	0.578	0.583	0.587	0.589	0.597	0.598	0.602	0.599	0.594	0.561	0.506
12.012	0.595	0.594	0.584	0.585	0.589	0.594	0.597	0.598	0.602	0.6	0.597	0.566	0.517
13.024	0.626	0.624	0.615	0.617	0.616	0.619	0.622	0.624	0.626	0.623	0.622	0.59	0.539
14.036	0.599	0.595	0.591	0.596	0.597	0.597	0.605	0.604	0.608	0.607	0.602	0.573	0.525
15.048	0.566	0.565	0.558	0.56	0.564	0.57	0.572	0.574	0.576	0.58	0.58	0.552	0.514
16.06	0.693	0.692	0.69	0.696	0.694	0.692	0.698	0.694	0.698	0.695	0.694	0.662	0.61
17.072	0.692	0.69	0.686	0.688	0.684	0.688	0.69	0.689	0.69	0.687	0.681	0.655	0.602
18.0	0.652	0.648	0.651	0.655	0.655	0.652	0.657	0.66	0.659	0.662	0.656	0.634	0.584
19.012	0.63	0.63	0.63	0.631	0.627	0.63	0.633	0.635	0.636	0.64	0.638	0.611	0.569
20.024	0.626	0.63	0.617	0.617	0.615	0.617	0.624	0.62	0.625	0.623	0.626	0.596	0.56
21.036	0.609	0.596	0.586	0.592	0.589	0.598	0.593	0.6	0.603	0.596	0.597	0.572	0.541
22.048	0.585	0.586	0.569	0.572	0.568	0.566	0.573	0.576	0.573	0.577	0.574	0.549	0.53
23.06	0.563	0.573	0.559	0.558	0.549	0.555	0.562	0.56	0.56	0.562	0.553	0.535	0.517
24.072	0.567	0.57	0.566	0.553	0.547	0.557	0.56	0.546	0.555	0.575	0.555	0.542	0.513
25.0	0.538	0.561	0.566	0.538	0.541	0.578	0.559	0.535	0.56	0.566	0.547	0.53	0.525

B Measurement Diagrams for Directional Spectral Emissivity

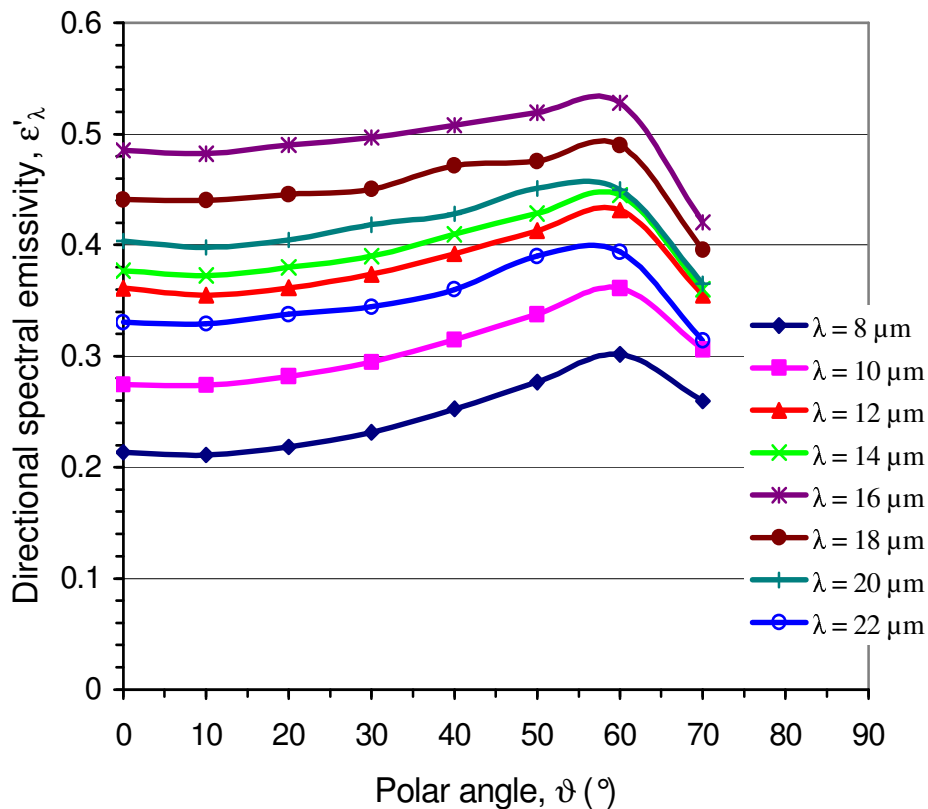
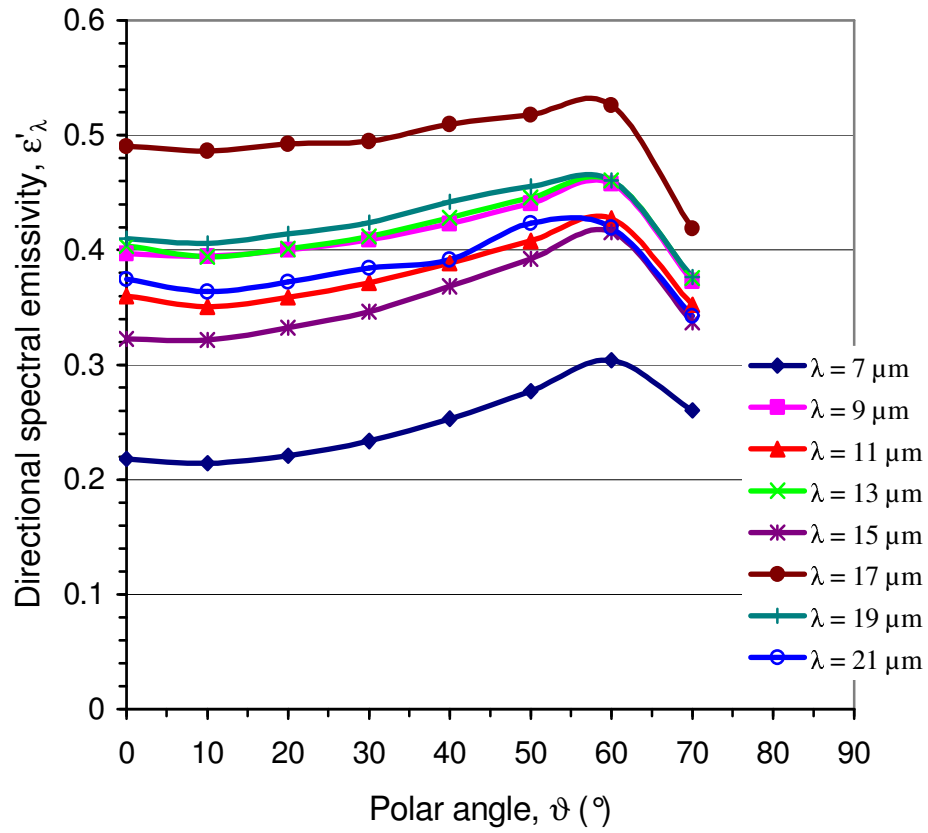


Fig. B.1. Directional spectral emissivity of a smooth undoped silicon surface with the wavelength of radiation as parameter at the surface temperature 199.1°C .

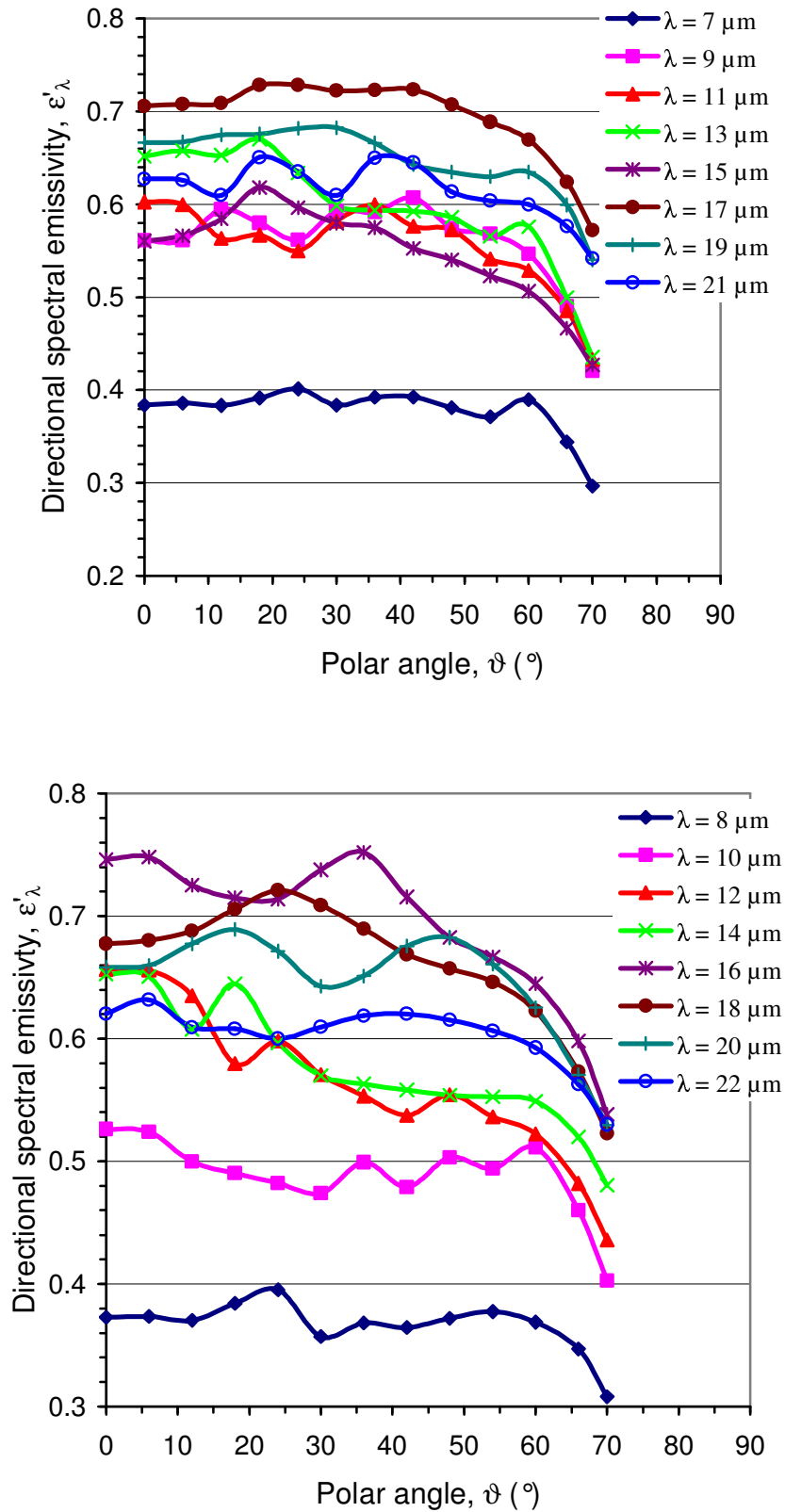


Fig. B.2. Directional spectral emissivity of a microgrooved undoped silicon surface with the wavelength of radiation as parameter at an azimuthal angle, $\varphi = 90^\circ$ for a groove depth, $H = 34.2 \mu\text{m}$ ($T = 200 \text{ }^\circ\text{C}$).

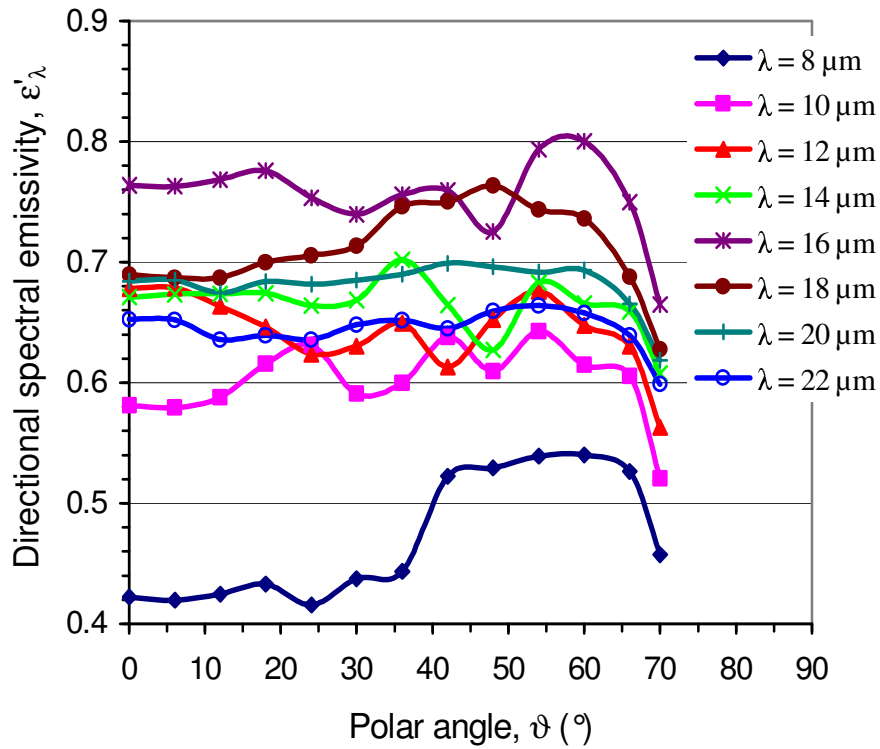
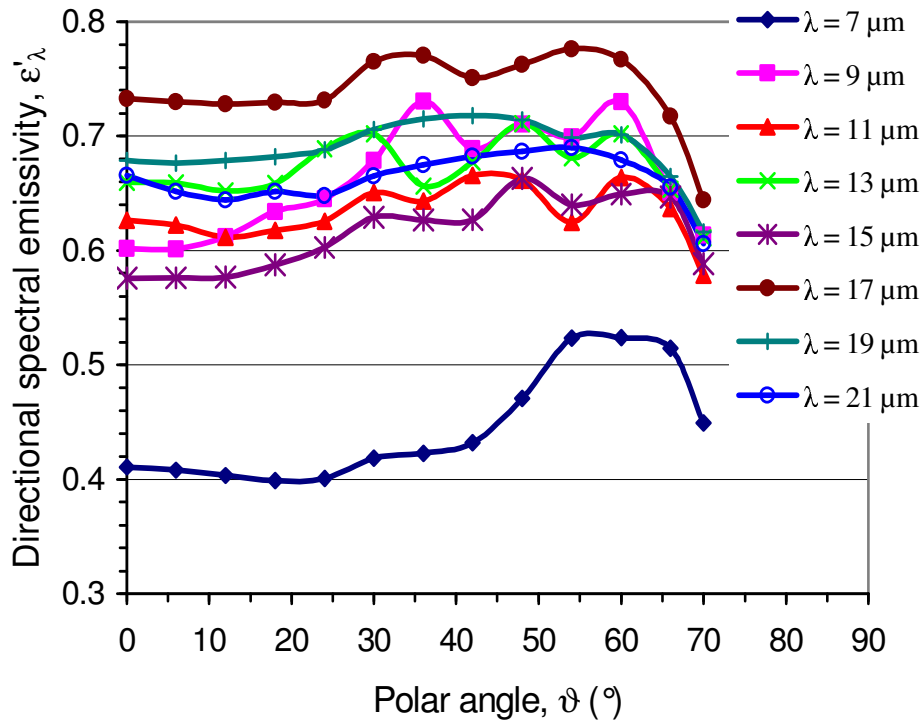


Fig. B.3. Directional spectral emissivity of a microgrooved undoped silicon surface with the wavelength of radiation as parameter at an azimuthal angle, $\varphi = 0^\circ$ for a groove depth, $H = 34.2 \mu\text{m}$ ($T = 200^\circ\text{C}$).

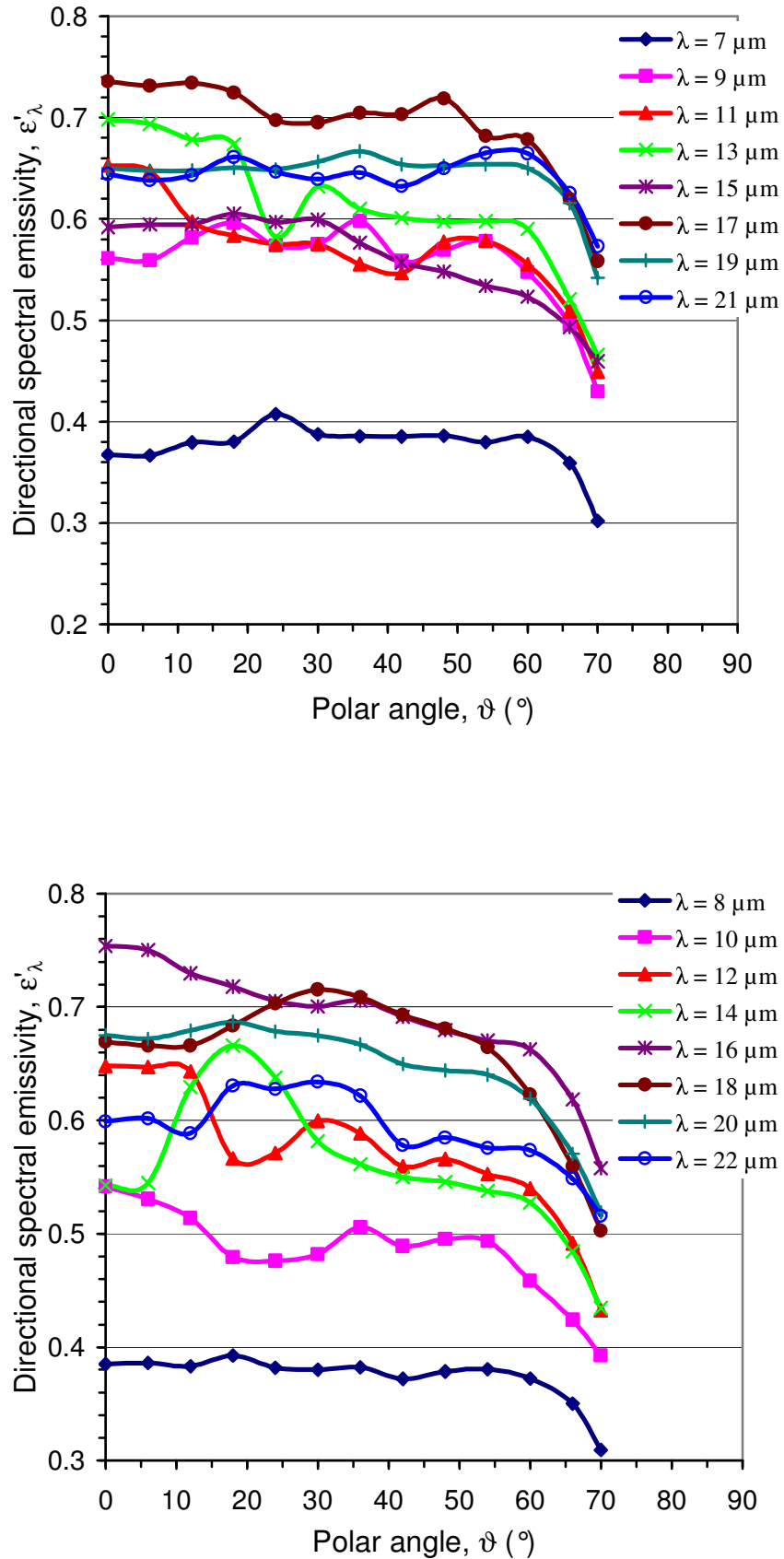


Fig. B.4. Directional spectral emissivity of a microgrooved undoped silicon surface with the wavelength of radiation as parameter at an azimuthal angle, $\varphi = 90^\circ$ for a groove depth, $H = 21.4 \mu\text{m}$ ($T = 200^\circ\text{C}$).

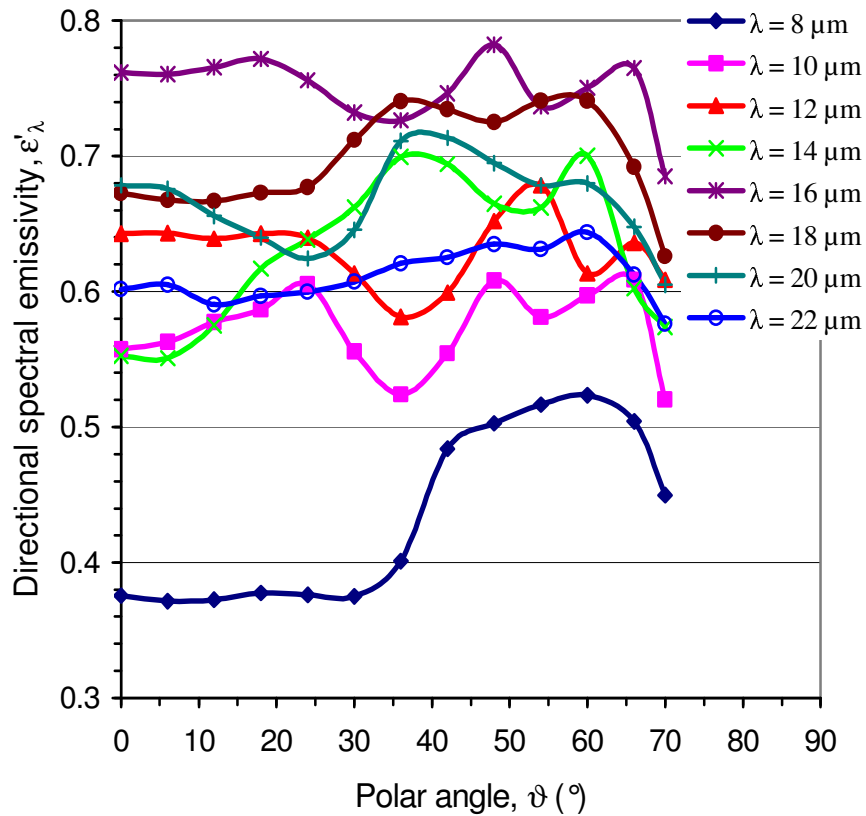
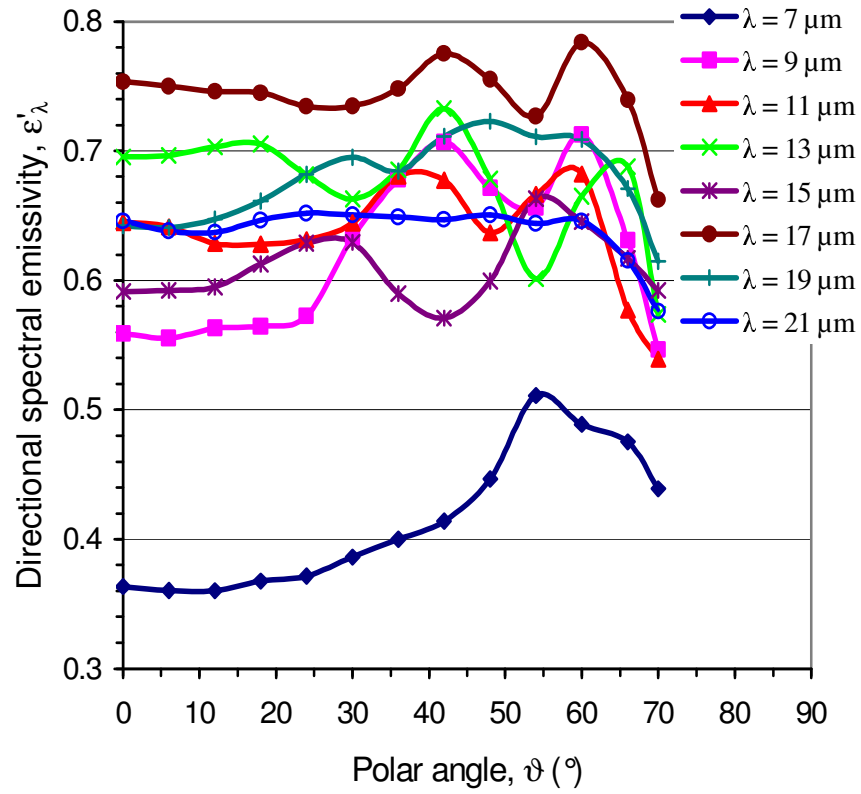


Fig. B.5. Directional spectral emissivity of a microgrooved undoped silicon surface with the wavelength of radiation as parameter at an azimuthal angle, $\varphi = 0^\circ$ for a groove depth, $H = 21.4 \mu\text{m}$ ($T = 200 \text{ }^\circ\text{C}$).

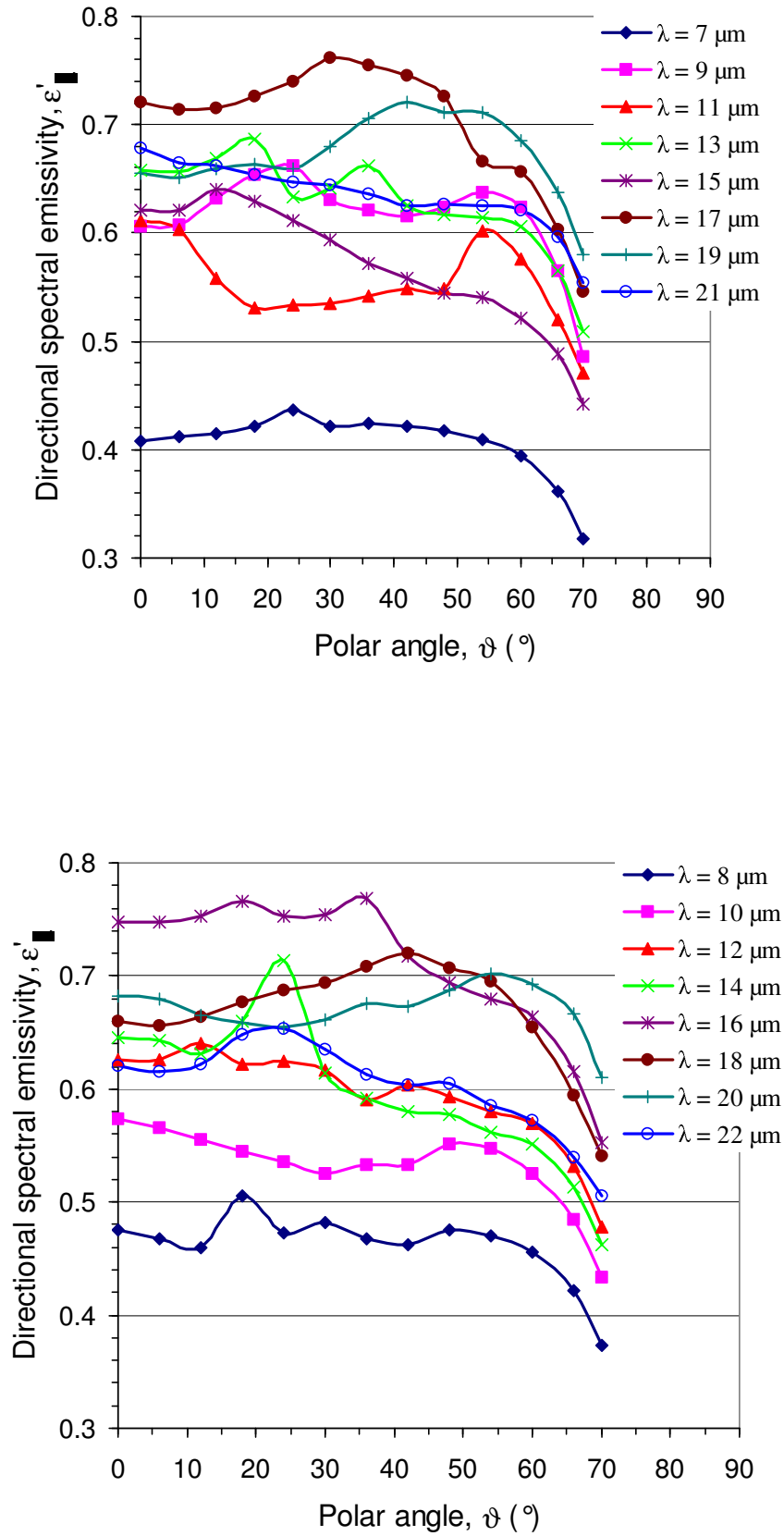


Fig. B.6. Directional spectral emissivity of a microgrooved undoped silicon surface with the wavelength of radiation as parameter at an azimuthal angle, $\varphi = 90^\circ$ for a groove depth, $H = 11.2 \mu\text{m}$ ($T = 200^\circ\text{C}$).

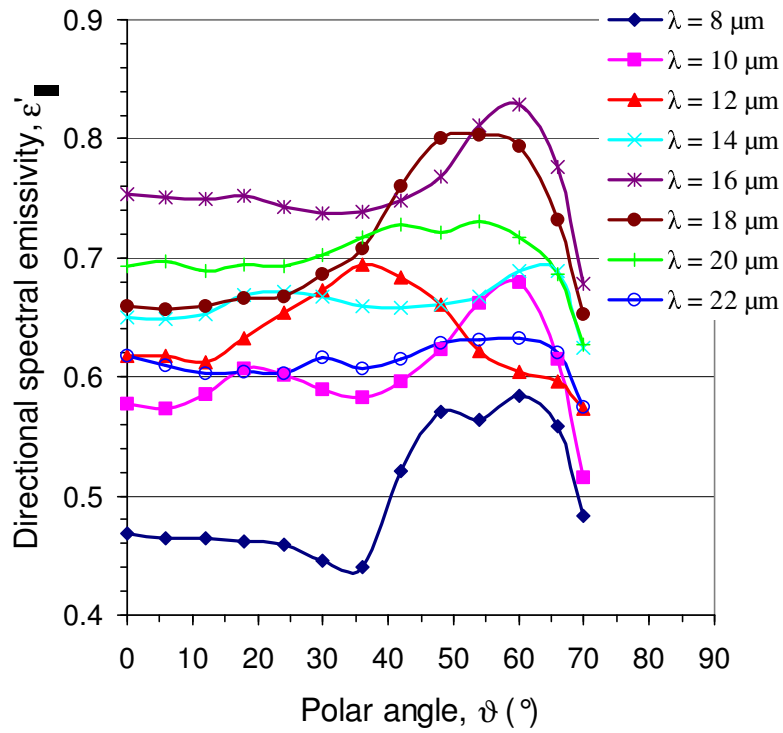
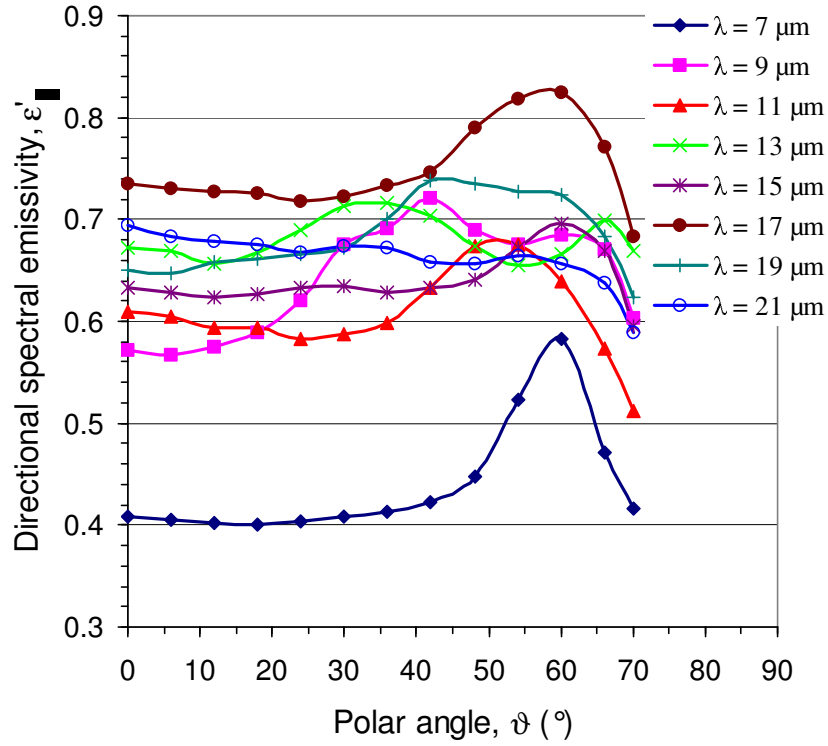


Fig. B.7. Directional spectral emissivity of a microgrooved undoped silicon surface with the wavelength of radiation as parameter at an azimuthal angle, $\varphi = 0^\circ$ for a groove depth, $H = 11.2 \mu\text{m}$ ($T = 200^\circ\text{C}$).

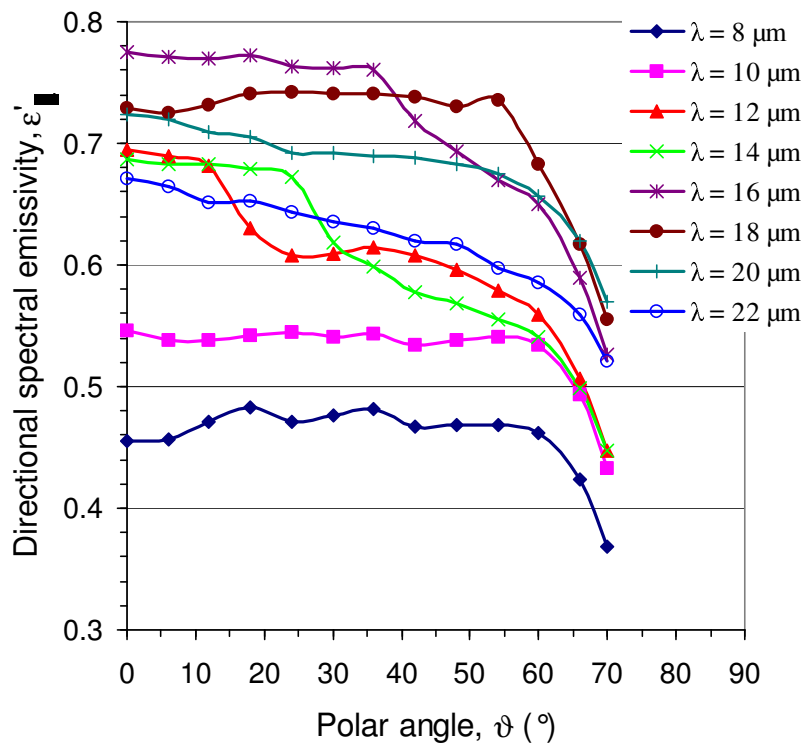
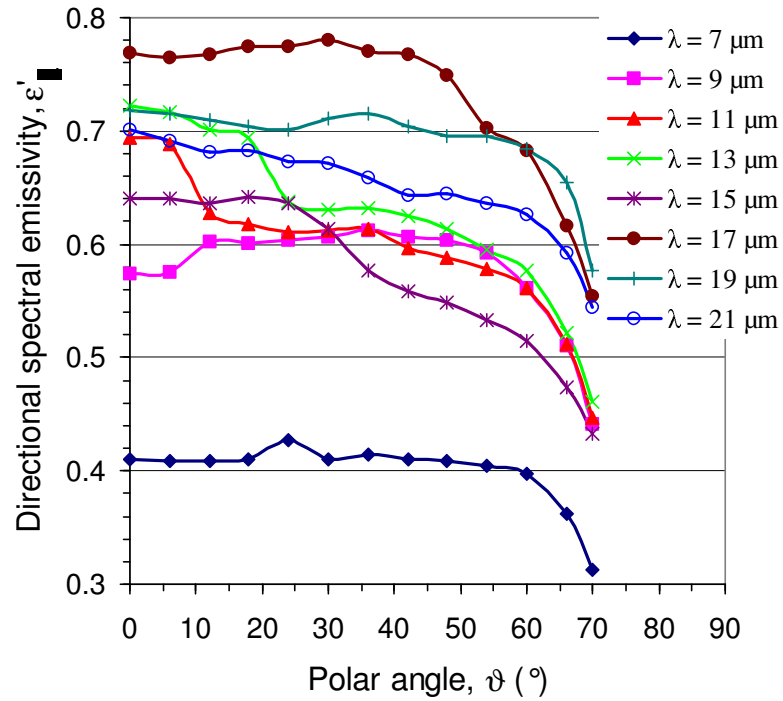


Fig. B.8. Directional spectral emissivity of a microgrooved undoped silicon surface with the wavelength of radiation as parameter at an azimuthal angle, $\varphi = 90^\circ$ for a groove depth, $H = 3.4 \mu\text{m}$ ($T = 200^\circ\text{C}$).

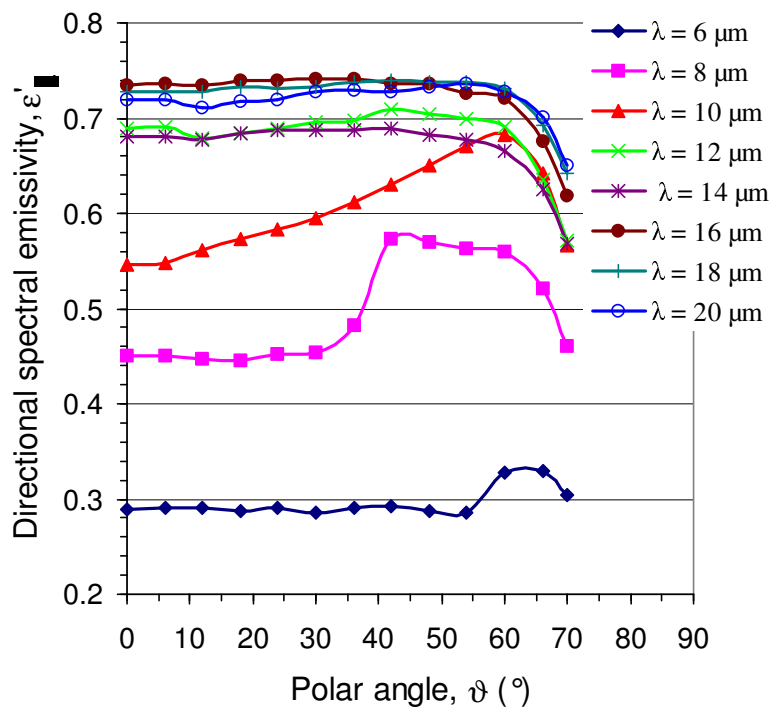
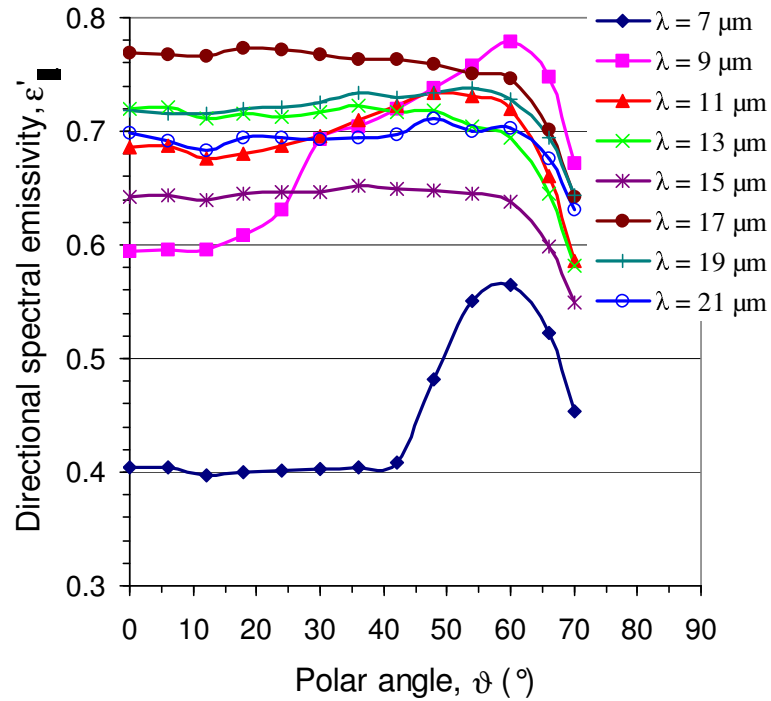


Fig. B.9. Directional spectral emissivity of a microgrooved undoped silicon surface with the wavelength of radiation as parameter at an azimuthal angle, $\varphi = 0^{\circ}$ for a groove depth, $H = 3.4 \mu\text{m}$ ($T = 200^{\circ}\text{C}$).

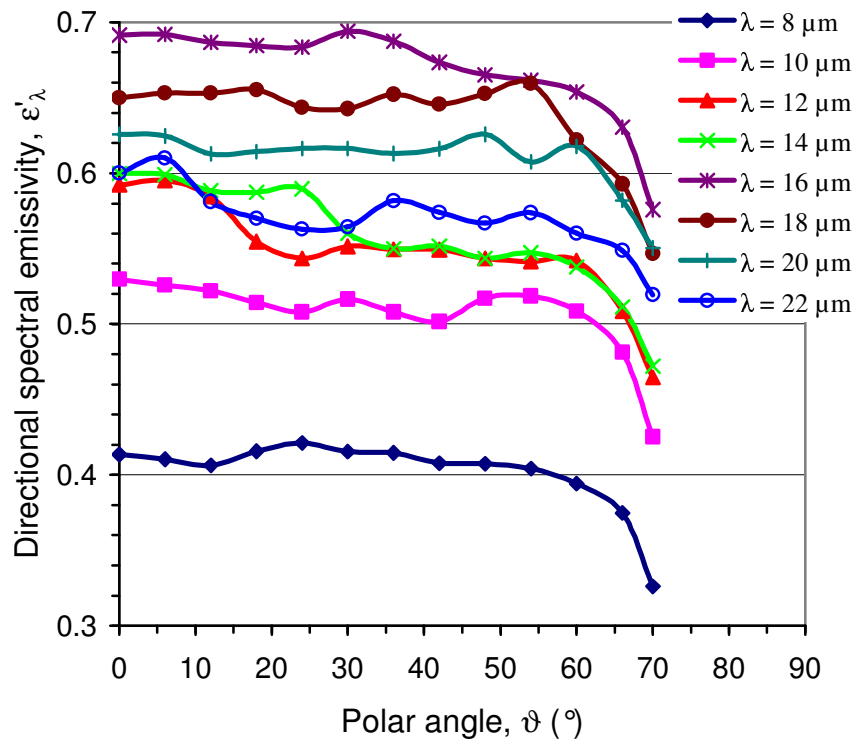
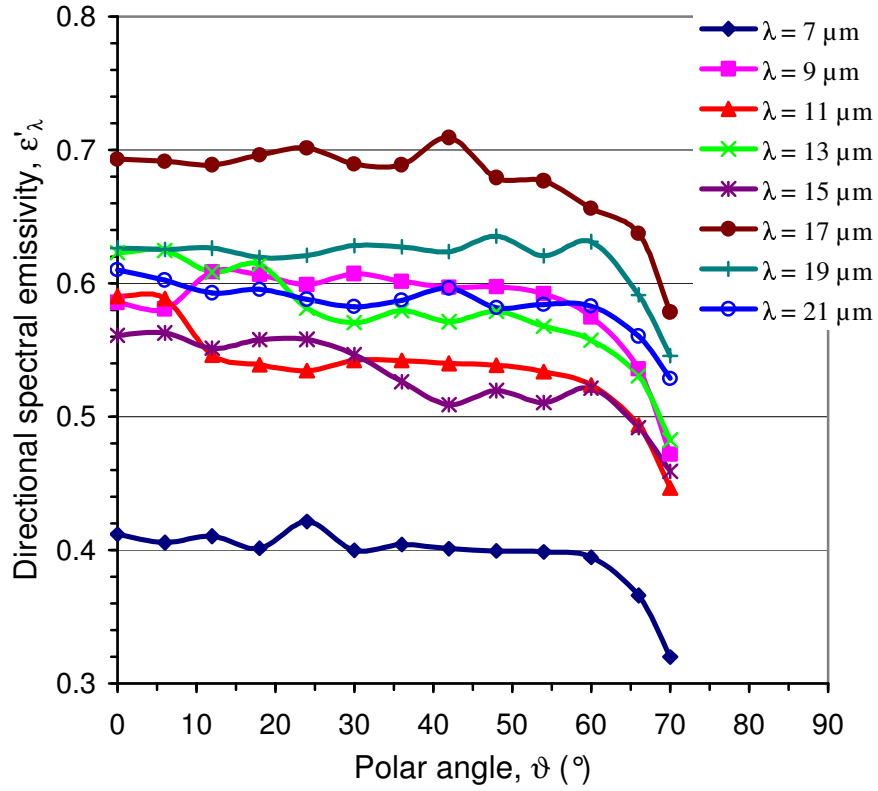


Fig. B.10. Directional spectral emissivity of a microgrooved undoped silicon surface with the wavelength of radiation as parameter at an azimuthal angle, $\varphi = 90^\circ$ for a groove depth, $H = 1 \mu\text{m}$ ($T = 200^\circ\text{C}$).

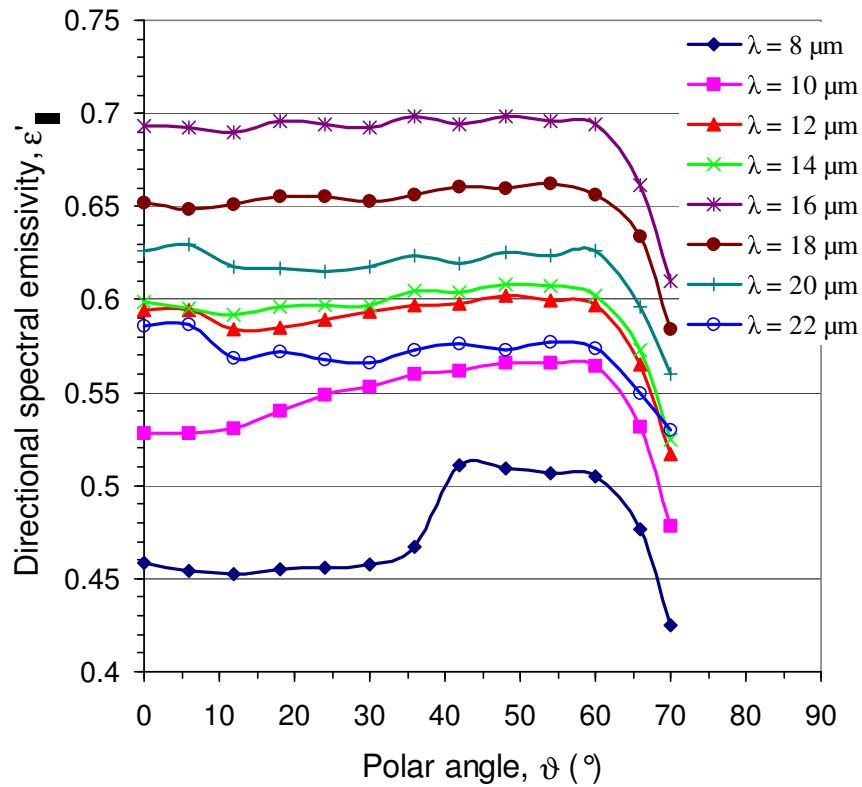
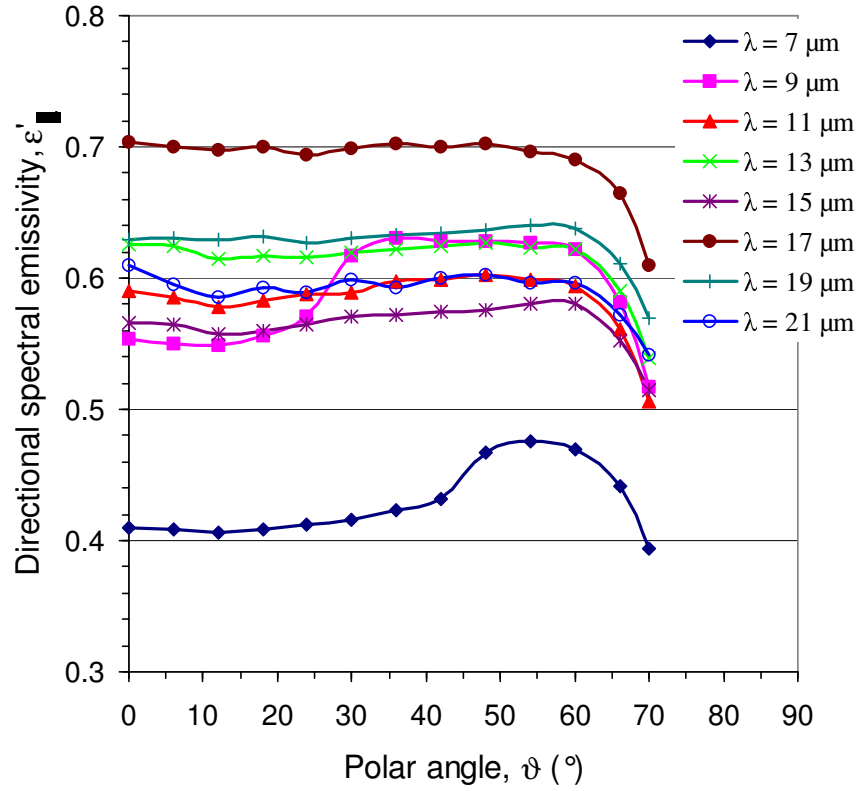


Fig. B.11. Directional spectral emissivity of a microgrooved undoped silicon surface with the wavelength of radiation as parameter at an azimuthal angle, $\varphi = 0^\circ$ for a groove depth, $H = 1 \mu\text{m}$ ($T = 200^\circ\text{C}$).

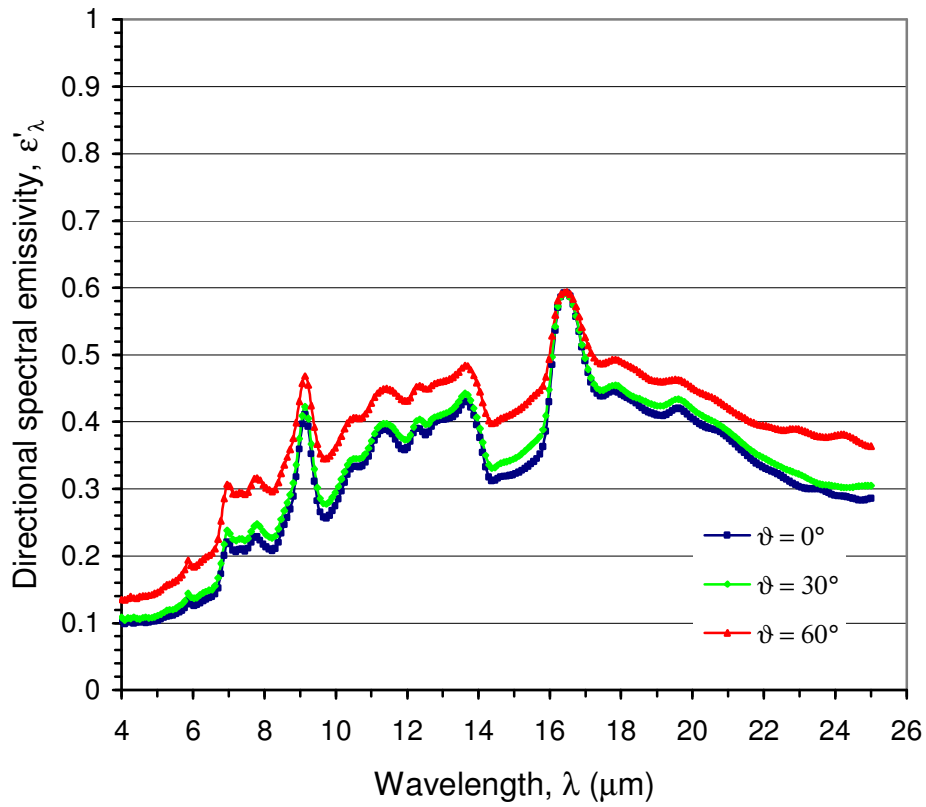


Fig. B.12. Directional spectral emissivity of a smooth undoped silicon at the surface temperature 199.1 °C.

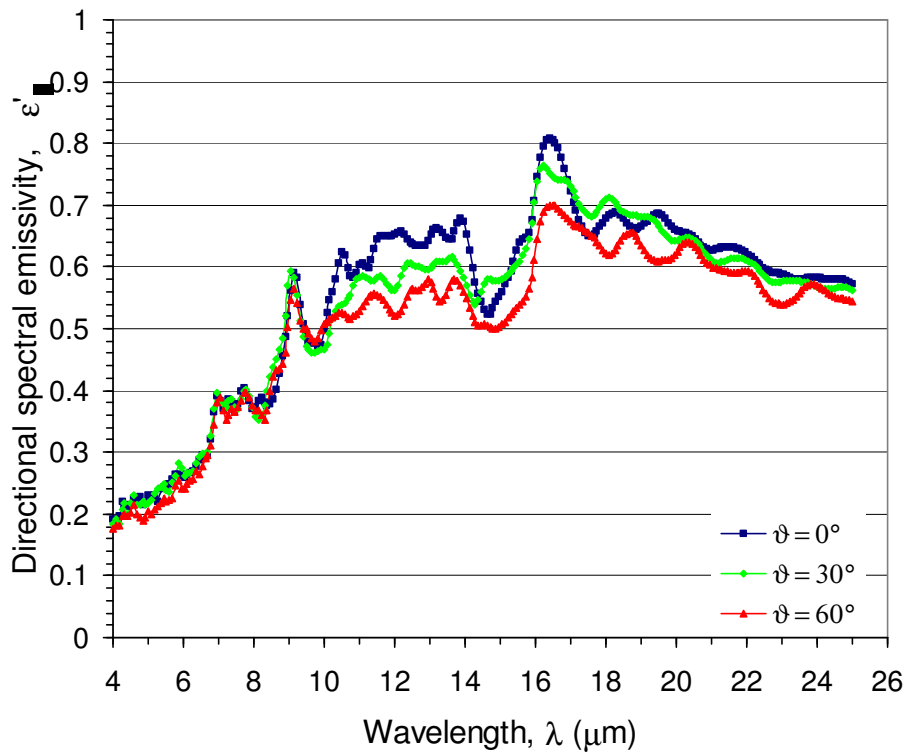


Fig. B.13. Directional spectral emissivity of a microgrooved undoped silicon surface with the polar angle of radiation as parameter at an azimuthal angle, $\phi = 90^\circ$ for a groove depth, $H = 34.2 \mu\text{m}$ ($T = 200 \text{ }^\circ\text{C}$).

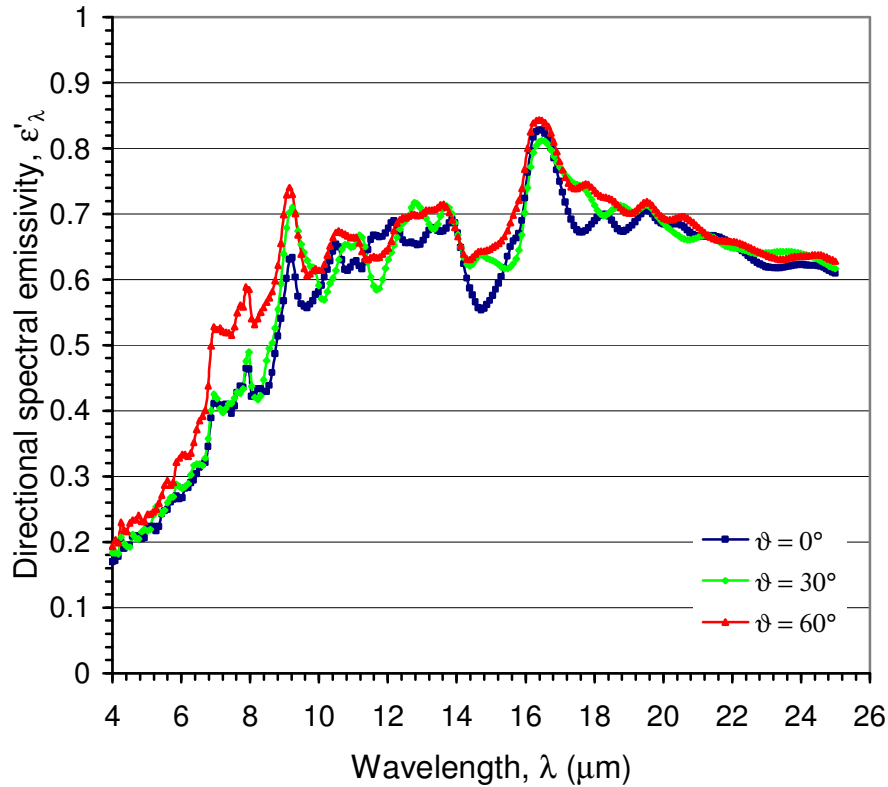


Fig. B.14. Directional spectral emissivity of a microgrooved undoped silicon surface with the polar angle of radiation as parameter at an azimuthal angle, $\varphi = 0^\circ$ for a groove depth, $H = 34.2 \mu\text{m}$ ($T = 200^\circ\text{C}$).

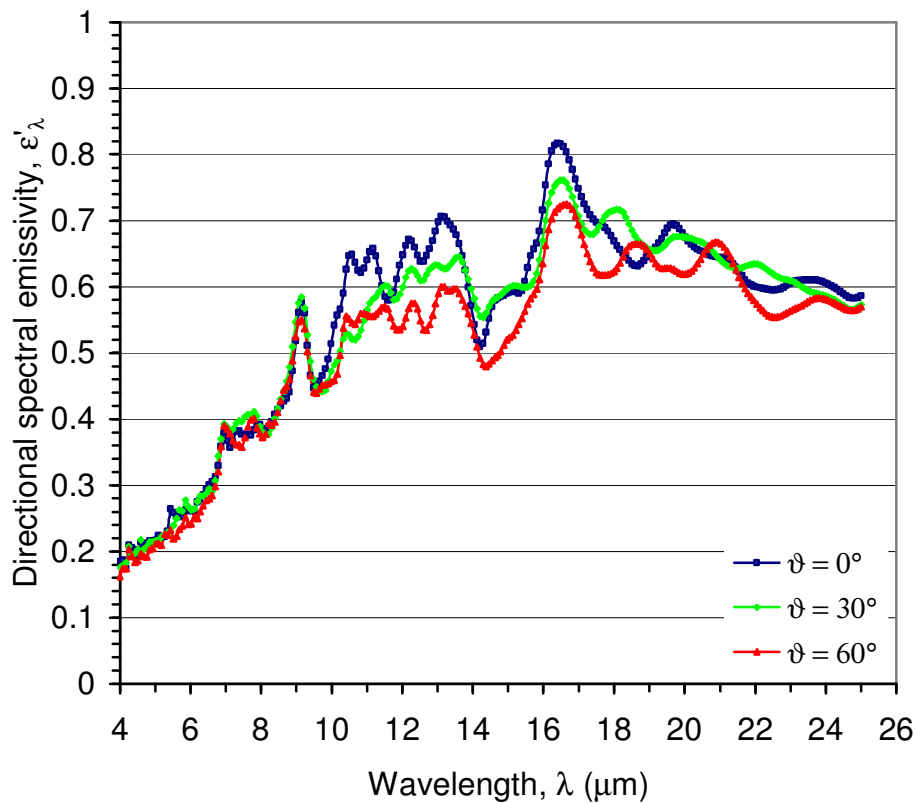


Fig. B.15. Directional spectral emissivity of a microgrooved undoped silicon surface with the polar angle of radiation as parameter at an azimuthal angle, $\varphi = 90^\circ$ for a groove depth, $H = 21.4 \mu\text{m}$ ($T = 200^\circ\text{C}$).

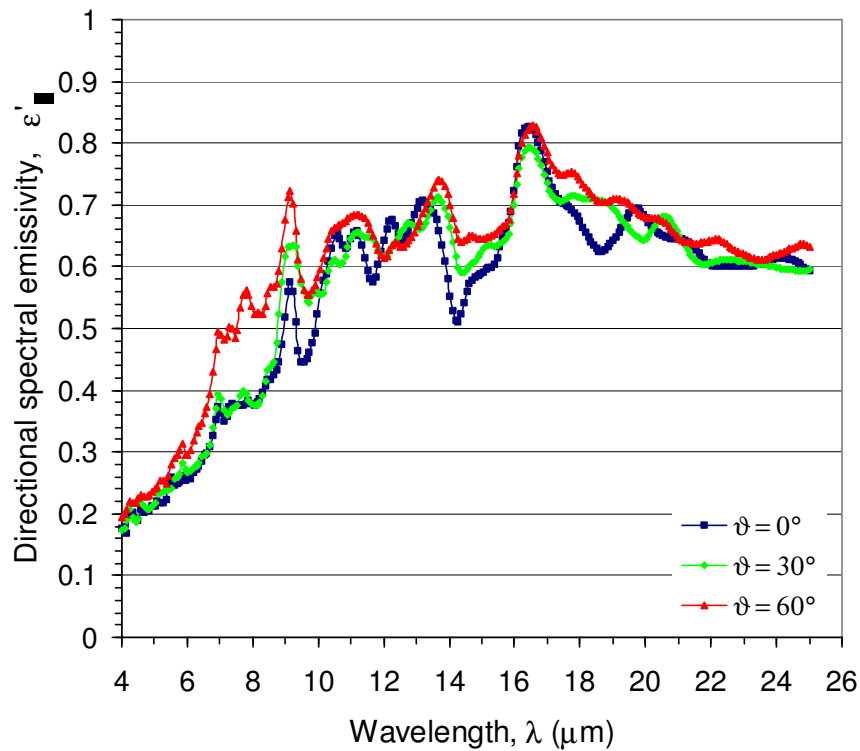


Fig. B.16. Directional spectral emissivity of a microgrooved undoped silicon surface with the polar angle of radiation as parameter at an azimuthal angle, $\varphi = 0^\circ$ for a groove depth, $H = 21.4 \mu\text{m}$ ($T = 200^\circ\text{C}$).

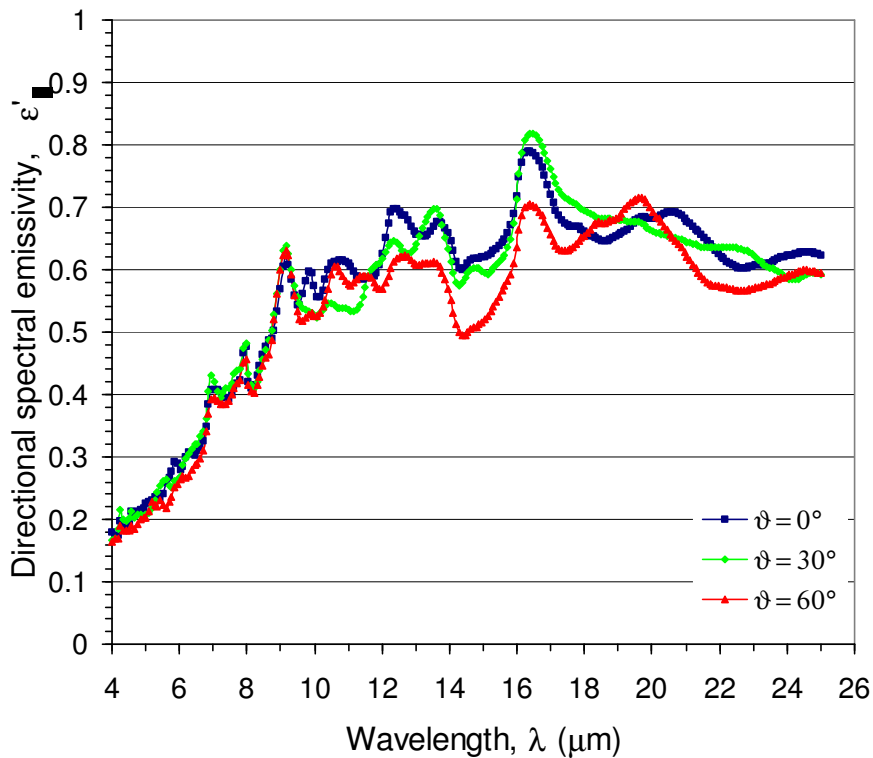


Fig. B.17. Directional spectral emissivity of a microgrooved undoped silicon surface with the polar angle of radiation as parameter at an azimuthal angle, $\varphi = 90^\circ$ for a groove depth, $H = 11.2 \mu\text{m}$ ($T = 200^\circ\text{C}$).

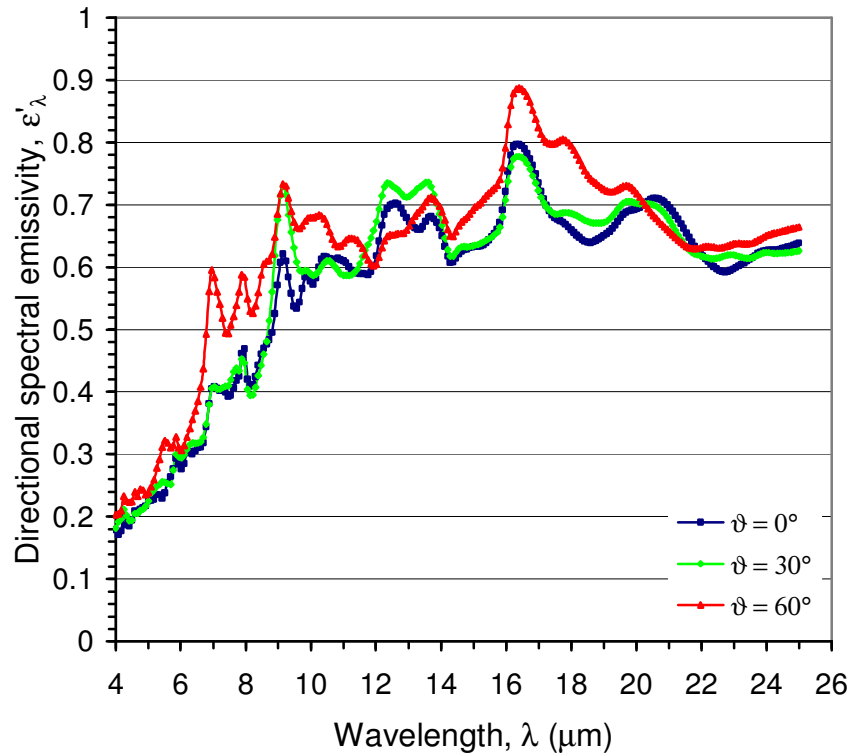


Fig. B.18. Directional spectral emissivity of a microgrooved undoped silicon surface with the polar angle of radiation as parameter at an azimuthal angle, $\varphi = 0^\circ$ for a groove depth, $H = 11.2 \mu\text{m}$ ($T = 200^\circ\text{C}$).

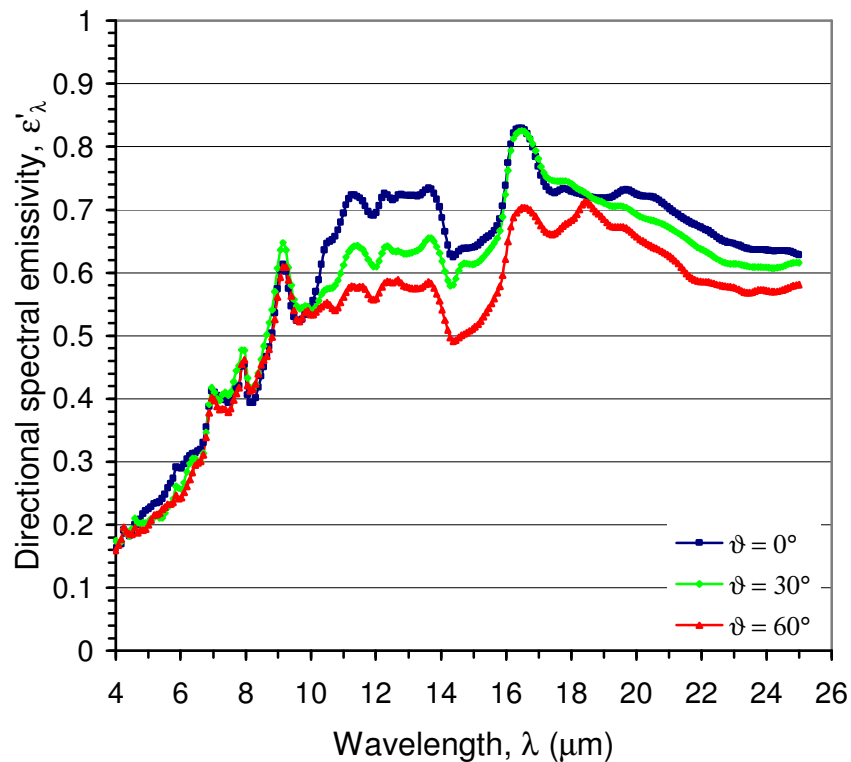


Fig. B.19. Directional spectral emissivity of a microgrooved undoped silicon surface with the polar angle of radiation as parameter at an azimuthal angle, $\varphi = 90^\circ$ for a groove depth, $H = 3.4 \mu\text{m}$ ($T = 200^\circ\text{C}$).

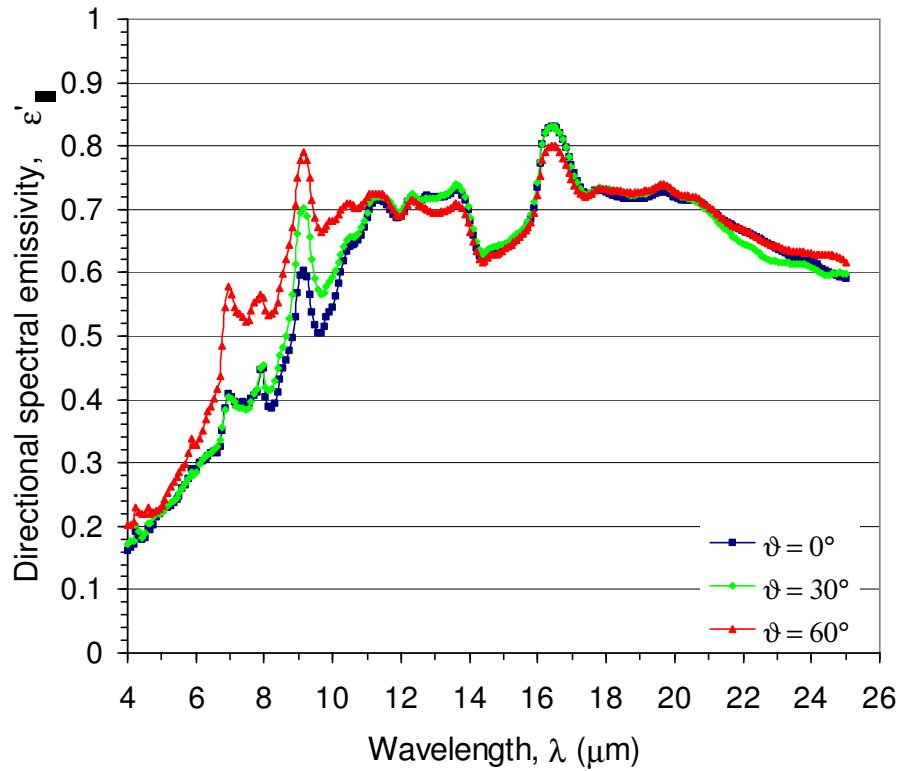


Fig. B.20. Directional spectral emissivity of a microgrooved undoped silicon surface with the polar angle of radiation as parameter at an azimuthal angle, $\varphi = 0^\circ$ for a groove depth, $H = 3.4 \mu\text{m}$ ($T = 200^\circ\text{C}$).

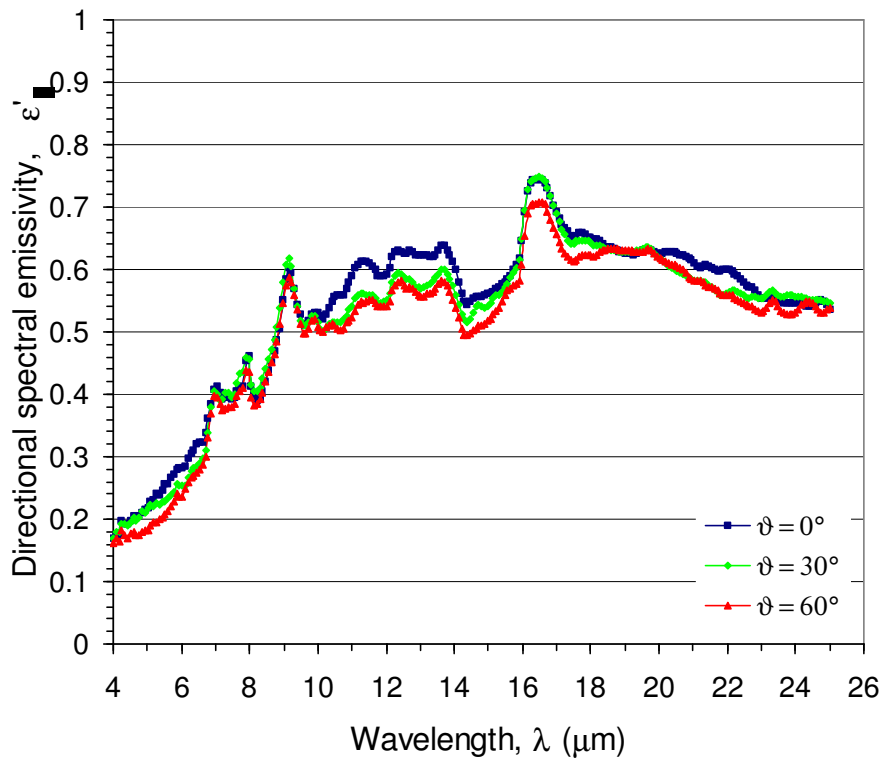


Fig. B.21. Directional spectral emissivity of a microgrooved undoped silicon surface with the polar angle of radiation as parameter at an azimuthal angle, $\varphi = 90^\circ$ for a groove depth, $H = 1 \mu\text{m}$ ($T = 200^\circ\text{C}$).

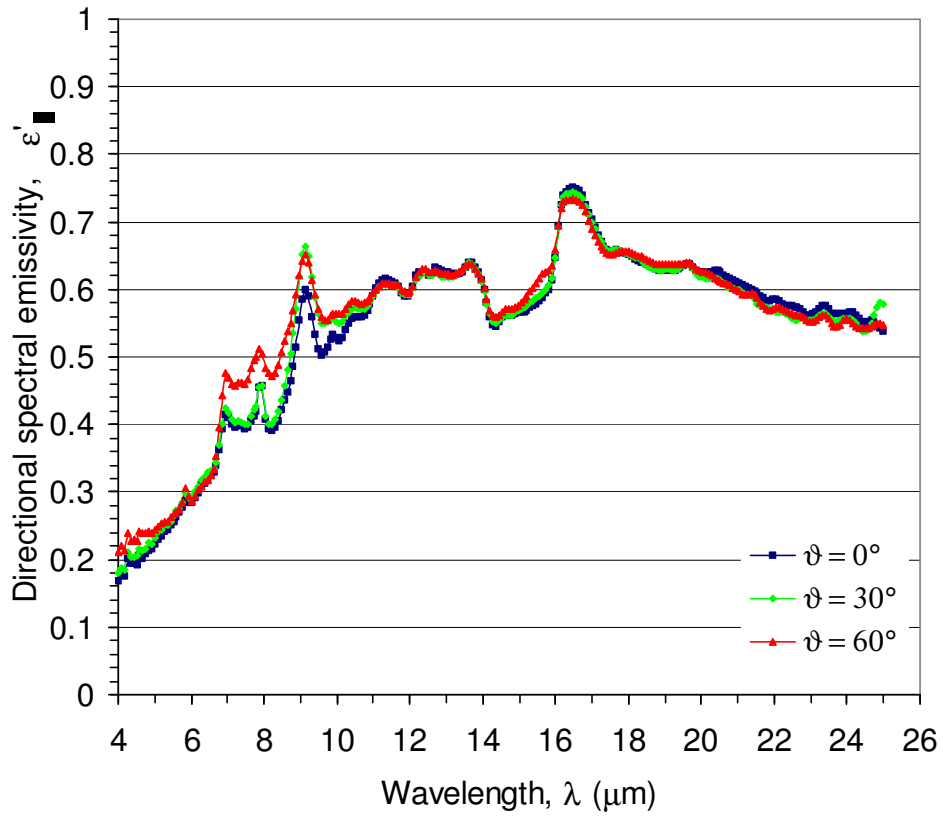


Fig. B.22. Directional spectral emissivity of a microgrooved undoped silicon surface with the polar angle of radiation as parameter at an azimuthal angle, $\varphi = 0^\circ$ for a groove depth, $H = 1 \mu\text{m}$ ($T = 200^\circ\text{C}$).

C References

- [1] Agababov S. G.: Effect of the roughness of the surface of a solid body on its radiation properties and methods for their experimental determination. *High Temperature*, vol. 6, pp. 76-85, 1968.
- [2] Agababov S. G.: Effect of the roughness factor on radiation properties of solids (experimental check), *High Temperature*, vol. 8, pp. 728-731, 1970.
- [3] Agababov S. G.: Effect of secondary roughness on the emissive properties of solid bodies, *High Temperature*, vol. 8, pp. 212-215, 1970.
- [4] Allara D. L., Teicher D. and Durana J. F.: Fourier transform infrared emission spectrum of a molecular monolayer at 300 K, *Chemical physics letters*, vol. 84, no. 1, pp. 20-24, 1981.
- [5] Aspnes D. E.: Optical functions of intrinsic Si: Table of refractive index, extinction coefficient and absorption coefficient vs energy (0 to 400 eV), in *Properties of silicon*, ed. T. H. Ning, INSPEC, The institution of electrical engineers, London and New York, pp. 72-79, 1988.
- [6] Baehr H. D. and Stephan K.: *Heat and mass transfer*, translated by N. J. Park, Springer-Verlag, Berlin Heidelberg, 1998.
- [7] Ballico M. J. and Jones T. P.: Novel experimental technique for measuring high-temperature spectral emissivities, *Applied spectroscopy*. vol. 49, no. 3, pp. 335-340, 1995.
- [8] Bauer G.: Reflexionsmessungen an offenen Hohlräumen, *PTB Mitteilungen, Optik (Stuttgart)* 18, Heft 12, pp. 603-622, 1961.
- [9] Bauer W., Oertel H. and Rink M.: Spectral emissivities of bright and oxidized metals at high temperatures, 15th symposium on thermophysical properties, June 22-27, 2003, Boulder, Colorado, USA.
- [10] Bell R. J.: *Introductory Fourier transform spectroscopy*, Academic press, New York, 1972.
- [11] Berman A.: *Total pressure measurements in vacuum technology*, Academic press, Inc., Orlando, 1985.
- [12] Birkebak R. C. and Eckert E. R. G.: Effects of roughness of metal surfaces on angular distribution of monochromatic reflected radiation, *Journal of heat transfer (Transactions of the ASME)*, pp. 85-93, 1965.

-
- [13] Black W. Z. and Schoenhals R. J.: A study of directional radiation properties of specially prepared v-groove cavities, *Journal of heat transfer (Transactions of the ASME)*, vol. 90, series C, no. 4, pp. 420-428, 1968.
- [14] Black W. Z.: Optimization of the directional emission from v-groove and rectangular cavities, *Journal of heat transfer (Transactions of the ASME)*, pp. 31-36, 1973.
- [15] Born M. and Wolf E.: *Principles of optics*, 6. corr. ed., Pergamon press, Oxford, 1987.
- [16] Brandenburg W. M.: The reflectivity of solids at grazing angles. In Richmond J. C. (ed.), *Measurement of thermal radiation properties of solids*, NASA SP-31, pp. 75-82, 1963.
- [17] Brandenburg W. M. and Clausen O. W.: The directional spectral emittance of surfaces between 200° and 600° C, *Symp. thermal radiation solids*, S. Katzoff (ed.), NASA SP-55 (AFML-TDR-64-159), pp. 313-319, 1965.
- [18] Brewster M. Q.: *Thermal radiative transfer and properties*, Wiley, New York, 1992.
- [19] Bronstein I. N. and Semendjajew K. A.: *Taschenbuch der Mathematik*, Teubner Verlagsgesellschaft, Stuttgart-Leipzig, 1991.
- [20] Brun J. F., De Sousa Meneses D. and Echegut P.: Spectral emissivity of dielectric oxides, below and above the melting point, 15th symposium on thermophysical properties, June 22-27, 2003, Boulder, Colorado, USA.
- [21] Carminati R. and Greffet J. J.: Near-field effects in spatial coherence of thermal sources, *Physical review letters*, vol. 82, no. 8, pp. 1660-1663, 1999.
- [22] Celli V., Maradudin A. A., Marvin A. M. and McGurn A. R.: Some aspects of light scattering from a randomly rough metal surface, *Journal of optical society of America A*, vol. 2, pp. 2225-2239, 1985.
- [23] Chang R. K. and Furak T.E.: *Surface enhanced Raman scattering*, Ed., Plenum, New York, 1982.
- [24] Chase D. B.: The sensitivity and limitations of condensed phase infrared emission spectroscopy, *Applied spectroscopy*, vol. 35, no. 1, pp. 77-81, 1981.
- [25] Chen C. J., Gilgen H. H. and Osgood R.M.: Resonant optical growth of submicrometer metal gratings, *Optical Letters*, vol. 10, no. 4, pp. 173-175, 1985.
- [26] Churchill S. W. and Chu H. H. S.: Correlating equations for laminar and turbulent free convection from a vertical plate, *International journal of heat and mass transfer*, vol. 18, pp. 1323-1329, 1975.
- [27] Clarke F. J. J. and Larkin J. A.: Measurement of total reflectance, transmittance and emissivity over the thermal IR spectrum, *Infrared Physics*, vol. 25, no. 1/2, pp. 359-367, 1985.

- [28] Clausen O. W. and Neu J. T.: The use of directionally dependent radiation properties for spacecraft thermal control, *Astronautica Acta*, vol. 11, no. 5, pp. 328-339, 1965.
- [29] Cohn D. W., Tang K. and Buckius R. O.: Comparison of theory and experiments for reflection from microcontoured surfaces, *international journal of heat mass transfer*, vol. 40, no. 13, pp. 3223-3235, 1997.
- [30] Conroy C. M., Guthrie J. D., Sharkins A. J., Sparr B. J., Crocombe R. A. and Curbelo R.: An infrared accessory for studying the emissivity of aluminium surfaces, *Applied spectroscopy*. vol. 41, no. 4, pp. 688-692, 1987.
- [31] Daws L. F.: The emissivity of a groove, *British journal of applied physics*, vol. 5, pp. 182-187, 1954.
- [32] De Blase F. J. and Compton S.: Infrared emission spectroscopy: A theoretical and experimental review, *Applied Spectroscopy*, vol. 45, no. 4, pp. 611-618, 1991.
- [33] Demont P., Huetz-Aubert M. and N'Guyen H. T.: Experimental and theoretical studies of the influence of surface conditions on radiative properties of opaque materials, *International journal of thermophysics*, vol. 3, no. 4, pp. 335-364, 1982.
- [34] De Silva A. A. and Jones B. W.: Bi-directional spectral reflectance and directional-hemispherical spectral reflectance of six materials used as absorbers of solar energy, *Solar energy Mater.*, vol. 15, no. 5, pp. 391-401, 1987.
- [35] De Silva A. A. and Jones B. W.: The directional-total emittance at 368 K of some metals, solar absorbers and dielectrics, *Journal of Physics, D: Applied Physics*, vol. 20, pp. 1102-1108, 1987.
- [36] De Witt D. P. and Richmond J. C.: *Theory and practice of radiation thermometry*, ed. D.P. DeWitt and G.D. Nutter, Wiley, New York, 1988.
- [37] Dimenna R. A. and Buckius R. O.: Microgeometrical contour contributions to surface scattering, *Thermal science and engineering*, vol. 2, no.1, pp. 166-171, 1994.
- [38] Dimenna R. A. and Buckius R. O.: Electromagnetic theory predictions of the directional scattering from triangular surfaces, *Journal of heat transfer (Transactions of the ASME)*, vol. 116, pp. 639-645, 1994.
- [39] Durana J. F.: Infra-red emission studies of thin polymer films, *Polymer*, vol. 20, pp. 1306-1307, 1979.
- [40] Elich J. J. P. and Wieringa J. A.: Temperature effects influencing the spectral and total emissivity of refractories, *Experimental thermal and fluid sciences*, vol. 10, 1995.
- [41] Especel D. and Mattei S.: Total emissivity measurements without use of an absolute reference, *Infrared Physics & Technology*, vol. 37, pp. 777-784, 1996.

- [42] Ferber J., Aschaber J., Hebling C., Heinzl A., Wiehle R., Zenker M. and Luther J.: Microstructured tungsten surfaces as selective emitters in thermophotovoltaic systems, Presented in 16th European photovoltaic solar energy conference and exhibition, Glasgow, 2000.
- [43] Fleming J. G., Lin S. Y., El-Kady I., Biswas B. and Ho K. M.: All-metallic three-dimensional photonic crystals with a large infrared bandgap, *Nature (London)*, vol. 417, pp. 52-55., 2002.
- [44] Foley M.: Technical advances in microstructured plastic optics for display applications, Fresnel Optics, Rochester, NY and Apolda, Germany.
- [45] Ford M. A. and Spragg R. A.: A simple method of measuring emission spectra with an FT-IR spectrometer, *Applied spectroscopy*, vol. 40, no. 5, pp. 715-716, 1986.
- [46] Ford J. N., Tang K. and Buckius R. O.: Fourier transform infrared system measurement of the bidirectional reflectivity of diffuse and grooved surfaces, *Journal of heat transfer (Transactions of the ASME)*, vol. 117, pp. 955-962, 1995.
- [47] Gall J. L., Olivier M. and Greffet J. J.: Experimental and theoretical study of reflection and coherent thermal emission by a SiC grating supporting a surface-phonon polariton, *Physical review B*, vol. 55, no. 15, pp. 10105-10114, 1997.
- [48] Govindarajan K. and Gopal E. S. R.: A note on the hot wire method for measurement of heat capacity of gases at low pressures, *Journal of the indian institute of science*, vol. 53, pp. 21-27, 1971.
- [49] Greenler R. G.: Light emitted from molecules adsorbed on a metal surface, *Surface science*, vol. 69, pp. 647-652, 1977.
- [50] Greffet J. J., Carminati R., Joulain K., Marquier F., Mulet J. P., Mainguy S. and Chen Y.: Design of coherent thermal sources of radiation, *Proceedings of the twelfth international heat transfer conference*, pp. 435-440, Heat transfer 2002.
- [51] Gray D.E.: *American institute of physics handbook*, McGraw-Hill, New York, 1972.
- [52] Griffiths P. R.: Infrared emission spectroscopy. I. Basic considerations, *Applied spectroscopy*, vol. 26, no.1, pp. 73-76, 1972.
- [53] Griffiths P. R. and De Haseth J. A., *Fourier transform infrared spectrometry*, John Wiley and Sons, New York, 1986.
- [54] Handke M. and Harrick N. J.: A new accessory for infrared emission spectroscopy measurements, *Applied Spectroscopy*, vol. 40, no. 3, pp. 401- 405, 1986.

- [55] Heinzl A., Boerner V., Gombert A., Wittwer V. and Luther J.: Microstructured tungsten surfaces as selective emitters, in proceedings of the thermophotovoltaic generation of electricity 4th NREL conference, Denver, Colorado, 1998, T. J. Coutts, J. P. Benner and C. S. Allman eds. (American institute of physics, New York, 1999), pp. 191-196.
- [56] Heinzl A., Boerner V., Gombert A., Blaesi B., Wittwer V. and Luther J.: Radiation filters and emitters for the NIR based on periodically structured metal surfaces, *Journal of modern optics*, vol. 47, no. 13, pp. 2399-2419, 2000.
- [57] Herres W. and Groenholz J.: Understanding FT-IR data processing, Reprint vol. 3, Dr. Alfred Huethig publishers, 1985.
- [58] Hesketh P. J., Zemel J. N. and Gebhart B.: Organ pipe radiant modes of periodic micromachined silicon surfaces, *Nature*, vol. 324, pp. 549-551, 1986.
- [59] Hesketh P. J.: The Emittance of heavily doped microconfigured silicon surfaces, Dissertation, Electrical engineering, University of Pennsylvania, Philadelphia, 1987.
- [60] Hesketh P. J., Gebhart B. and Zemel J. N.: Measurements of the spectral and directional emission from microgrooved silicon surfaces, *Journal of heat transfer*, vol. 110, pp. 680-686, 1988.
- [61] Hesketh P. J. and Zemel J. N.: Polarized spectral emittance from periodic micromachined surfaces. I. Doped silicon: the normal direction, *Physical Review B* 37 , pp. 10795-10802, 1988.
- [62] Hesketh P. J. and Zemel J. N.: Polarized spectral emittance from periodic micromachined surfaces. II. Doped silicon: angular variation, *Physical Review B* 37 , pp. 10803-10813, 1988.
- [63] Hessel A. and Oliner A. A.: A new theory of Wood's anomalies on optical gratings, *Applied optics*, vol. 4, pp. 1275-1297, 1965.
- [64] Hollands K. G. T.: Directional selectivity, emittance, and absorptance properties of vee corrugated specular surfaces, *Solar energy*, vol. 7, no. 3, pp. 108-116, 1963.
- [65] Howell J. R. and Perlmutter M.: Directional behaviour of emitted and reflected radiant energy from a specular, gray, asymmetric groove, National aeronautics and space administration, Technical note D-1874, 1963.
- [66] Hsieh C. K. and Su K. C.: Thermal radiative properties of glass from 0.32 to 206 μm , *Solar Energy*, vol. 22, pp. 37-43, 1979.
- [67] Hutley M. C.: *Diffraction Gratings*, Academic press, London, 1982.

-
- [68] Ishii J. and Ono A.: Fourier transform spectrometer for thermal-infrared emissivity measurements near room temperature, *Proceedings of SPIE*, vol. 4103, pp. 126-132, 2000.
- [69] Jaecklin V. P., Linder C., Brugger J., De Rooij N. F., Moret J. M. and Vuilleumier R.: Mechanical and optical properties of surface micromachined torsional mirrors in silicon, polysilicon, and aluminium, *Sens. Actuators A. Phys.*, vol A43, nos. 1-3, pp. 269-275, 1994.
- [70] Janßen D.: Verfahren zur Bestimmung des senkrechten und des hemisphärischen Gesamtemissionsgrades von Gläsern unter Atmosphärenbedingungen im Temperaturbereich von 50° C bis 100° C, Dissertation, Technischen Universität Carolo-Wilhelmina Braunschweig, 1991.
- [71] Janes J.: Herstellung von regelmäßigen Gitterstrukturen in Siliziumwafer mittels Trockenätzen, Fraunhofer Institut Siliziumtechnologie, ISIT, pp. 1-4, November 2003.
- [72] Jones P. D., Dorai-Raj D. E. and Mcleod D. G. : Spectral - directional emittance of fully oxidized copper, American institute of aeronautics and astronautics (AIAA-95-3521), ASME/AIAA national heat transfer conference, August 6-9, Portland, 1995.
- [73] Kabelac S.: *Thermodynamik der Strahlung* , Vieweg, Braunschweig, 1994.
- [74] Kember D. and Sheppard N.: The use of ratio-recording interferometry for the measurement of infrared emission spectra: Applications to oxide films on copper surfaces, *Applied spectroscopy*, vol. 29, no. 6, pp. 496-500, 1975.
- [75] Kember D., Chenery D. H., Sheppard N. and Fell J,: Fourier-transform i.r. emission studies of weakly emitting overlayers on metal surfaces; experimental and spectral-ratioing procedures and the comparative use of room temperature triglycine sulphate and low-temperature mercury cadmium telluride detectors. *Spectrochimica Acta*, vol. 35A, pp. 455-459, 1979.
- [76] Klein M. V. and Furtak T. E.: *Optics*, Wiley, New York, pp. 253-328, 1993
- [77] Kola B. O., Mulwa B. and Mate P.: A transient technique for determination of thermophysical properties in an absorption calorimeter, *Measurement Science and Technology*, vol. 6, pp. 888-892, 1995.
- [78] Kwor E. T. and Mattei S.: Emissivity measurements for Nextel Velvet Coating 811-21 between -36° C and 82° C, *High temperatures-High pressures*, vol. 33, pp. 551-556, 2001.

-
- [79] Labuhn D.: Die Bedeutung der Strahlungsentropie zur thermodynamischen Bilanzierung der Solarenergiewandlung, Dissertation, Universität Hannover, Shaker Verlag, Aachen, 2001.
- [80] Labuhn D. and Kabelac S.: The spectral directional emissivity of photovoltaic surfaces, *International journal of thermophysics*, vol. 22, no. 5, pp. 1577-1592, 2001.
- [81] Lauer J. L. and Vogel P.: Emission FTIR analyses of thin microscopic patches of jet fuel residues deposited on heated metal surfaces, *Applications of surface science*, vol. 18, pp. 182-206, 1984.
- [82] Lin S. Y., Fleming J. G., Chow E., Bur J., Choi K. K. and Goldberg A.: Enhancement and suppression of thermal emission by a three-dimensional photonic crystal, *Physical review B*, vol. 62, pp. 2243-2246, 2000.
- [83] Lindermeir E., Tank V. and Haschberger P.: Contactless measurement of the spectral emissivity and temperature of surfaces with a Fourier transform infrared spectrometer, *SPIE*, vol. 1682, *Thermosense XIV*, pp. 354-364, 0-8194-0843-3/92.
- [84] Lindermeir E., Haschberger P., Tank V., and Dietl H.: Calibration of a Fourier transform spectrometer using three blackbodies sources, *Applied optics*, vol. 31, no. 22, pp. 4527-4533, 1992.
- [85] Lippig V., Waibel R., Wilhelmi H. and Straub D.: Measurements of the spectral emissivity of surfaces used in jet engines and space technology, *Wärme- und Stoffübertragung*, vol. 26, pp. 241-251, 1991.
- [86] Lohrengel J.: Temperatur- und Winkelabhängigkeit des Gesamtemissionsgrades schlechter Wärmeleiter im Temperaturbereich von -60° C bis 250° C, Dissertation, Rheinisch – Westfälischen Technischen Hochschule Aachen, 1969.
- [87] Lohrengel J.: Gesamtemissionsgrad von Schwärzen, *Wärme- und Stoffübertragung*, vol. 21, pp. 311-315, 1987.
- [88] Lohrengel J. and Tingwaldt C.: Bestimmung des hemisphärischen Gesamtemissionsgrades aus zwei Meßwerten des Gesamtemissionsgrades bei 0° und 45° , *Optik* 31, Heft 5, pp. 404-409, 1970.
- [89] Lohrengel J., Todtenhaupt R. and Ragab M.: Bestimmung des gerichteten spektralen Emissionsgrades von Feststoffen im Wellenlängenbereich von 2,5 mm bis 45 mm bei Temperaturen zwischen 80° C und 350° C, *Wärme- und Stoffübertragung*, vol. 28, pp. 321-327, 1993.

- [90] Lohrengel J. and Todtenhaupt R.: Wärmeleitfähigkeit, Gesamtemissionsgrade und spektrale Emissionsgrade der Beschichtung Nextel-Velvet-Coating 811-21 (RAL 900 15 tiefschwarz matt), PTB (Physikalisch-Technische Bundesanstalt) - Mitteilungen 106, pp. 259-265, 4/1996.
- [91] Low M. J. D.: Applications of multiple-scan interferometry to the measurement of infrared spectra, *Applied spectroscopy*, vol. 22, no. 5, pp. 463-465, 1968.
- [92] Makino T., Kawasaki H. and Kunitomo T.: Study of the radiative properties of heat resisting metals and alloys (1st report, optical constants and emissivities of nickel, cobalt and chromium) , *Bulletin of the JSME*, vol. 25, no. 203, pp. 804-811, 1982.
- [93] Makino T., Kaga K. and Murata H.: Numerical simulation on transient behaviour of reflection characteristics of real surfaces of metallic materials, *JSME international journal, Series B*, vol 38, no. 2, pp. 206-212, 1995.
- [94] Makino T.: Thermal radiation characteristics of real surfaces of solid materials in natural/industrial environments, *High Temperatures-High Pressures*, vol. 29, pp. 581-590, 1997.
- [95] Makino T., Nakamura A. and Wakabayashi H.: Directional characteristics of radiation reflection on rough metal surfaces with description of heat transfer parameters, *Heat Transfer-Asian Research*, vol. 31, no. 2, pp. 76-88, 2002.
- [96] Makino T.: Thermal radiation spectroscopy for heat transfer science and for engineering surface diagnosis, *proc. 12th international heat transfer conference*, Grenoble, keynote lecture, August 2002.
- [97] Maradudin A. A., Michel T., McGurn A. R. and Mendez E. R.: Enhanced backscattering of light from a random gratings, *Annals of physics*, vol. 23, pp. 255-307, 1990.
- [98] Maruyama S., Kashiwa T., Yugami H. and Esashi M.: Thermal radiation from two-dimensionally confined modes in microcavities, *Applied physics letters*, vol. 79, no. 9, pp. 1393-1395, 2001.
- [99] Masuda H. and Higano M.: Measurement of total hemispherical emissivities of metal wires by using transient calorimetric technique, *Journal of heat transfer (Transactions of the ASME)*, vol. 110, pp. 166-172, 1988.
- [100] Masuda H., Sasaki S., Kou H. and Kiyohashi H.: An improved transient calorimetric technique for measuring the total hemispherical emittance of nonconducting materials (emittance evaluation of glass sheets), *International journal of thermophysics*, vol. 24, no. 1, pp. 259-276, 2003.

- [101] Matsumoto T. and Ono A.: Specific heat capacity and emissivity measurements of Ribbon-shaped graphite using pulse current heating, *International journal of thermophysics*, vol. 16, no. 1, pp. 267-275, 1995.
- [102] Matsumoto T. and Cezairliyan A.: A combined transient and brief steady-state technique for measuring hemispherical total emissivity of electrical conductors at high temperatures: application to Tantalum, *International journal of thermophysics*, vol. 18, no. 6, pp. 1539-1557, 1997.
- [103] Matsumoto T., Cezairliyan A. and Basak D.: Hemispherical total emissivity of niobium, molybdenum and tungsten at high temperatures using a combined transient and brief steady-state technique, *International journal of thermophysics*, vol. 20, no. 3, pp. 943-953, 1999.
- [104] Matsumoto T. and Ono A.: A measurement technique for hemispherical total emissivity using feedback – controlled pulse current heating, *High Temperatures – High Pressures*, vol. 32, pp. 67-72, 2000.
- [105] Matsumoto T. and Ono A.: Hemispherical total emissivity and specific heat capacity measurements by electrical pulse-heating method with a brief steady state, *Measurement science and technology*, vol. 12, pp. 2095-2102, 2001.
- [106] Maystre D.: General study of grating anomalies from electromagnetic surface modes, in *Electromagnetic surface modes*, A. D. Boardman ed., John Wiley & Sons, New York, 1982.
- [107] Mekhontsev S. N., Sapritsky V. I., Prokhorov A. V., Khromchenko V. B. and Samoilov M. L.: Modeling, design, and characterization of medium background blackbodies for full aperture calibration of spaceborne infrared systems and imagers, *Russian institute for opto-physical measurements*, 46 Ozernaya street, Moscow 119361, Russia.
- [108] Nagasawa Y. and Ishitani A.: Application of Fourier transform infrared emission spectrometry to surface analysis, *Applied spectroscopy*, vol. 38, no. 2, pp. 168-173, 1984.
- [109] Neuer G.: Emissivity measurements on graphite and composite materials in the visible and infrared spectral range, *QIRT 92 – Eurotherm Series 27 – EETI ed.*, pp. 359-364, Paris 1992.
- [110] Neuer G.: Spectral and total emissivity measurements of highly emitting materials, *International journal of thermophysics*, vol. 16, no. 1, pp. 257-265, 1995.
- [111] Neuer G. and Jaroma-Weiland G.: Spectral and total emissivity of high-temperature materials, *International journal of thermophysics*, vol. 19, no. 3, pp. 917-929, 1998.

- [112] Nieto-Vesperinas M. and Sanchez-Gil J. A.: Light scattering from a random rough interface with total internal reflection, *Journal of optical society of America A*, vol. 9, pp. 424-436, 1992.
- [113] O'Brien P. F. and Heckert B. J.: Effective emissivity of a blackbody cavity at nonuniform temperature, *Illuminating Engineering*, vol. 4, pp. 187-195, 1965.
- [114] Özisik M. N.: Radiative transfer and interactions with conduction and convection, John Wiley and sons, New York, 1973.
- [115] Özisik M. N.: Basic heat transfer, Robert E. Krieger publishing company, Malabar, Florida, 1987
- [116] Palik E. D.: Handbook of optical constants of solids, vol. I-III, Academic press, San Diego, London, 1998.
- [117] Palmer C. H.: Parallel diffraction grating anomalies, *Journal of optical society of America*, vol. 42, no. 4, pp. 269-276, 1952.
- [118] Palmer C. H. and Evering F. C., Jr.: Diffraction anomalies with a dielectric grating, *Journal of optical society of America*, vol. 54, pp. 844-845, 1964.
- [119] Pantinakis A. and Kortsalioudakis N.: A simple high-sensitivity radiometer in the infrared for measurements of the directional total emissivity of opaque materials at near-ambient temperatures, *International journal of thermophysics*, vol. 22, no. 6, pp. 1843-1854, 2001.
- [120] Perlmutter M. and Howell J. R.: A strongly directional emitting and absorbing surface, *Journal of heat transfer (Transactions of the ASME)*, vol. 85, series C, no. 3, pp. 282-283, 1963.
- [121] Planck M.: Theory of heat radiation, English translation of "Theorie der Wärmestrahlung", 2nd Ed. 1913, Dover, New York, 1959.
- [122] Prokhorov A. V., Mekhontsev S. N. and Hanssen L. M.: Emissivity modeling of thermal radiation sources with concentric grooves, Presented at the 16th European conference on thermophysical properties, London, UK, 1-4 September 2002.
- [123] Psarouthakis J.: Apparent thermal emissivity from surfaces with multiple v-shaped grooves, *AIAA Journal*, vol. 1, no. 8, pp. 1879-1882, 1963.
- [124] Puscasu I., Schaich W. and Boreman G. D.: Resonant enhancement of emission and absorption using frequency selective surfaces in the infrared, *Infrared physics and technology*, vol. 43, pp. 101-107, 2002.
- [125] Ramanathan K. G., Yen S. H. and Estalote E. A.: Total hemispherical emissivities of copper, aluminium and silver, *Applied Optics*, vol. 16, no. 11, pp. 2810-2817, 1977.

- [126] Ravindra N. M., Sopori B., Gokce O. H., Cheng S. X., Shenoy A., Jin L., Abedrabbo S., Chen W. and Zhang Y.: Emissivity measurements and modeling of silicon-related materials: An overview, *International journal of thermophysics*, vol. 22, no. 5, pp. 1593-1611, 2001.
- [127] Roger C. R., Yen S. H. and Ramanathan K. G.: Temperature variation of total hemispherical emissivity of stainless steel AISI 304, *Journal of optical society of America*, vol. 69, no. 10, pp. 1384-1390, 1979.
- [128] Sabuga W. and Todtenhaupt R.: Effect of roughness on the emissivity of the precious metals silver, gold, palladium, platinum, rhodium and iridium; *High Temperatures-High Pressures*, vol. 33, pp. 261-269, 2001.
- [129] Sai H., Yugami H., Akiyama Y., Kanamori Y. and Hane K.: Spectral control of thermal emission by periodic microstructured surfaces in the near-infrared region, *Journal of optical society of America A*, vol. 18, no. 7, pp. 1471-1476, 2001.
- [130] Sai H., Yugami H., Kanamori Y. and Hane K.: Spectrally selective radiators and absorbers with periodic microstructured surface for high temperature applications, Graduate school of engineering, Tohoku University, 01 Aoba, Aramaki, Aoba-ku, Sendai, 980-8579, Japan.
- [131] Sai H., Kanamori Y. and Yugami H.: High-temperature resistive surface grating for spectral control of thermal radiation, *Applied physics letters*, vol. 82, no. 11, pp.1685-1687, 2003.
- [132] Sala A.: Radiant properties of materials, Tables of radiant values for black body and real materials, *Physical sciences data 21*, Elsevier, PWN-Polish scientific publishers-Warsaw, 1986.
- [133] Sanchez-Gil J. A. and Nieto-Vesperinas M.: Light scattering from random dielectric surfaces, *Journal of optical society of America A*, vol. 8, pp. 1270-1286, 1991.
- [134] Sato T.: Spectral emissivity of silicon, *Japanese journal of applied physics*, vol. 6, no. 3, pp. 339-347, 1967.
- [135] Seifert A., Sachsenhofer F., Krishnan S. and Pottlacher G.: Microsecond laser polarimetry for emissivity measurements on liquid metals at high temperatures – application to Niobium, *International journal of thermophysics*, vol. 22, no. 5, pp. 1537-1547, 2001.
- [136] Shchegrov A. V., Joulain K., Carminati R. and Greffet J. J.: Near-field spectral effects due to electromagnetic surface excitations, *Physical review letters*, vol. 85, no. 7, pp.1548-1551, 2000.

- [137] Siegel R. and Howell J. R.: Thermal radiation heat transfer, 2nd Ed., Mc Graw Hill, New York, 1981.
- [138] Siegel R., Howell J. R. and Lohrengel J.: Wärmeübertragung durch Strahlung, Teil 1: Grundlagen und Materialeigenschaften, Springer-Verlag, Berlin, Heidelberg, 1988.
- [139] Siegel R., Howell J. R. and Lohrengel J.: Wärmeübertragung durch Strahlung, Teil 2: Strahlungsaustausch zwischen Oberflächen und in Umhüllungen, Springer-Verlag, Berlin, Heidelberg, 1991.
- [140] Smetana W. and Reicher R.: A new measuring method to determine material spectral emissivity, Measurement Science and Technology, vol. 9, pp. 797-802, 1998.
- [141] Sparrow E. M. and Lin Lin S. H.: Absorption of thermal radiation in a V-groove cavity, International journal of heat mass transfer, vol. 5, pp. 1111-1115, 1962.
- [142] Sparrow E. M. and Gregg J. L.: Radiant emission from a parallel-walled groove, Journal of heat transfer (Transactions of the ASME), vol. 84, series C, pp. 270-271, 1962.
- [143] Sparrow E. M. and Jonsson V. K.: Thermal radiation absorption in rectangular-groove cavities, Journal of applied mechanics (Transactions of the ASME), vol. 30, series E, pp. 237-244, 1963.
- [144] Stierwalt D. L., Bernstein J. B. and Kirk D. D.: Measurement of the infrared spectral absorptance of optical materials, Applied optics, vol. 2, no. 11, pp. 1169-1173, 1963.
- [145] Stratton J. A.: Electromagnetic theory, International series in pure and applied physics, McGraw-Hill, New York, 1941.
- [146] Tanaka H., Sawai S., Morimoto K. and Hisano K.: Evaluation of hemispherical total emissivity for thermal radiation calorimetry, International journal of thermophysics, vol. 21, pp. 927-940, 2000.
- [147] Tang K. and Buckius R. O.: Bi-directional reflection measurements from two-dimensional microcontoured metallic surfaces, Microscale thermophysical engineering, vol. 2, pp. 245-260, 1998.
- [148] Tang K. and Buckius R. O.: The geometric optics approximation for reflection from two-dimensional random rough surfaces, International journal of heat and mass transfer, vol. 41, no. 13, pp. 2037-2047, 1998.
- [149] Tank V.: Infrarottemperaturmessung mit selbsttätiger Berücksichtigung des Emissionsgrades, Forschungsbericht Nr. DFVLR-FB-88-22, Cologne, 1988.
- [150] Teng Y. Y. and Stern E. A.: Plasma radiation from metal grating surfaces, Physical review letters, vol. 19, no. 9, pp. 511-514, 1967.

- [151] Touloukian Y. S., DeWitt D. P. and Hertzberg R. S.: "Thermal radiative properties", in "Thermophysical properties of matter- The TPRC data series", vols. 7-9, IFI/Plenum, New York, 1970-1972.
- [152] Verein Deutscher Ingenieure, VDI-Gesellschaft Verfahrenstechnik und Chemieingenieurwesen: VDI-Wärmeatlas, 8. Auflage, VDI-Verlag, Düsseldorf, 1997.
- [153] Wagatsuma K., Monma K. and Suetaka W.: Infrared emission spectra of thin films on metal surfaces by a polarization modulation method, Applications of surface science, vol. 7, pp. 281-285, 1981.
- [154] Wakabayashi H. and Makino T.: A new spectrophotometer system for measuring thermal radiation phenomena in a 0.30 – 11 μm wavelength region, Measurement science and technology, vol. 12, no. 12, pp. 2113-2120, 2001.
- [155] Wakabayashi H. and Makino T.: A thermal radiation spectroscopy technique for diagnosis of temperature and microstructure of real surfaces, The 6th ASME-JSME thermal engineering joint conference, March 16-20, 2003.
- [156] Wang T.K. and Zemel J. N.: Polarized spectral emittance from periodic micromachined surfaces. III. Undoped silicon: the normal direction in shallow lamellar gratings, Infrared Physics , vol. 32, pp. 477-488, 1991.
- [157] Wang T.K. and Zemel J. N.: Polarized spectral emittance from periodic micromachined surfaces. IV. Undoped silicon: normal direction in deep lamellar gratings, Applied Optics , vol. 31, pp. 732-736, 1992.
- [158] Wang T.K. and Zemel J. N.: Polarized spectral emittance from periodic micromachined surfaces. V. Undoped silicon: angular measurement in shallow lamellar gratings, Infrared Physics , vol. 32, pp. 2021-2025, 1993.
- [159] Wolf E.: A generalized extinction theorem and its role in scattering theory, In coherence and quantum optics, Edited by E. Wolf, Plenum, pp. 339-357, 1973.
- [160] Wood R. W.: On a remarkable case of uneven distribution of light in a diffraction gratings spectrum, Phil. Mag., vol. 4, pp. 396-402, 1902.
- [161] Wutz M., Adam H. and Walcher W.: Theorie und Praxis der Vakuumtechnik, 4. Auflage, Friedr. Vieweg & Sohn Verlagsgesellschaft mbH, Braunschweig, 1988.
- [162] Yi F., Xiaogang S. and Righini F.: A multiwavelength reflectometric technique for normal spectral emissivity measurements by a pulse-heating method, International journal of thermophysics, vol. 24, no. 3, pp. 849-857, 2003.

- [163] Zaworski J. R., Welty J. R. and Drost M. K.: Measurement and use of bi-directional reflectance, *International journal of heat mass transfer*, vol. 39, no. 6, pp. 1149-1156, 1996.
- [164] Zhang Q. C., Simko M., Dey C. J., Collins R. E., Turner G. M., Brunotte M. and Gombert A.: The measurement and calculation of radiative heat transfer between uncoated and doped tin oxide coated glass surfaces, *International journal of heat mass transfer*, vol. 40, no. 1, pp. 61-71, 1997.
- [165] Zhimin Z.: A method for calculating the effective emissivity of a groove structure, *SPIE*, vol. 810, *Optical systems for space applications*, pp. 270-277, 1987.
- [166] Zou J., Balberg M., Byrne C., Liu C. and Brady D. J.: Optical properties of surface micromachined mirrors with etch holes, *Journal of microelectromechanical systems*, vol. 8, no. 4, pp. 506-513, 1999.

Curriculum Vitae

Name: Lila Raj Koirala
Date of Birth: 02.10.1967
Place of Birth: Pokhara 5, Kaski, Nepal
Marital Status: married, two children
Nationality: Nepali

Year	Education	Professional Experience
1972-1975	Primary School in Pokhara, Nepal	
1976-1979	Lower Secondary School in Pokhara, Nepal	
1980-1983	Higher Secondary School in Pokhara, Nepal	
1984-1986	Studies leading to Intermediate for Science (I. Sc.) at Prithwi Narayan Campus Pokhara, Nepal	
1987-1988	Studies leading to Bachelor of Science (B. Sc.) at Amrit Science Campus Kathmandu, Nepal	
since Dec. 1988		Employee of Sundarijal Arsenal Office, Royal Nepalese Army, Kathmandu, Nepal
1990-1994	Studies leading to degree of Diplomingenieur (Dipl.-Ing.) at the University of Federal Armed Forces Hamburg, Germany	
1994-2001		Head of Machine Tool Production Department at Sundarijal Arsenal Office, Royal Nepalese Army, Kathmandu, Nepal
2001-2004	Dissertation at the Institute of Thermodynamics, Helmut-Schmidt University / University of Federal Armed Forces Hamburg, Germany	Research Assistant at the Institute of Thermodynamics, Helmut-Schmidt University / University of Federal Armed Forces Hamburg, Germany